BEATRIZ MARIA CAMPOS ESTRADA, MSci

FROM DUSTY TAILS TO CLOUDY SKIES

Exploring exoplanetary environments through self-consistent modelling

DOCTORAL THESIS

to achieve the university degree of
Doctor of Philosophy at the University of Copenhagen
and
Doktor der Naturwissenschaften at the Graz University of Technology

submitted to the

PhD School of The Faculty of Science, University of Copenhagen

and the

Graz University of Technology

Supervisors

Prof. Uffe Gråe Jørgensen
Niels Bohr Institute, Faculty of Science, University of Copenhagen
and
Univ.-Prof. Dr.rer.nat. Christiane Helling
Institute of Theoretical and Computational Physics, Graz University of Technology

August 2024

Beatriz Campos Estrada is part of the CHAMELEON MC ITN EJD which received funding from the European Union's Horizon 2020 research and innovation programme under the Marie Sklodowska-Curie grant agreement no. 860470.

All illustrations by Isabel Campos.

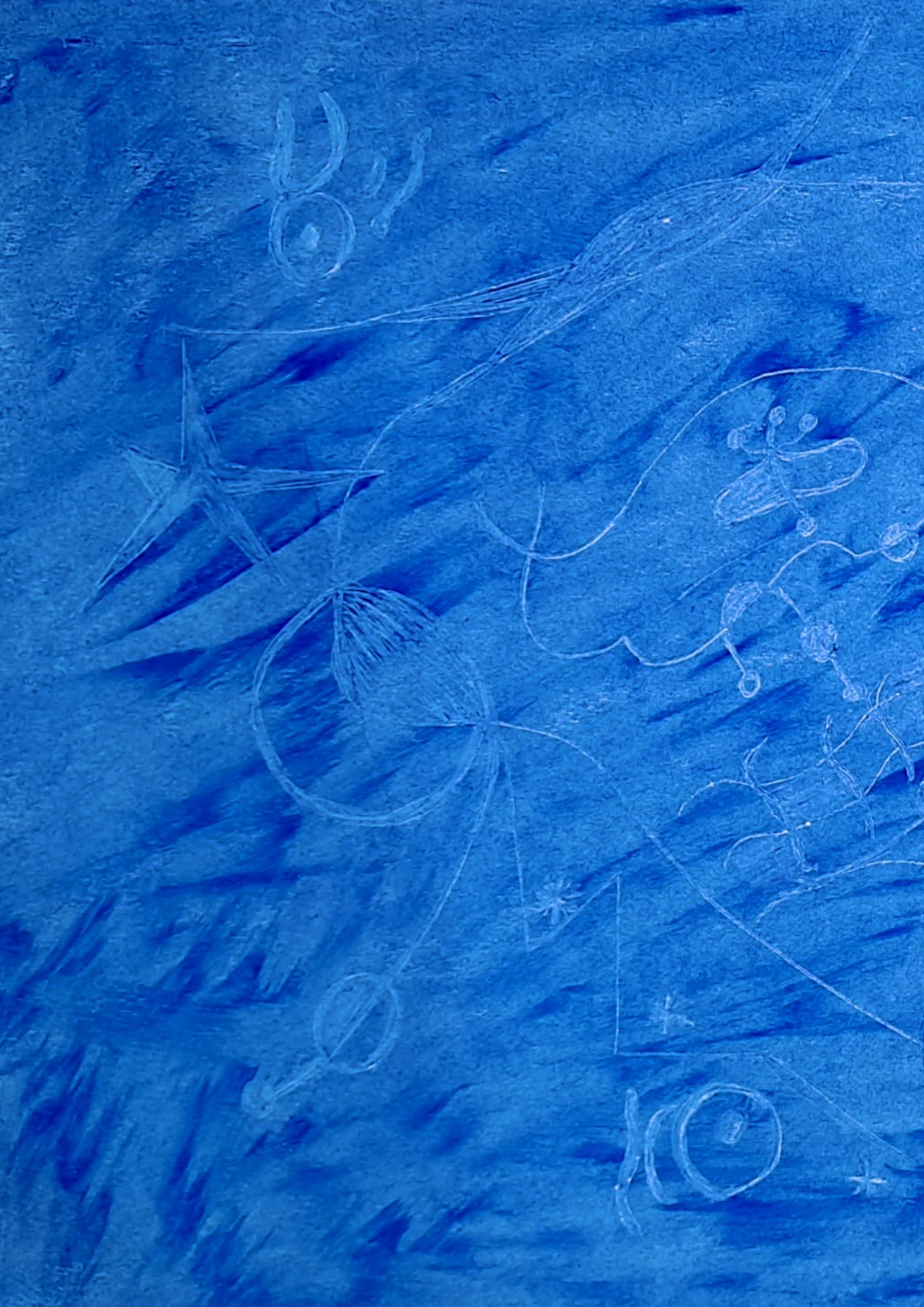

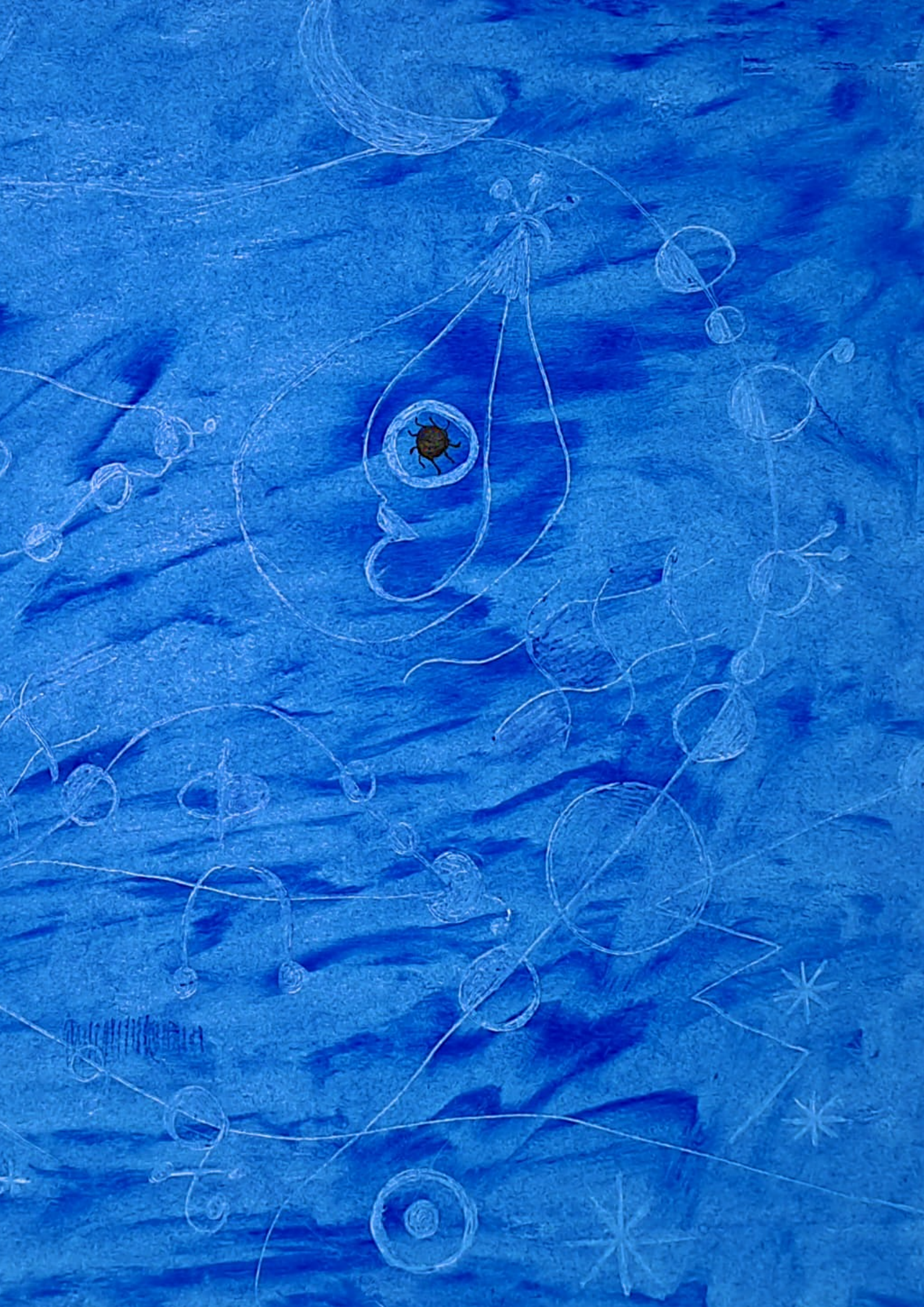

Para o Di
e para a minha mãe.

Se podes olhar, vê.
Se podes ver, repara.

— Livro dos Conselhos,
in *Ensaio sobre a Cegueira* de José Saramago (1995)

Acknowledgements

Há males que a gente pode escolher,
outros só servem para nos juntar.

— Slow J, in *Nascidos e Criados*

This thesis is the result of my work, but it would not have been possible without the incredible support system I had: my friends (i.e., my chosen family), my partner, my family, and my therapist (shout-out to Darina!). **You cannot do science on your own.** I think this is the message I would like anyone reading this to take home.

I have many people I would like to thank, but I have never had any doubts about who I would like, and need, to thank first. James (Owen), I would not have gotten here without you. Thank you for introducing me to the world of exoplanets and for always believing in me. I feel extremely grateful and lucky to have had you as a mentor. Your passion for astrophysics was contagious enough to convince me to pursue this PhD, and here I am. However, I would not have been able to do any of it without your support, and I am not even sure if I will ever be able to thank you enough. It is people like you who make me believe academia can still be a nice place and that doing science for the rest of my life is not just a dream, but it can be a reality. Thank you James.

Max, Maxi, Maximilian: do I even dare to ask how hard it must have been to be with me over these past four years? And yet you were always there, for the good, the bad, and the ugly, always saying "you can do it baby!". Max, I did it! Thank you for always supporting me throughout this insane lifestyle, with not so much work-life balance at times. I will try my best to not fall asleep while coding during my postdoc, and to make sure I always drink my coffee in the morning. Thank you for always holding my hand, and keeping me down to earth. I cannot thank you enough for always backing me up and coming with me where I go. I love you

very much, and I hope you keep holding my hand. I promise I will always hold yours.

This next paragraph will be in portuguese, but for context, I am thanking the person that I believe made me into who I am today: my mum. Isabel, mais conhecida como Guedes nos últimos meses, mãe querida, amo-te muito. Obrigada por tudo o que fizeste e fazes por mim. Tenho a certeza de que uma das maiores razões pelas quais estou onde estou é a maneira como me educaste, mas também todo o amor e carinho que me deste e dás. Sem amor, ninguém faz nada da vida. Dediquei a tese ao Di, mas também a ti, porque tu e o Di foram as pessoas que sempre acreditaram em mim, mesmo quando eu não acreditei em mim própria. Obrigada, mãe, és a maior. Tenho um prazer imenso em ter as tuas ilustrações na tese. E já está, está feito!

Another one in portuguese: for context, I am thanking Di, my grandpa who passed away during my PhD. Di, onde quer que esteja, ou não esteja, obrigada. Tenho saudades suas, mas levo-o comigo sempre. As primeiras memórias que tenho de alguém a celebrar e a puxar por mim são suas. Está gravado no meu cérebro quando me ligou uma semana antes de partir e me disse: "Eu sempre acreditei em ti". Eu sei que sim, Di. Obrigada por ter tomado conta de mim, por ter brincado comigo e por me ter ajudado a sonhar. Quando não tinha mais por onde pegar, lembrei-me sempre do que me disse e continuei. O resultado é esta tese e, por isso, dedico-a a si.

I was lucky to make really good friendships along the journey of my PhD. I would not have finished this PhD without these friends. Fran, I lost count of how many times I texted you going "tiooooooo" and proceeded to annoy you with random physics questions or just telling you that I was ready to give up. For all those times I texted, you always had a good answer and reasons for why I should keep going and believe in myself. You were a pillar for me during this PhD, and I am only sad I did not get to meet you earlier. Your calmness and confidence gave me a new perspective on academic life, and I genuinely want to be more like you. The manner in which you balance your love for astrophysics with the rest of your life is incredible, and meanwhile, you are always there for all your friends. I am excited about the potential of continuing to do science with you while being best friends. You make me want to give the best of myself in everything. Gracias por todo, tio. Te quiero.

Flavia and Marie, thank you, gringas, for always being there for me, for watching me cry a thousand times over broken code in that office, for a great camping trip, and for many great dinners, coffees, and whatever else. You became like the sisters I never had. You are chosen family, and I think I chose pretty well. Remember, we can always have a farm in the Swiss Alps if everything goes wrong.

James (Rogers): I have a vivid memory of having a monumental breakdown at Exo IV, and you just sitting with me, telling me all the reasons why I am and will be a great scientist. I'm still not 100% sure I agree, but at that moment, it changed my brain chemistry and gave me a new perspective on what I can be in

the exoplanet world. We both know I would not have such a good postdoc lined up if it weren't for you and all your support. Thank you for always being there for the crisis club and for always answering my desperate messages with silly requests (including the hundreds of times I asked you for good references while writing this thesis). I hope I get to do cool science with you in the future!

David (Lewis) and Dominic: thank you for bringing the British spirit to Graz. I guess more importantly, thank you for teaching me all about cloud microphysics. I hope the opportunities come to do science with both of you in the near future. David, could you please let me know where you get your patience for me? I need some of it. It was a pleasure to do science with you, and if you ask me, I think we did pretty decent work for two early-career scientists. Thank you for helping to proofread this thesis and, of course, for helping shape the `MSG` cloudy grid paper into what it is. Also, thank you for letting me open a lot of the advent calendar duckies - that really helped my mental health (I say as Queen Elizabeth the ducky stares at me).

I must thank all the CHAMELEON ESRs: guys, what we have achieved is amazing, and I believe the friendship we've built is beautiful. I hope to see you at a yearly retreat. Thank you Pieter for the incredible opportunity to participate in the Exploring Exoplanets exhibition, it was a great experience and you did something brilliant there. Also, as the most senior ESR, thank you for calling me out when I was childish. Thank you to all the other great friends I made in Copenhagen, in particular Courtney, Jesper, Joana, Georgy, and Elsa. Thank you also to the IWF crew, in particular Helena, Sven, Nanna, Nidhi, Till, Sandra, Irene, Andreas, Jayatee, Patrick, Thorsten, and Kundan.

Of course, I had a life before the PhD, and some very important people from that life remain with me until today. They have always believed in me and helped me get where I am. Martim, where do I even start? It has been 11 years of friendship, and what a joy. You are family to me. I will never forget your reaction when you found out I got into Imperial - I had never felt that supported or loved by someone other than my mum (even though you still struggle up to today to say how you feel, but that is a conversation for another day). Not sure how to feel about the fact that you told me 20 minutes ago that you fell asleep while reading my thesis introduction... I guess I still love you even though you do not love exoplanets? Anyways, thank you for always being there; I can't wait to have you "by my side" forever. Sorry, not sorry.

To my Imperial family: Rohan, David (Dai), and Clara. Guys... Baby Astro did it! I must admit it is the hardest to write a thank you to you three. You were there for all of it. You saw it all. And you never left my side, stopped helping me, hyping me up, or calling me out. I would not have survived Imperial without you, and most certainly not this PhD. I still find it insane we all decided to do PhDs, but I guess that sort of defines our ambition and passion for what we do. I love you guys. I did this for us. Do not let me down; we must become the four random PhDs.

I would like to thank Richard (Booth) for, on a random day in June(?) 2023, when I came to visit Leeds for Exoclimes Connect, sitting down with me and helping me find a way of making the `MSG` cloudy models converge. This changed the direction of my PhD, and I am not sure I would have had a thesis to write otherwise. Thank you, Richard, for your patience and help that day. You taught me how to approach a certain numerical problem, but more than anything, showed me that collaboration and asking for help are crucial in science.

Thank you to everyone that helped me with all the bureaucracy at the universities, or unresponsive people, in particular Sylvia, Anja and Cosima.

I would like to thank Uffe and Christiane for giving me the opportunity to be a CHAMELEON ESR. It was a challenging and ambitious PhD project. Thank you Uffe for making me notice that the reason we get sad and miss people when they pass away is because we have incredible memories with them. This really helped me put my grandpa's passing in a more positive picture. Thank you Christiane for the interesting discussions we've had and for always having your door open. I have never looked at a cloud in the same manner since having you as a supervisor.

Thank you to all my family, in particular my dad and my aunt (portuguese incoming). Pai, obrigada pela oportunidade de fazer o curso na Imperial, e de teres apostado em mim. Tia Bebé, obrigada por acreditar sempre em mim. E a alguém que nem sei bem como agradecer mas acho que o devo fazer: obrigada Helder.

Thank you also to the Moynan family: Peter, Sue and James, you are great and I am very thankful to have you in my life.

I want to thank the artists I listened to on repeat over this PhD, and to celebrate that I made a Spotify playlist with some of the songs that were the soundtrack of my PhD, enjoy: The PhD Soundtrack.

Finally, I would like to quote my fellow chameleon, Nanna, and say "good job me". As Beyoncé says, "I'ma keep running 'cause a winner don't quit on themselves".

Abstract

There are now over 5600 known exoplanets, and their characterisation is of primary importance to better understand the still uncertain planet formation processes. However, exoplanet characterisation presents some challenges. We often encounter observational limitations or the existence of complex atmospheric processes which limit our ability to characterise exoplanets. In this thesis, we consider how dust condensation in distinct exoplanetary environments can help us reach a better understanding of the composition of exoplanet's interiors, surfaces, and atmospheres.

In the first part of this thesis, we investigate the composition of small close-in exoplanets via modelling catastrophically evaporating rocky planets. A catastrophically evaporating planet is a low-mass (similar to Mercury), evaporating, ultra-short-period planet (orbital period of less than 1 day) with a comet-like tail of dust. Catastrophically evaporating planets offer a unique window into constraining the composition of small close-in planets. The dust in the comet-like tail originates from the planet's molten day-side surface. The light curves of these planets are shaped by the optical properties of the dust. It is then possible to constrain the dust composition, and therefore the planet's surface composition, via comparing synthetic light curves to the observed ones.

We present a new self-consistent model of the dusty-tails: we physically model the trajectory of the dust grains after they left the gaseous outflow including an on-the-fly calculation of the dust cloud's optical depth. This is the first time the dust cloud's optical depth is modelled self-consistently. We investigate two planets in detail, KIC 1255 b and K2-22 b. The planet KIC 1255 b presents a trailing tail of dust, whilst K2-22 b presents a leading tail of dust. For both planets, we find the dust is likely composed of magnesium-iron silicates (olivine and pyroxene), consistent with an Earth-like composition. We constrain the dust to be micron sized (1.25 - 1.75 μm) and the average planetary mass-loss rate to be approximately $\sim 3\, M_{\oplus}\mathrm{Gyr}^{-1}$. We conclude the origin of the leading tail of dust of K2-22 b is likely

a combination of the geometry of the outflow and a low radiation pressure force to stellar gravitational force ratio. In addition to this, the optical depth of the dust cloud is a factor of a few at the vicinity of the planet. The composition constraint we find supports the recently suggested idea that the dusty outflows of these planets go through a greenhouse effect–nuclear winter cycle, which gives origin to the observed transit depth time variability. Magnesium-iron silicates have the necessary visible-to-infrared opacity ratio to give origin to this cycle in the high mass-loss state.

In the second part of the thesis, we explore microphysical cloud formation in substellar atmospheres of self-luminous objects. Clouds present a challenge to atmospheric characterisation as they can often hide spectral features of the gaseous components of atmospheres. However, we have entered an era with JWST where silicate clouds are detectable in the atmospheres of planetary-mass companions. This allows for a unique opportunity to test our understanding of cloud formation, and to help us characterise cloudy atmospheres. To date, no forward model has been able to reproduce the $\sim 10\,\mu$m silicate absorption feature detected in the emission spectra of these objects.

We compute a new grid of self-consistent 1D cloudy radiative-convective substellar atmospheres: the `MSG` cloudy grid. The grid accounts for both cloud microphysics and cloud radiative feedback (i.e., self-consistency). We use the `MSG` model which couples the atmospheric model `MARCS`, with the equilibrium chemistry model `GGchem`, and the microphysical cloud formation model `DRIFT`. To mitigate typical convergence problems, we apply a novel algorithm based on control theory. The grid spans the parameter space of brown dwarfs and directly imaged planets. We investigate the impact of cloud opacities on the resulting cloud radiative feedback on the atmosphere. We compute synthetic atmosphere spectra for each model to explore the observable impact of the cloud microphysics. The impact of choosing different nucleation species (TiO_2 or SiO) and the effect of less efficient atmospheric mixing on these spectra are also explored.

The new `MSG` cloudy grid, which utilises TiO_2 nucleation, produces spectra that appear redder in the near-infrared compared to the known substellar atmospheres. We observe that models incorporating SiO nucleation and those with reduced mixing efficiency exhibit less redness in the near-infrared. Additionally, we find that detached convective zones emerge at effective temperatures of $T_{\rm eff} \leq 1600\,$K due to a backwarming effect caused by the clouds. Unfortunately, our grid fails to replicate the silicate features observed in recent JWST data and *Spitzer* archival observations. We discuss in detail further research that could more accurately represent the effects of convection in cloud-forming regions and propose steps to better capture the silicate cloud feature.

Resumé

Vi kender idag mere end 5600 exoplaneter, og karakterisering af dem er af vital betydning for at opnå en bedre forståelse af dannelsesprocessen for planeter. Karakterisering af exoplaneter har imidlertid nogle udfordringer. Vi støder ofte på begrænsninger i observationerne eller opdagelsen af komplekse atmosfæriske processer som begrænser vores muligheder for at karakterisere exoplaneterne. I indeværende afhandling ser vi på hvordan støvkondensation i exoplaneternes forskelligartede omgivelser kan hjælpe os til en bedre forståelse af sammensætningen af exoplaneternes indre, overflade, og atmosfærer.

I den første del af afhandlingen, undersøger vi sammensætningen af små exoplaneter i små baner om deres stjerne via modellering af såkaldte katastrofisk fordampende klippeplaneter. En katastrofisk fordampende planet er en lav-masse (fx som Merkur), fordampende, ultra-kort-periode planet (med omløbstid mindre en 1 dag) med en kometagtig hale af støv. Katastrofisk fordampende planeter giver os et unikt vindue til at indkredse værdierne for sammensætningen af små planeter i små baner. Støvet i den kometlignende hale har sin oprindelse i planetens glohede flydende dag-side overflade. Lyskurven af den slags planeter bestemmes af de optiske egenskaber af støvet. Det er derfor muligt at indkredse støv-sammensætningen, og derfor også planetens overflade-sammensætning, ved at sammenligne beregnede lyskurver med de observerede.

Vi præsenterer her en ny selvkonsistent model for støvhaler: vi modellerer den fysiske bane af støvkornene efter de har dekoplet sig fra den udstrømmende gas, inklusiv en simultan beregning af støvskyens optiske dybde. Det er første gang en støvskys optiske dybde er beregnet selvkonsistent. Vi undersøger to planeter i detaljer, KIC 1255 b og K2-22 b. Planeten KIC 1255 b har en bagudrettet ("slæbende") støvhale i forhold til baneretningen, mens K2-22 b har en fremad rettet ("ledende") støvhale. For begge planeterne, finde vi at støvet sandsynligvis består af magnesium-jern silikater (olivin og pyroxen), i lighed med Jordens sammensætning. Vi estimerer støvkornene til at være af mikrometer størrelse (1.25

til 1.75 μm) og middel massetabet fra planeterne til at være ca $3\,M_{\oplus}\mathrm{Gyr}^{-1}$. Vi konkluderer at oprindelsen af af den fremadrettede støvhale fra K2-22 b sandsynligvis er en kombination af geometrien af udstrømningen og et lavt strålingstryk i forhold til tyngdekraftens træk. Derudover er den optiske dybde af støvskyen nogle størrelsesordner mindre end i nærheden af planeten. De afgrænsninger vi finder i værdien af sammensætningen understøtter den ide som er fremsat for nyligt, at støv udstrømningerne gennemgår en drivhus-drevet nuklear-vinter cyklus, som giver anledning til den observerede variabilitet i dybden af formørkelses lyskurven. Magnesium-jern silikater har det nødvendige forhold mellem synlig og infrarød opacitet til at forårsage cyklusen i høj-masse-tabs tilstanden.

I den anden del af afhandlingen, undersøger vi mikrofysiken i skydannelsen i atmosfæreren af sub-stellare selvlysende objekter. Skyer repræsenterer en udfordring i karakteriseringen af atmosfæren, eftersom de ofte skygger for de spektrale træk af gaskomponenten af atmosfæren. Ikke destomindre er vi nu i en tid hvor JWST gør det muligt at detektere silikat-skyer i atmosfæren af planet-masse objekter. Det åbner en unik mulighed for at teste vores forståelse af skydannelses processen, og for at hjælpe os i at karakterisere skyrige atmosfærer. Indtil idag har ingen selvkonsistent model været istand til at reproducere det $\sim 10\,\mu$m absorptions træk man ser i emissionen fra den slags objekter.

Vi har beregnet et netværk af selvkonsistente 1D skyrige strålings-konventions sub-stellare atmosfæremodeller: `MSG` sky netværket. Modellerne tager hensyn til både mikrofysikken i skydannelsen og strålings feed-back fra skyerne (dvs selvkonsistens). Vi tager udgangspunkt i `MSG` modellerne, som sammenkobler `MARCS` atmosfære modeller med `GGchem` modeller for kemisk ligevægt og `DRIFT` modelleringen af mikrofysikken i skydannelse. For at afbøde typiske konvergensproblemer anvender vi en ny algoritme baseret på kontrol-teori. Netværket strækker sig fra brune dværge til direkt-observerbare exoplaneter. Vi undersøger inflydelsen af sky opaciteter på skyernes strålings feed-back på atmosfæren. Vi regner syntetiske atmosfære spektra for hver model for at undersøge den observerbare indflydelse af skyernes mikrofysik. Betydningen af at vælge forskellige nukleerings kerner (TiO_2 eller SiO) og den spektrale effekt af en formindsket effektiv atmosfærisk opblending undersøges også.

Det nye `MSG` sky-netværk, som anvender sig af TiO_2 nuklering, producerer spektra der fremtræder mere røde i det nær-infrarøde sammenlignet med kendte substellare atmosfærer. Vi bemærker at modeller som inkorporerer SiO nukleering, og dem med reducerede opblandings effektivitet, udviser mindre rødlighed i det nær-infrarøde. Derudover finder vi at separate konvektionszoner opstår ved effektive temperaturer på $T_{\mathrm{eff}} \leq 1600\,\mathrm{K}$ pga effekter af bagudrettet opvarmning ("backwarming-effekter") som skyldes skyerne. Desværre kan vores net af modeller ikke reproducere de silikat træk som er observeret i de nyeste JWST data og i Spitzer's arkiv data. Vi diskuterer i detaljer fremtidige undersøgelser som kunne give en mere præcis beskrivelse af konvektionen i skydannelses områderne, og vi foreslår skridt som bedre kunne reproducere de spektrale træk af silikat skyer.

Abstrakt

Es gibt inzwischen über 5600 bekannte Exoplaneten. Ihre Charakterisierung ist von größter Bedeutung, um die noch immer unsicheren Prozesse der Planetenentstehung besser zu verstehen. Jedoch bringt diese Charakterisierung einige Herausforderungen mit sich. So stoßen wir häufig an die Grenzen der Beobachtbarkeit. Gleichzeitig beschränkt die Existenz komplexer Prozesse in den Atmosphären von Exoplaneten unsere Fähigkeit der Charakterisierung dieser Planeten. In dieser Arbeit untersuchen wir, wie die Kondensation von Staub in verschiedenen Exoplanetenumgebungen uns helfen kann, die Zusammensetzung des Inneren, der Oberflächen und der Atmosphären von Exoplaneten besser zu verstehen. Im ersten Teil der Arbeit untersuchen wir die Zusammensetzung kleiner Exoplaneten mit kurzen Umlaufzeiten, indem wir katastrophal verdampfende Gesteinsplaneten modellieren. Unter katastrophal verdampfenden Gesteinsplaneten versteht man verdampfende Planeten mit Massen ähnlich zu Merkur und ultrakurzer Umlaufzeiten von weniger als einem Tag, die einen kometenartigen Staubschweif besitzen. Diese Planeten bieten einen einzigartigen Einblick in die Zusammensetzung kleiner Planeten mit kurzen Umlaufzeiten. Der Staub, aus dem der kometenartigen Schweif besteht, stammt von der geschmolzenen Oberfläche der Tageseite des Planeten. Die Lichtkurven dieser Planeten werden durch die optischen Eigenschaften des Staubs beeinflusst. Es ist daher möglich, die Staubzusammensetzung und damit die Zusammensetzung der Planetenoberfläche einzugrenzen, indem die beobachteten Lichtkurven mit synthetische Lichtkurven verglichen werden. Wir präsentieren ein neues selbstkonsistentes Modell der Staubschweife. Wir modellieren die physikalische Flugbahn der Staubkörner nachdem sie den Gasausfluss des Planeten verlassen haben und die optischen Tiefe der Staubwolke. Dieses Modell ist das erste Modell, in dem die optische Tiefe der Staubwolke selbstkonsistent berechnet wird. Wir untersuchen zwei Planeten, KIC 1255 b und K2-22 b, genauer. Der Planet KIC 1255 b weist einen nachfolgenden Staubschweif auf, während K2-22 b einen vorauseilenden Staubschweif aufweist. Bei beiden Planeten stellen wir fest, dass der Staub wahrscheinlich aus Magnesium-Eisen-Silikaten (Olivin und

Pyroxen) besteht. Dies stimmt mit einer erdähnlichen Zusammensetzung überein. Wir begrenzen die Größe der Staubkörner auf Mikrongröße (1,25 - 1,75 μm). Die durchschnittliche Massenverlustrate der Planeten ist circa $\sim 3 M_{\oplus}$ Gyr^{-1}. Wir kommen zu dem Schluss, dass der Ursprung des vorauseilenden Staubschweifs von K2-22 b wahrscheinlich in einer Kombination aus der Geometrie des Ausflusses und einem niedrigen Verhältnis der Strahlungsdruckkraft zu der Gravitationskraft des Sternes liegt. Darüber hinaus ist die optische Tiefe der Staubwolke in der Nähe des Planeten höher als im Äußeren der Wolke. Die von uns gefundene Staubzusammensetzung unterstützt die kürzlich vorgeschlagene Theorie, dass die staubigen Ausflüsse dieser Planeten einen Treibhauseffekt-Nuklearen-Winter-Zyklus durchlaufen, der die beobachtete zeitliche Variabilität der Transittiefe verursacht. Magnesium-Eisen-Silikate weisen das notwendige Verhältnis von sichtbarer zu infraroter Opazität auf, um diesen Zyklus bei hohem Massenverlustraten zu verursachen.

Im zweiten Teil der Arbeit untersuchen wir die mikrophysikalische Wolkenbildung in Atmosphären von substellaren, selbstleuchtenden Objekten. Wolken stellen eine Herausforderung für die Charakterisierung von Atmosphären dar, da sie häufig spektrale Merkmale der gasförmigen Bestandteile von Atmosphären verbergen können. Mit JWST sind wir jedoch in eine Ära eingetreten, in der Silikatwolken in den Atmosphären von Objekten mit planetarer Masse beobachtbar sind. Dies bietet eine einzigartige Gelegenheit, unser Verständnis der Wolkenbildung zu testen, was uns bei der Charakterisierung bewölkter Atmosphären hilft. Bisher konnte jedoch kein Vorwärtsmodell das in den Emissionsspektren dieser Objekte festgestellte Absorptionsmerkmal bei $\sim 10\,\mu$m reproduzieren. Wir berechnen neue Tabellen von selbstkonsistenten 1D-Modellen von substellaren Atmosphären im Strahlungsgleichgewicht mit Wolken: Das `MSG` cloudy grid. Die Modelle berücksichtigt sowohl die Mikrophysik von Wolken als auch die Wolken-Strahlungs-Rückkopplung (d.h. Selbstkonsistenz). Wir verwenden das `MSG`-Modell, dass das Atmosphärenmodell `MARCS` mit dem Gleichgewichtschemiemodell `GGchem` und dem mikrophysikalischen Wolkenbildungsmodell `DRIFT` verbindet. Um typische Konvergenzprobleme zu mildern, benutzen wir einen neuartigen Algorithmus auf Basis der Kontrolltheorie. Das Tabellen erstrecken sich über den Parameterraum von Braunen Zwergen und direkt beobachteten Planeten. Wir untersuchen die Auswirkungen der Opazität von Wolken auf die resultierende Wolken-Strahlungs-Rückkopplung in der Atmosphäre. Für jedes Model berechnen wir synthetische Spektren der Atmosphäre, um die beobachtbaren Auswirkungen der Mikrophysik von Wolken zu untersuchen. Die Auswirkungen der Wahl verschiedener Arten von Kondensationskeime (TiO_2 oder SiO) und einer weniger effizienten atmosphärischen Durchmischung auf die Spektren werden ebenfalls untersucht. Modelle im neuen MSG cloudy grid, welches die TiO_2 als Kondensationskeime verwenden, erzeugen Spektren, die im Nahinfrarot rötlicher erscheinen als die bekannten substellaren Atmosphären. Modelle, die SiO als Kondensationskeime verwenden und solche mit reduzierter Durchmischungseffizienz, weisen weniger Röte im Nahinfrarot auf. Darüber hinaus stellen wir fest, dass bei effektiven Temperaturen von $T_{\rm eff} \leq 1600\,$K, aufgrund eines durch die Wolken verursachten Rücker-

wärmungseffekts, isolierte Kovenktionszonen entstehen. Leider gelingt es unseren Tabellen nicht, die in den jüngsten JWST-Daten und in den Archivbeobachtungen von *Spitzer* beobachteten Silikatmerkmale zu reproduzieren. Wir diskutieren ausführlich weitere Forschungsarbeiten, welche die Auswirkungen der Konvektion in wolkenbildenden Regionen genauer untersuchen können und schlagen Schritte vor, mit denen die Eigenschaft der Silikatwolken besser zu erfassen sind.

Resumo

Atualmente são conhecidos mais de 5600 exoplanetas, e a sua caracterização é de extrema importância para entender melhor os ainda incertos processos de formação planetária. No entanto, a caracterização de exoplanetas apresenta alguns desafios. Frequentemente, enfrentamos limitações observacionais ou a existência de processos atmosféricos complexos que limitam a nossa capacidade de caracterizar exoplanetas. Nesta tese, consideramos como a condensação de poeira em ambientes exoplanetários distintos pode ajudar-nos a alcançar uma melhor compreensão da composição dos interiores, superfícies e atmosferas dos exoplanetas.

Na primeira parte desta tese, investigamos a composição de pequenos exoplanetas rochosos através de modelos de planetas rochosos em evaporação catastrófica. Um planeta em evaporação catastrófica é um planeta com uma massa pequena (semelhante a Mercúrio), em evaporação, com um período orbital extremamente curto, inferior a um dia. Estes planetas apresentam uma cauda de poeira semelhante a um cometa. Os planetas em evaporação catastrófica apresentam uma oportunidade única para estudar a composição de pequenos planetas rochosos. A poeira na cauda tem origem na superfície diurna do planeta. As curvas de luz desses planetas são moldadas pelas propriedades ópticas da poeira. É então possível estudar a composição da poeira, e portanto a composição da superfície do planeta, comparando curvas de luz sintéticas com as observadas.

Apresentamos um novo modelo auto-consistente (*self-consistent*) das caudas de poeira: modelamos fisicamente a trajetória dos grãos de poeira após deixarem o fluxo gasoso, incluindo um cálculo em tempo real da profundidade óptica da nuvem de poeira. Esta é a primeira vez que a profundidade óptica da nuvem de poeira é modelada de forma auto-consistente. Investigamos dois planetas em detalhe, KIC 1255 b e K2-22 b. O planeta KIC 1255 b apresenta uma cauda de poeira que o segue, enquanto K2-22 b apresenta uma cauda de poeira que o precede. Para ambos os planetas, descobrimos que a poeira é provavelmente composta por olivina e piroxena, uma composição semelhante à da Terra. Restringimos o tamanho da

poeira a valores micrométrico entre 1.25 - 1.75 μm e a taxa média de perda de massa planetária a aproximadamente $\sim 3\, M_{\oplus}\mathrm{Gyr}^{-1}$. Concluímos que a origem da cauda de poeira que precede K2-22 b é provavelmente uma combinação da geometria do fluxo gasoso e um rácio reduzido entre a força de pressão de radiação e a força gravitacional estelar. Além disso, a profundidade óptica da nuvem de poeira é acima de 1.0 na proximidade do planeta. A restrição de composição que encontramos suporta a ideia recentemente sugerida de que os fluxos de poeira destes planetas passam por um ciclo de efeito de estufa–inverno nuclear, que dá origem à variabilidade temporal observada na profundidade do trânsito planetário. A olivina e piroxena têm o rácio de opacidade visível-infravermelha necessário para dar origem a este ciclo.

Na segunda parte da tese, exploramos a formação de nuvens microfísicas em atmosferas subestelares de objetos auto-luminosos. As nuvens apresentam um desafio à caracterização atmosférica, porque podem frequentemente ocultar características espectrais dos componentes gasosos das atmosferas. No entanto, com o JWST entrámos numa era em que as nuvens de silicato são detectáveis nas atmosferas de objetos de massa planetária. Este facto permite uma oportunidade única para testar a nossa compreensão da formação de nuvens e para nos ajudar a caracterizar atmosferas de exoplanetas com nuvens. Até à data, nenhum modelo de previsão conseguiu reproduzir a característica de absorção de silicato nos $\sim 10\,\mu$m detectada nos espectros de emissão desses objetos.

Calculamos uma nova grelha auto-consistente e unidimensional de modelos de atmosferas subestelares radiativo-convectivas com nuvens: a *`MSG` cloudy grid*. A grelha tem em conta tanto a microfísica das nuvens como o feedback radiativo das nuvens (ou seja, auto-consistência). Utilizamos o modelo `MSG` que associa o modelo atmosférico `MARCS`, com o modelo de química de equilíbrio `GGchem` e o modelo microfísico de formação de nuvens `DRIFT`. Para mitigar os problemas típicos de convergência, aplicamos um novo algoritmo baseado na teoria de controlo. A grelha abrange o espaço de parâmetros das anãs castanhas e dos planetas diretamente fotografados. Investigamos o impacto da opacidade das nuvens no feedback radiativo resultante sobre a atmosfera. Calculamos espectros sintéticos da atmosfera para cada modelo para explorar o impacto observável da microfísica das nuvens. O impacto da escolha de diferentes espécies de nucleação (TiO_2 ou SiO) e o efeito de uma mistura atmosférica menos eficiente nestes espectros são também explorados.

A *`MSG` cloudy grid* que utiliza a nucleação de TiO_2, produz espectros que parecem mais vermelhos no infravermelho próximo em comparação com as atmosferas subestelares conhecidas. Observamos que os modelos que incorporam a nucleação de SiO e aqueles com eficiência de mistura reduzida exibem menos vermelhidão no infravermelho próximo. Além disso, descobrimos que zonas convectivas destacadas emergem a temperaturas efetivas de $T_{\mathrm{eff}} \leq 1600\,\mathrm{K}$ devido a um efeito de retroaquecimento causado pelas nuvens. Infelizmente, a nossa grelha não consegue replicar as características de silicato observadas em dados recentes do JWST e em observações de arquivo do *Spitzer*. Discutimos em pormenor outras investigações

que poderiam representar com maior precisão os efeitos da convecção em regiões de formação de nuvens e propomos passos para melhor captar a caraterística das nuvens de silicato.

Publications list

Publications part of this thesis

Campos Estrada, B., Lewis, D. A., Helling, Ch., et al. "The `MSG` model for cloudy substellar atmospheres: A grid of self-consistent substellar models with micrphysical cloud formation" (submitted to A&A)

Campos Estrada, B., Owen, J. E., Jankovic, M. R., et al. "On the likely magnesium-iron silicate dusty tails of catastrophically evaporating rocky planets", MNRAS, vol. 528, no. 2, pp. 1249–1263, 2024, doi:10.1093/mnras/stae095

Other publications

Jørgensen, U. G., Amadio, F., **Campos Estrada, B.**, et al. "A grid of self-consistent `MSG` (`MARCS-StaticWeather-GGchem`) cool stellar, sub-stellar, and exoplanetary model atmospheres", arXiv e-prints, 2024, doi:10.48550/arXiv.2407.09397 (accepted for publication in A&A)

Van Eylen V., Astudillo-Defru N., Bonfils X., **et al.** "Masses and compositions of three small planets orbiting the nearby M dwarf L231-32 (TOI-270) and the M dwarf radius valley", MNRAS, vol. 507, no. 2, pp. 2154-2173, 2021, doi:0.1093/mnras/stab2143

Owen, J. E & **Campos Estrada, B.** "Testing exoplanet evaporation with multi-transiting systems", MNRAS, vol. 491, no. 4, pp. 5287-5297, 2020, doi:10.1093/mnras/stz3435

Contents

Acronyms

EGP	Extrasolar giant planet.
HST	Hubble Space Telescope.
LTE	Local thermodynamic equilibrium.
RCE	Radiative-convective equilibrium.
RV	Radial velocity.
TOA	Top of the atmosphere.
USP	Ultra-short-period.

CHAPTER 1

INTRODUCTION

All we have to decide is what to do with the time that is given us.

— Gandalf, in *The Fellowship of the Ring* by J.R.R. Tolkien

The first extrasolar planets (planets outside the Solar System, i.e. exoplanets) were discovered over 30 years ago in 1992. Two exoplanets were observed orbiting the pulsar PSR1257 + 12 by Wolszczan and Frail (1992). Only three years later, in 1995, the first exoplanet orbiting a sun-like star was discovered by Mayor and Queloz (1995), this is the planet 51 Pegasi b. Michel Mayor and Didier Queloz later received the Nobel Prize in Physics in 2019 for this discovery which would come to shed a new light into the community's understanding of planet formation. 51 Pegasi b is a so-called hot Jupiter type exoplanet: a planet with a similar mass and radius to that of Jupiter, but with a fairly short orbital period of typically less than 10 Earth days. The discovery of 51 Pegasi b came as a surprise to the community who did not expect planets of this size to exist in such close-in orbits.

Over the past 30 years, the search for exoplanets has been increasingly prosperous. Many dedicated ground based searches, for example HARPS (Mayor et al., 2003), HAT (Bakos et al., 2002) and WASP (Pollacco et al., 2006), and space missions, for example CoRoT (Fridlund et al., 2006), Kepler (Borucki et al., 2010) and TESS (Ricker et al., 2014), have been very successful and at the time of writing this thesis there are 5690 confirmed exoplanets[1].

In the introduction of this thesis we will discuss the diversity of the exoplanet population, motivate why one should study exoplanets, and discuss the definition

[1] All information regarding the number of confirmed exoplanets has been retrieved from the NASA Exoplanet Archive on 21/07/2024.

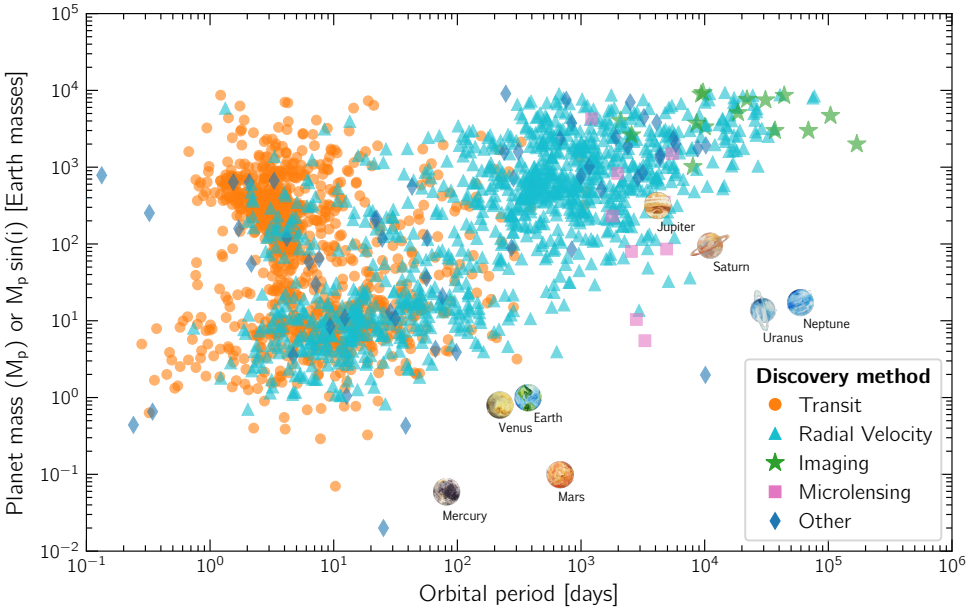

Figure 1.1: The 2496 exoplanets with a mass or minimum mass measurement. Data retrieved from the NASA Exoplanet Archive on 21/07/2024. The Solar System planets are shown for reference. The discovery method of each planet is shown with different symbols and colours: transit - orange circles; radial velocity - cyan triangles; imaging - green stars; microlensing - pink squares; other methods - blue diamonds.

of a planet. Finally we provide an overview and outline of the thesis.

1.1 A universe of alien worlds

Figure 1.1 shows the 2496 exoplanets which currently have a mass or minimum mass measurement, in a mass versus orbital period plot. The data was taken from the NASA Exoplanet Archive on 21/07/2024. The figure also shows the Solar System planets for reference. Firstly, it is immediately obvious that the Solar System planets sit where very few exoplanets have been observed. This does not necessarily mean there are few exoplanets in this part of the parameter space. However, there are observational biases for the planet detection techniques which could explain the observed low occurrence rate of planets in this part of the parameter space. Secondly, it is possible to see that there exist some types of planets which are not present in the Solar System.

There exist a few different methods for detecting exoplanets. Here we briefly go through three of those methods, however for a more in-depth explanation of each methodology we refer the reader to chapters 30 to 39 of the *Handbook of Exoplanets* (Deeg and Belmonte, 2018).

The most straightforward detection method to understand is the imaging method. As the name indicates the method consists of a detection of a point source im-

age of an exoplanet/companion. We use the term companion as the definitions of planet and brown dwarf are currently highly debated. A lot of the imaged companions have masses above the deuterium burning limit (13 $M_{\rm Jupiter}$), which in some definitions would make them brown dwarfs. We will discuss the definitions of planet and brown dwarf in more detail in the next section, but for now we will use the term companion. For detecting companions, this imaging can be done by observing the light from the host star which is reflected by the object (in the optical), or through the object's thermal emission (in the infrared). All imaged companions known today have been detected via their thermal emission. The first imaging detections in reflected light are expected within the current decade (Carrión-González et al., 2020, 2021). The imaging method is generally limited to detecting companions located far from their host stars, and which are massive, bright and young (e.g. Marois et al., 2008; Macintosh et al., 2015; Faherty et al., 2021). The first images of companions with the JWST/MIRI coronagraph are currently being obtained, which allow for imaging in the mid-infrared for the very first time, providing a new view into these companions (Boccaletti et al., 2024). Recently, the JWST/MIRI coronagraph has allowed for the confirmation of the most Jupiter-like exoplanet known to date, Eps Ind A b (Matthews et al., 2024). We are at a turning point where coronagraphs are becoming better at suppressing stellar light, which allows for detections of Jupiter analogues. The upcoming Nancy Grace Roman Space Telescope will fly such a coronagraph, with the goal of detecting and imaging many Jupiter analogues orbiting Sun-like stars. The imaging method also allows for the detection of protoplanets still embedded in their forming discs (e.g. Wagner et al., 2018; Currie et al., 2022; Hammond et al., 2023). It is difficult to accurately extract an object's properties (e.g. mass, radius) with the imaging method as most of the properties can only be constrained via a combination of the observations with theoretical models. At the time of writing there are 82 confirmed imaged companions, 25 of which have a mass below the deuterium burning limit.

We now briefly describe the two most successful planet detection methods (in terms of the number of detections): the transit method and the radial velocity (RV) method. Both of these methods rely on observations of a planet's host star rather than the planet itself. The RV method, also known as the Doppler spectroscopy method, is based on the fact that if a planet is orbiting a star, then the gravitational interaction between the planet and the star will make the star "wobble". This is because the planet and the star orbit a common centre of mass. When the star moves away from the observer, the star's spectral lines are red-shifted, and when it moves towards the observer, the spectral lines are blue-shifted - this is known as the Doppler effect. It is then possible to obtain the star's radial velocity from the spectral line shifts, and from that a measurement of the minimum mass of the planet (or the actual mass if the planet's inclination is known). The radial velocity method is biased towards more massive planets, in close-in orbits, around lower mass stars. This is because these planets will induce a larger RV amplitude on its host star, making it easier to detect. For example, 51 Pegasi b was detected via the RV method: with a minimum mass of

approximately $0.4\,M_{\rm Jupiter}$ and an orbital period of 4.2 days, its RV amplitude is a relatively large $60\,{\rm m\,s^{-1}}$. For reference, Jupiter induces an RV amplitude on the Sun of $12\,{\rm m\,s^{-1}}$, while Earth only induces $0.9\,{\rm m\,s^{-1}}$. The state-of-the-art RV precision of the latest generation of spectrographs, which are aimed at searching for Earth-like planets around Sun-like stars, is of about $0.3\,{\rm m\,s^{-1}}$ (ESPRESSO, Pepe et al. 2021; EXPRES, Jurgenson et al. 2016; NEID, Schwab et al. 2016). At the time of writing there are over 1000 planets detected via the RV method. For a more in-depth explanation of the RV method, we refer the reader to Wright (2018).

The transit method is based on the fact that if a planet transits a star (i.e. passes between the star and the line-of-sight of the observer), then the star's flux will be reduced periodically by an amount approximately equal to the ratio of the cross sections of the planet to the star. We provide an in-depth explanation of the transit method in Chapter 2 of this thesis. The transit method allows us to obtain measurements of planetary radii. This method is biased towards planets close-in to their host stars and with a large radius. This is because larger, close-in, planets will block more light and transit more frequently so they are easier to detect. At the time of writing there are over 4000 planets detected via the transit method. We can characterise a planet more accurately when it is possible to combine the RV and transit methods. This is because we can measure both its mass and radius, and therefore its density. We later discuss in Chapter 3 how informative a planetary density measurement can truly be. The remaining exoplanet detection methods are of equal interest. However, we do not emphasise them here as they are not directly relevant to this thesis. Within the remaining methods, two of the most relevant are microlensing (223 detections) and transit timing variations (29 detections).

As we briefly mentioned above, from Figure 1.1 it is possible to see that there are various planet "types" which the Solar System does not host. Before we go on to describe the various planet types, it is important to note that Figure 1.1 is somewhat biased in that we cannot necessarily obtain mass measurements for all detected exoplanets. Mass measurements are generally performed with the RV technique, which as described earlier, is biased towards more massive, close-in planets. Therefore, Figure 1.1 misses some planets for which we are yet to obtain mass measurements but for example, have radius measurements for. For completeness, in Figure 1.2 we show the 4295 planets with a radius measurement. Earlier we described 51 Pegasi b as a so-called hot Jupiter. Hot Jupiters are planets which have a similar mass to that of Jupiter, but are close-in to their host stars (planets in the top left of Figures 1.1 and 1.2). Although at a first glance it could seem like hot Jupiters are common, their occurrence rate around Sun-like stars is in fact only 0.5-1.0% for orbital periods between 1-10 days (e.g. Howard et al., 2010, 2012; Mayor et al., 2011; Petigura et al., 2018). Around M-dwarf stars, the hot Jupiter occurrence rate is even smaller at about 0.3-0.4% (e.g. Bonfils et al., 2013; Bryant et al., 2023; Gan et al., 2023).

There are two types of planets that are fairly common throughout our galaxy, and

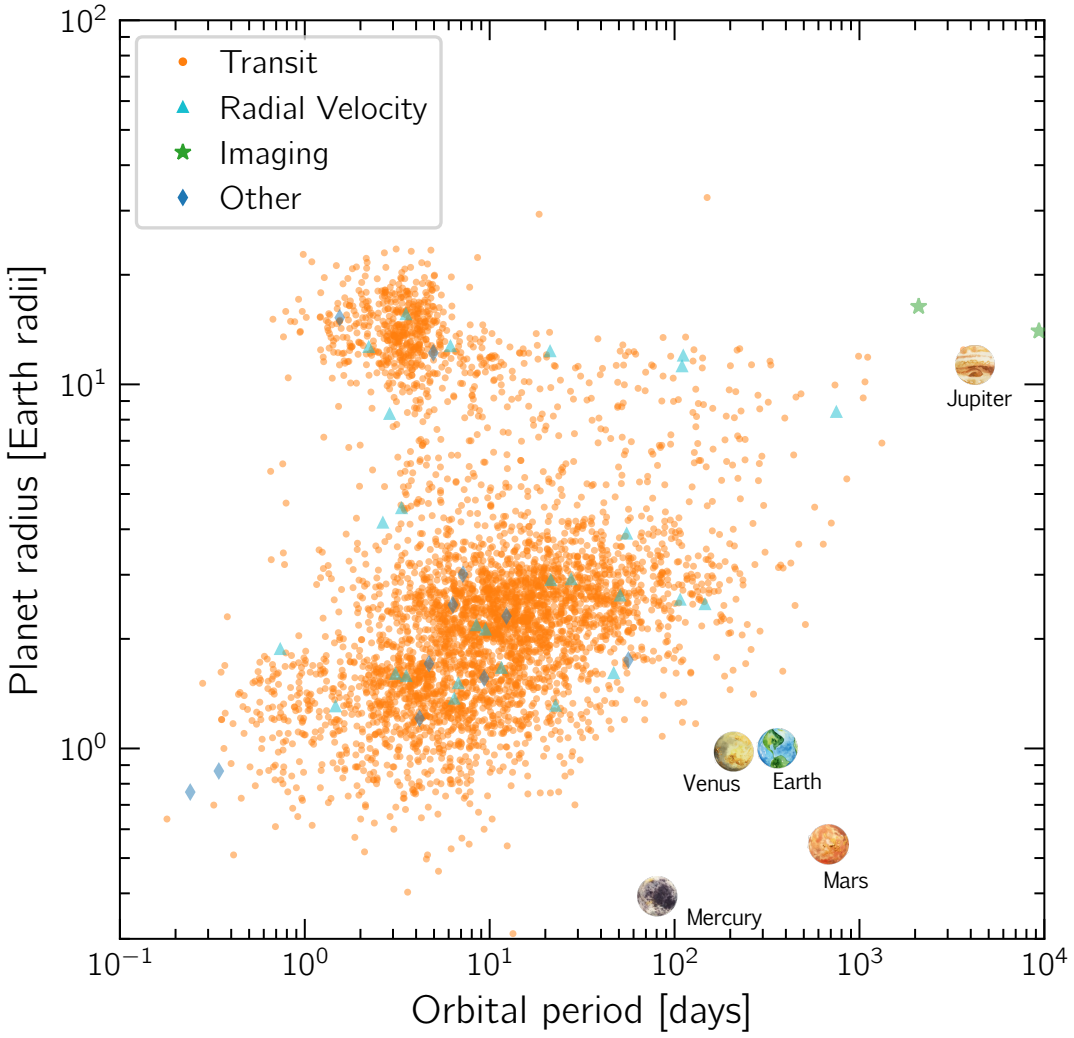

Figure 1.2: The 4295 exoplanets with radius measurement. Data retrieved from the NASA Exoplanet Archive on 21/07/2024. The Solar System planets are shown for reference. The discovery method of each planet is shown with different symbols and colours: transit - orange circles; radial velocity - cyan triangles; imaging - green stars; other methods - blue diamonds.

which our Solar System does not host: super-Earths and sub-Neptunes. As their names indicate, these planets have sizes between those of Earth and Neptune, and have orbital periods shorter than a year. It is easy to identify them in Figure 1.2 as the big "cluster" of orange circles with radii below that of Neptune ($\sim 3.9\,R_\oplus$). Although not so clear in this representation, this big "cluster" of planets actually presents a gap at around $2\,R_\oplus$, where there is a general lack of planets. This is the so-called radius-gap: the super-Earths and sub-Neptunes present a bi-modal radius distribution (e.g. Fulton et al., 2017; Fulton and Petigura, 2018; Van Eylen et al., 2018; Petigura et al., 2022; Ho et al., 2024). Here we will not describe in-depth the potential origin of the radius-gap, however we refer the reader to, for example, Owen and Wu (2013, 2017), Lopez and Fortney (2013), and Gupta and Schlichting (2019) for thorough discussions on the topic. These planets were not predicted to exist from planet formation theories prior to observations. In fact, some of the most complex theories predicted that planets of this type would be rare (Ida and Lin, 2008). New planet formation theories in which small planets form in close-in orbits (without migration) have now been developed to address the formation of such planets (e.g. Hansen and Murray, 2012; Chiang and Laughlin, 2013). From two distinct Doppler surveys, the occurrence rate of these planets with periods shorter than 50 days, and masses between 3 and 30 $M_\oplus$ was estimated to be $(15 \pm 5)\%$ (Howard et al., 2010) and $(27 \pm 5)\%$ (Mayor et al., 2011). (Zhu et al., 2018) estimate that approximately a third of Sun-like stars host what Winn and Petigura (2024) call "miniature Solar Systems" (note this study considered planets with orbital periods of less than 400 days and sizes between 1 to $4\,R_\oplus$).

Above we talk about three broad exoplanet types we do not find in the Solar System. However, throughout the past almost 30 years of exoplanet detections, many interesting and peculiar planets have been found even within these broad planet types. For example, lava worlds have been detected. Lava worlds are super-Earths with extremely short orbital periods ($\leq$ 1-2 days), which are therefore tidally locked (e.g. Demory et al., 2012). These planets have a permanent day-side, and their day-side surface is molten. Puffy planets with similar masses to that of Saturn, but with radii larger than that of Jupiter have also been detected (e.g. Hartman et al., 2015; Anderson et al., 2017). Planets orbiting binary stars (e.g. Doyle et al., 2011), pulsars (e.g. Spiewak et al., 2018), and white dwarfs (e.g. Vanderburg et al., 2020) have also been found. Overall, planets seem to exist in all kinds of varieties. Several studies find that in our galaxy there exists at least one planet per star, and therefore stars with planets are the rule (e.g. Cassan et al., 2012; Mulders et al., 2018; Zink et al., 2020; Ribas et al., 2023).

1.2 Why study exoplanets?

Given there are so many planets out there in our galaxy, the most natural question to ask ourselves as human beings is "are we alone?". Two other questions which naturally arise from questioning if we are alone in such a vast universe are, "how did the Solar System form?", and consequently "how did planet Earth get here?".

The study of exoplanets can help us answer these questions. Although the quest for finding alien life is an enticing one, here we will focus on providing reasoning from the perspective of understanding how planets form. Learning about how other planetary systems form can help us understand the formation of the Solar System. Planets hold the fingerprints of planet formation. By constraining a planet's bulk and/or atmospheric composition, we are able to make links to its formation path.

The idea of using planetary compositions to constrain a planet's formation path was first notably proposed by Öberg et al. (2011). Öberg et al. (2011) suggested it is possible to constrain the formation location of a planet in a protoplanetary disc via the C/O ratio of the planet's atmosphere. The C/O ratio in a protoplanetary disc varies with distance from the star and is majorly regulated by the locations of the H_2O, CO_2 and CO ice lines (e.g. Öberg et al., 2011; Mollière et al., 2022). Inside the ice line we expect to find the compounds in their volatile form, while outside we expect to find them in their solid form. As the temperature of the disc decreases with distance from the star, in a disc with a solar-like star we expect H_2O to freeze out first at about $\sim$1 - 2 AU, followed by CO_2 at about $\sim$10 AU and then CO at a few dozen AU. As these compounds freeze out, the C/O changes because these compounds can either add or remove C and O from the gas-phase when they condense. In more recent studies it has been shown that the C/O ratio in protoplanetary discs is time-dependent (e.g. Helling et al., 2014), where chemical (Eistrup et al., 2016) and kinematic processes (Booth et al., 2017; Schneider and Bitsch, 2021a) bring a large level of complexity to the simple scenario proposed by Öberg et al. (2011). A different but potentially more insightful option is to measure the planet's atmosphere refractory content (Lothringer et al., 2021; Schneider and Bitsch, 2021b; Mollière et al., 2022). Schneider and Bitsch (2021b) and Mollière et al. (2022) argue that the refractory-to-oxygen ratio could be useful to constrain the relative importance of pebble and planetesimal accretion, in the core accretion planet formation scenario. Here we will not describe planet formation theories in depth as it is beyond the focus of this thesis. We refer the reader to Drążkowska et al. (2023) for a recent review on planet formation. Mollière et al. (2022) argue that inferring planet formation from constraints on a planet's atmospheric composition is still "a long way off". However, they end on a positive note stating that the future is exciting because upcoming observatories will lead to more and more precise measurements of atmospheric abundances. These more precise measurements will in turn help to begin accessing the degree by which we can inform planet formation by atmospheric composition measurements of exoplanets.

On the journey to try and understand how planets form, it is particularly interesting to study exoplanets which we do not find in the Solar System, but which are very abundant in our galaxy: the super-Earths and sub-Neptunes. It seems to be well agreed within the community, both from planetary density measurements and formation and evolution models, that super-Earths have Earth-like compositions and no primordial atmospheres (the atmosphere which was accreted during formation) (e.g. Rogers and Owen, 2021; Lee et al., 2022; Burn et al., 2024). On the

other hand, the composition of sub-Neptunes is currently one of the most highly debated topics in the community. The reason for this is that density measurements alone are degenerate, and suggest that sub-Neptunes could either be rocky cores with a high-molecular-weight volatile, such as H_2O, layer atop, or rocky cores with a H/He dominated atmosphere (e.g. Luque and Pallé, 2022; Rogers et al., 2023b). A rocky core with a H/He envelope was the first composition being proposed which could explain the observed radius-gap in the small planet population (e.g. Owen and Wu, 2013, 2017; Lopez and Fortney, 2013; Fulton et al., 2017). More recently, alternative scenarios have been proposed to explain the lower densities of sub-Neptunes: the "water-worlds" with a rocky core and a steam (water mixed with H/He) envelope (Burn et al., 2024; Benneke et al., 2024); the "hycean worlds" with a rocky core and a liquid water ocean, and a H/He layer on top (e.g. Hu et al., 2021; Madhusudhan et al., 2021, 2023); the rocky core with a molten magma surface, with a H/He envelope scenario (e.g. Kite and Schaefer, 2021; Lichtenberg, 2021; Schlichting and Young, 2022; Misener et al., 2023). The composition of sub-Neptunes can be directly linked to their formation and evolution paths. If sub-Neptunes happen to be water and heavy element rich, then this indicates they likely formed further away from their host-stars where there are large amounts of water and volatiles available. The water and volatiles can be efficiently accreted in the form of solid material before migrating to the location where they are observed today (e.g. Lambrechts et al., 2014; Morbidelli et al., 2015; Burn et al., 2024). This is known as the *migration* model. On the other hand, if sub-Neptunes have a smaller volatile content, then they probably formed within the ice line, where their mass is then obtained via accretion of drifting rocky pebbles (Johansen and Lambrechts, 2017). This is known as the *drift* model. Nevertheless, Venturini et al. (2020) recently showed that planets starting their formation beyond the ice-line can end up being purely rocky, while Bitsch et al. (2021) showed that wet sub-Neptunes can form within the ice line in multi-planet systems. Therefore, there is a need for high-precision measurements of the bulk densities of small close-in planets, coupled with interior structure models, as well as a need for constraining the atmospheric composition of these planets (Bean et al., 2021).

1.3 Planet or brown dwarf? Brown dwarfs as extrasolar giant planet's analogues

Spoiler alert: in this section we will not be providing an answer to the question "planet of brown dwarf?", but rather we will provide a brief overview of the ongoing debate of how to determine what is a planet and what is a brown dwarf. Additionally, we will discuss how brown dwarfs are analogues of extrasolar giant planets, and how that can be extremely useful when modelling and observing these objects.

The *official working definition of an exoplanet* by the International Astronomical Union (IAU) (Lecavelier des Etangs and Lissauer, 2022) states that an exoplanet

must have a true mass below the limiting mass for deuterium burning (approximately 13 M_{Jupiter} for objects with solar metallicity), and that it must orbit a star, a brown dwarf, or a stellar remnant. The IAU further states that the definition of exoplanet is independent of how the object formed. Brown dwarfs are then defined by the IAU as substellar objects with masses above the limiting mass for deuterium burning, once again independently of how they formed or where they are located. Finally, the IAU defines any free-floating objects with masses below the limiting mass for deuterium burning as "sub-brown dwarfs" and not "planets".

For astronomers and astrophysicists that study substellar objects with masses near the limiting mass for deuterium burning, the IAU definition is most certainly simplistic. As Schneider (2018) argue, *"names are arbitrary conventions but the natural trend is to classify objects using sufficiently elaborated concepts"*. Based on this argument, formation is the concept which can provide the most discrimination between planets and brown dwarfs. However, the formation itself is not observable. Relying on actual observables of these objects, (such as mass, radius and temperature) it also seems impossible to make a true distinction because these objects share observables - they have similar masses, effective temperatures and radii. Atmospheric characterisation of these objects with state-of-the-art observatories, such as JWST, could potentially help obtain more advanced observables such as spectral type and atmospheric composition, in a quest to potentially constrain their formation mechanism and therefore correctly classifying them as planets or brown dwarfs. It is generally thought that brown dwarfs form via gravitational instability (if they are not companions) (e.g. Whitworth, 2018). However, the formation mechanism of giant planets and companion brown dwarfs is still debated. As details on planet formation are beyond the scope of this thesis, we refer the reader to Chabrier et al. (2014), Helled et al. (2014), Drążkowska et al. (2023), Lesur et al. (2022) and Guillot et al. (2022) for more details on (giant) planet formation.

Defining the deuterium burning minimum mass as the official distinction between planets and brown dwarfs is extremely limiting and ultimately not based in any strong physical justification (e.g. Chabrier, 2003; Chabrier et al., 2007, 2014). For example, it has been shown that planets which form via core-accretion, with a heavy-element enrichment, can reach masses above 13 M_{Jupiter} and ignite deuterium burning in their core (Baraffe et al., 2008; Mollière and Mordasini, 2012; Bodenheimer et al., 2013). On the other hand, some brown dwarf binary systems indicate that brown dwarfs do not necessarily have masses above the deuterium burning limit mass (for example 2M 1207 b (Chauvin et al., 2005), a $\sim$ 4 M_{Jupiter} companion to a $\sim$ 20 M_{Jupiter} brown dwarf). In addition to this, there is growing evidence for the existence of non-deuterium burning free floating Jupiter-mass objects (e.g. Chabrier et al., 2014; Pearson and McCaughrean, 2023).

As described in the discussion above, brown dwarfs and giant planets share masses, radii (i.e. surface gravities), effective temperatures and even ages (e.g. Faherty, 2018). This means brown dwarfs are giant planet's analogues. The study of isolated brown dwarf's atmospheres brings some advantages compared to studying

the atmospheres of giant planets/brown dwarf companions. From an observational point of view, one avoids the interference from the host star's brightness, and there is no need of using a coronagraph. It is therefore more straightforward to make spectroscopic measurements of isolated brown dwarf's atmospheres than it is to use transit spectroscopy to characterise hot Jupiter atmospheres (for example). We describe transmission spectroscopy in Chapter 2. From a modelling perspective, one does not need to model an extra radiation field from the irradiating star, which greatly simplifies computations.

1.4 Thesis overview and outline

In this thesis we have performed two distinct studies which help constrain the composition of different types of exoplanets. Although the studies are independent, they both highlight the importance of self-consistent modelling. No physical process happens on its own. Processes are connected via feedback loops more often than not, if not always. There are many examples of this on planet Earth such as the water cycle (e.g. Sherwood Lollar et al., 2024), or even the prey-predator interaction (e.g. Abrams, 2000). This is not different for the studies which we have performed in this thesis, and in each of them we highlight the importance of considering these feedback loops, in order to not miss the physical reasoning behind a given behaviour.

In the first study we model catastrophically evaporating rocky planets, in order to constrain the composition of small rocky planets. We provide the necessary background and theoretical information in Chapter 2. In Chapter 3 we present the research context and motivation for this study, along with a summary of the work published in Campos Estrada et al. (2024), including conclusions and future prospects. In Chapter 4, the Campos Estrada et al. (2024) paper is reproduced.

In the second study we model cloudy substellar atmospheres self-consistently, including microphysical cloud formation. We provide a detailed background in substellar atmospheres theory and modelling in Chapter 5. The theory of microphysical cloud formation is described in Chapter 6. In Chapter 7, we present the research context and motivation, as well as a summary of the manuscript presented in Chapter 8, which has been submitted to *Astronomy & Astrophysics*. This includes a summary of the discussion points presented and future prospects. In Chapter 8 the manuscript *The MSG model for cloudy substellar atmospheres: A grid of self-consistent substellar atmosphere models with microphysical cloud formation*, submitted to *Astronomy & Astrophysics* is reproduced.

CHAPTER 2

Catastrophically evaporating rocky planets: Background and Observations

Potential is the drug they never knew you never tried.

— Caroline Polachek, in *Pretty in Possible*

In this chapter we present fundamental concepts and background in order to understand the observations of catastrophically evaporating rocky planets. We start by introducing the most successful exoplanet detection method (by number of planets found), the transit method. This is the method which was used to detect the three catastrophically evaporating rocky planets which are known up to date. Next, we describe transmission spectroscopy and how it can be used to constrain the composition of exoplanet atmospheres. Finally, we present an overview of the current observations of these catastrophically evaporating rocky planets.

Unless otherwise stated this chapter is based on Deeg and Alonso (2018), Roberge and Seager (2018), Kreidberg (2018) and Lieshout and Rappaport (2018).

2.1 Detecting exoplanets: the transit method

As briefly mentioned in the introductory chapter, most exoplanet detection methods rely on observations of their host stars, rather than direct observations of the planets themselves. Here, we describe the transit photometry detection method in more detail. A transiting planet is one that periodically passes in front of its host star as seen from Earth. The first transiting exoplanet, HD 209458 b, was discovered in 2000 (Henry et al., 2000; Charbonneau et al., 2000), although it had previously been observed via the radial velocity (RV) method in 1999 (Mazeh

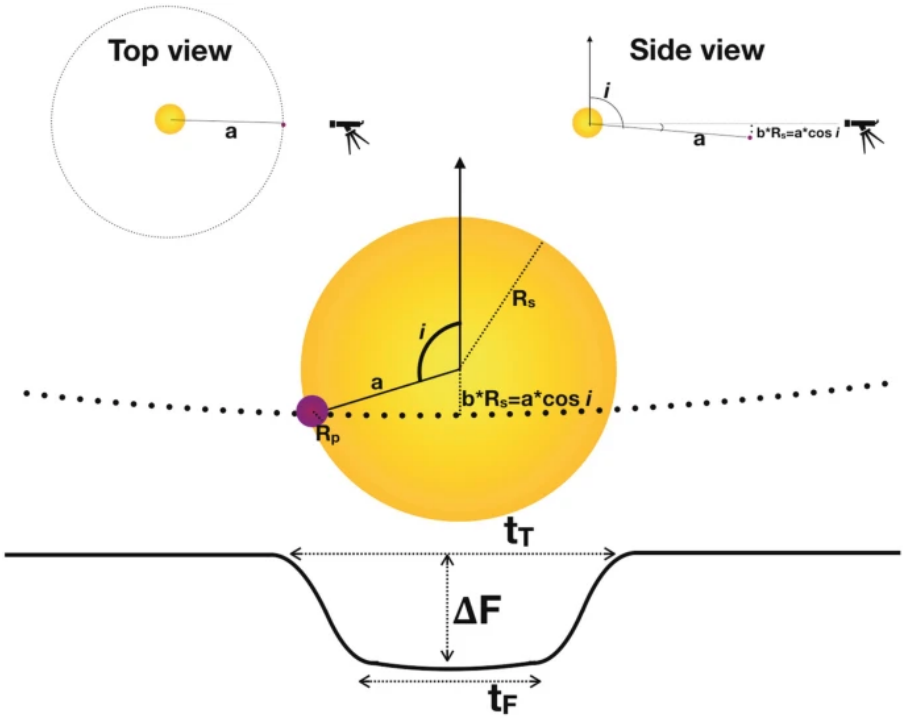

Figure 2.1: Schematic view of a planetary transit event with the major quantities used to describe a planet's orbital configuration shown, along with the transit method observables. The bottom part of the figure shows the observed light curve of the star as the planet transits. In the middle part, the figure shows a schematic of the frontal view of the observed star and the transiting planet. At the top part of the figure, schematics of the top and side views are shown. Reproduced from Deeg and Alonso (2018) with permission. Copyright © 2018 Springer International Publishing AG, part of Springer Nature.

et al., 2000). The transit method, first proposed by Struve (1952) alongside the RV method, was initially not considered promising by the scientific community. For example, the 1996 NASA roadmap for the Exploration of Neighboring Planetary Systems (Elachi et al., 1996) gave it minimal attention. However, the first detections of transiting exoplanets led to the establishment of dedicated ground-based transit searches, such as the multiple transit campaigns of the OGLE-III survey (e.g. Udalski, 2007), which resulted in the first planetary detections by the transit method, including OGLE-TR-56 b (Konacki et al., 2003). This solidified the method's credibility, which continued to grow as it allowed for detailed information extraction from planets orbiting bright host stars. Significant advances came with space-based missions like CoRoT (e.g. Fridlund et al., 2006) and Kepler (e.g. Borucki et al., 2010). These missions discovered a wide range of transiting planets, including Earth-sized planets and multi-planet systems, providing a deeper understanding of exoplanet populations such as size distributions, multiplicity and occurrence rates (e.g. Fressin et al., 2013; Fulton et al., 2017; Weiss et al., 2018; Petigura et al., 2018). At the time of writing this thesis, over

2700 exoplanets have been detected from the Kepler mission alone[1]. For a brief overview of past, current and upcoming transit surveys, we refer the reader to Deeg and Alonso (2018).

Figure 2.1 shows a schematic view of a transit event. The bottom part of Figure 2.1 shows the observed flux of the planetary system. If a planet transits between a star and the observer (represented by the telescope in Figure 2.1), the star's flux is diminished periodically. The transit depth is the fractional reduction of the stellar flux due to the planetary transit, ΔF. Assuming the planet and star to be spherical, the transit depth is approximately equal to the ratio of the cross sections of the planet to the star, this is

$$\Delta F \equiv \frac{F_{\text{no transit}} - F_{\text{transit}}}{F_{\text{no transit}}} \approx \frac{R_p^2}{R_s^2}, \tag{2.1}$$

where R_p is the radius of the planet and R_s is the radius of the star. In Figure 2.1, the total duration of the transit is represented by t_T, and the time of totality, when the entire planetary disc is in front of the stellar disc, is represented by t_F. Seager and Mallén-Ornelas (2003) derived analytic expressions that relate the observables ΔF, t_F and t_T to the planet's orbital parameters. Of particular importance is the impact parameter b, which is the minimal projected distance to the centre of the stellar disc during the transit. Following Seager and Mallén-Ornelas (2003), the impact parameter is given by

$$b \equiv \frac{a}{R_s}\cos i = \left(\frac{\left(1-\sqrt{\Delta F}\right)^2 - \left[\sin^2\left(\frac{t_F\,\pi}{P}\right) / \sin^2\left(\frac{t_T\,\pi}{P}\right)\right]\left(1+\sqrt{\Delta F}\right)^2}{\cos^2\left(\frac{t_F\,\pi}{P}\right) / \cos^2\left(\frac{t_T\,\pi}{P}\right)} \right)^{1/2}, \tag{2.2}$$

where a is the orbital semimajor axis, i is the orbital inclination, and P is the planet's orbital period. The equations above ignore the limb-darkening of the star, which is the non-uniform brightness of the stellar disc which is darker at its limbs, as the name indicates. The reason for this is the star's temperature gradient from its core to its surface (the top of the stellar atmosphere), where the temperature is much higher in the core than at the top of the stellar atmosphere. At the centre of the stellar disk, the optical depth is equal to unity at a deeper, and therefore hotter, part of the atmosphere. Towards the limbs, the optical depth is equal to unity at a colder part of the atmosphere. Therefore, to the observer, the disk appears brighter in the centre and darker towards the limbs. The exact extent of the limb-darkening effect is wavelength dependent, however in the relevant wavelengths for observations of exoplanets, it is generally observed. The planet's orbit is also assumed to be circular for simplicity. For formalisms which take into account the limb-darkening of the star and the planet's eccentricity, we refer the reader to, for example, Mandel and Agol (2002) and Winn (2010) respectively.

[1]Information extracted from the NASA Exoplanet Archive on 08/07/2024.

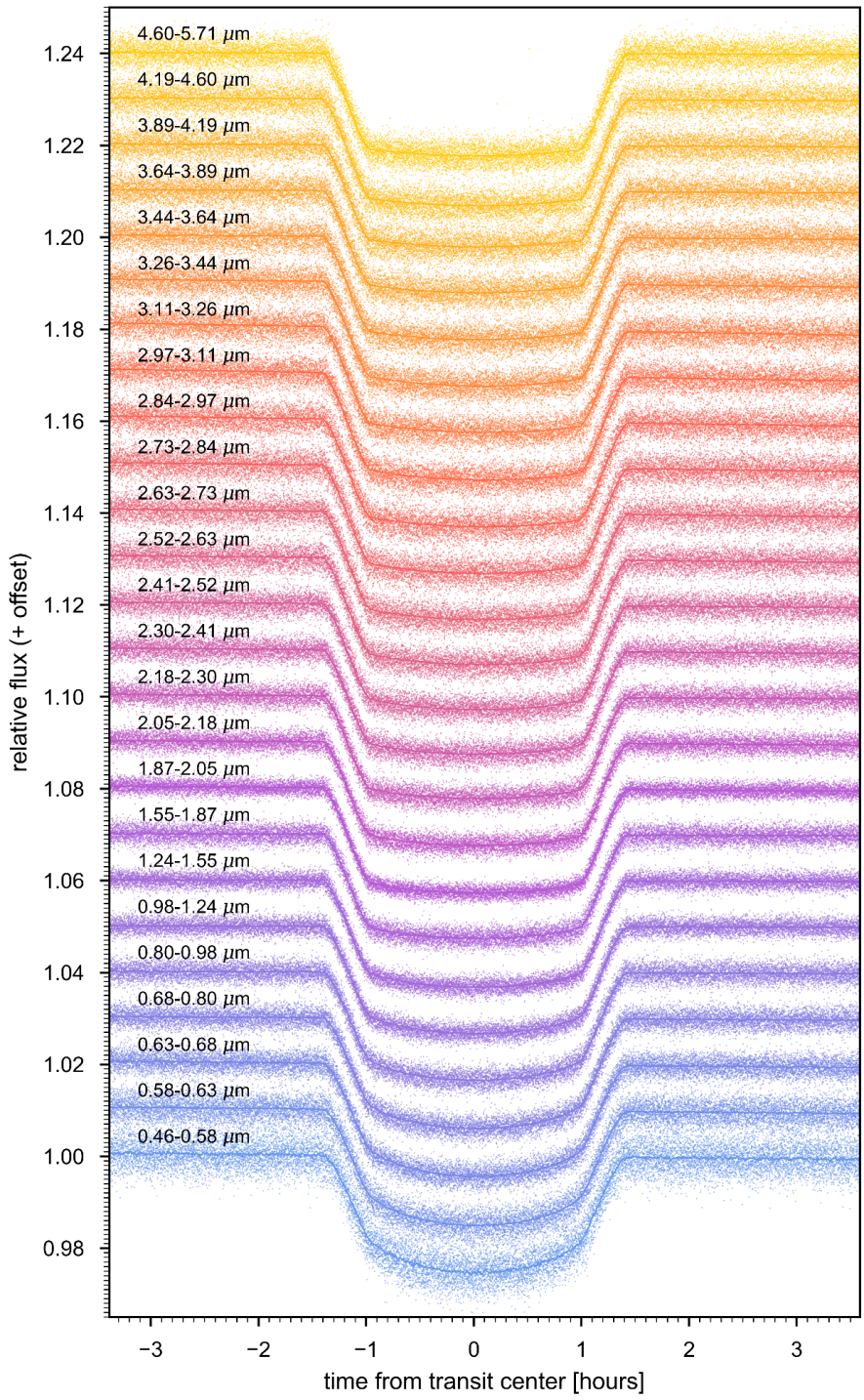

Figure 2.2: A set of normalised spectrophotometric light curves of WASP-39 b obtained with JWST/NIRSpec-PRISM by Rustamkulov et al. (2023). The light curve were produced by summing over wide wavelength channels. The best-fit models are overplotted on each light curve. Figure reproduced and caption partially reproduced from Rustamkulov et al. (2023) under the Creative Commons Attribution 4.0 International License.

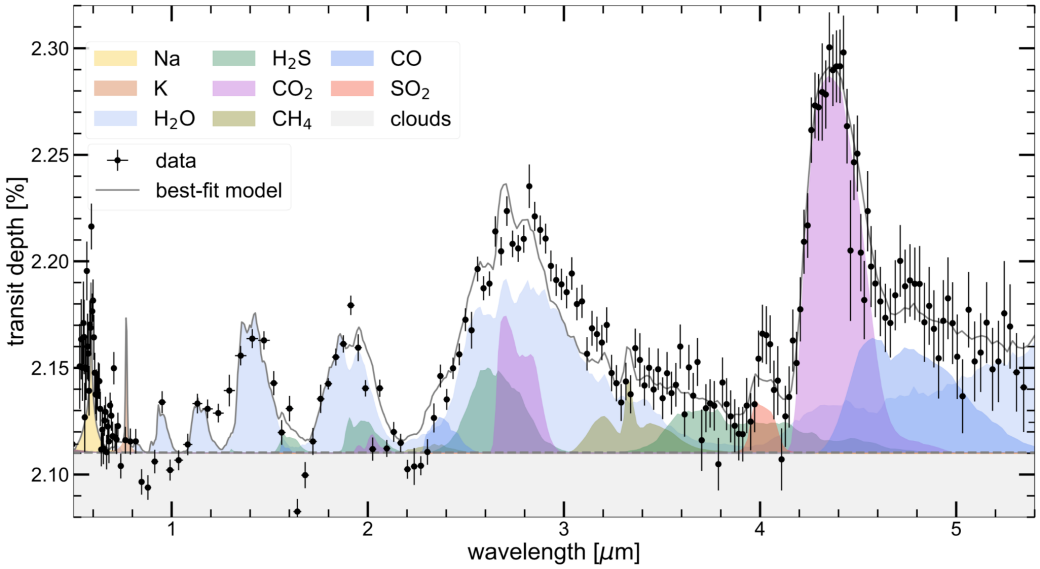

Figure 2.3: The transmission spectrum of WASP-39 b obtained with JWST/NIRSpec-PRISM by Rustamkulov et al. (2023), where key contributions to the spectrum are indicated with different colours. The transmission spectrum is explained by contribution from Na (19σ), H_2O (33σ), CO_2 (28σ), CO (7σ), SO_2 (2.7σ) and cloud (21σ). The data does not provide evidence of CH_4, H_2S or K absorption. Figure reproduced and caption partially reproduced from Rustamkulov et al. (2023) under the Creative Commons Attribution 4.0 International License.

2.2 Transmission spectroscopy

In the previous section we have defined the transit depth for a so-called white light curve, i.e. for starlight at all wavelengths. However, if a planet has an atmosphere, the transit depth will be dependent on the wavelength of the starlight passing through the planet's atmosphere. This implies the planet's radius will appear smaller or larger depending on how the atmospheric constituents interact with the starlight. The starlight may be scattered and/or absorbed through the atmosphere. At wavelengths where an atmospheric constituent absorbs strongly, the stellar photons are completely attenuated in the upper atmosphere, and therefore the planet will appear larger and the transit depth will be deeper. During a planet's transit, the spectral features of the planet's atmosphere will be imprinted in the host star's spectrum, and we can obtain what is called a transmission spectrum. The transmission spectrum is obtained by plotting the wavelength dependent transit depth versus the wavelength.

Using the Hubble Space Telescope (HST), Charbonneau et al. (2002) did follow-up observations of HD 209458 b, and found the transit depth of the planet to be deeper in the bandpass centred on the sodium resonance doublet at 589.3 nm. They concluded the deeper transit depth was due to sodium (Na) absorption in the planet's atmosphere, which theoretical models had previously predicted (e.g. Seager and Sasselov, 2000). This was the first detection of atmospheric absorption

in a transiting exoplanet's atmosphere. Since this first detection, there have been many more detections of atmospheric absorption in transiting exoplanet atmospheres. Before the launch of JWST, many of these detections were obtained with the HST/WFC3 instrument in hot Jupiters, with water being the most common molecule detected (e.g. Deming et al., 2013; Kreidberg et al., 2014; Line et al., 2016). Unsurprisingly, some molecules remained undetected with transmission spectroscopy, such as ammonia (NH_3) and methane (CH_4). One reason is because these molecules do not have significant absorption features in the wavelength range of the HST/WF3 instrument. In addition to this, we expect such molecules to be present in cooler targets than hot Jupiters, as they tend to be unstable at higher temperatures. For a review of pre-JWST detections we refer the reader to Kreidberg (2018) and Table 4 in Guillot et al. (2022).

We have now entered the JWST era where transmission spectroscopy can be done at an unprecedented resolution and at wavelengths which were previously unexplored. Figure 2.2 shows a set of light curves for the exoplanet WASP-39 b obtained with JWST/NIRSpec-PRISM by Rustamkulov et al. (2023) at different wavelength bins (indicated in the figure). The y-axis of the figure shows the relative flux, this is the measured stellar flux normalised by the unblocked stellar flux. The light curves are offset by a constant for clarity. For example, it is possible to see that the planet appears to have a larger radius at wavelengths between 0.46-0.58 μm (bottom light curve) than at wavelengths between 4.60-5.71 μm (top light curve).

Figure 2.3 shows the transmission spectrum of exoplanet WASP-39 b between 0.5 and 5.5 μm, obtained with JWST/NIRSpec-PRISM by Rustamkulov et al. (2023). In WASP-39 b's transmission spectrum, Rustamkulov et al. (2023) have found evidence for the absorption of Na, H_2O, CO_2, CO, SO_2 and clouds. However, they do not find clear evidence for the absorption of CH_4, K or H_2S. More recently, CH_4 has been detected with JWST in the sub-Neptune K2-18 b (Madhusudhan et al., 2023), in the warm Jupiter WASP-80 b (Bell et al., 2023) and in the warm Neptune WASP-107 b (Welbanks et al., 2024; Sing et al., 2024). A detection of NH_3 is also reported for WASP-107 b by Welbanks et al. (2024).

2.3 Observations of catastrophically evaporating rocky planets

During the Kepler mission, three exoplanets were identified which appear to have dusty tails trailing (or leading) them as they orbit their host stars: KIC 12557548 b (or KIC 1255 b for short, and more recently Kepler-1520 b) (Rappaport et al., 2012), KOI-2700 b (Rappaport et al., 2014), and K2-22 b (Sanchis-Ojeda et al., 2015). These exoplanets share several features. They are ultra-short-period (USP) planets, with orbital periods of less than 24 hours, of 15.7, 22, and 9.5 hours respectively. The depth of their transits varies between 0.02% to 0.5%, often blocking areas of 1-18 times that of Earth. More interestingly, these transits are asymmetric

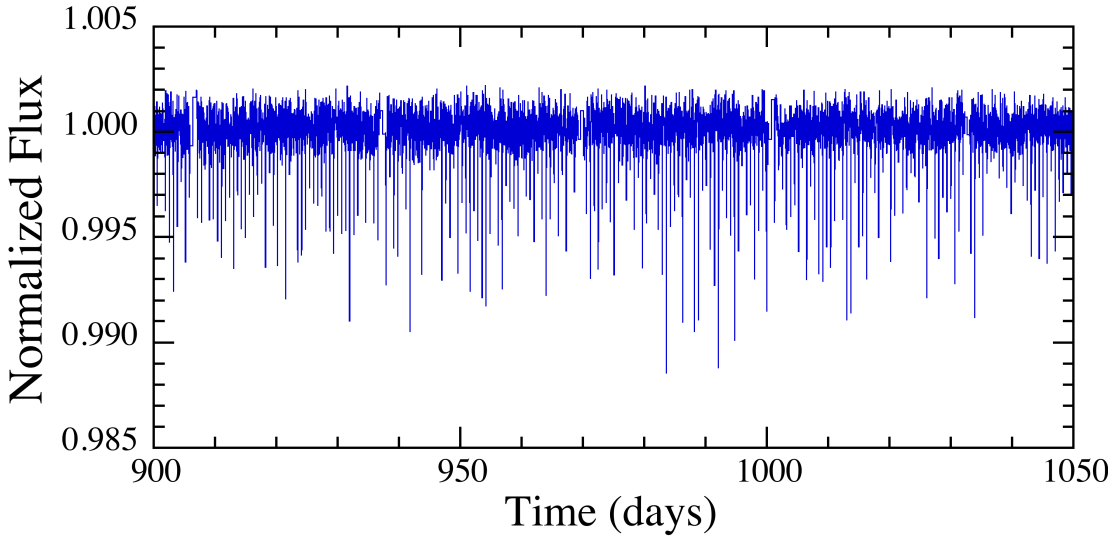

Figure 2.4: Light curve of KIC 1255 spanning 150 days of the Kepler mission. Note the highly variable transit depths. Reproduced from Lieshout and Rappaport (2018) with permission. Copyright © 2018, Springer International Publishing AG, part of Springer Nature.

and differ from those expected of solid-body planets, as the example discussed in Section 2.1. The light curves present a pre-transit brightening, followed by a sharp ingress and a very long egress (or a post-transit brightening). The transit depths for all three exoplanets change over time with KIC 1255 b and K2-22 b showing rapid variations from one transit to another, while the KOI-2700 b's changes are more gradual over four years of observations by Kepler.

These characteristics suggest that the transiting objects have elongated tails of dusty material originating from an underlying rocky exoplanet. However, it's currently challenging to determine the exact mass or size of these "disintegrating" planets.

This section is intended to provide a brief overview of the observations of these dusty tails planets. In Chapters 3 and 4 we discuss our work on modelling these planets, and how we can constrain small (exo)planet compositions via observations and models of catastrophically evaporating rocky planets.

While KOI-2700 b was mainly identified in Kepler data due to its asymmetric transit profile (Rappaport et al., 2014), KIC 1255 b and K2-22 b were identified in Kepler and K2 data due to their unique transit depth variations (Rappaport et al., 2012; Sanchis-Ojeda et al., 2015). These variations are frequently drastic from transit to transit, as can be seen in Figure 2.4 which shows a 150-day portion of the light curve of KIC 1255. Throughout the four years of the Kepler mission, KIC 1255 b exhibited over 2000 transits, with depths varying from 0% to 1.2%. There were also several week long periods during which no transits were detected.

Figure 2.5 presents the mean transit profiles for KIC 1255 b, KOI-2700b, and K2-22b, illustrating their characteristic features. The profiles for KIC 1255 b and

KOI-2700 b show notable asymmetry with a sharp ingress and long egress, unlike K2-22 b, which exhibits a more symmetric transit shape. The positive bump in flux which occurs just before the transit for KIC 1255 b is statistically significant. Both the pre- and post- transit bumps seen in K2-22 b's light curve are also statistically significant. In Chapters 3 and 4 we describe how such transit profiles can be explained by a planet with a comet-like tail of dust either trailing or leading the planet. Known properties of the dusty tail planets and their host stars are listed in Table 2.1. The host stars are mid-K to early-M spectral type. We particularly note that the planetary orbits are only 1 to 2.5 times that of the star's diameter above the surface of the host stars.

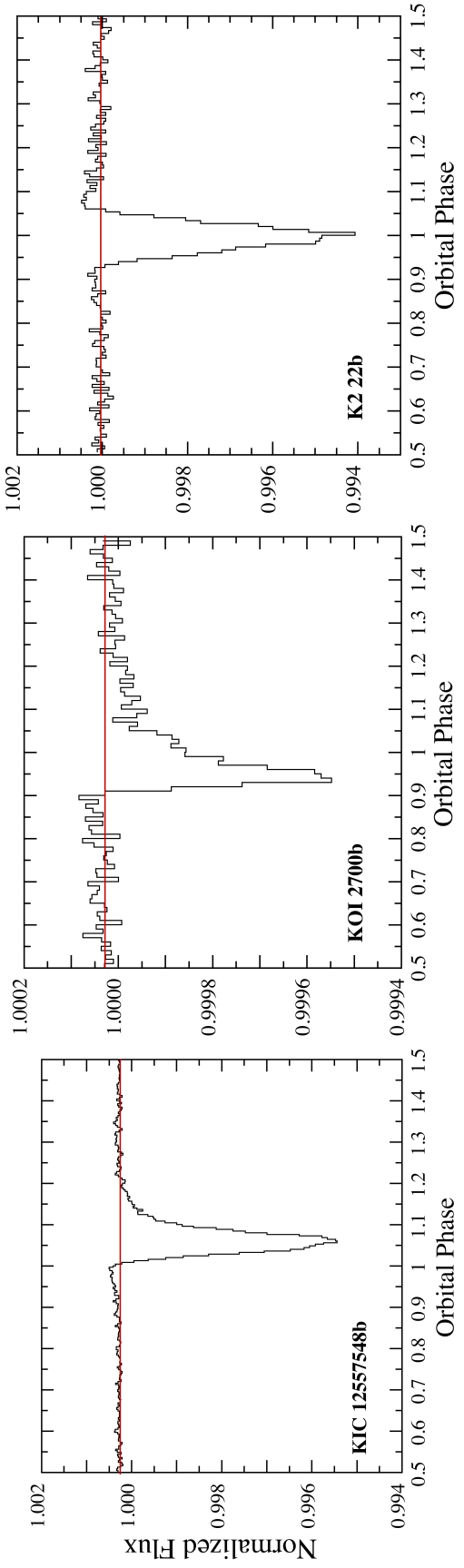

Figure 2.5: Mean transit profiles for KIC 1255 b, KOI-2700 b, and K2-22 b. The first two are characterised by a sharp ingress followed by a long egress. Note that the mean transit depth of KOI-2700 b is about an order of magnitude more shallow than that of the other two objects. Also note the small pre-ingress "bump" for KIC 1255 b and the post-egress "bump" for K2-22 b. Reproduced from Lieshout and Rappaport (2018) with permission.

Table 2.1: Comparative properties of the dusty tails planets and their host stars. Table partially reproduced from Lieshout and Rappaport (2018) with permission. Copyright

Parameter	Symbol [units]	KIC 1255 b	KOI-2700 b	K2-22 b
Host star parameters				
Stellar temperature	$T_{\rm eff,*}$ [K]	4550 ± 135	4300 ± 140	3830 ± 100
Surface gravity	$\log g$ [cgs]	4.62 ± 0.04	4.71 ± 0.05	4.65 ± 0.12
Metallicity	[Fe/H]	-0.2 ± 0.3	-0.7 ± 0.3	0.03 ± 0.08
Stellar mass	M_* [$M_\odot$]	0.67 ± 0.06	0.55 ± 0.04	0.60 ± 0.07
Stellar radius	R_* [$R_\odot$]	0.67 ± 0.06	0.54 ± 0.05	0.57 ± 0.06
Stellar luminosity	L_* [$L_\odot$]	0.17 ± 0.04	0.09 ± 0.02	0.063 ± 0.008
Stellar rotation period	$P_{\rm rot}$ [days]	22.9	11.0	15.3
Planet: light curve properties				
Orbital period	$P_{\rm orb}$ [hr]	15.68	21.84	9.146
Transit depth (range)	δ [%]	0–1.4	0.031–0.053	0–1.3
Mean transit depth	$\langle\delta\rangle$ [%]	0.5	0.036	0.55
Variability		Fast	Slow	Fast
Long egress		Yes	Yes	No
Pre-ingress bump		Yes	?	Weak
Post-egress bump		No	Yes	No

Data were compiled from Rappaport et al. (2012), Brogi et al. (2012), Budaj (2013) and van Werkhoven et al. (2014) for KIC 1255 b; from Rappaport et al. (2014) for KOI-2700b; from Sanchis-Ojeda et al. (2015) for K2-22b; and from Huber et al. (2014) for most stellar parameters.

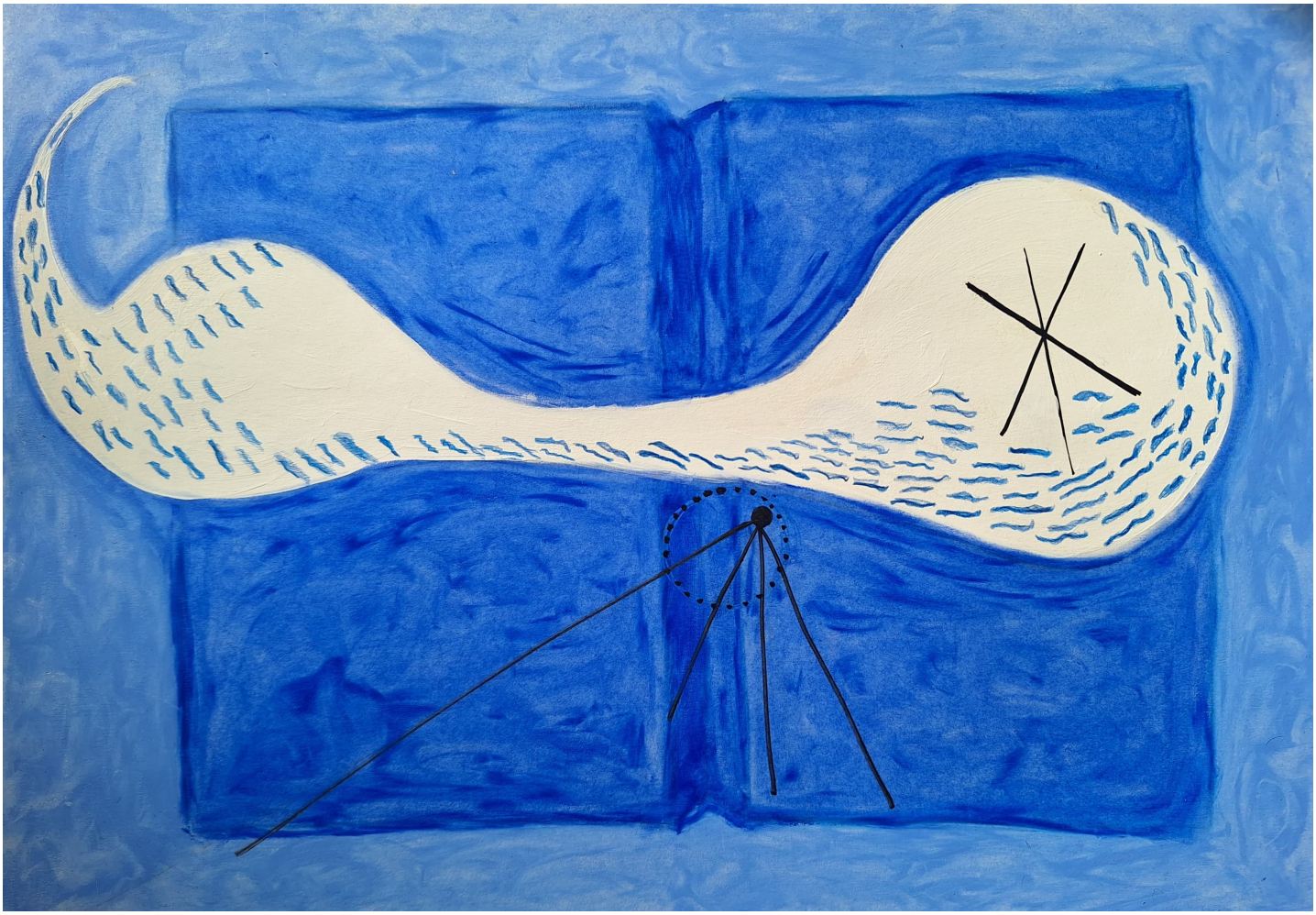

CHAPTER 3

Constraining small planet compositions with catastrophically evaporating rocky planets: Research summary

Fais de ta vie un rêve, et d'un rêve, une réalité.

— Antoine de Saint-Exupéry, in *Le Petit Prince*

In this chapter we summarise the work presented in Campos Estrada et al. (2024), which is reproduced in its entirety in Chapter 4. We start by describing the research context and motivation in the context of the international state-of-art. Next, we present a summary of our methods and results. Finally we describe our conclusions in the context of the international state-of-the-art and provide an outlook for future research in the topic. The chapter is entirely based on Campos Estrada et al. (2024).

3.1 Research context and motivation

The interiors of small planets ($R_p \lesssim 1.5\ R_\oplus$) remain a subject of significant scientific curiosity and uncertainty. Studying small planet's interiors can help us better understand their formation paths and evolution (see Schlichting (2018) for a review on super-Earths formation and evolution). While density measurements (e.g. Dressing et al., 2015; Van Eylen et al., 2021) and modelling constraints (e.g. Rogers, 2015; Dorn et al., 2019; Gupta and Schlichting, 2019; Rogers and Owen, 2021; Rogers et al., 2023a,b) provide some insight, they often fall short of offering a definitive understanding of the bulk composition of these planets. Studies indicate

that many of these planets might have an Earth-like composition, consisting of approximately two-thirds silicate rock and one-third iron by mass. However, density measurements alone cannot definitively determine composition due to the diversity of possible bulk compositions among planets with similar densities (e.g. Seager et al., 2007; Valencia et al., 2007; Rogers and Seager, 2010; Unterborn et al., 2016; Dorn et al., 2017b,a; Neil and Rogers, 2020; Neil et al., 2022). For example, Rogers and Seager (2010) investigate possible interior compositions for the super-Earth CoRoT-7 b by assuming the planet to have an iron core and a mantle composed of a mix of enstatite ($MgSiO_3$) and ferrosilite ($FeSiO_3$), i.e. $Mg_{1-\chi}Fe_{\chi}SiO_3$ where χ is the mantle iron fraction. Although they find the planet to have an Earth-like composition, it is not possible to constrain the planet's iron core mass fraction or the mantle's iron fraction χ (see Rogers and Seager, 2010, figures 1 and 2). This is because multiple values of χ and of the iron core mass fraction correspond to the measured density within the observational uncertainties (even considering the most up-to-date measurements of CoRoT-7 b), and therefore the density measurement is degenerate. There also exists a degeneracy for sub-Neptunes where many are consistent with hydrogen/helium envelopes atop silicate-rich cores, or bodies composing of 50% silicate rock and 50% water, often referred to as "water worlds" (e.g. Rogers et al., 2023b).

One promising approach to overcoming this compositional ambiguity is the analysis of the elemental abundance ratios of the bodies. This method has been applied to material accreted by polluted white dwarfs (e.g. Gänsicke et al., 2012; Farihi et al., 2016; Harrison et al., 2018; Bonsor et al., 2020), which can offer valuable insights into the composition of exoplanetary material. However, this method has its limitations as it remains unclear what planetary reservoirs are being probed (e.g. Jura and Young, 2014; Buchan et al., 2022; Brouwers et al., 2023), and it may not be representative of close-in planets, although it clearly must probe further out than close-in planets which do not survive the post-main sequence stage.

USP planets offer a unique opportunity to study the composition of small planets. These planets are tidally locked and highly irradiated by their host stars, leading to extreme surface temperatures, often exceeding 2000 K on the day-side. This intense irradiation is likely to cause the loss of any primordial atmosphere (e.g. Valencia et al., 2010; Owen and Wu, 2013), exposing the planet's core and forming a rock-vapour atmosphere from the day-side's molten surface (e.g. Schaefer and Fegley, 2009; Miguel et al., 2011; Ito et al., 2015; Kite et al., 2016; Mahapatra et al., 2017; Zilinskas et al., 2022). The composition of this atmosphere can provide direct insights into the planet's interior, as it is in vapour pressure equilibrium with the magma below. However, current observations of the atmospheres of these planets have yielded no evidence for thick atmospheres (e.g. Kreidberg et al., 2019; Crossfield et al., 2022; Zieba et al., 2023). Moreover, comprehensive modelling of the interaction and evolution between these planets' interiors and their atmospheres is necessary to interpret the observations and gain insights into their planetary interiors.

In this thesis, we aim to provide a new manner of constraining the composition of

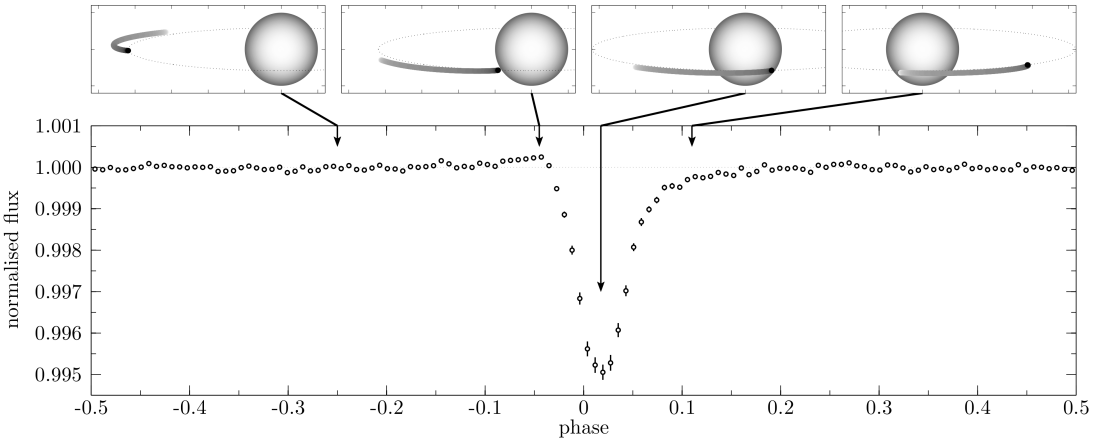

Figure 3.1: Dust-tail geometry shown for a sequence of four orbital phases of the underlying planet. Reproduced from van Lieshout et al. (2016) with permission © ESO.

small rocky exoplanets which could be more robust than the methods described above. As described in the previous chapter in Section 2.3, during the Kepler mission, three USP planets with comet-like tails of dust were detected. The comet-like tail scenario can be described as follows: dust from the planet's molten surface condenses within a thermally driven wind (Rappaport et al., 2012; Perez-Becker and Chiang, 2013; Booth et al., 2023) and is carried by a gaseous outflow to a region where the gas density is sufficiently low for the dust to decouple from the gas dynamically. At this stage, the dust's path is determined by the stellar radiation pressure and the stellar gravity, forming it into a cometary-like tail that trails (or leads) the planet (e.g. Brogi et al., 2012; Rappaport et al., 2012; Budaj, 2013; Sanchis-Ojeda et al., 2015; Lieshout and Rappaport, 2018). As the gas density decreases further from the planet, the sublimation temperature decreases (e.g. Booth et al., 2023). This causes the dust to gradually sublimate as it travels along the tail, leading to a reduction in the optical depth with increasing distance from the planet (Rappaport et al., 2012; van Lieshout et al., 2016). Figure 3.1 shows how a planet with a comet-like tail can explain the observed light curves shown in Figure 2.5. The sharp ingress and slow egress observed in the light curve can be explained by the optical depth pattern of the dust cloud (e.g. Rappaport et al., 2012; Lieshout and Rappaport, 2018). Additionally, the positive "bumps" in flux observed either prior to, or following, the transits are attributed to forward scattering of starlight by the dust grains towards the line-of-sight of the observer (e.g. van Lieshout et al., 2016). The scenario of a comet-like tail of dust is further supported by the fact that there is no evidence for close binary companions, and no evidence for any secondary eclipses or occultations. There are no binary star systems with periods of less than one day with the observed characteristics Lieshout and Rappaport (2018). In addition to this, no transits of a hard-body are anything like the transits described above. Upper limits on the planet's radius reinforce the idea that the observed light curve is due to the dust cloud rather than the planet itself (van Werkhoven et al., 2014). Furthermore, the variability in the transit depth observed in these planets (see Figure 2.4) is thought to result

from erratic variations in dust production rates, a hypothesis supported by models of planetary outflows (e.g. Perez-Becker and Chiang, 2013; Booth et al., 2023; Bromley and Chiang, 2023).

Models of the planetary outflow have constrained the mass and planetary mass-loss rate of KIC 1255 b (Perez-Becker and Chiang, 2013; Kang et al., 2021; Booth et al., 2023). These models also find scenarios where the outflows are marginally optically thick near the planet. Morphological models of KIC 1255 b's dusty tail reproduce the observed light curve characteristics and suggest that the dust grains are micron-sized (e.g. Brogi et al., 2012; Budaj, 2013; van Werkhoven et al., 2014). Morphological models have also been used to study the dust-tail properties of K2-22 b. Sanchis-Ojeda et al. (2015) found K2-22 b also has a leading tail of dust, which gives rise to post-transit brightening in flux observed.

Catastrophically evaporating rocky exoplanets can be used to constrain small planet compositions because the dust carried by the planetary outflow is a direct sample from the magma pool on the planet's surface. Thus, analysing the dusty tails allows for direct constraints on the planet's composition. The optical properties of the dust, which are highly dependent on grain sizes and compositions, significantly affect the morphology of the white light curve, particularly the pre-transit brightening and the long egress. In contrast, the planetary mass-loss rate primarily influences the transit depth. Previous studies have shown that the dust in the tails of KIC 1255 b and KOI-2700 b might be composed of corundum (Al_2O_3) or iron-rich silicates, while other compositions such as pure iron or graphite have been ruled out (van Lieshout et al., 2014, 2016). However, the previous models have their limitations. All previous models assume that the dusty tail is optically thin throughout and use simplified formulations for dust optical properties. Moderate optical depths can significantly affect the dust's trajectory and temperature, impacting the morphology of the dusty tail and the survival time of dust grains.

In this thesis we develop a new model that couples the dust particle dynamics with the optical depth evolution of the dusty tails in order to address the limitations of previous models. Our model aims to provide robust compositional constraints from comparing synthetic light curves to those observed, offering a more accurate representation of the dusty tails of evaporating rocky planets.

3.2 Methods summary

We developed a hybrid model that combines Lagrangian super-particles with a grid-based approach for calculating the optical depth. The super-particles represent collections of dust grains with shared properties, and their dynamics are coupled with the evolution of the optical depth to derive compositional constraints from observations. We determined the mass of each super-particle by considering the planetary mass-loss rate, the initial dust grain size, the composition of the dust grains, and the frequency of super-particle introduction into the simulation.

To solve the equations of motion and sublimation for the super-particles, we em-

ployed the Dormand-Prince (RKDP) method (Dormand and Prince, 1980) for numerical integration with a relative tolerance of 10^{-8}. The RKDP method is an ODE integrator of the Runge-Kutta type of the order 5(4) which includes an adaptive stepsize control for computational efficiency (see Press et al., 2002, section 17.2). We used Brent's root finding method (Brent, 1973) to determine the temperature of dust grains with an absolute tolerance of 10^{-4} and a relative tolerance of 10^{-8} and ensured efficient computation by synchronising timesteps between particles when calculating the optical depth and transit depth. Our initial conditions assume that dust grains leave the planetary atmosphere at the thermal velocity of gas particles and are distributed either from the entire planetary surface (spherical outflow geometry) or just the day-side (day-side outflow geometry).

The simulations begin with initialising an optical depth grid representing the dust cloud. We introduced super-particles at the planetary outflow, and these particles evolve according to their initial conditions, equation of motion and sublimation rate. The optical depth of the dust cloud is updated iteratively by tracking the positions and properties of all super-particles. We run the simulations until the light curve converges, which generally occurs after approximately five orbits.

We compute synthetic light curves using a two-stage method incorporating extinction and forward scattering. Extinction is calculated by gridding the star into cells and summing the optical depth contributions from overlapping super-particles. Forward scattering is included using the Henyey-Greenstein phase function (Henyey and Greenstein, 1941) and the single scattering approximation (van Lieshout et al., 2016). The combined extinction and forward scattering components produce the synthetic transit profiles, providing a basis for comparing our model to observations. We compare the obtained synthetic light curves with observations to find the best-fit models.

The methods and model are explained in full detail in Chapter 4, Section 4.2.

3.3 Results summary

We have applied our model to study the dusty-tails of KIC 1255 b and K2-22 b. We ran a grid of models, exploring various dust compositions (listed in Table 4.1), initial dust grain sizes and planetary mass-loss rates. We estimate average mass-loss rates by comparing our model to phase-folded, average light curves due to the variability of the transits and the precision limitations of individual transits. We find a linear relationship between the transit depth and the dust mass-loss rate, which allows us to use average light curves to estimate average mass-loss rates.

For KIC 1255 b we find that corundum dust grains with sizes below 2 μm sublimate too quickly. Nevertheless, corundum dust grains with sizes between 3.5 and 5.5 μm, combined with a planetary mass-loss rate of about 8.0 $M_{\oplus}\mathrm{Gyr}^{-1}$ provided a good fit. However, aluminium's low cosmic abundance makes corundum an unlikely candidate. Iron-rich magnesium silicates (olivine and pyroxene) offered the best fits, with grain sizes around 1.25 to 1.75 μm and an average mass-loss rate of

approximately 3.0 $M_{\oplus}\mathrm{Gyr}^{-1}$ matching with the observed transit features. Olivine and pyroxene are consistent with an Earth-like composition.

Corundum and magnesium-iron silicates have distinct absorption features in the near-infrared and mid-infrared regions, with silicates showing a distinct broad absorption feature around 10 μm. We show JWST observations of these planets might allow us to conclude whether corundum or magnesium-iron silicates are a plausible composition of the dust.

We remind the reader that unlike KIC 1255 b, K2-22 b exhibits flux increases both before and after the transit, suggesting the presence of a dust tail leading the planet. Our best-fit models for K2-22 b are also for dust composed of iron-rich magnesium silicates, with initial dust grain sizes of about 1.0 to 1.5 μm and an average mass-loss rate of approximately 2.5 to 3.0 $M_{\oplus}\mathrm{Gyr}^{-1}$. These results align well with the observational constraints obtained by Schlawin et al. (2021), who determined that the dust grain sizes must be larger than 0.5-1.0 μm, leading to an estimated average mass-loss rate of around 1.6 $M_{\oplus}\mathrm{Gyr}^{-1}$.

To investigate the origin of the leading dust tail of K2-22 b, we test two outflow geometries: a spherical outflow, where dust particles are launched radially outward from the entire Hill sphere, and a day-side outflow, where particles are launched only from the planet's day-side. In our simulations, we launch the super-particles from just outside the Hill sphere, bearing in mind the physical reality that the outflow originates from the day-side surface of the planet. Our findings suggest that the spherical outflow model better fits the pre-transit brightening observed in K2-22 b's light curve, while the day-side outflow model better matches the egress and post-transit brightening. This indicates that K2-22 b's outflow geometry likely falls somewhere between these two scenarios. The radiation pressure force is weaker for K2-22 b compared to KIC 1255 b due to its cooler host star, allowing dust grains to occupy orbits closer to the star. Therefore, even though we cannot produce a model light curve that matches all features of K2-22 b, the leading tail of dust can exist in both outflow geometries within certain parameter ranges.

Our findings indicate that KIC 1255 b's dusty tail is marginally optically thick in the vicinity of the planet, significantly impacting the observed light curve. This supports earlier speculations by Rappaport et al. (2012) that the dust cloud's optical depth plays a critical role in shaping the light curve. Although we have incorporated the optical depth evolution of the dusty tail into our model, our simulations do not exhibit transit depth time variability. One limitation of our model is that the planetary mass-loss rate is treated as a free parameter, making it independent of the dust cloud's optical depth. In reality, the planetary mass-loss rate is influenced by the optical depth of the dust cloud. The rock vapour pressure depends exponentially on the planet's surface temperature, so even a small change in the dust cloud's optical depth could lead to significant variations in the planetary mass-loss rate.

Models by Booth et al. (2023) and Bromley and Chiang (2023) suggest that the

transit depth variability could result from a cycle involving the star's radiation and the planet's mass loss. Recently, Bromley and Chiang (2023) found that chaotic transit depth variability could occur if the planet's surface temperature increases with increasing optical depth in an optically thin atmosphere and decreases with increasing optical depth in an optically thick atmosphere. This scenario is only possible if, when the atmosphere is optically thin, the dust has lower opacity in visible light than in the infrared, allowing it to radiate away energy efficiently while absorbing less visible light. For the planet's surface temperature to rise with increasing optical depth in an optically thin atmosphere, the dust must create a greenhouse effect, raising the planet's surface temperature via infrared back-warming. Iron-poor, silicate-rich dust has the right opacity characteristics for this. Once enough dust has condensed and the atmosphere becomes optically thick to starlight, more iron can condense onto the grains via heterogeneous growth (e.g. Booth et al., 2023), causing the dust to absorb more visible light than infrared, thus cooling the planet and creating what Bromley and Chiang (2023) call a "nuclear winter". They propose that this cycle between greenhouse warming and nuclear winter likely causes the observed chaotic transit depth variability.

For a detailed description of all our findings see Chapter 4, Sections 4.3, 4.4 and 4.5.

3.4 Conclusions and outlook

We conclude detailed modelling of the dusty tails of catastrophically evaporating rocky planets can provide robust constraints on the composition of small rocky planets. This approach offers a new method for studying the compositions of small rocky exoplanets, which has been challenging with traditional techniques.

We find the dusty-tails are likely composed of magnesium-iron silicates, consistent with an Earth-like composition. Future research should focus on extended observations of these planets, particularly in detecting dust features via transmission spectroscopy (e.g. **?**). K2-22 b has recently been observed with JWST under the JWST GO program 3315 (PIs: Wright, J.; Tusay, N.; Wright et al., 2023). These observations will provide higher resolution data, enabling more precise constraints on dust properties and mass-loss rates as we will be able to compare our synthetic spectra to the observed JWST spectra.

We find the dust cloud is marginally optically thick in the vicinity of the planet, a hypothesis initially suggested by Rappaport et al. (2012). This characteristic greatly influences the light curve. Consequently, future models of dusty tails should consider the tail's optical depth, as was done in this study.

The composition constraint we find supports the idea of Bromley and Chiang (2023) of a greenhouse effect–nuclear winter cycle. Magnesium-iron silicates have the ideal visible-to-infrared opacity ratio to give rise to this cycle in the high mass-loss regime. In order to fully validate this hypothesis, we would need to combine the model here developed with a model of the outflow dynamics and dust formation (e.g. Booth et al., 2023). In addition to this, the formation of heterogeneous dust

grains should be considered (i.e. mixed materials dust grains).

Furthermore, there is a need for more experimental research on the sublimation properties and optical properties of various minerals. A lot of the optical data available for the minerals considered in this study were obtained at pressures and temperatures which do not correspond to the ones found in these planetary environments, perhaps introducing unwanted inaccuracies in our modelling. This is of crucial importance because the optical properties of the dust define the shape of the catastrophically evaporating rocky planets transits.

CHAPTER 4

On the likely magnesium–iron silicate dusty tails of catastrophically evaporating rocky planets

Beatriz Campos Estrada[a b c d], James E. Owen[d], Marija R. Jankovic[e], Anna Wilson[d] & Christiane Helling [b c]

[a] Centre for ExoLife Sciences, Niels Bohr Institute, Copenhagen, Denmark
[b] Space Research Institute, Austrian Academy of Sciences, Graz, Austria
[c] TU Graz, Fakultät für Mathematik, Physik und Geodäsie, Graz, Austria
[d] Astrophysics Group, Imperial College London, London, UK
[e] Institute of Physics Belgrade, University of Belgrade, Belgrade, Serbia

Published in *Monthly Notices of the Royal Astronomical Society*, Volume 528, Issue 2, February 2024, Pages 1249–1263,
doi.org/10.1093/mnras/stae095

Author contributions: Beatriz Campos Estrada conducted the research, developed the model, and wrote the manuscript. James E. Owen supervised the project and contributed to the writing and editing of the manuscript, and the interpretation and discussion of the results. Marija R. Jankovic developed the method to compute dust opacities and contributed to the writing and editing of the manuscript. Anna Wilson contributed to the development of the initial self-consistent optical depth computations. Christiane Helling supervised Beatriz Campos Estrada and provided feedback to the manuscript.

Material in the chapter from another degree/thesis: The numerical method algorithm presented in Section 4.2.5 was developed and presented in Beatriz Campos Estrada's MSci thesis, which was titled "Modelling dusty tails of ultra-short-period evaporating exoplanets", and presented at Imperial College London's Department of Physics in May 2020. The remaining methods, including the inclusion

of a self-consistent calculation of the optical depth, and the self-consistent determination of the dust opacities, were developed during Beatriz Campos Estrada's PhD. The publication was written in its entirety during the PhD time.

Original Abstract

Catastrophically evaporating rocky planets provide a unique opportunity to study the composition of small planets. The surface composition of these planets can be constrained via modelling their comet-like tails of dust. In this work, we present a new self-consistent model of the dusty tails: we physically model the trajectory of the dust grains after they have left the gaseous outflow, including an on-the-fly calculation of the dust cloud's optical depth. We model two catastrophically evaporating planets: KIC 1255 b and K2-22 b. For both planets, we find the dust is likely composed of magnesium-iron silicates (olivine and pyroxene), consistent with an Earth-like composition. We constrain the initial dust grain sizes to be ~ 1.25 - $1.75\,\mu$m and the average (dusty) planetary mass-loss rate to be $\sim 3\,M_{\oplus}\mathrm{Gyr}^{-1}$. Our model shows the origin of the leading tail of dust of K2-22 b is likely a combination of the geometry of the outflow and a low radiation pressure force to stellar gravitational force ratio. We find the optical depth of the dust cloud to be a factor of a few in the vicinity of the planet. Our composition constraint supports the recently suggested idea that the dusty outflows of these planets go through a greenhouse effect–nuclear winter cycle, which gives origin to the observed transit depth time variability. Magnesium-iron silicates have the necessary visible-to-infrared opacity ratio to give origin to this cycle in the high mass-loss state.

4.1 Introduction

The nature and composition of small planets' ($R_p \lesssim 1.5$ R$_\oplus$) interiors remain uncertain. Measurements of planetary densities (e.g. Dressing et al., 2015; Van Eylen et al., 2021) and modelling constraints (e.g. Rogers, 2015; Dorn et al., 2019; Gupta and Schlichting, 2019; Rogers and Owen, 2021; Rogers et al., 2023a,b) show most have an "Earth-like" composition of 2/3 silicate rock and 1/3 iron. However, density measurements alone do not provide enough information to determine a planet's bulk composition because planets with similar densities can vary greatly in terms of their bulk composition (e.g. Seager et al., 2007; Valencia et al., 2007; Rogers and Seager, 2010; Unterborn et al., 2016; Dorn et al., 2017b,a; Neil and Rogers, 2020; Neil et al., 2022). One way around this degeneracy would be to constrain the elemental abundance ratios of the bodies. For example, this analysis can be performed for the material accreted by polluted white dwarfs (e.g. Gänsicke et al., 2012; Farihi et al., 2016; Harrison et al., 2018; Bonsor et al., 2020). However, it is uncertain what planetary reservoirs polluted white dwarfs probe (e.g Jura and Young, 2014; Buchan et al., 2022; Brouwers et al., 2023), and they are unlikely to represent close-in planets.

Alternatively, ultra-short-period (USP) planets (planets with an orbital period of less than one day) provide a unique opportunity to study the composition of small planets. USP planets are tidally locked and highly irradiated by their host stars, often achieving sub-stellar (day-side) surface temperatures $\gtrsim 2000$ K. Their primordial atmosphere is expected to be lost quickly (e.g. Valencia et al., 2010; Owen and Wu, 2013), leaving a "bare" core exposed to stellar radiation. Under these conditions, the surface of the planet becomes molten on its day-side, and a rock-vapour atmosphere forms from magma outgassing (e.g. Schaefer and Fegley, 2009; Miguel et al., 2011; Ito et al., 2015; Kite et al., 2016; Mahapatra et al., 2017; Zilinskas et al., 2022). Measuring the composition of this rock-vapour atmosphere could directly probe the planetary interior composition since the planet's atmosphere is likely in vapour pressure equilibrium with the magma. Zieba et al. (2022) recently argued the small ($1.5\,R_\oplus$) rocky USP planet K2-141 b probably has a thin rock-vapour atmosphere. Further, *JWST* observations will likely unveil more about the nature of these planets (Zilinskas et al., 2022). However, current observations have yielded no evidence for thick atmospheres (Kreidberg et al., 2019; Crossfield et al., 2022). Furthermore, detailed modelling of these planets' interior–atmosphere interaction and evolution is required to interpret the observations and understand their planetary interiors.

In 2012, Rappaport et al. (2012) reported the discovery of KIC 12557548 b (often shortened to KIC 1255 b and more recently Kepler-1520 b), a transiting object with an orbital period of approximately 15.7 h which displays an asymmetric light curve. The KIC 1255 b light curve presents a sharp transit ingress and a slow egress. Additionally, the light curve shows a positive bump in stellar flux before the transit occurs and high transit depth time variability. Rappaport et al. (2012) suggested this light curve could be explained by the existence of a low-mass (similar to Mercury) evaporating USP planet with a comet-like tail of dust. The comet-like tail scenario can be explained as follows: dust from the planet's molten surface condenses in a thermally-driven wind (Rappaport et al., 2012; Perez-Becker and Chiang, 2013; Booth et al., 2023) and is transported by a gaseous outflow out to the point where the gas density is low enough that dust dynamically decouples from the gas. At this point, the trajectory of the dust is dictated by the stellar radiation pressure and the stellar gravity, which shapes the dust into a cometary tail, trailing the planet (e.g Rappaport et al., 2012; Brogi et al., 2012; Budaj, 2013; Sanchis-Ojeda et al., 2015; Lieshout and Rappaport, 2018). As the gas density decreases away from the planet, the sublimation temperature decreases (e.g. Booth et al., 2023). This results in the gradual sublimation of the dust as it moves along the tail, ultimately resulting in a tail where the optical depth drops with distance from the planet (Rappaport et al., 2012; van Lieshout et al., 2016).

The optical depth pattern of the dust cloud can explain the sharp ingress and slow egress observed. Furthermore, the forward scattering of stellar photons by the dust grains towards the line-of-sight of the observer can give rise to the pre-transit brightening (e.g. van Lieshout et al., 2016). This dusty tail scenario has been validated by studies of the colour dependence of the transit depth (e.g. Bochinski

et al., 2015). In addition to this, van Werkhoven et al. (2014) obtained an upper limit on the KIC 1255 b's radius of 4600 km, supporting the idea that we are observing the dust cloud and not the planet.

Since the discovery of KIC 1255 b, two more examples of evaporating rocky planets have been observed: KOI-2700 b (Rappaport et al., 2014) and K2-22 b (Sanchis-Ojeda et al., 2015). KOI-2700 b presents a very similar light curve to KIC 1255 b. K2-22b presents a symmetric light curve, with increased observed flux both before and after the transit, where the post-transit brightening is explained with a leading tail of dust (Sanchis-Ojeda et al., 2015).

To explain the high transit depth time variability, Rappaport et al. (2012) state an erratic variation in the dust production rate is needed, and a detailed understanding of the origin of this variability remains uncertain. Perez-Becker and Chiang (2013) speculated and Booth et al. (2023) found the planetary outflow can be unsteady. For fast dust growth rates and moderate optical depths, there is a cycle between periods of dust production and no dust production, which could give rise to the observed transit depth variability. The variability was investigated further by Bromley and Chiang (2023), following the speculation of heterogeneous condensation by Booth et al. (2023). Bromley and Chiang (2023) demonstrated a chaotic evolution could arise when iron-poor silicates condensed at low-mass loss rates (low optical depths), while iron-rich silicate dust condensed at high mass-loss rates (high optical depths).

Using models of the planetary outflow, Perez-Becker and Chiang (2013), Kang et al. (2021) and Booth et al. (2023) constrained the mass of KIC 1255 b and the planetary mass-loss rate. In addition to this, the models agree with a scenario where the outflows are marginally optically thick in the planet's vicinity.

Morphological models of KIC 1255 b's dusty tail reproduce the characteristics of the observed light curve and place constraints on the size of the dust grains by comparing synthetic light curves to the observed ones (e.g. Brogi et al., 2012; Budaj, 2013; van Werkhoven et al., 2014). These models do not attempt to model the formation and launch of the dusty outflow but to study the properties of the dust under the assumption it is launched from the planets. The models indicate the dust grains are around micron-sized.

K2-22 b's dust tail properties have also been studied using similar morphological models. Sanchis-Ojeda et al. (2015) determined K2-22 b has a leading dust tail, giving origin to the observed post-transit brightening in flux. This implies the ratio of radiation pressure forces to stellar gravity (β) to be less than 2%. The value of β can be this small for low luminosity host stars and small particle sizes ($\lesssim 0.1\mu$m) or large particle sizes ($\gtrsim 1.0\mu$m). More recently, observations and models of K2-22 b by Schlawin et al. (2021) show the average particle size must be larger than about 0.5 - 1.0μm, leading to mass-loss rates of about 1.6 - 1.8 $M_\oplus\,\mathrm{Gyr}^{-1}$.

The dust in the planetary outflow is a direct sample of the magma pool on the planet's surface. Therefore, studying the dusty tails can be used to directly place

constraints on the planetary composition. The composition of the dust was investigated in detail by van Lieshout et al. (2014, 2016). This work was done by assuming the planet launched an outflow with dust particles of a certain size and composition and studying how long they survived before they completely sublimated. van Lieshout et al. (2014) used the dust's survival timescale to compute the distance it could travel from the planet, and compared this to the length of the tail inferred from the light-curve. They found the models where the dust was composed of corundum (Al_2O_3[s]) or iron-rich silicates to be consistent with the observations of KIC 1255 b and KOI-2700 b. Pure iron, graphite or silicon carbide grains were ruled out. van Lieshout et al. (2016) directly simulated the dynamics and size evolution of dust particles in KIC 1255 b's tail to study the dust composition, the dust grain sizes and the planetary mass-loss rate of the planet. They found the dusty tail to be most likely composed of Al_2O_3[s] micron-sized grains, with a planetary mass-loss rate ranging from 0.6 to 15.6 $M_\oplus \mathrm{Gyr}^{-1}$. Enstatite ($MgSiO_3$[s]) and forsterite ($Mg_2SiO_4$[s]) had previously been suggested as potential compositions of the dust grains by Rappaport et al. (2012), Brogi et al. (2012) and Perez-Becker and Chiang (2013). However, van Lieshout et al. (2016) found iron-free magnesium-silicates were too cold to sublimate efficiently due to their low optical, but high IR opacities, and hence survived too long in the dust cloud to be consistent with the observed transit duration.

All previous dusty tail models are limited because they assume the dusty tail to be optically thin throughout. In addition to this, many of the previous models use a simplified formulation for the complex refractive index in the calculation of dust optical properties. Considering the dust cloud to be optically thin throughout is an assumption that requires detailed investigation. The trajectory of a dust grain is highly dictated by the radiation pressure force, which is obviously highly sensitive to the optical depth to stellar light once it reaches moderate values. Thus, even moderate optical depths can cause significant changes in the morphology of the dusty tail. In addition to this, the temperature of a dust grain, and hence the sublimation rate of the dust, is highly sensitive to moderate or higher optical depths. Therefore, the more optically thick the environment, the cooler the dust grains will be, causing them to survive longer in the dusty tail.

In this work, we construct a new model of the dusty tails. We couple the dust particle dynamics to the self-consistently determined optical depth. Introducing the optical depth evolution allows for robust compositional constraints to be derived from the observations. Our methods are presented in Section 4.2. In Section 4.3 we apply our model to KIC 1255 b and in Section 4.4 to K2 22 b. In Section 4.5, we discuss our results in the context of the observations. Finally, in Section 4.6, we summarise our findings.

4.2 Model and methods

We aim to develop a model with all the necessary physics to compare directly to the observations, but that is still computationally feasible. To achieve this, we adopt a hybrid method, where similar to van Lieshout et al. (2016), the dust grains are modelled as Lagrangian "super-particles", but the optical depth is computed by ray-tracing on a grid of dust densities. Our super-particle is a collection of dust grains that share the same but evolving properties. The number of actual dust grains (N_d) inside a super-particle depends on the planetary mass-loss rate, the grain's initial size and composition, and how often/many super-particles we introduce into the simulation. Thus, we introduce the super-particle mass $m_{sp} = m_d N_d$, where m_d is the mass of an individual dust grain.

4.2.1 Dust motion

The stellar radiation pressure force and the stellar gravity dominate the trajectory of the dust grains. For full consistency, we include planetary gravity and the Poynting-Robertson drag (Robertson, 1937) acting on the dust grains, but we ignore collisions between the individual dust grains. Following the results from Booth et al. (2023), we assume the planet to have a mass of $0.03 M_\oplus$ although we note the choice does not affect our results. Using the Fortney et al. (2007) mass-radius relationship, we estimate the planetary radius to be 0.33 $R_\oplus$, assuming mass fractions of 2/3 silicate rock and 1/3 iron. The equation of motion for the dust grain is solved in the co-rotating frame of reference, centred at the centre of mass of the star-planet system. The planetary and stellar orbits are assumed to be circular. The equation of motion of a dust grain is given by:

$$\ddot{\mathbf{r}} = -\frac{GM_\star}{|\,\mathbf{r}-\mathbf{r}_\star\,|^3}(\mathbf{r}-\mathbf{r}_\star) - \frac{GM_{\rm planet}}{|\,\mathbf{r}-\mathbf{r}_{\rm planet}\,|^3}(\mathbf{r}-\mathbf{r}_{\rm planet}) - \boldsymbol{\omega}\times(\boldsymbol{\omega}\times\mathbf{r}) - 2(\boldsymbol{\omega}\times\dot{\mathbf{r}}) + \beta\frac{GM_\star}{|\,\mathbf{r}-\mathbf{r}_\star\,|^2}\left[\left(1-\frac{\dot{\mathbf{r}}_{\rm radial}}{c}\right)\frac{(\mathbf{r}-\mathbf{r}_\star)}{|\,\mathbf{r}-\mathbf{r}_\star\,|} - \left(\frac{\dot{\mathbf{r}}+(\boldsymbol{\omega}\times\mathbf{r})}{c}\right)\right] \tag{4.1}$$

where $\mathbf{r}$ is the position vector of the dust grain, $\mathbf{r}_{\star,\rm planet}$ are the position vectors of the star and planet, respectively; $M_{\star,\rm planet}$ are the mass of the star and planet respectively; $\boldsymbol{\omega}$ is the rotation vector of the frame-of-reference, β is the ratio between the norms of the direct radiation pressure force and the star's gravitational force, G is the gravitational constant and c is the speed of light. The final term on the RHS of Equation 4.1 represents the radiation forces acting on the dust grains (Robertson, 1937; Burns et al., 1979).

We assume our dust grains are spherical, and as such, β is given by

$$\beta = \frac{1}{4\pi c G}\frac{L_\star}{M_\star}e^{-\tau_\star}\kappa(T_\star, s) \tag{4.2}$$

where $L_\star$ is stellar luminosity, $\tau_\star$ is the optical depth of the dust cloud to stellar irradiation at the grain's position, and κ is the radiation-pressure Planck-mean opacity at the stellar temperature $T_\star$, for a particle of radius s.

4.2.2 Dust sublimation

We take a similar approach to van Lieshout et al. (2016) for determining the sublimation rate of a spherical dust grain in a gas-free environment. In thermodynamic equilibrium, when the partial pressure of a molecule equals its equilibrium vapour pressure, the condensation rate must equal the sublimation rate; thus, the sublimation rate can be expressed in terms of the condensation rate using the principle of detailed balance (c.f. Booth et al., 2023). In our models, the dust grains have large numbers of atoms ($\sim 10^9$ atoms for a 0.1μm particle); thus, we assume their sublimation rate is solely dependent on the dust's internal properties (e.g. its temperature, Gail and Sedlmayr 2013). Consequently, the sublimation rate for a dust grain in thermodynamic equilibrium with the gas surrounding it is equal to its sublimation rate in a gas-free environment (Langmuir, 1913). Therefore, the change of the radius of a dust grain (s) can be written as (Kimura et al., 2002; Gail and Sedlmayr, 2013; van Lieshout et al., 2014),

$$\frac{\mathrm{D}s}{\mathrm{D}t} = -\frac{\alpha p_v(T_d)}{\rho_d}\left(\frac{\mu m_u}{2\pi k_B T_d}\right)^{1/2} \tag{4.3}$$

where α is the evaporation coefficient which parameterises the kinetic inhibition of the sublimation[1], p_v is the equilibrium vapour pressure, μ is the molecular weight of the sublimating molecules in atomic mass units[2], m_u is the atomic mass unit, k_B is Boltzmann's constant, and T_d is the dust grain's temperature. The equilibrium vapour pressure is given by the Clausius-Claperyon relation (Kimura et al., 2002),

$$p_v(T) = \exp(-\mathcal{A}/T + \mathcal{B})\ [\mathrm{cgs}] \tag{4.4}$$

where $\mathcal{A}$ and $\mathcal{B}$ are material-specific parameters. Quantities α, $\mathcal{A}$ and $\mathcal{B}$ are assumed to be temperature independent.

The balance between the received and emitted energy by a dust grain is used to determine the dust's temperature, which we approximate as:

$$\kappa_{\mathrm{abs}}(T_\star, s)\ \frac{L_\star}{4\pi r_d^2}\ e^{-\tau_\star} = 4\ \kappa_{\mathrm{abs}}(T_d, s)\ \sigma_{SB}\ T_d^4 \tag{4.5}$$

where $\kappa_{\mathrm{abs}}(T_\star, s)$ is the Planck-mean absorption opacity at the stellar temperature $T_\star$, $\kappa_{\mathrm{abs}}(T_d, s)$ is the absorption opacity at the dust temperature T_d, r_d is the dust grain-star distance and σ_{SB} is Stefan-Boltzmann's constant. This equation assumes that while we are including the attenuation of stellar light due to the dust cloud's optical depth, we are assuming the dust cloud is optically thin to its own cooling radiation. This assumption is justified, as for our best fit models, the dusty outflow is optically thin to its re-emitted thermal emission. As discussed in our

[1] α has been experimentally measured to be approximately the same as the growth/sticking coefficient (Gail and Sedlmayr, 2013).

[2] Following van Lieshout et al. (2014) and for simplicity, we assume μ to be the molecular weight of the dust sublimating. In reality, μ is the average molecular weight of the molecules recondensing from the gas-phase in the sublimation-condensation equilibrium.

results, the dust's temperature (and hence sublimation rate) depends critically on the opacity ratio $\kappa_{\rm abs}(T_\star, s)/\kappa_{\rm abs}(T_d, s)$, which at higher ratios gives higher temperatures and hence faster sublimation. It is this opacity ratio that ultimately allows us to constrain the dust's composition and size through its impact on the temperature and, subsequently, the sublimation rate.

4.2.3 Optical depth evolution

To calculate the optical depth of the dust cloud, we implement the clouds-in-cells (CIC) method (Birdsall and Fuss, 1969). Consider a staggered-mesh grid, where scalar variables (e.g. extinction) are defined at the grid-cell centres (red diamonds in Figure 4.1) and direction-dependent variables (e.g. optical depth) at the centres of the grid-cell interfaces (black circles in Figure 4.1). The extinction to be attributed to the grid-cell centres is obtained by sharing a dust super-particle's extinction over the grid points surrounding it. A 2D representation of our 3D method is shown in Figure 4.1. Considering a dust grain at a position $P(x, y)$, we can regard the grain as a small cloud and spread it over an area of $\Delta x \Delta y$, the shaded area surrounding the black star. The extinction in the horizontal-lines-shaded area is assigned to point (i, j); that in the diamond-shaded area to point $(i + 1, j)$; that in the vertical-lines-shaded area to point $(i + 1, j + 1)$ and that in the diagonal-lines-shaded area to point $(i, j + 1)$.

We adapt and apply the method described above to a uniform three-dimensional spherical polar grid centred at the star, i.e. the volume of each grid cell is approximately the same. Here, r is the radial distance from the star's centre, θ is the polar angle, and ϕ is the azimuthal angle. The contribution to the extinction of a super-particle at a position (r_d, θ_d, ϕ_d) is given by

$$\chi_{sp}(r_d, \theta_d, \phi_d) = \frac{m_{sp}\, \kappa_{\rm ext}(T_\star, s)}{\Delta V}, \tag{4.6}$$

where $\kappa_{\rm ext}$ is the extinction opacity of the dust grains in a super-particle, and ΔV is the "volume"[3] of the super-particle, taken to be the volume element of the cell in which it resides. For better numerical accuracy, volumes are calculated with the spherical volume element in the following form (c.f. Stone and Norman, 1992):

$$\Delta V = \Delta(R^3/3)\ \Delta(-\cos\theta)\ \Delta\phi. \tag{4.7}$$

The extinction of the grid cell centred at $(r(i), \theta(j), \phi(k))$ can now be written as

$$\chi(i, j, k) = \sum_{sp} V^f_{ijk}\ \chi_{sp}(r_d, \theta_d, \phi_d) \tag{4.8}$$

where V^f_{ijk} is the fraction of the super-particle's volume that resides in cell (i, j, k) (see Figure 4.1). The sum is performed over all super-particles that have any

[3]It's important not to confuse this "volume" with any physical volume. This "volume" is used to smooth the extinction over our grid in the CIC method and thus scales with the grid's resolution. Our choice for its size is confirmed by our resolution tests.

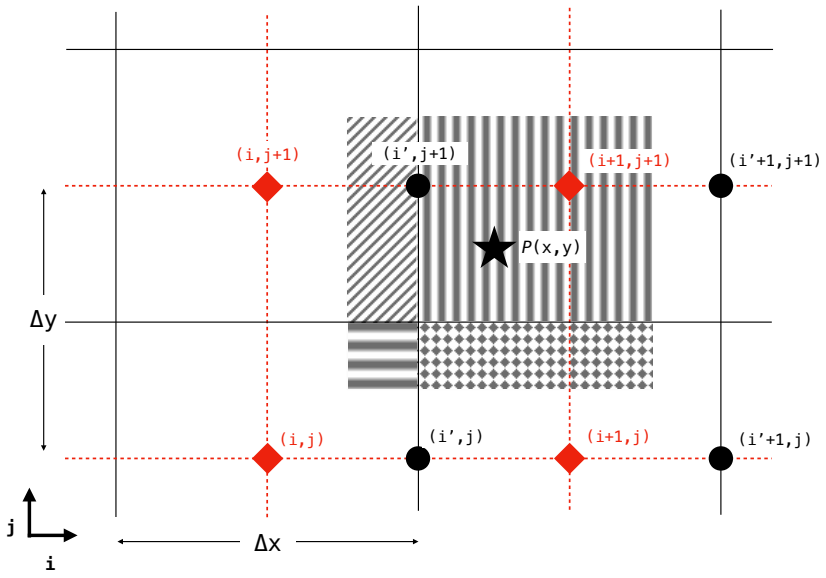

Figure 4.1: A 2D representation of our staggered mesh, similar to the 3D one used to estimate the dust cloud's optical depth. Scalar variables are measured at the centres of the grid cells, represented by the red diamonds. Vector quantities/direction-dependent variables are measured at the grid-cells interfaces, represented by the black circles. We apply the clouds-in-cells method (Section 4.2.3) where the extinction contribution of a dust grain in position $P(x, y)$ (black star) is shared between the grid-cells surrounding it (shaded area) with the value determined between the volume assigned to the grain and the volume of the cell.

volume that overlaps with that cell. Once the extinction grid is computed via Equation 4.8, we obtain the optical depth by numerically integrating the extinction over the radial distance from the star to the grid-cell interface centres in the radial direction **i**, using:

$$\tau(i,j,k) = \sum_{i'=0}^{i-1} \chi(i',j,k)\ \Delta r,\ \text{for } i \geq 1 \tag{4.9}$$

where $\tau(i,j,k)$ is the optical depth at the grid-cell interface centred at $(r(i), \theta(j), \phi(k))$ and Δr is grid-cell size in the radial direction **i**. The grid boundaries are set as,

$$r(i=0) = R_{\min},\ r(i=N_{\rm R}) = R_{\max};$$

$$\theta(j=0) = \theta_{\min} + \frac{\Delta\theta}{2},\ \theta(j=N_\theta-1) = \theta_{\max} - \frac{\Delta\theta}{2};$$

$$\phi(j=0) = \phi_{\min} + \frac{\Delta\phi}{2},\ \phi(j=N_\phi-1) = \phi_{\max} - \frac{\Delta\phi}{2};$$

where $N_{{\rm R},\theta,\phi}$ are the number of grid-cells in the radial **i**, polar **j** and azimuthal **k** directions respectively, $(R,\theta,\phi)_{\min}$ are the lower boundaries in each direction and similarly $(R,\theta,\phi)_{\max}$ are the upper boundaries. We note that $r(i') = r(i) + \frac{\Delta r}{2}$. In

this case, at $i = 0$, $\tau = 0$ for all j and k. After testing, we set $N_{\rm R} = 75$, $N_\theta = 25$ and $N_\phi = 250$, and the grid limits to be

$$R_{\rm min} = 0.95\ a,\ R_{\rm max} = 1.10\ a;$$
$$\theta_{\rm min} = 1.55\ {\rm rad},\ \theta_{\rm max} = 1.60\ {\rm rad};$$
$$\phi_{\rm min} = -\ 0.40\ {\rm rad},\ \phi_{\rm max} = 0.10\ {\rm rad};$$

where a is the semi-major axis of the planet's orbit. These values allow for approximately cubic grid-cells with constant grid-cell sizes in each direction, where $\Delta r = 0.002\,a$ and $\Delta\theta = \Delta\phi = 0.002\,{\rm rad}$. The grid limits were chosen according to where the optical depth is dynamically important. A lower limit of 0.001 for the optical depth is placed. Outside the chosen grid limits, the optical depth of the dust cloud is set to 0.001. To obtain the optical depth at the position of a super-particle, we perform a tri-cubic spline interpolation (Press et al., 2002) over the optical depth grid.

4.2.4 Dust opacities

Dust opacities are calculated for the materials listed in Table 4.1 as follows. First, using the MIESCAT module of RADMC3DPY[4], which applies Mie theory, we calculate the dust absorption ($\kappa^\lambda_{\rm abs}$) and scattering opacities ($\kappa^\lambda_{\rm sca}$), as well as the scattering g-factor ($g^\lambda_{\rm sca}$), as functions of wavelength ($\lambda = 10^{-5}$–$10\,{\rm cm}$) and grain size ($s = 0.1$–$10\,\mu{\rm m}$)[5]. Where the optical constants are not available for the entire wavelength range indicated above, they are extrapolated by keeping them constant at shorter wavelengths and with a log-log function at longer wavelengths, as would be expected from simple diffraction theory (e.g. Bohren and Huffman, 1983). The extrapolation of optical constants to shorter wavelengths may somewhat affect the opacities at the stellar temperatures, especially for corundum (Al_2O_3[s]), for which the optical constants are only available down to $0.5\,\mu$m, but they do not change our conclusions. At the lower end of relevant temperatures, the calculated values are unaffected by the extrapolation since the available data covers the relevant range of wavelengths.

For each grain size s, the opacities are averaged over a Gaussian size distribution centred at s, and of width $\Delta\ln(s) = 0.02$ to avoid "ringing". We adopt the dust bulk densities shown in Table 4.1.

To obtain the Planck-mean opacities as functions of temperature and grain size, we integrate $\kappa^\lambda_{\rm abs}$, $\kappa^\lambda_{\rm sca}$ and $g^\lambda_{\rm sca}$ over frequency. In our problem, we have four relevant opacities:

1. The absorption opacity to stellar light, $\kappa_{\rm abs}(T_\star, s)$, used in Equation 4.5;

[4] www.ita.uni-heidelberg.de/ dullemond/software/radmc-3d/manual_rmcpy/

[5] For some materials, in some wavelength ranges, optical constants are different for different crystal axes. In such cases, we follow van Lieshout et al. (2016) and combine the optical constants for different axes using the Bruggeman (1935) mixing rule.

Table 4.1: Dust species used in this study and the corresponding densities, sublimation parameters and references for optical data and sublimation parameters.

Dust species	Density	Optical data	Sublimation parameters				Notes
	[g cm^{-3}]	ref.	$\mathcal{A}$ [10^4 K]	$\mathcal{B}$	α	ref.	
Al_2O_3[s] (Corundum)[1]	4.00	K95	7.74	39.3	0.1	S04, L08	
$MgSiO_3$[s] (Enstatite)[1,2]	3.20	J94, D95, J98	6.89	37.8	0.1	M88	(a)
$Mg_{[0.5,0.7,0.95]}Fe_{[0.5,0.3,0.05]}SiO_3$[s] (Pyroxene)[1]	3.20, 3.01, 2.74	J94, D95	6.89	37.8	0.1	M88	(a), (b)
Mg_2SiO_4[s] (Forsterite)[1]	3.27	F01	6.53	34.1	0.1	N94	
$Mg_{1.72}Fe_{0.21}SiO_4$[s] (San Carlos Olivine)[2]	3.30	F01, Z11	6.53	34.1	0.1	N94	(a), (c), (d)
$Mg_{1.56}Fe_{0.40}Si_{0.91}O_4$[s] (Sri Lanka Olivine)[2]	3.30	Z11	6.53	34.1	0.1	N94	(a), (c),(d)
$Mg_{[1.0,0.8]}Fe_{[1.0,1.2]}SiO_4$[s] (Olivine)[1]	3.71, 3.80	J94, D95	6.53	34.1	0.1	N94	(a), (d)
Fe_2SiO_4[s] (Fayalite)[2]	4.39	F01	6.04	37.7	0.1	N94	(a)

Notes. [1]Amorphous. [2]Crystalline. (a) Following van Lieshout et al. (2014), $\alpha = 0.1$ is adopted for materials with no evaporation coefficient measurement. (b) Following Kimura et al. (2002), the sublimation parameters of enstatite are adopted for all other types of pyroxene. (c) The density chosen for this olivine is the average density of low-Fe olivine. (d) Following Kimura et al. (2002), the sublimation parameters of forsterite are adopted for all other types of olivine.

References. K95 Koike et al. (1995a); S04 Schaefer and Fegley (2004); L08 Lihrmann (2008); J94 Jaeger et al. (1994); D95 Dorschner et al. (1995); J98 Jaeger et al. (1998); M88 Mysen and Kushiro (1988); F01 Fabian et al. (2001); N94 Nagahara et al. (1994); Z11 Zeidler et al. (2011a).

2. The absorption opacity at the grain's temperature, $\kappa_{\rm abs}(T_d, s)$, used in Equation 4.5;

3. The extinction opacity to the star light, $\kappa_{\rm ext}(T_\star, s) = \kappa_{\rm abs}(T_\star, s) + \kappa_{\rm sca}(T_\star, s)$, used in Equation 4.6;

4. The radiation pressure opacity, $\kappa(T_\star, s) = \kappa_{\rm abs}(T_\star, s) + \kappa_{\rm sca,eff}(T_\star, s)$, used in Equation 4.2, where $\kappa_{\rm sca,eff}(T_\star, s)$ is given by $(1-g_{\rm sca}(T_\star, s))\,\kappa_{\rm sca}(T_\star, s)$.

4.2.5 Numerical methods

To determine the trajectory of a super-particle, we solve its equations of motion (Equation 4.1) and sublimation (Equation 4.3) simultaneously. To solve equations 4.1 and 4.3, we use the Dormand-Prince (DP) method (Dormand and Prince, 1980) with an absolute and relative tolerance of 10^{-8}. We apply Brent's method (Brent, 1973) to solve Equation 4.5 numerically for the temperature of a dust grain with an absolute tolerance of 10^{-4} and a relative tolerance of 10^{-8}. Each super-particle has an optimal timestep for the DP solver. In order to make the model as efficient as possible, we use the optimal timestep for each individual super-particle and synchronise the timestep between particles when obtaining the optical depth of the dust cloud and calculating the transit depth (see Section 4.2.6). This approach only updates the optical depth at every synchronised time step; however, we confirmed this does not affect our results by varying the synchronised time step.

The model's free parameters are the distribution of the grain's initial positions and velocities, the initial dust grain sizes, the planetary mass-loss rate and the dust composition. To ensure the dust grains are not gravitationally bound to the planet, we start them off at a distance of 1.1 Hill radii from the planet's centre. We assume the dust grains have left the planetary atmosphere at the thermal velocity of the gas particles (Booth et al., 2023) in the radial direction. The super-particles are either randomly distributed to leave from the entire planetary surface (spherical outflow) or just the planet's day-side, both at the level of the Hill radius (see Section 4.4).

The simulations are initialised by obtaining the optical depth grid of the initial dust cloud. The planetary mass-loss rate is set to be constant throughout our simulations. We launch 250 super-particles every $100^{\rm th}$ of a planetary orbit, enough to guarantee convergence in the light curve (see Figure 4.2). We trace the optical depth every $200^{\rm th}$ of an orbit. We consider a dust grain completely sublimated when it is smaller than $0.1\mu m$, at which point it does not significantly contribute to the extinction or scattering of the dust cloud. We run the simulations until the transit profile is converged, i.e. it has reached a steady state and does not significantly change from one transit to the next; this typically requires five orbits (or until it becomes apparent there is no steady state for a given material; see Section 4.3.2).

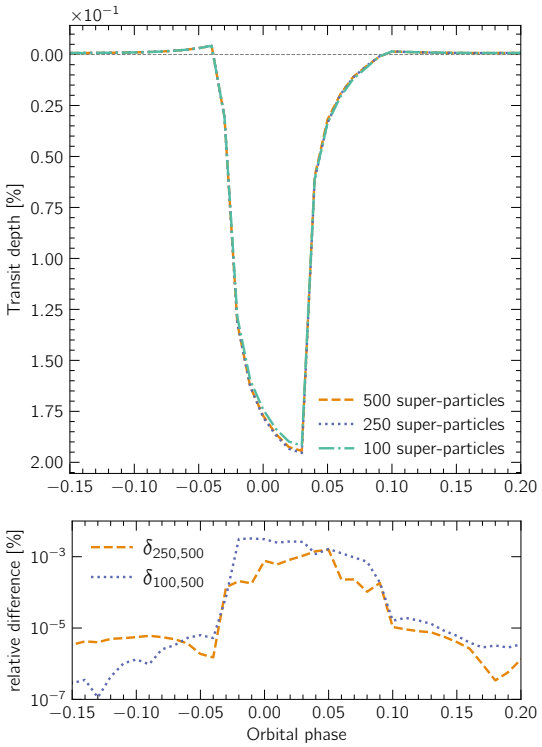

Figure 4.2: **Top:** Simulated transit of KIC 1255 b for different numbers of super-particles launched every 100$^{\text{th}}$ of an orbit. The dust is assumed to be composed of olivine ($Mg_{0.8}Fe_{1.2}SiO_4$[s]). The dust cloud is assumed to be optically thin throughout (τ=0.1) and the outflow is assumed to be radially outwards from the entire planetary surface (spherical outflow). **Bottom:** The relative percentage difference between the transits simulated on the top plot. The difference is smaller than the observed error ($\approx$ 200 ppm Rappaport et al., 2012), therefore, we launch 250 super-particles every 100$^{\text{th}}$ of an orbit.

4.2.6 Transit profile calculation

The final stage is to compute a synthetic light curve from our simulations. We adopt a two-stage method, including extinction and forward scattering. For the extinction calculation, we implement the CIC method once again (see Section 4.2.3). We grid the star into cells with area A_{cell} and spread each super-particle over an area A_{cell}. If a super-particle overlaps with a given grid cell, the optical depth contribution from the super-particle in that cell is given by

$$\tau_{sp} = \frac{f\,\kappa_{\text{ext}}(T_\star, s)\,m_{sp}}{A_{\text{cell}}}, \tag{4.10}$$

where f is the fraction of the super-particle's area which overlaps with the grid cell. To obtain the total optical depth τ in a grid cell, we sum all the individual τ_{sp}'s corresponding to that cell. The flux from that cell is then attenuated by a factor of $e^{-\tau}$. Finally, the total stellar flux is obtained by adding all the individual fluxes from each grid cell.

Forward scattering of light by dust grains can increase the observed stellar flux. The increase in flux is proportional to the scattering opacity of the dust grain, $\kappa_{\rm sca}(T_\star, s)$ (Section 4.2.4), and the scattering phase function at the scattering angle. We use the Henyey-Greenstein analytical scattering phase function for dust grain mixtures (Henyey and Greenstein, 1941), which is solely dependent on $g_{\rm sca}$ and the scattering angle, and use the single scattering approximation (van Lieshout et al., 2016). We ignored limb-darkening effects for both the extinction and forward scattering computations. The extinction and forward scattering components are combined into synthetic transit profiles.

4.3 KIC 1255 b: Dust composition, grain sizes and mass-loss rate constraints

One of our key goals is to determine the dust composition and size. The size of the dust grains has been constrained through measurements of the transit depth dependence on wavelength, i.e. colour dependence. Croll et al. (2014) and Schlawin et al. (2016) observed the transit depths of KIC 1255 b not to be colour dependent and set a lower limit of the dust grain size of $\sim$0.2-0.5 μm. Previous modelling efforts (e.g. Brogi et al., 2012; Budaj, 2013) predict the dust grain sizes to be 0.1 - 1.0 μm based on the shape of the forward-scattering bump. However, these models did not consider the sublimation rate of the dust grains and simply assumed an exponential decay of the size distribution. Furthermore, van Lieshout et al. (2016) curiously found corundum (Al_2O_3 [s]) to be the best fit with the observations for KIC 1255 b, using a model that didn't include the dust tail's optical depth self-consistently on the dust dynamics.

Therefore, using our new, self-consistent approach, we constrain the tail's dust composition, grain sizes and planetary mass-loss rate. We run a grid of models and compare the synthetic light curves with observations. The dust's optical properties, which are highly dependent on the dust grain sizes and compositions, control the morphology of the white light curve, specifically the pre-transit brightening and the long egress. On the other hand, the planetary mass-loss rate mainly influences the transit depth (see Section 4.3.3). We define the best-fit models to be the ones where the pre-transit brightening and the long egress shapes are best represented with a transit depth comparable to that of the average observed light curves. Therefore, the reported mass-loss rate is an attempt to estimate the *average* dusty mass-loss rates (see Section 4.3.3).

Since the planet itself is not detected, we do not know exactly when, in its orbit, the planet is at mid-transit in the observations. Thus, one needs to align the models with the observations by defining when an orbital phase of 0 occurs. We do this by aligning our synthetic light curves with the observations by the pre-transit brightening (if necessary). Additionally, we also align our out-of-eclipse flux to that of the observations. In our simulations, we compute the transit depth every 5 minutes. To obtain the synthetic light curves to compare to the observations,

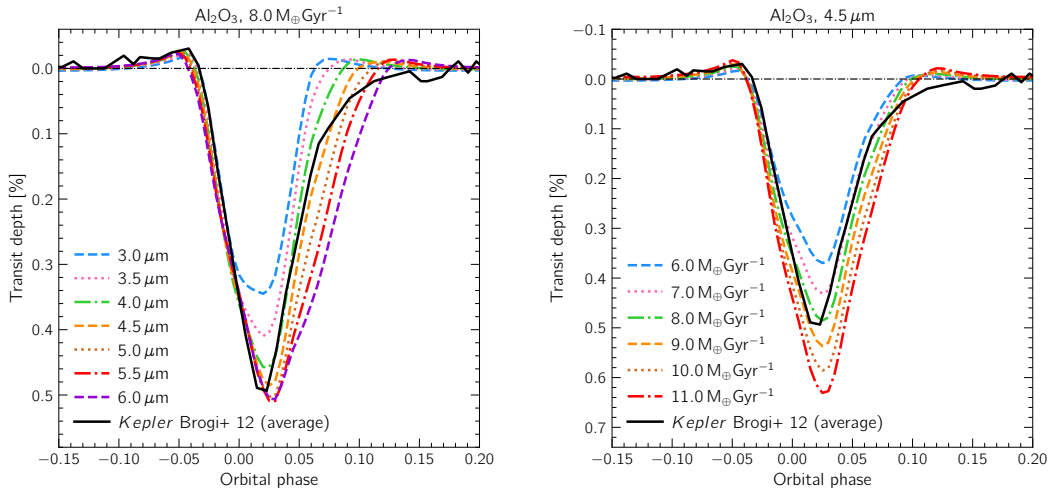

Figure 4.3: Synthetic light curves of KIC 1255 b for dust composed of corundum (Al_2O_3[s]). The observed *Kepler* light curve averaged over six quarters by Brogi et al. (2012) is shown as the black solid curve. **Left**: Synthetic light curves for models at a constant planetary mass-loss rate of 8.0 $M_\oplus \mathrm{Gyr}^{-1}$ and different initial dust grain sizes. **Right**: Synthetic light curves for models at a constant initial dust grain size of 4.5 μm and different planetary mass-loss rates.

we smooth the data over the *Kepler* long cadence (30 minutes).

We first apply our model to KIC 1255 b. KIC 1255 b orbits a K-type star with $T_\star \approx 4550\,K$, $R_\star \approx 0.66\,R_\odot$ and $M_\star \approx 0.67\,M_\odot$ (Thompson et al., 2018). We run the model for the dust compositions listed in Table 4.1. We study the parameter space of initial dust grain sizes ranging from 0.5 to 8.0 μm, and (dusty) planetary mass-loss rates from 1.0 to 15.0 $M_\oplus \mathrm{Gyr}^{-1}$. The models we discuss throughout Section 4.3 assume the outflow is spherical. We also explored models with a day-side outflow geometry, but we found the spherical outflow to consistently be a better fit for KIC 1255 b (Appendix 4.A.1). This is because the day-side outflow models produce a more symmetric transit, which is less consistent with KIC 1255 b's light curve. We discuss the issue of outflow geometry further in Section 4.4.

4.3.1 Corundum

We find corundum dust grains with initial sizes below 2.0 μm sublimate too fast to produce the observed light curve of KIC 1255 b. This is expected as small corundum grains achieve very high temperatures (Figure 4 in Booth et al. 2023), due to their low IR opacity. We find corundum could give origin to the observed light curve of KIC 1255 b with initial dust grain sizes of ~3.5 - 5.5 μm and an average mass-loss rate of 8.0 $M_\oplus \mathrm{Gyr}^{-1}$ (Figure 4.3). This result arises because as the particles get larger, the ratio between their optical and IR opacity falls resulting in lower temperatures and longer lifetimes; however, larger particles have a lower opacity and we must increase the mass-loss rate to match the observed transit

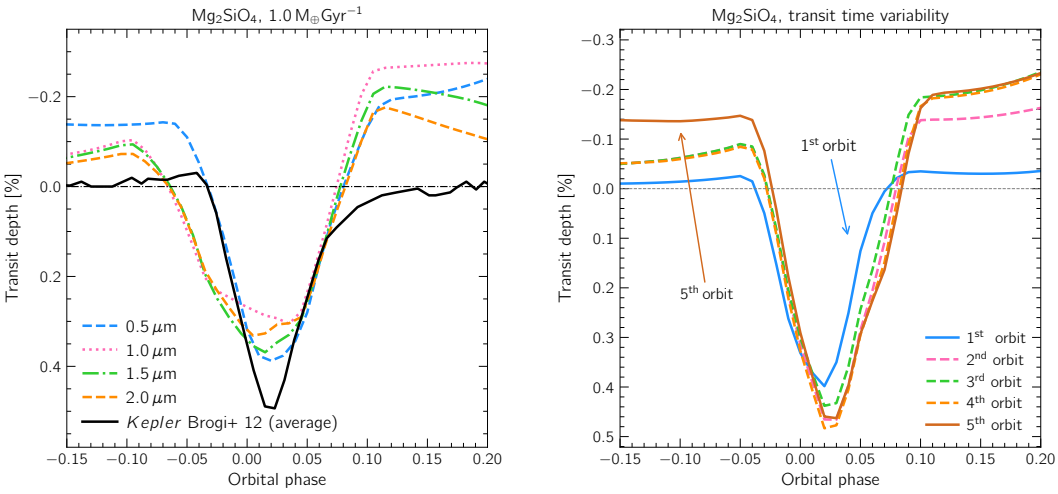

Figure 4.4: Synthetic light curves of KIC 1255 b for dust composed of forsterite (Mg_2SiO_4[s]). **Left**: Synthetic light curves for models at a constant planetary mass-loss rate of $1.0\,M_\oplus \mathrm{Gyr}^{-1}$ and different initial dust grain sizes after 5 orbits. The observed *Kepler* light curve averaged over six quarters by Brogi et al. (2012) is shown as the black solid curve. **Right**: Synthetic light curves over 5 orbits at an initial dust grain size of $0.5\,\mu$m and a planetary mass-loss rate of $1.0\,M_\oplus \mathrm{Gyr}^{-1}$. Note how the light curve does not converge, particularly for the pre-transit brightening region.

depth.

The initial dust grain sizes we estimate for dust composed of corundum are above the lower limit estimated from colour dependence measurements. The average dust mass-loss rate we estimate is within the findings of van Lieshout et al. (2016) but considerably higher than the theoretical models of Perez-Becker and Chiang (2013) and Booth et al. (2023). The estimate of the dust mass-loss rate in other studies (e.g. Kawahara et al., 2013) is generally obtained solely from the transit depth, ignoring any forward scattering effects. Forward scattering reduces the transit depth and therefore, higher mass-loss rates are needed to fit the observations (Appendix 4.A.2).

As discussed by van Lieshout et al. (2016), aluminium has a low cosmic abundance and is likely a minor component of rocky planets (e.g. Schaefer and Fegley, 2009; Jura and Young, 2014). In addition to this, corundum is measured to have a relatively low abundance in the bulk silicate earth (BSE) composition (see Table 1.7 in O'Neill and Palme 1998). Therefore, the existence of a corundum dust tail combined with such high mass-loss rates would be surprising. While corundum can fit the data, we consider it an unlikely candidate for the composition of the dust in the tail.

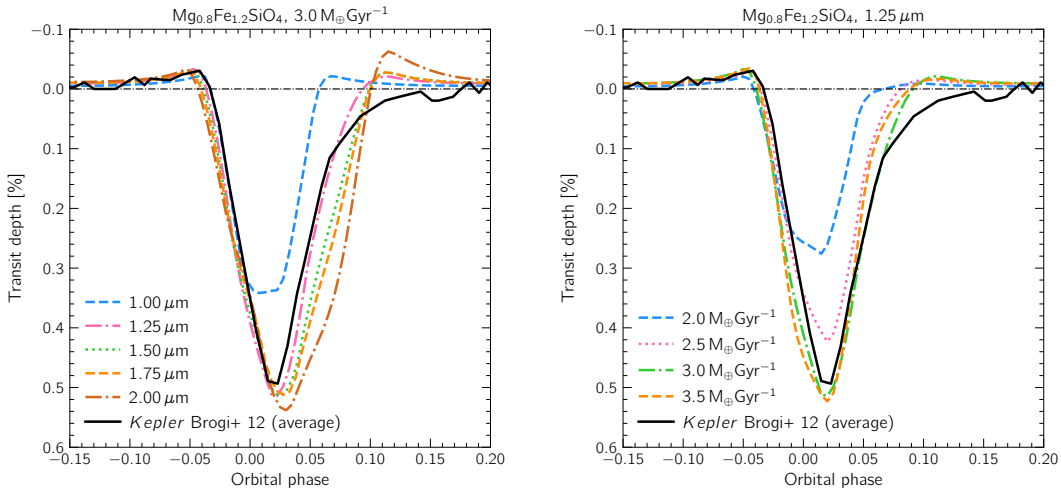

Figure 4.5: Synthetic light curves of KIC 1255 b for dust composed of iron-rich olivine ($Mg_{0.8}Fe_{1.2}SiO_4$[s]). The observed *Kepler* light curve averaged over six quarters by Brogi et al. (2012) is shown as the black solid curve. **Left**: Synthetic light curves for models at a constant planetary mass-loss rate of $3.0\,M_\oplus \mathrm{Gyr}^{-1}$ and different initial dust grain sizes. **Right**: Synthetic light curves for models at a constant initial dust grain size of $1.25\,\mu$m and different planetary mass-loss rates.

4.3.2 Olivine and Pyroxene

We have studied compounds we know are predominant in the Earth's mantle (e.g. O'Neill and Palme, 1998): olivine, $(Mg, Fe)_2SiO_4$[s], and pyroxene, $(Mg, Fe)SiO_3$[s].

First, we consider the end-members of these two types of minerals. The iron end-member of olivine (fayalite), Fe_2SiO_4 [s], is too volatile in the entire parameter space studied, i.e. it sublimates too fast to explain an observable dusty tail. On the other hand, the magnesium end-members of olivine (forsterite), Mg_2SiO_4[s], and pyroxene (enstatite), $MgSiO_3$[s], have low optical to IR opacity ratio and do not achieve high enough temperatures to sublimate. The dust survives for multiple orbits, accumulating over time, and the transit profile never converges (see the right panel of Figure 4.4). Additionally, the synthetic light curves produced show no agreement with the observations at any time-point (see the left panel of Figure 4.4). The pre-transit brightening occurs earlier than expected for most of the parameter space. Furthermore, there is a significant post-transit brightening, which does not match the observations. Therefore, we rule out dust grains predominately composed of fayalite, forsterite or enstatite. We test other types of pyroxene (see Table 4.1). For $Mg_{0.95}Fe_{0.05}SiO_3$[s], the scenario is similar to that of forsterite and enstatite, i.e. the dust is too cold due to its low optical to IR opacity ratio. $Mg_{0.7}Fe_{0.3}SiO_3$[s] and $Mg_{0.5}Fe_{0.5}SiO_3$[s] behave similarly to fayalite - these compounds are too volatile and do not survive long enough to create the dusty tail observed. Given the contrasting behaviours of the different types of pyroxene tested here, we believe low-iron pyroxene with an iron content between 0.05 and 0.3 should be explored in future work.

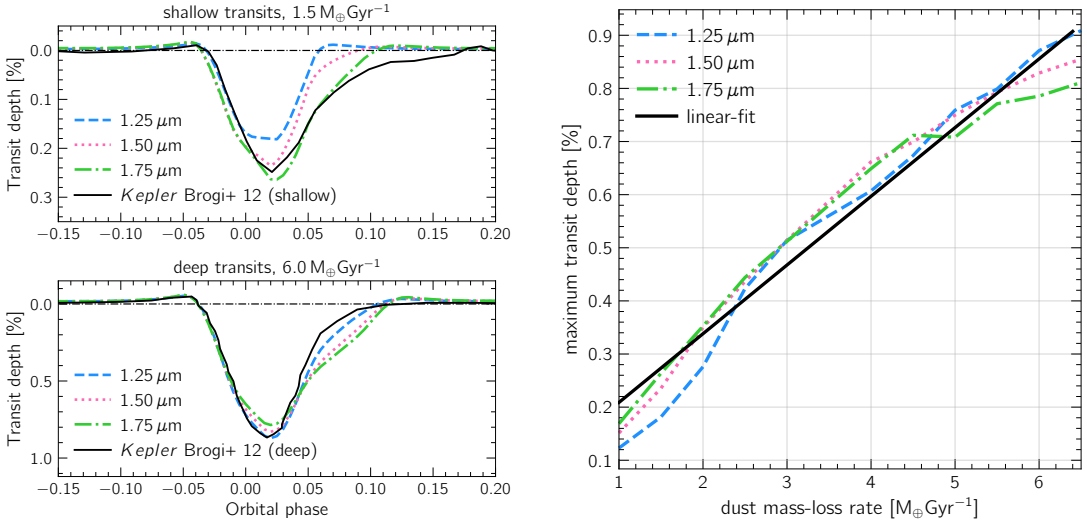

Figure 4.6: **Left**: Synthetic light curves for models at a constant planetary mass-loss rate of $1.5\,M_{\oplus}\mathrm{Gyr}^{-1}$ (*top*) and $6.0\,M_{\oplus}\mathrm{Gyr}^{-1}$ (*bottom*) at different initial dust grain sizes. The observed *Kepler* light curve averaged over six quarters by Brogi et al. (2012) is shown as the black solid curve. Shallow transits correspond to observed light curves with transit depths between 0.2 - 0.5 %, deep transits correspond to observed light curves with transit depths larger than 0.8 % (see, Brogi et al., 2012). **Right**: The maximum transit depth for the synthetic light curves of $Mg_{0.8}Fe_{1.2}SiO_4$ versus the dust mass-loss rate, at different initial dust grain sizes. The black solid curve represents a linear fit to the data.

The dust compositions tested which best fit with the observations of KIC 1255 b are magnesium-iron olivines, i.e. compounds of the form $(Mg, Fe)_2SiO_4$[s] with an iron content of at least 10%. Figure 4.5 shows that for $Mg_{0.8}Fe_{1.2}SiO_4$[s], the pre-transit brightening and the long-egress match the observation for dust grain sizes between 1.25 μm and 1.75 μm and an average planetary mass-loss rate of $3.0\,M_{\oplus}\mathrm{Gyr}^{-1}$. Similar results are obtained for Sri Lanka olivine, San Carlos olivine and $MgFeSiO_4$[s].

These results are in agreement with the BSE abundances (e.g Kargel and Lewis, 1993) and white dwarf measurements for evaporating exoplanets (e.g Bonsor et al., 2020). Curry et al. (2023) show that the observed dust is coming from a localised region where the planet has been evaporated down to. This supports the idea that the dust originates from the mantle of the planet, where magnesium-iron silicates like olivine and pyroxene are expected to be abundant. In addition to this, Bromley and Chiang (2023) argued iron-rich silicates are required to be able to produce an observable mass loss rate for catastrophically evaporating exoplanets.

4.3.3 Estimating the average mass-loss rate

Since the transits are variable, and the precision on an individual transit is poor, we must compare our model to phase-folded, average light curves. Therefore, we must evaluate whether the mass-loss rate reported by our model, when compared

to averaged light curves, is representative of the average mass-loss rate. We did this by computing the relationship between the mass-loss rates and the transit depth in our models. As shown in the right panel in Figure 4.6, we find the transit depth has an approximately linear relation with the dust mass-loss rate. A linear relationship implies that average light curves can be used to estimate average mass-loss rates. Additionally, we compared our synthetic light curves for $Mg_{0.8}Fe_{1.2}SiO_4$ to two sets of observed light curves of KIC 1255 b as divided by Brogi et al. (2012): a set where the transit depths are shallow (0.2%,- 0.5%) and a set where the transit depths are deep ($>0.8\,\%$). We find the best-fit for the shallow and deep transits require smaller and larger mass-loss rates, respectively, but the same range of dust grain sizes as for the average mass-loss rate case (left panel Figure 4.6). Therefore, our reported best-fit mass-loss rates to the average light curves are a reasonable approximation to the average mass-loss rate.

4.3.4 Synthetic JWST spectra: corundum vs magnesium-iron silicates

While we have argued corundum is an unlikely composition, we suggest that this can be directly confirmed with additional observations. Corundum and magnesium-iron silicates have distinct absorption features in the near-infrared and mid-infrared regions. In particular, silicates show a very broad absorption feature at about $10\,\mu$m. Observing the dusty tails in these wavelengths can help us understand what the dust is composed of and validate our models. We produce synthetic JWST absorption spectra of KIC 1255 b for the $Mg_{0.8}Fe_{1.2}SiO_4$[s] best-fit model with an initial dust grain size of $1.25\,\mu$m and an average mass-loss rate of $3.0\,M_\oplus \mathrm{Gyr}^{-1}$ (pink dot-dashed curve in Figure 4.5 left), and the corundum best-fit model with an initial dust grain size of $4.5\,\mu$m and an average mass-loss rate of $8.0\,M_\oplus \mathrm{Gyr}^{-1}$ (green dot-dashed curve in Figure 4.3 left). We use the wavelength range and resolution of the MIRI-MRS mode and the NIRSpec-PRISM mode. The spectra are shown in Figure 4.7. The synthetic spectra show that we would be able to distinguish if the dust is composed of corundum or magnesium-iron silicates with JWST observations if a bright target is identified [6]. This inference is in line with the results of Bodman et al. (2018) and Okuya et al. (2020), who also found JWST observations could help constrain the dust composition.

4.4 The leading dust tail of K2-22b and the outflow geometry

In addition to modelling KIC 1255 b, we also model K2-22 b. As mentioned earlier, K2-22 b shows a light curve with increases in the observed flux both before and after the transit (Sanchis-Ojeda et al., 2015). This agrees with a scenario where there is a tail of dust also leading the planet. K2-22 b orbits an M-type star

[6] It is likely KIC 1255 b is too faint to perform this experiment with a small number of transits; however, K2-22 b may be bright enough.

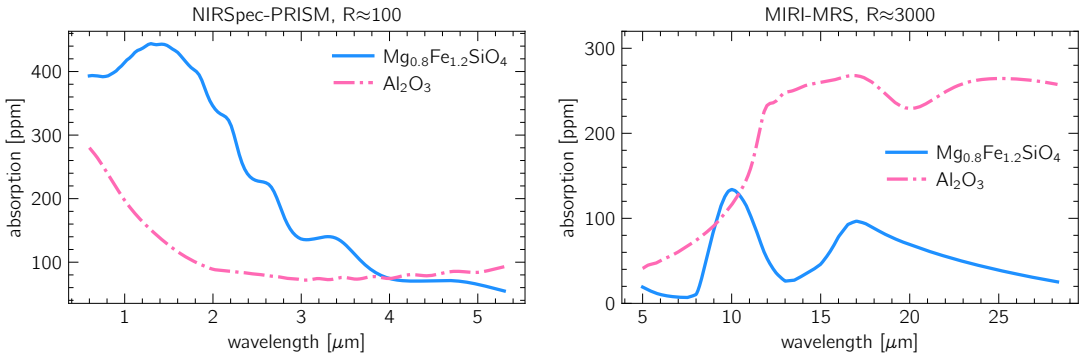

Figure 4.7: **Left**: NIRSpec-PRISM synthetic absorption spectra of KIC 1255 b for the best-fit model of corundum (4.5 μm and 8.0 $M_{\oplus}\mathrm{Gyr}^{-1}$ - green dot-dashed curve in Figure 4.3 left) and iron-rich olivine (1.25 μm and 3.0 $M_{\oplus}\mathrm{Gyr}^{-1}$ - pink dot-dashed curve in Figure 4.5 left). The resolution used was 100. **Right**: Same as the top panel but for the MIRI-MRS mode. The resolution used was 3000. Note the distinct absorption feature of the olivine at about 10 μm.

with $T_{\star} \approx 3830\,K$, $R_{\star} \approx 0.58\,R_{\odot}$ and $M_{\star} \approx 0.60\,M_{\odot}$, with an orbital period of approximately 9.2h (Sanchis-Ojeda et al., 2015).

Sanchis-Ojeda et al. (2015) state a "substantial" ($\beta \gtrsim 0.05$) radiation pressure force necessarily blows the dust into orbits trailing the planet. However, they find if β is sufficiently small ($\lesssim 0.02$) some dust can fall into faster orbits than that of the planet, creating a tail of dust leading the planet.

The best-fit models we find for the K2-22 b average light curve (Sanchis-Ojeda et al., 2015), assuming the dust is composed of $Mg_{0.8}Fe_{1.2}SiO_4$[s], are for initial dust grain sizes $\sim$1.0 - 1.5μm and a mass-loss rate $\sim$2.5 - 3.0 $M_{\oplus}\mathrm{Gyr}^{-1}$. These results compare favourably to Schlawin et al. (2021), who observationally constrained the dust grain sizes of K2-22 b to be larger than 0.5-1.0 μm. Based on this measurement, they constrained the average mass-loss rate of K2-22 b to be $\sim$ 1.6 $M_{\oplus}\mathrm{Gyr}^{-1}$.

Here, we investigate if the origin of the leading tail is a consequence of the launch geometry of the dusty outflow. We test two outflow geometries: a spherical outflow, where the super-particles leave from the Hill sphere radially outwards over the full 4π, and a day-side outflow, where the super-particles leave the Hill sphere only from the day-side of the planet, radially outwards. As discussed in our methods, we always launch our super-particles from just outside the planet's Hill sphere. Physically, the outflow is always launched from the day-side surface of the planet; however, multi-dimensional simulations of photoevaporating planets with H/He-rich atmospheres (e.g. Stone and Proga, 2009; Owen and Adams, 2014; Tripathi et al., 2015) indicate the outflow can wrap around to the nightside, yielding a quasi-spherical outflow through the Hill sphere. Thus, we speculate a high-mass planet could have an outflow similar to those seen in these photoevaporation simulations, while a low-mass planet might have an outflow geometry that is day-side dominated at the Hill sphere (Figure 4.8, right).

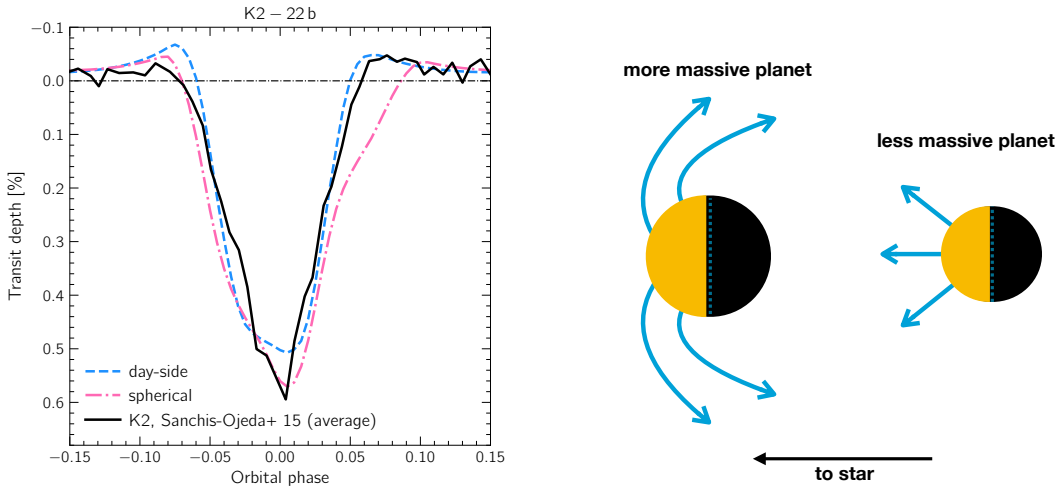

Figure 4.8: **Left**: Synthetic light curves of K2-22 b for dust composed of iron-rich olivine ($Mg_{0.8}Fe_{1.2}SiO_4$[s]). The blue dashed curve is for a day-side outflow with an initial dust grain size of 1.5 μm and a mass-loss rate of 3.0 $M_\oplus \mathrm{Gyr}^{-1}$. The pink dot-dashed curve is for a spherical outflow with an initial dust grain size of 1.0 μm and a mass-loss rate of 2.5 $M_\oplus \mathrm{Gyr}^{-1}$. The observed *K2* light curve is the black solid curve (Sanchis-Ojeda et al., 2015). **Right:** Cartoon of the dust outflow trajectory. The yellow represents the planet's day-side. The dust forms on the planet's day-side. If the planet is massive enough, the dust will follow a trajectory similar to that shown on the planet on the left - this is what the spherical outflow in our model depicts. If the planet is not massive enough, the dust will follow a trajectory similar to that shown on the planet on the right - this is what the day-side outflow in our model assumes.

We find the spherical outflow is a better fit for the pre-transit brightening of K2-22 b. However, we find the day-side outflow to be a better fit for the egress and post-transit brightening (Figure 4.8, left). We find a post-transit brightening and a symmetric light curve (i.e. a leading tail of dust) can exist for both geometries in certain ranges of the parameter space, even though they don't fit the light curve perfectly. Thus, even in the spherical outflow scenario, this implies that changing the stellar parameters and the planet's orbital period is enough to give rise to a leading tail of dust. This result is a consequence of the strength of the radiation pressure force. The radiation pressure is weaker for K2-22 compared to KIC 1255 because K2-22 is cooler than KIC 1255 by about 700K. Therefore, dust grains can occupy orbits closer to the star. While we cannot produce a model light curve that matches all the features of K2-22b, we speculate that K2-22 b's outflow geometry probably lies somewhere between a spherical and a day-side outflow. Coupling this launching geometry with a lower radiation pressure force to stellar gravitational force ratio than KIC 1255 b , would likely yield K2-22 b's light curve.

We find a day-side outflow at the level of the Hill sphere is not a good fit with the observations of KIC 1255 b (Appendix 4.A.1). Thus, the fact that KIC 1255 b is consistent with a spherical outflow and K2-22b with an outflow geometry that sits between our spherical and day-side models might imply KIC 1255 b is more mas-

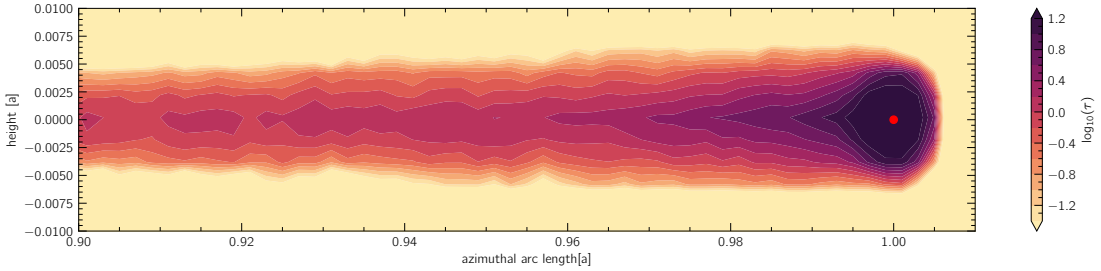

Figure 4.9: Optical depth density map at the radial edge of the optical depth grid ($R = 1.10\,a$) for the best-fit $Mg_{0.8}Fe_{1.2}SiO_4$[s] model ($1.25\,\mu$m, $3.0\,M_\oplus \mathrm{Gyr}^{-1}$, dot-dashed pink curve in the left panel of Figure 4.5). The red circle indicates the position of the planet. Note how the optical depth is moderate in the vicinity of the planet, implying attenuation of stellar light is important for controlling the dust's dynamics.

sive than K2-22b. In this scenario KIC 1255 b is massive enough for a significant fraction of the escaping dust grains to wrap around the planet as they escape, as seen in hydrodynamic simulations (e.g. Stone and Proga, 2009; Owen and Adams, 2014; Tripathi et al., 2015), while for K2-22 b they are effectively unbound when they leave the planet's surface.

4.5 Optical depth and transit depth time variability

As speculated by Rappaport et al. (2012), Perez-Becker and Chiang (2013) and van Lieshout et al. (2016), we find the dust cloud to be optically thick in the vicinity of the planet (see Figure 4.9). This affects the transit light curve of the planet and its tail in our models significantly, as shown in Figure 4.10. The transit depth for the models where the optical depth is traced is consistently larger than the transit depth in the models in which we assume a fixed low value for the optical depth. This is because the dust is cooler in the optically thicker environment, and the grains do not sublimate as fast. Although the optical depth also affects the radiation pressure force (i.e., β parameter, see Equation 4.2), its effect on the sublimation is stronger as the sublimation rate is exponentially dependent on the dust temperature (although radiation pressure is also exponentially sensitive to optical depth, our models only reach moderate optical depths).

Although we have included the optical depth evolution of the dusty tail, we do not find a transit depth time variability in our simulations. One of the limitations of our model is the fact that the planetary mass-loss rate is a free parameter and, therefore, independent of the optical depth of the dust cloud. In reality, the planetary mass-loss rate of the planet is dependent on the optical depth of the dust cloud. The rock vapour pressure is exponentially dependent on the surface temperature of the planet. So, a fractional change in the dust cloud's optical depth could cause large differences in the planetary mass-loss rate (e.g. Perez-Becker and Chiang, 2013). Furthermore, we have disregarded the dynamical impact of

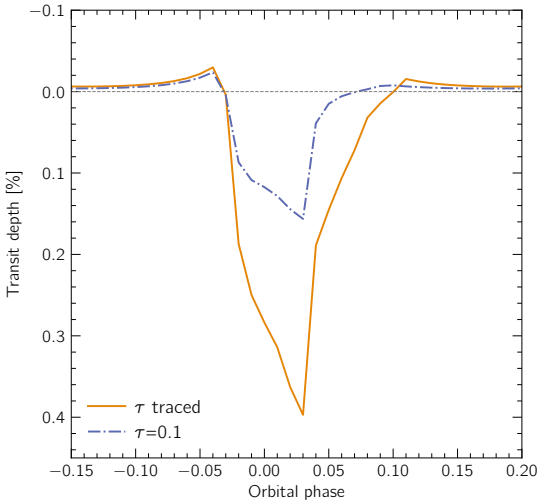

Figure 4.10: Comparison of two synthetic light curves for a model where the optical depth of the dust cloud is kept thin at 0.1 (dash-dotted curve) and a model where the optical depth is traced (solid curve).

the stellar wind on the dust grains as for micron-sized particles, the stellar wind pressure is generally negligible compared to the radiation pressure (e.g. Strubbe and Chiang, 2006). However, the stellar wind may become relevant for extremely large stellar wind rates. These rates can happen during, for example, coronal mass ejections, which can be a source of the observed variability (cf. Kawahara et al., 2013; Croll et al., 2015; Schlawin et al., 2018). The observations of KIC 1255 b show that its transit depth variability presents no pattern (e.g Lieshout and Rappaport, 2018). Both Perez-Becker and Chiang (2013) and Booth et al. (2023) have argued the variability might be driven by a cycle involving stellar insolation and mass loss. In addition to this, Booth et al. (2023) found that non-steady outflows can arise for fast dust growth rates and moderate optical depths. However, a chaotic behaviour, like the one the observations show, was not reproduced. Recently, Bromley and Chiang (2023) found a chaotic behaviour for the transit depth when they consider the planetary surface temperature to increase with increasing optical depth when the atmosphere is optically thin, and when it decreases with increasing optical depth when the atmosphere is optically thick. Such behaviour is only possible if, when the atmosphere is optically thin, the dust has lower opacities in the visible wavelengths than in the infrared. This is because, in order to condense, the dust grains need to radiate away their energy more efficiently than they absorb visible light. In addition to this, for the planetary surface temperature to increase with increasing optical depth in an optically thin atmosphere, the dust needs to induce a greenhouse effect, which will raise the planetary surface temperature via infrared back-warming. Iron-poor silicate-rich dust presents the ideal visible-to-infrared opacity ratio to give rise to the conditions described above. When enough dust grains have condensed, and the atmosphere has therefore become optically thick to starlight, more iron can condense onto the grains. The dust will begin to absorb more efficiently in the visible than in the infrared, and the

planetary surface temperature will decrease, inducing what Bromley and Chiang (2023) denominate a nuclear winter. Bromley and Chiang (2023) state this cycle between the greenhouse effect and the nuclear winter is the most likely cause of the transit depth time variability.

Booth et al. (2023) discuss heterogeneous condensation might give rise to the transit depth time variability. They argue stable iron-free or iron-poor silicates will condensate first in the wind (e.g. Mg_2SiO_4[s]) at low temperatures. This will allow iron to condense into these grains, causing the dust temperature to rise. However, iron evaporates more promptly than magnesium from silicates (e.g. Costa et al., 2017) which will increase the dust temperature, causing the iron content to decrease. This means the dust grains might reach a composition that is controlled by the feedback between the iron content and the temperature of the dust.

We find the dust is likely composed of magnesium-iron silicates (iron-poor or iron-rich) (Section 4.3). This is in agreement with both the greenhouse effect-nuclear winter cycle (Bromley and Chiang, 2023) and heterogeneous condensation (Booth et al., 2023). A complete model which couples the dust formation to the outflow dynamics and tail morphology is needed to accurately study which processes are giving rise to the transit depth time variability. In addition to this, compositionally heterogeneous dust grains should be considered.

4.6 Summary

Catastrophically evaporating rocky planets provide a unique opportunity to study the composition of rocky worlds. We have developed a self-consistent model of the dusty tails of catastrophically evaporating rocky planets. For the first time, we have introduced the optical depth evolution of the dust cloud in a model of this kind. We apply the model to two catastrophically evaporating exoplanets: KIC 1255 B and K2-22 b.

For both planets, we find the dust is likely composed of magnesium-iron silicates. The synthetic light curves of KIC 1255 b match the observed light curve for average (dusty) planetary mass-loss rates of $\sim 3\,M_{\oplus}\mathrm{Gyr}^{-1}$ and initial dust grain sizes between ~ 1.25 and $\sim 1.75\,\mu$m. Although corundum also produces models that fit the *Kepler* observations, this is for very large initial dust grain sizes ($\sim 4\,\mu$m) and large planetary mass-loss rates ($\sim 8\,M_{\oplus}\mathrm{Gyr}^{-1}$). The existence of a corundum dust tail combined with such high mass-loss rates would be surprising as aluminium is likely a minor component of rocky planets (e.g. Schaefer and Fegley, 2009). JWST observations in the wavelength range of 1-28 μm could explicitly rule out corundum as the composition of the dust.

We show K2-22 b probably has a different outflow geometry than KIC 1255 b. Thus, K2-22b is likely less massive than KIC 1255 b and presents a leading tail of dust. We find the leading tail of dust is likely a consequence of the outflow geometry and low radiation pressure force to stellar gravity force ratios (β).

We find the dust cloud is marginally optically thick to stellar light in the vicinity of the planet, as first speculated by Rappaport et al. (2012). This has a significant impact on the light curve, and therefore, future models of dusty tails should account for the optical depth of the tail, as was done in this work. Furthermore, Bromley and Chiang (2023) recently showed the observed transit depth time variability could have an origin in a greenhouse effect–nuclear winter cycle. Magnesium-iron silicates have the ideal visible-to-infrared opacity ratio to give rise to this cycle in the high mass-loss regime. In order to fully validate this hypothesis, we need to combine the model here developed with a model of the outflow dynamics and dust formation (e.g. Booth et al., 2023).

Acknowledgements

We thank the anonymous reviewer for their comments, which improved the manuscript. We are grateful to Richard Booth, Subhanjoy Mohanty, Alfred Curry, Francisco Ardévol Martínez, David A. Lewis and Courtney J. Rundhaug for interesting discussions. We thank Eugene Chiang and Joshua Bromley for helpful comments on an earlier version of the manuscript. BCE is part of the CHAMELEON MC ITN EJD which received funding from the European Union's Horizon 2020 research and innovation programme under the Marie Sklodowska-Curie grant agreement no. 860470. BCE was supported by a Royal Society 2020 Enhancement Award. JEO is supported by a Royal Society University Research Fellowship. MRJ acknowledges support from the European Union's Horizon Europe programme under the Marie Sklodowska-Curie grant agreement No. 101064124, and funding provided by the Institute of Physics Belgrade, through the grant by the Ministry of Science, Technological Development, and Innovations of the Republic of Serbia. This project has received funding from the European Research Council (ERC) under the European Union's Horizon 2020 research and innovation programme (Grant agreement No. 853022, PEVAP).

Data Availability

The synthetic light curves data presented in the paper are available at the Electronic Research Data Archive (ERDA) of the University of Copenhagen at https://sid.erda.dk/cgi-sid/ls.py?share_id=cceKwPeLFV.

4.A Appendix

4.A.1 KIC 1255 b, day-side outflow

The simulations for KIC 1255 b that assume a day-side outflow fail to reproduce the observed long-egress. This happens consistently in the parameter space explored. Figure 4.11 shows the synthetic spectra for different dust mass-loss rates and initial dust grain sizes when assuming a day-side outflow for KIC 1255 *b*.

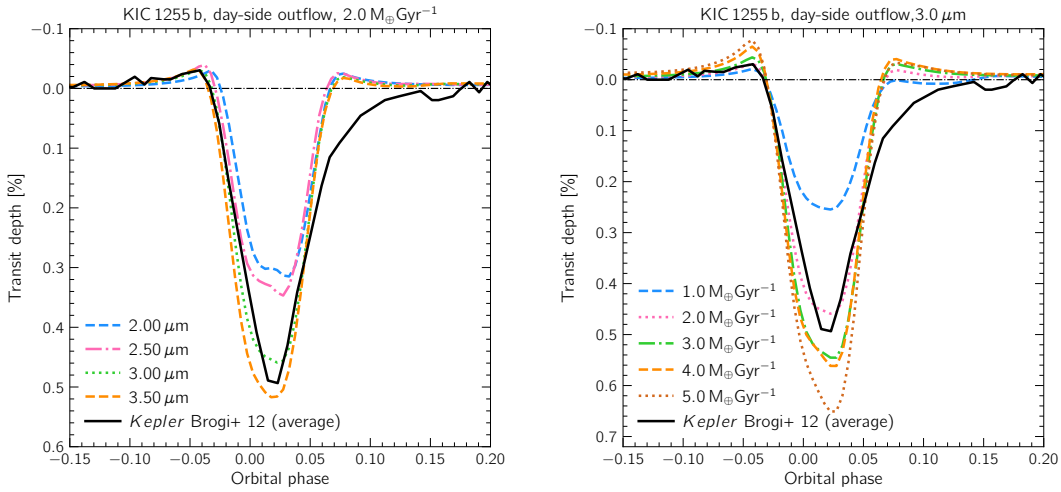

Figure 4.11: Synthetic light curves of KIC 1255 b for dust composed of iron-rich olivine ($Mg_{0.8}Fe_{1.2}SiO_4$[s]) and a day-side dusty outflow. **Left**: Synthetic light curves for models at a constant planetary mass-loss rate of 2.0 $M_\oplus \mathrm{Gyr}^{-1}$ and different initial dust grain sizes. The observed *Kepler* light curve averaged over six quarters by Brogi et al. (2012) is shown as the black solid curve. **Right**: Synthetic light curves over 5 orbits at an initial dust grain size of 0.5 μm and a planetary mass-loss rate of 1.0 $M_\oplus \mathrm{Gyr}^{-1}$.

4.A.2 The extinction and forward scattering competition

While the extinction increases the transit depth, forward scattering fills up the light curve. When including forward scattering in the modelling of dusty tails, we require larger mass-loss rates to fit the observations (see also Figure 3, van Lieshout et al. 2016). Figure 4.12 shows the contribution from scattering and extinction for the best-fit models of corundum and iron-rich olivine.

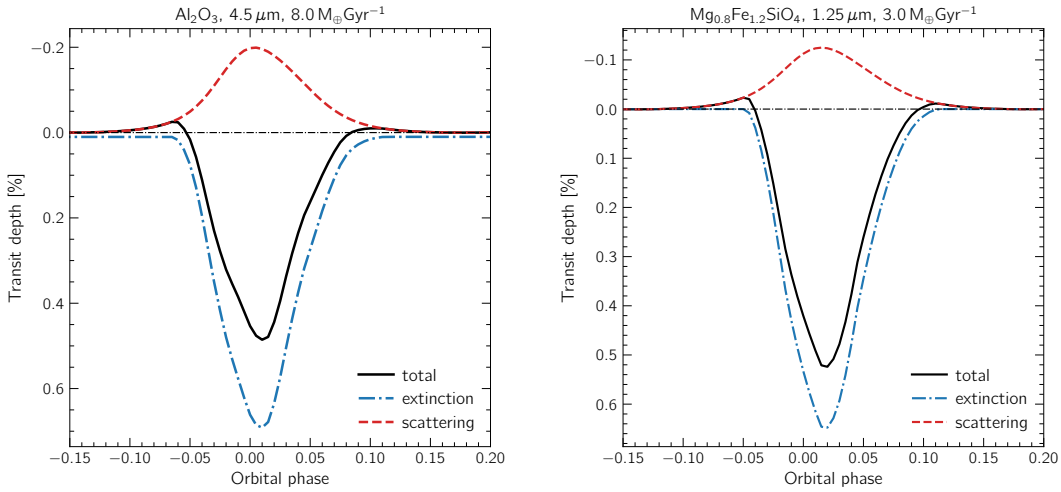

Figure 4.12: Synthetic light curves (black solid curves) of the best-fit corundum (*left*) and iron-rich olivine (*right*) models, and the scattering (dashed red curves) and extinction (dot-dashed blue curves) components. The components are smoothed to *Kepler*'s long cadence. Note how the scattering component reduces the transit depth by a significant factor in both cases.

CHAPTER 5

Substellar atmospheres: Theory and Modelling

Dream only a dream if work don't follow it.

— Kendrick Lamar, in *Institutionalized*

In this chapter we describe the fundamental concepts for modelling substellar atmospheres, including a brief overview of the numerical methods used by the `MARCS` atmosphere model. Unless otherwise stated, the descriptions of the assumptions and fundamentals are based on Chapters 1, 2 and 5 of Mihalas (1978), Chapter 1 of Rybicki and Lightman (1986), Chapters 2 and 5 of Seager (2010), and Chapters 5, 6 and 7 of Gray (2021). In particular the description of the gas-phase equilibrium chemistry is based on Chapters 7 and 10 of Fegley and Osborne (2013), Chapter 4 of Seager (2010) and Woitke et al. (2018).

5.1 Assumptions in plane-parallel substellar atmosphere models

Here we describe the major assumptions considered by the `MARCS` model. Although different substellar atmosphere models can make different assumptions, the ones described below are generally implemented by the majority of one-dimensional substellar atmosphere models.

- Geometry: Considering the radius of the object is much larger than the thickness of its atmosphere, the atmosphere is assumed to be composed of homogeneous plane-parallel layers.

- Steady state: Substellar objects evolve in timescales of millions of years or more. The timescales of hydrodynamics, radiative and chemical processes are much shorter than the evolution timescales of these objects. The atmosphere is therefore assumed to be in a steady state, and all time dependencies are dropped. The radiative transfer equation (defined in Section 5.8) is therefore assumed to be time-independent, and local thermodynamic equilibrium (LTE) is assumed (defined in Section 5.6).

- Momentum balance: Following the steady state assumption, it is safe to assume the atmosphere is in hydrostatic equilibrium. This means the weight of overlying atmospheric layers is balanced by the total pressure gradient. This balance defines the density structure of the atmosphere. The equation of hydrostatic equilibrium is therefore,

$$\frac{dP}{dz} = -\rho g, \tag{5.1}$$

  where z is the atmospheric altitude which increases towards the upper layers of the atmosphere, ρ is the mass density, g is the surface gravity and P is the total pressure. In `MARCS`, the surface gravity g is an input parameter of the model and is assumed to be constant. The total pressure P is given by

$$P = P_{\text{gas}} + P_{\text{rad}} + P_{\text{turb}}, \tag{5.2}$$

  where P_{gas} is the gas pressure, P_{rad} is the radiation pressure and P_{turb} is the turbulence pressure. In this thesis we model substellar objects with effective temperatures between 1200 K and 2500 K. At these temperatures, P_{gas} accounts for the majority of the total pressure. The gas pressure is given by the sum of the partial pressures of each of the constituents of the gas (electrons, molecules, atoms, ions). The radiation pressure P_{rad} is still accounted for, however the turbulent pressure P_{turb} is disregarded. For a comparison of the different pressures for different spectral types see Table 9.1 in Gray (2021).

- Energy balance: The atmosphere is assumed to be in radiative-convective equilibrium (RCE), which once again implies the steady state. The condition of flux constancy is therefore given by

$$\frac{d}{dz}\left(F_{\text{rad}} + F_{\text{conv}}\right) = 0, \tag{5.3}$$

  where F_{rad} is the radiative flux and F_{conv} is the convective flux. Following Stefan-Boltzmann's law (Boltzmann, 1884), the total emergent flux of the object, $F_{\text{total}} = F_{\text{rad}} + F_{\text{conv}}$, is related to the object's effective temperature T_{eff} by

$$F_{\text{rad}} + F_{\text{conv}} = \sigma T_{\text{eff}}^4, \tag{5.4}$$

  where σ is Stefan-Boltzmann's constant. In `MARCS` models, the effective temperature T_{eff} is an input parameter.

5.2 Intensity and flux

In order to model substellar atmospheres, we need to describe how radiation propagates in an atmosphere. In its essence, radiation is energy in the form of photons (i.e. light) travelling through the atmosphere, interacting with the different matter particles in the atmosphere.

For a formal description of radiation and its propagation, it is essential to define the specific intensity I of radiation. The specific intensity I of radiation at a position $\mathbf{r}$ is defined such that the amount of energy transported by radiation across an element of area dS, into a solid angle $d\Omega$, per frequency ν, per unit time t is

$$dE = I(\mathbf{r}, \mathbf{n}, \nu, t) \cos\theta \, dS \, d\Omega \, d\nu \, dt, \tag{5.5}$$

where θ is the angle between the direction of travel of the radiation $\mathbf{n}$ and the normal to the surface $\mathbf{dS}$, this is $\mathbf{n} \cdot \mathbf{dS} = \cos\theta \, dS$. Following the plane-parallel assumption and employing Cartesian (x, y, z) coordinates, we consider the planes of constant z to be the homogeneous layers and therefore can write $I = I(z, \theta, \nu, t)$. Hereinafter, we define $\mu \equiv \cos\theta$.

The moments of the specific intensity are also useful to describe the radiation field. The zero-order moment of the intensity, known as the mean intensity J, is defined as the integral of the specific intensity over all solid angles, this is

$$J(\mathbf{r}, \nu, t) = \frac{1}{4\pi} \int_\Omega I(\mathbf{r}, \mathbf{n}, \nu, t) \, d\Omega. \tag{5.6}$$

The element of the solid angle is given by $d\Omega = \sin\theta \, d\theta \, d\phi = -d\mu \, d\phi$, where ϕ is the azimuthal angle. Following this and assuming the atmosphere is one-dimensional, I is independent of ϕ and we can rewrite the mean intensity as

$$J(z, \nu, t) = \frac{1}{2} \int_{-1}^{1} I(z, \mu, \nu, t) \, d\mu \tag{5.7}$$

where we have used the definition of $d\Omega$ for simplification.

Next, we define the first-moment of the radiation field with respect to angle, this is the flux $\mathbf{F}$. The flux $\mathbf{F}$ is a vector quantity, such that $\mathbf{F} \cdot \mathbf{dS}$ is the net flow of energy across an arbitrarily oriented surface $\mathbf{dS}$, per unit time, per frequency interval. The flux can then be derived from Equation 5.5 as the intensity in direction $\mathbf{n}$ over all solid angles, this is

$$\mathbf{F}(\mathbf{r}, \nu, t) = \int_\Omega I(\mathbf{r}, \mathbf{n}, \nu, t) \, \mathbf{n} \, d\Omega. \tag{5.8}$$

As a vector quantity, we can write $\mathbf{F}$ in terms of each of its components in Cartesian coordinates, $\mathbf{F} = F_x \, \mathbf{x} + F_y \, \mathbf{y} + F_z \, \mathbf{z}$, with $(\mathbf{x}, \mathbf{y}, \mathbf{z})$ being the unit vectors in the (x, y, z) directions respectively. Assuming the planar atmosphere which is homogeneous in x and y, only the F_z component remains. This F_z component will now be referred to as the flux F, and we will only write its scalar quantity.

Following Equation 5.8 and applying the $\mu \equiv \cos\theta$ relation, and $\mathbf{n} \cdot \mathbf{z} = \cos\theta$, the flux is given by

$$F(z, \nu, t) = 2\pi \int_{-1}^{1} I(z, \mu, \nu, t)\, \mu \, d\mu. \tag{5.9}$$

We can define the commonly used Eddington flux as $H = \frac{1}{4\pi} F$. Finally, we define the second moment of the intensity $\mathbf{K}$ as

$$\mathbf{K}(\mathbf{r}, \nu, t) = \frac{1}{4\pi} \int_{\Omega} I(\mathbf{r}, \mathbf{n}, \nu, t)\, \mathbf{n}\, \mathbf{n}\, d\Omega. \tag{5.10}$$

Note, the second moment $\mathbf{K}$ of the intensity I is a tensor quantity and is physically related to the radiation pressure $\mathbf{P}_{\rm rad}$ by $\mathbf{P}_{\rm rad} = \frac{1}{3}\,\mathbf{K}$. Following the plane-parallel approximation and the homogeneity in x and y, similarly to the flux, only the $K_{\rm z}$ component remains. Defining $K = K_{\rm z}$ we can write

$$K(z, \mu, t) = \frac{1}{2} \int_{-1}^{1} I(z, \mu, \nu, t)\, \mu^2 \, d\mu. \tag{5.11}$$

Considering the steady state assumption, we can disregard the time dependency and the 1D plane-parallel moments of specific intensity become

$$[J_\nu, H_\nu, K_\nu] = \frac{1}{2} \int_{-1}^{1} I(z, \mu, \nu)\, [1, \mu, \mu^2]\, d\mu \tag{5.12}$$

where we have omitted the μ and z dependencies on the l.h.s., and write the ν dependency as a subscript for simplicity.

For substellar atmospheres we are particularly interested in the emergent surface flux as this is the measurable quantity for these atmospheres. In this case the term 'surface' refers to the top of the atmosphere (TOA). From Equation 5.9, we can divide the flux into two components: $F_\nu^{\rm in}$ for the flux entering the atmospheric layer in question, and $F_\nu^{\rm out}$ for the flux leaving. Considering these components we can rewrite Equation 5.9 as

$$F_\nu = F_\nu^{\rm out} + F_\nu^{\rm in} = 2\pi \int_{0}^{1} I_\nu\, \mu \, d\mu \, + 2\pi \int_{-1}^{0} I_\nu\, \mu \, d\mu. \tag{5.13}$$

We compute the emergent surface flux at the very TOA, at $z = z^{\rm top}$. For an atmosphere that is not irradiated, $F_\nu^{\rm in} = 0$. Therefore, the emergent surface flux $F_\nu^{\rm surf}$ is given by

$$F_\nu^{\rm surf} = 2\pi \int_{0}^{1} I_\nu(z^{\rm top}, \mu)\, \mu \, d\mu \tag{5.14}$$

where we have explicitly written the I_ν dependency on z and μ for clarity.

5.3 Opacity

Next we must consider how the radiation can change as it travels through the atmosphere. We must consider 'loss' processes where energy is removed from the beam of radiation, and 'addition' processes where energy is added to the beam of radiation. Before we macroscopically define these 'loss' and 'addition' processes, it is important to introduce the concept of opacity. As the name indicates, the opacity is a measure of how opaque a medium is to radiation (in this case the medium being the atmosphere). This means the opacity is an indicator of how hard it is for radiation to pass through the atmosphere. The opacity is dependent on several variables, namely the absorption, scattering, and emitting properties of the atmospheric particles. These absorption, scattering and emitting properties are themselves dependent on properties such as temperature, pressure and wavelength. To be able to describe how the radiation changes as it travels through the atmosphere, we need to define absorption, scattering and emission coefficients.

In this thesis we will only define these coefficients macroscopically. The underlying microphysical processes which give origin to these absorption and emission coefficients are not discussed in detail here. However, a detailed description of these processes can be found in, for example, Chapter 8 of Seager (2010), Chapter 4 of Mihalas (1978), and Chapters 8 and 11 of Gray (2021). In Section 8.3.2 we give a brief description of how the gas and continuum opacities are computed in `MARCS`.

5.4 The extinction coefficient and optical depth

We start by considering the 'loss' processes, where energy is removed from the radiation beam. Remember we are disregarding time-dependencies and assuming a 1D plane-parallel geometry. The intensity $I_\nu = I(z, \mu, \nu)$ of the radiation is reduced across a layer of thickness $ds = \cos\theta\, dz = \mu\, dz$ by an amount dI_ν given by

$$dI_\nu = -\alpha_\nu\, I_\nu\, \mu\, dz \tag{5.15}$$

where α_ν is the extinction coefficient. Note the extinction coefficient has dimensions of length^{-1}. In some literature, α_ν is called the opacity. The extinction coefficient α_ν is the sum of two physical processes: (1) true absorption which describes processes where photons are destroyed; (2) scattering which describes photons that are removed from the radiation beam by a change of direction. Therefore, we can write the extinction coefficient as

$$\alpha_\nu = \alpha_\nu^{\text{abs}} + \alpha_\nu^{\text{scat}} \tag{5.16}$$

where α_ν^{abs} is the frequency dependent absorption coefficient, and α_ν^{scat} is the frequency dependent scattering coefficient. We note extinction is isotropic in a static medium because the absorbing or scattering particle is indifferent to which direction the photon comes from. Therefore, α_ν has no dependency in $\mathbf{n}$. It is now

useful to define the optical depth τ along a 1D path z, this is

$$d\tau_\nu = -\alpha_\nu \, dz. \tag{5.17}$$

The optical depth is a dimensionless quantity and it describes how opaque a part of the atmosphere is to the radiation travelling through it. In other words, it is a measure of how deeply an outside observer can see into the atmosphere (Mihalas, 1978). The optical depth is therefore dependent on both the frequency ν of the radiation and the atmospheric altitude z. The optical depth has a negative sign so that it increases inward into the atmosphere, such that it is zero at the TOA ($z = z^{\text{top}}$). Following Equation 5.17, we can write

$$\tau_\nu = -\int_z^{z^{\text{top}}} \alpha_\nu \, dz = -\int_z^{z^{\text{top}}} n \, \sigma_\nu \, dz = -\int_z^{z^{\text{top}}} \rho \, \kappa_\nu \, dz, \tag{5.18}$$

where z to z^{top} is the path length travelled by the photons, n is the number density, σ_ν is the cross-section of the gas to absorb or scatter a photon, ρ is the mass density and κ_ν is the cross-section per unit mass (i.e. the opacity), where $\alpha_\nu = n \, \sigma_\nu = \rho \, \kappa_\nu$. When a medium is fully transparent, its optical depth is zero. We say a medium is optically thin if $\tau \ll 1$. In an optically-thin medium we expect the photon to travel the path without being absorbed or scattered. A medium is optically thick when $\tau > 1$.

It is useful to define the mean free path of a photon, l, this is the mean distance a photon can travel until it interacts with an atmospheric particle. The mean free path is given by

$$l = \frac{1}{\rho \, \kappa} = \frac{1}{n \, \sigma}, \tag{5.19}$$

and it relates to the optical depth

$$d\tau = \frac{1}{l} \, dz. \tag{5.20}$$

Variable dependencies were dropped in Equations 5.19 and 5.20 for simplicity.

5.5 The emission coefficient

We now consider 'addition' processes. The hot gas in the atmosphere will emit light. An increase in the radiation emitted by an atmospheric layer of thickness $ds = \mu \, dz$ is given by

$$dI_\nu = \varepsilon_\nu \, \mu \, dz \tag{5.21}$$

where ε_ν is the emission coefficient, also called emissivity. The emissivity includes both thermal emission and scattering, i.e. $\varepsilon_\nu = \varepsilon_\nu^{\text{thermal}} + \varepsilon_\nu^{\text{scat}}$. The thermal emission is described by the Kirchoff-Planck relation (Kirchhoff, 1860; Planck, 1906),

$$\varepsilon_\nu^{\text{thermal}} = \alpha_\nu^{\text{abs}} \, B_\nu(T) \tag{5.22}$$

where $B_\nu(T)$ is the Planck function, dependent on the local atmospheric temperature T. This equation is valid in local thermodynamic equilibrium (LTE) (which we define in the next section) because it assumes any time a photon is absorbed, the energy will be re-emitted as radiation. In a static medium, the thermal emission is isotropic and is therefore independent of $\mathbf{n}$. The Planck function is given by

$$B_\nu(T) = \frac{2h\nu^3}{c^2}\frac{1}{e^{h\nu/kT}-1} \tag{5.23}$$

where h is Planck's constant, k is Boltzmann's constant and c is the speed of light.

Within the `MARCS` model, only pure-isotropic scattering is considered. This means the emitted energy due to scattering is due to photons getting scattered into the considered direction. Any potential angular dependency of the scattering coefficient is not considered. In this case, the emission coefficient for scattering is given by

$$\varepsilon_\nu^{\text{scat}} = \alpha_\nu^{\text{scat}} J_\nu \tag{5.24}$$

where J_ν is the mean intensity defined in Equation 5.7.

5.6 Local thermodynamic equilibrium (LTE)

Thermodynamic equilibrium describes a system that is in thermal, chemical and mechanical equilibrium. It is straightforward to notice that a substellar atmosphere is never in complete thermodynamic equilibrium: it has an open boundary at its top, and large changes in temperature and pressure are expected along the atmosphere. Local thermodynamic equilibrium (LTE) holds in a location of the atmosphere where temperature, pressure or chemical gradients are smaller than the photon mean free path. In LTE we assume thermodynamic equilibrium conditions hold, but the radiation field is allowed to depart from its thermodynamic value of $B(T)$. LTE provides a major simplification of the radiative transfer problem (see Section 5.8), largely simplifying the computation of substellar atmosphere models.

LTE is valid where densities are high enough in the atmosphere, such that collisional processes dominate over radiative processes. This is because collisional processes enable the atmospheric particles and radiation to be at the same temperature. At the bottom of the atmosphere where densities are high, we expect LTE to be a valid approximation. Towards the TOA, we expect to deviate more and more from the conditions where LTE is valid. This is because radiation freely escapes through the open boundary, densities drop, and collisional processes stop being dominant over radiative processes.

5.7 The source function

In this section we define the so-called source function while considering both thermal emission and isotropic scattering, allowing for a slight departure from LTE.

The source function is the ratio of the emission coefficient to the extinction coefficient, i.e.

$$S_\nu = \frac{\varepsilon_\nu}{\alpha_\nu} = \frac{\alpha_\nu^{\text{abs}}\, B_\nu(T) + \alpha_\nu^{\text{scat}}\, J_\nu}{\alpha_\nu}. \tag{5.25}$$

In the next section we use the source function to simplify the radiative transfer equation, equation which is also defined in the next section.

5.8 Radiative transfer

We are now ready to write the equation which describes the intensity change of a radiation beam as it travels a distance s through the atmosphere. Recall we disregard time-dependencies, and assume a 1D plane-parallel geometry, implying $ds = \cos\mu dz$. The radiative transfer equation can then be written by adding Equations 5.15 and 5.21, which gives

$$\mu \frac{dI_\nu}{dz} = -\alpha_\nu I_\nu + \varepsilon_\nu. \tag{5.26}$$

Using the definition of optical depth (Equation 5.18) and the definition of the source function (Equation 5.25), we can rewrite the radiative transfer equation as

$$\mu \frac{dI_\nu}{d\tau_\nu} = I_\nu - S_\nu. \tag{5.27}$$

Recall I_ν and S_ν are both dependent on z, and therefore τ_ν, and μ, although these dependencies have been omitted for simplicity.

The upper boundary condition for a substellar atmosphere that is not irradiated is given by

$$I_\nu(\tau_\nu = 0, -1 \leq \mu \leq 0) = 0. \tag{5.28}$$

The lower boundary condition is given by

$$I_\nu(\tau_\nu = \tau_\nu^{\max}, 0 \leq \mu \leq 1) = B_\nu\Big(T(\tau_\nu^{\max})\Big). \tag{5.29}$$

The formal solution of the radiative transfer equation

We can obtain a formal solution to Equation 5.26 by using the integrating factor $e^{-\tau_\nu/\mu}$. Multiplying the radiative transfer equation by this integrating factor gives

$$\frac{dI_\nu}{d\tau_\nu} e^{-\tau_\nu/\mu} - I_\nu \frac{1}{\mu} e^{-\tau_\nu/\mu} = -\frac{1}{\mu} S_\nu e^{-\tau_\nu/\mu}. \tag{5.30}$$

Integrating from an initial optical depth of τ_ν^i to a final optical depth of τ_ν^f, we obtain the solution

$$I_\nu(\tau_\nu^f) = I_\nu(\tau_\nu^i)\, e^{-(\tau_\nu^i - \tau_\nu^f)/\mu} - \frac{1}{\mu} \int_{\tau_\nu^i}^{\tau_\nu^f} S_\nu(\tau_\nu')\, e^{-(\tau_\nu' - \tau_\nu^f)/\mu}\, d\tau_\nu' \tag{5.31}$$

where the dependency of I_ν and S_ν on μ has been omitted for simplicity. The first term on the r.h.s. of the solution describes the initial intensity which is reduced by an exponential attenuation of absorption. The second term on the r.h.s. describes the atmosphere's emission as an exponentially weighted average of S_ν along the radiation beam up to the location of interest.

We are interested in obtaining the emergent flux at the TOA by solving the equation of radiative transfer. This implies integrating from $\tau_\nu^i = \infty$ to $\tau_\nu^f = 0$. Recognising that

$$\lim_{\tau_\nu \to \infty} I_\nu \, e^{-\tau_\nu/\mu} = 0, \tag{5.32}$$

we obtain that the emergent intensity is given by

$$I_\nu(\tau_\nu = 0) = \frac{1}{\mu} \int_0^\infty S_\nu(\tau_\nu) \, e^{-\tau_\nu/\mu} \, d\tau_\nu. \tag{5.33}$$

We can derive the emergent surface flux from Equation 5.14, giving

$$F_\nu^{\text{surf}} = 2\pi \int_0^1 \int_0^\infty S_\nu(\tau_\nu, \mu) \, e^{-\tau_\nu/\mu} \, d\tau_\nu \, d\mu \tag{5.34}$$

where we have explicitly written the S_ν dependency on τ_ν and μ for clarity. It is straightforward to solve Equations 5.33 and 5.34 if the source function S_μ is known. However, in `MARCS` models, the source function includes a scattering term which depends on the mean intensity J_ν, which in turn depends on the intensity I_ν. Therefore, we require a numerical approach to the problem. In Section 5.10 we summarise the numerical methods used by `MARCS`.

5.9 Convection

As mentioned earlier, we consider the atmosphere to be in RCE. Therefore we are left with defining the convective flux and the conditions in which we expect the energy to be transported by convective processes and not radiative ones.

To understand if the atmosphere is stable against convection at a given location, we must understand if an element of atmospheric material, when moved from its original location, experiences forces that move it further in the direction of its motion. If this is the case, the atmosphere is not stable against convection. If this is not the case, then radiative transfer dominates.

Schwarzschild criterion

Let us consider a packet of gas (cell) which is displaced upwards. The cell must be buoyant at each atmospheric layer if it is to continue being displaced upwards. We assume the displacement is slow enough that the cell remains in pressure equilibrium with its surroundings and that the process is adiabatic (i.e. no energy exchange with its surroundings). Following the adiabatic assumption, for an ideal gas, $P\rho^\gamma = \text{constant}$, where P is the total gas pressure, ρ is the density of the cell

and γ the ratio of the specific heats. For the cell to be buoyant, we require its density to decrease more rapidly than the average atmospheric density, i.e.

$$\frac{1}{\gamma} = \left[\frac{d\log\rho}{d\log P}\right]_{\rm cell} > \left[\frac{d\log\rho}{d\log P}\right]_{\rm atm}. \tag{5.35}$$

When modelling atmospheres, it is often more convenient to define these gradients in terms of temperature instead of density. Assuming an ideal gas we can write $\log P = \log\rho + \log T - \log\mu + \mathrm{C}$, where μ is the mean molecular weight and C a constant. Thus,

$$\left[\frac{d\log\rho}{d\log P}\right]_{\rm atm} = 1 - \frac{d\log T}{d\log P} + \frac{d\log\mu}{d\log P}. \tag{5.36}$$

The inequality in Equation 5.35 can be rewritten as

$$\left[\frac{d\log T}{d\log P}\right]_{\rm atm} > 1 - \frac{1}{\gamma} + \frac{d\log\mu}{d\log P} \tag{5.37}$$

This is the condition required for convection, known as the Schwarzschild criterion (Schwarzschild, 1906). The Schwarzschild criterion can be met when the $[d\log T/d\log P]_{\rm atm}$ gradient is large enough or if the adiabatic gradient (r.h.s. of Equation 5.37) is reduced. Since the opacity typically increases as one moves deeper into an atmosphere, the radiative temperature gradient also becomes steeper. Therefore, we expect the deepest atmospheric layers to be convective. The value of γ is closer to unity for polyatomic gases as the degrees of freedom increase with molecular complexity.

The mixing length formulation

In 1D model atmospheres, convection is generally treated with the mixing length formulation (e.g. Gustafsson et al., 2008; Tremblin et al., 2015; Mollière et al., 2017). As described above, convection works through buoyancy: energy is transported due to a rising (or falling) cell which has more (or less) heat than its surroundings. At the end of the displacement of the cell of some characteristic distance, known as the mixing-length, the cell is considered to dissolve abruptly into its surroundings (Prandtl, 1925). The `MARCS` model applies the mixing length formulation as described by Henyey et al. (1965), based on the work of Böhm-Vitense (1958). Here we define the crucial variables to be included in the atmosphere model. For a complete description of the mixing length formulation and how it is implemented in `MARCS`, we refer the reader to Böhm-Vitense (1958), Henyey et al. (1965) and Nordlund (1974).

Let us first define the temperature versus pressure gradient in an atmospheric layer as

$$\nabla = \frac{d\log T}{d\log P}, \tag{5.38}$$

this is the l.h.s. of Equation 5.37. The convective flux is given by

$$F_{\rm conv} = \frac{1}{2}\,\rho\,C_p\,T\,v_{\rm conv}\frac{\ell}{H}\delta\Delta, \tag{5.39}$$

where C_p is the specific heat at constant pressure, $v_{\rm conv}$ is the mean convective velocity, and ℓ is the mixing length which is a free parameter of the model. $H = \frac{P}{g\,\rho}$ is local pressure scale height. The value of $\delta\Delta$ is given by

$$\delta\Delta = \frac{\Gamma}{1+\Gamma}(\nabla - \nabla_{\rm ad}) \tag{5.40}$$

where $\nabla_{\rm ad}$ is the adiabatic gradient (given by the r.h.s. of Equation 5.37), and Γ is the efficiency factor for convection, this is the ratio between the energy transported by convection and the energy lost through radiation (e.g. Kippenhahn et al., 2013). The efficiency factor for convection is given by

$$\Gamma = v_{\rm conv}\,\rho\,C_p\frac{1+y(\rho\,\kappa_{\rm R}\,\ell)^2}{8\,\sigma\,T^3(\rho\,\kappa_{\rm R}\,\ell)}, \tag{5.41}$$

where y is a free parameter related to the assumed temperature distribution within the convective cells. The convective velocity is given by

$$v_{\rm conv}^2 = \frac{g\,Q}{\nu}\frac{\ell^2}{H}\,\delta\Delta, \tag{5.42}$$

with

$$Q = -\frac{T}{\rho}\left(\frac{\partial\rho}{\partial T}\right)_{\rm p}, \tag{5.43}$$

the derivative taken at constant thermodynamic pressure (Henyey et al., 1965; Gustafsson et al., 2008). We note that in this case ν is not a frequency but rather a free parameter which deals with the energy dissipation by turbulent viscosity. We define the mixing length parameter α as $\alpha = \ell/H$. Following the suggestions of Böhm-Vitense (1958) and Henyey et al. (1965), we set $\nu = 8$ and $y = 0.076$. Following Ludwig et al. (2002) we set the mixing length parameter α to a value appropriate for brown dwarfs, $\alpha = 2.0$.

We recall the atmospheric layers where $\nabla < \nabla_{\rm ad}$ are stable against convection and layers where $\nabla > \nabla_{\rm ad}$ are unstable (Schwarzchild criterion).

5.10 Numerical methods in `MARCS`

The computational method used by `MARCS` is of the Feautrier type (Feautrier, 1964). The variable Eddington factor technique of Auer and Mihalas (1970) is applied to eliminate high-order angular dependencies. To compute the variable Eddington factors, `MARCS` uses the method described in Cannon (1973).

The radiative transfer equation (Equation 5.26), the condition of flux constancy (Equation 5.4), and the equation of hydrostatic equilibrium (Equation 5.1) are

solved simultaneously by means of a Newton-Raphson procedure on a Rosseland optical depth scale. The Rosseland optical depth $\tau_{\rm R}$ can be obtained via the Rosseland mean opacity $\kappa_{\rm R}$, introduced by the Norwegian astrophysicist Svein Rosseland (1894-1985). A mean opacity is an opacity that has been averaged over all frequencies (or wavelengths) to create a function that is only dependent on composition, density, and temperature. The Rosseland mean opacity is a harmonic mean which gives a higher weight to frequencies with a smaller opacity than to those with a larger opacity. The Rosseland mean opacity is given by

$$\frac{1}{\kappa_{\rm R}} = \frac{\int_0^\infty \frac{1}{\kappa_\nu} \frac{dB_\nu(T)}{dT}\, d\nu}{\int_0^\infty \frac{dB_\nu(T)}{dT}\, d\nu} \tag{5.44}$$

where B_ν is the Planck function defined in Equation 5.23, and κ_ν is the cross-section per unit mass at a given frequency ν. As defined here, the Rosseland mean opacity has units of area per unit mass. Similarly to Equation 5.18, the Rosseland optical depth is $\tau_{\rm R} = \int \kappa_{\rm R}\, \rho\, dz$.

In a convective region, the condition of flux constancy is considered in the form

$$\int F_\nu\, d\nu + F_{\rm conv} = F_{\rm rad} + F_{\rm conv} = \sigma\, T_{\rm eff}^4, \tag{5.45}$$

where F_ν is given by Equation 5.9, and $F_{\rm rad}$ is the radiative flux.

In regions which are only radiative, i.e. $F_{\rm conv} = 0$, the condition of flux consistency is applied as

$$\int \alpha_\nu^{\rm abs} \left[B_\nu(T) - J_\nu\right] d\nu = 0, \tag{5.46}$$

where $\alpha_\nu^{\rm abs}$ is the absorption coefficient, J_ν the mean intensity defined in Equation 5.7, and $B_\nu(T)$ the Planck function defined in Equation 5.23. Equation 5.46 is derived from considering that in radiative equilibrium, the total energy absorbed by a given volume of material must be equal to the total energy emitted by it. In this case the total energy absorbed is given by $4\pi \int_0^\infty \alpha_\nu^{\rm abs}\, J_\nu\, d\nu$, while the total energy emitted is given by $4\pi \int_0^\infty \alpha_\nu^{\rm abs}\, S_\nu\, d\nu$. Following the definition of the source function (Equation 5.25), the condition in Equation 5.46 is obtained.

The Newton-Raphson procedure used to solve the equations is constructed in two steps as described in Nordlund (1974): (1) The equations are discretised in $\tau_{\rm R}$ and ν; (2) The resulting equations from the discritisation are linearised in the dependent variables (i.e. temperature, gas pressure, radiation pressure, mean intensity, convective flux, etc.). From the resulting system of linear equations, the radiative transfer part is solved with an elimination scheme based on Rybicki (1971), as described in Gustafsson and Nissen (1972) and Gustafsson et al. (1975). The input variables used to determine any necessary thermodynamic quantities or opacities are the temperature and gas pressure[1].

[1]We note earlier `MARCS` models for stellar atmospheres used the electron pressure instead of the gas pressure as input variable for thermodynamic and opacity calculations. Using the electron pressure is appropriate in hotter environments where we expect a large quantity of free electrons to exist. However, in substellar atmospheres it is more appropriate to use the gas pressure, which we expect to be the dominating pressure.

For more details on the numerical methods used in `MARCS`, we refer the reader to Gustafsson and Nissen (1972), Nordlund (1974), Gustafsson et al. (1975) and Gustafsson et al. (2008).

5.11 Gas-phase chemical equilibrium

In the models presented in this thesis, we assume the gas-phase to be in chemical equilibrium. The element abundances are an input parameter of the model. Chemical equilibrium exists when the number densities of atoms, molecules and ions do not change within a closed system, at a given pressure and temperature. Note this does not signify that no reaction is occurring but that chemical reactions occur without any net change in the number densities of the atmospheric particles. We want to determine the chemical composition of an atmospheric layer given we know its temperature, pressure and the element abundances.

We use the `GGchem` code (Woitke et al., 2018) to compute the gas-phase chemical equilibrium in both the `MARCS` model and the cloud formation model `DRIFT` (presented in the next Chapter). `GGchem` is based on the principle of minimisation of the Gibbs free energy, or the Gibbs function. The Gibbs free energy can be derived from a restatement of the first law of thermodynamics. The first law of thermodynamics describes the conservation of energy and is given by

$$dU = dQ - dW = TdS - PdV, \tag{5.47}$$

where dU is the change in internal energy of the system, dQ is the energy added to the system by heating and dW is the energy lost via work done by the system. For a reversible process, $dQ = TdS$ and $dW = PdV$, where T is the temperature, S is the entropy, P is the pressure and V the volume. The challenge of using the first law of thermodynamics as written in Equation 5.47 to compute the chemical equilibrium is that it is not possible to measure the change in entropy dS and in volume dV for a substellar atmosphere. However, we can use a formulation which uses the change in temperature dT and the change in pressure dP as these are quantities which can be inferred from spectral measurements. The Gibbs free energy is defined as

$$G = U + PV - TS. \tag{5.48}$$

The differential form of G is given by

$$dG = dU + PdV + VdP - TdS - SdT = VdP - SdT. \tag{5.49}$$

It is straightforward to notice that at equilibrium, the temperature and pressure are constant and therefore $dP = dT = 0$. From Equation 5.49 we see that at equilibrium $dG = 0$. Following the second law of thermodynamics which states that the entropy of a closed system never decreases, i.e. $dS \geq dQ/T$, we can rewrite Equations 5.47 and 5.49 as

$$TdS \geq dU + PdV \tag{5.50}$$

and

$$dG \leq V dP - S dT. \tag{5.51}$$

For a chemical change at constant temperature and pressure it follows that $dG \leq 0$. This means the Gibbs free energy tends to decrease for a system at constant temperature and pressure. When G reaches a minimum, dG becomes zero.

`GGchem` uses the law of mass action and molecular equilibrium constants based on Gibbs free energy data to determine the gas-phase chemical equilibrium. As an example, we consider a molecule $\mathrm{A}_a\mathrm{B}_b\mathrm{C}_c$, made of three elements A, B, C, where a, b and c are stoichiometric factors. Guldberg's and Waage's law of mass action (e.g. Waage and Guldberg, 1864) states that the rate of a chemical reaction is proportional to the product of the concentrations of the reactants. The law of mass action can be written as

$$\frac{p_{\mathrm{A}_a\mathrm{B}_b\mathrm{C}_c}}{p^0} = \left(\frac{p_\mathrm{A}}{p^0}\right)^a \left(\frac{p_\mathrm{B}}{p^0}\right)^b \left(\frac{p_\mathrm{C}}{p^0}\right)^c e^{-\Delta G^0_\mathrm{f}/RT}, \tag{5.52}$$

where $p_i = n_i k_b T$ are the partial pressures, n_i are the particle number densities, k_b is Boltzmann's constant, p^0 is a standard pressure and R is the ideal gas constant (e.g. Woitke et al., 2018). The Gibbs free energy of formation of the molecule is ΔG^0_f at a standard pressure from neutral atoms at the same temperature and it is given by

$$\Delta G^0_\mathrm{f} = G^0(\mathrm{A}_a\mathrm{B}_b\mathrm{C}_c, T) - a\, G^0(\mathrm{A}, T) - b\, G^0(\mathrm{B}, T) - c\, G^0(\mathrm{C}, T). \tag{5.53}$$

The equilibrium constant k_p is introduced as

$$p_{\mathrm{A}_a\mathrm{B}_b\mathrm{C}_c} = k_p(\mathrm{A}_a\mathrm{B}_b\mathrm{C}_c, T)\, p_\mathrm{A}^a\, p_\mathrm{B}^b\, p_\mathrm{C}^c \tag{5.54}$$

where

$$k_p(\mathrm{A}_a\mathrm{B}_b\mathrm{C}_c, T) = (p^0)^{1-a-b-c}\, e^{-\Delta G^0_\mathrm{f}/RT}. \tag{5.55}$$

For a derivation of the equilibrium constant k_p we refer the reader to Chapter 10 of Fegley and Osborne (2013).

To compute the chemical composition of the gas, `GGchem` solves the element and charge conservation equations as

$$\epsilon_k\, n_{\langle H\rangle} = \sum_i s_{i,k}\, n_i, \tag{5.56}$$

where ϵ_k are the element abundances normalised to Hydrogen (i.e. $\epsilon_\mathrm{H} = 1$), $n_{\langle H\rangle}$ is the total number density of Hydrogen nuclei ($n_{\langle H\rangle} = \sum_i s_{i,\mathrm{H}}\, n_i$), n_i is the number density of all gas particles, including free electrons, neutral and charged atoms, and neutral and charged molecules, and $s_{i,k}$ is the stoichiometric factor of element k in the gas particle i (Woitke et al., 2018). Charge neutrality is considered by including the charge as an element 'el' with zero abundance $\epsilon_{\mathrm{el}=0}$, where $s_{i,\mathrm{el}} = 0$ for neutrals, $s_{i,\mathrm{el}} = -1$ for anions and $s_{i,\mathrm{el}} = +1$ for cations.

The gas mass density ρ is given by

$$\rho = \sum_i m_i \, n_i = n_{\langle H \rangle} \sum_k m_k \, \epsilon_k \tag{5.57}$$

where m_i are the masses of the gas particles and m_k are the masses of the elements. The second part of Equation 5.57 follows from Equation 5.56. The total gas pressure P_{gas} is then given by

$$P_{\text{gas}} = \sum_i n_i \, k_b \, T = n(\rho, T) \, k_b \, T = \frac{\rho \, k_b \, T}{\mu(\rho, T)}, \tag{5.58}$$

where the total particle number density $n = \sum_i n_i$ and the mean molecular weight $\mu = \sum_i m_i \, n_i / n$. Both n and μ are results of the computations and therefore are dependent on the gas mass density and temperature (Woitke et al., 2018).

We recall that the partial pressures $p_i = n_i \, k_b \, T$, and it is therefore possible to eliminate the molecular number densities from Equation 5.56 by using the appropriate equilibrium constants k_p data. Following this, a system of non-linear equations with K unknowns is obtained from Equation 5.56 ($K = N + 1$ with N being the number of elements considered plus one to account for free electrons). The results are only dependent on $n_{\langle H \rangle}$, T and ϵ_k.

`GGchem` is called for every atmospheric layer to compute its gas-phase chemical equilibrium. The `GGchem` inputs are the atmospheric layer's gas pressure, the temperature and the element abundances. The iterative process, numerical methods and equilibrium constants data used by `GGchem` to solve the system of non-linear equations obtained are described in detail in Woitke et al. (2018).

CHAPTER 6

Cloud formation and the DRIFT model

You must live life with the full knowledge that your actions will remain.
We are creatures of consequence.

— Zadie Smith, in *White Teeth*

In the second part of this thesis, we focus on modelling cloudy substellar atmospheres of gaseous objects (i.e. brown dwarfs, planetary mass companions/objects or extrasolar giant planets). The objects we model have temperatures of hundreds to thousands of Kelvin more than Earth's temperature. On Earth, water clouds form in the troposphere where there are cloud condensation nuclei (CCN) available. The CCNs are, for example, salt from ocean spray, ashes from forest fires or volcano eruptions, and/or sand grains from sandstorms. In a gaseous object there is no solid rocky surface and therefore we do not expect these types of CCN to be available. On top of this, the objects we model are very hot ($T_{\rm eff} > 1000\,K$) and water clouds will not form. In these hotter gaseous objects, we expect mineral clouds to form. The mineral clouds are likely composed of materials like quartz (SiO_2[s]), corundum (Al_2O_3[s]), rutile (TiO_2[s]) or iron (Fe[s]).

In this chapter we describe the theory of cloud formation considered by the microphysical cloud formation model `DRIFT`. Unless otherwise stated, the theory sections presented in this chapter are based on Gail et al. (1984), Gail and Sedlmayr (1988), Woitke and Helling (2003), Woitke and Helling (2004), Helling and Woitke (2006), Helling et al. (2008c), Helling and Fomins (2013) and Gail and Sedlmayr (2013).

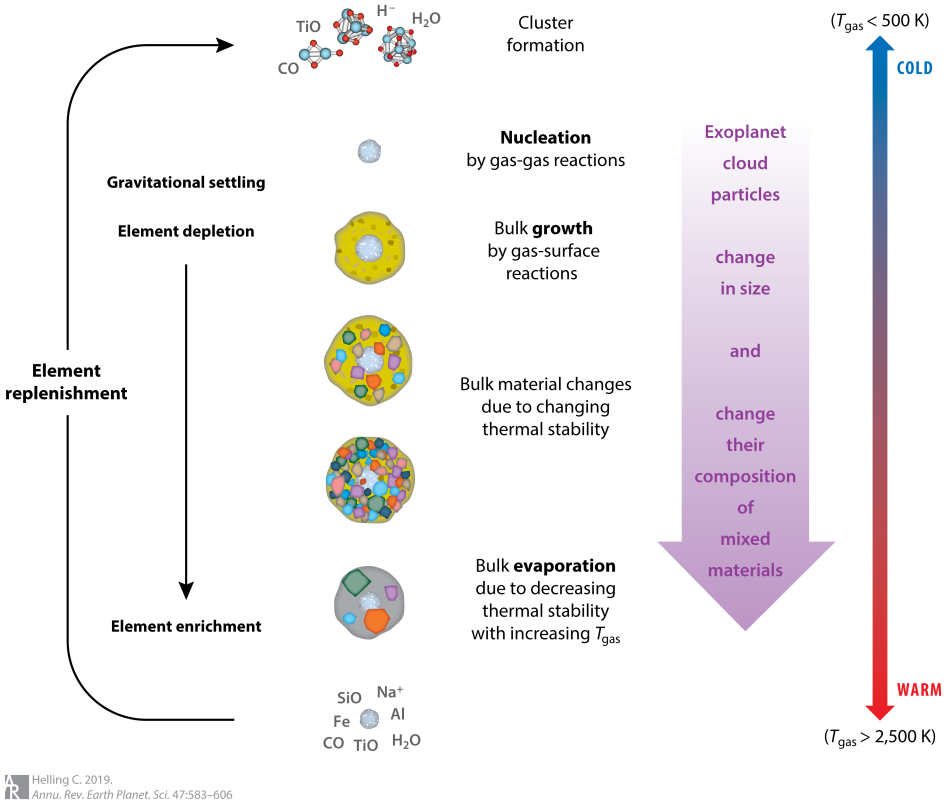

Figure 6.1: Cloud formation processes leading to cloud particles composed of a mix of materials that change with atmospheric height. These are the processes considered by the cloud formation model `DRIFT`. Copyright © 2019 by Annual Reviews. Reproduced from Helling (2019) with permission.

6.1 DRIFT

The `DRIFT` model considers the formation of clouds via the formation of cloud condensation nuclei, and their subsequent growth and evaporation. A system of dust moment and element conservation equations is solved in order to consider these processes. The influence of gravitational settling and element replenishment is also taken into account. Figure 6.1 shows a diagram of the cloud formation processes considered by `DRIFT`.

Cloud formation begins with the emergence of CCN, on which all thermally stable cloud species can grow through gas-surface reactions (e.g. Helling and Fomins, 2013; Helling, 2019). In `DRIFT`, the nucleation rate of CCN is considered by applying the modified classical nucleation theory of Gail et al. (1984), as outlined by Woitke and Helling (2004). The growth of mixed-material cloud particles is calculated using the methods of Woitke and Helling (2003), Helling and Woitke (2006) and Helling et al. (2008c). In the models presented in this thesis, 12 cloud species are considered: TiO_2[s], Mg_2SiO_4[s], $MgSiO_3$[s], MgO[s], SiO[s], SiO_2[s], Al_2O_3[s], $CaTiO_3$[s], Fe[s], FeO[s], FeS[s] and Fe_2O_3[s]. The cloud particles will settle due to gravity and, as they descend, they will encounter varying tempera-

tures and gas densities, causing their composition to change due to the shifting thermal stability of the cloud species. The cloud particles continue to grow as they fall until the temperature becomes so high that all considered cloud species begin to evaporate. The growth and evaporation processes alter the local gas-phase element abundances because elements involved in cloud formation are depleted. A mechanism for element replenishment must exist for a cloud layer to persist (i.e., a source of fresh, non-depleted elements must be present).

Below we present the governing equations for each of the microphysical processes considered by `DRIFT` and an overview of the moment method used by `DRIFT`. We note we define the time-dependent equations in the present chapter. However, in Chapter 8 we model plane-parallel quasi-static substellar atmospheres, and therefore the time dependencies will vanish. We reformulate crucial equations in their quasi-static form in Chapter 8. We define the element replenishment mechanism used (convective overshooting) in Chapter 8. For details on the numerical methods used by `DRIFT`, we refer the reader to Helling and Woitke (2006) and Helling et al. (2008c).

6.1.1 Nucleation

As mentioned above, nucleation is considered by applying the modified classical nucleation theory of Gail et al. (1984). In the atmosphere of a gaseous object, CCN are not readily available, and therefore they need to form from the gas-phase. Homogeneous classical nucleation theory describes how cloud condensation nuclei can form through a process called homogeneous nucleation (e.g. Gail and Sedlmayr, 1988). In this process, molecules that possess stable monomers in the gas-phase, can grow by simple polymerisation. This means the molecules can chemically bond to create larger, more stable clusters, eventually forming a solid.

We assume the nucleation process is homomolecular, and that the reaction chain to form larger clusters occurs via the addition of a single molecule at each reaction step. The rate of the slowest reaction will control the flux through the cluster space in this sequence of reactions. This bottleneck reaction results in the formation of the critical cluster, $N_\star$, which is the least stable cluster. Once this cluster forms, it will drive the growth of larger clusters. The goal of classical nucleation theory is to determine the rate at which particles can pass through the critical cluster size and grow into larger CCN of approximately 1000 monomer sizes.

The nucleation rate $J_\star(t)$ depends on the properties of the critical cluster. Thus, the stationary nucleation rate for a homogeneous, single-molecule process in thermal equilibrium with the gas-phase ($T_{\rm gas} = T_{\rm dust} = T$) can be expressed as follows (e.g. Gail and Sedlmayr, 2013; Helling and Fomins, 2013):

$$J_\star(t) = \frac{\mathring{f}(N_\star)}{\tau_{\rm gr}(r_i, N_\star, t)}\, Z(N_*)\, S(T)\, \exp[(N_* - 1)\ln S(T)], \tag{6.1}$$

where $\mathring{f}(N_\star)$ [cm^{-3}] is the equilibrium cluster size distribution, which is considered

as a Boltzmann-like distribution in LTE,

$$\mathring{f}(N) = \mathring{f}(1) \exp\left(-\frac{\Delta G(N)}{RT}\right), \tag{6.2}$$

where $\mathring{f}(1)$ is the equilibrium number density of the monomer (this is the smallest cluster unit), and $\Delta G(N)$ is the Gibbs free energy change due to the formation of a cluster of size N from the saturated vapour at a temperature T. We defined Gibbs free energy in the previous Chapter in Section 5.11.

In Equation 6.1, $\tau_{\rm gr}$ is the rate of growth for each individual cluster of size $N_\star$ and $Z(N_\star)$ is the Zeldovich factor which accounts for the contribution from Brownian motion to the nucleation rate. The supersaturation ratio S_N of a cluster with N is also present in Equation 6.1. If the monomers are in phase equilibrium with the solid phase, which is itself in thermal equilibrium with the gas, and if the gas-phase is in chemical equilibrium including both the N-mers and monomers, then the N-mers will also be in phase equilibrium with the solid (Helling and Fomins, 2013). Thus,

$$\frac{\mathring{p}(N)}{p^0} = \frac{\mathring{p}_{\rm sat}}{p^0} \Rightarrow S_N = \frac{\mathring{p}(N)}{\mathring{p}_{\rm sat}}, \tag{6.3}$$

where p^0 is a standard pressure, $\mathring{p}(N)$ is the partial pressure of the N cluster and $\mathring{p}_{\rm sat}$ is the saturation vapour pressure.

Following Equations 6.2 and 6.3, we can rewrite Equation 6.1 as

$$J_\star(t) = \frac{\mathring{f}(1,t)}{\tau_{\rm gr}(1, N_\star, t)} Z(N_*) \exp\left((N_* - 1)\ln S(T) - \frac{\Delta G(N_\star)}{RT}\right). \tag{6.4}$$

The nucleation rate becomes essentially a function of the equilibrium number density of the monomer and the temperature of the gas. For the derivation of the nucleation rate, along with other details on modified classical nucleation theory, we refer the reader to Helling and Fomins (2013), Gail and Sedlmayr (2013) and references therein.

6.1.2 Growth and evaporation

Once the CCN form, gas-phase materials can condense onto it, causing the cloud particle to grow. On the other hand, if any solid material on the cloud particle's surface becomes thermally unstable ($S < 1$) at some point during the particle's lifetime, it will start to evaporate back into the gas-phase, which decreases the particle's volume and mass. The growth of material on the cloud particle's surface happens through chemical reactions of gas-phase species on the particle's surface.

The net growth velocity for mixed-material spherical cloud particles is given by

$$\chi^{\rm net} = \sqrt[3]{36\pi} \sum_s \sum_r \frac{\Delta V_r \, n_r^{\rm key} \, v_r^{\rm rel} \, \alpha_r}{\nu_r^{\rm key}} \left(1 - \frac{1}{S_r \, b_{\rm surf}^s}\right), \tag{6.5}$$

where ΔV_r is the change in the cloud species volume caused by reaction r, $n_r^{\rm key}$ is the particle number density of the key reactant in the gas-phase, i.e. the reactant with the lowest abundance, $v_r^{\rm rel}$ is the relative thermal velocity of the gas species taking part in reaction r, α_r is the sticking coefficient (ratio between physisorption rate and thermal collision rate) of reaction r (which has been set to unity for all the models presented in this thesis), $\nu_r^{\rm key}$ is the stoichiometric factor of the key reactant in reaction r, S_r is the supersaturation ratio of the surface reaction r, and $1/b^s_{\rm surf} = V_s/V_{\rm tot}$ is the volume ratio of cloud species s to the total cloud particle volume $V_{\rm tot}$. For a reaction r there is growth if $S_r\, b^s_{\rm surf} > 1$ and evaporation if $S_r\, b^s_{\rm surf} < 1$.

For more details on the derivation of Equation 6.5 and on growth and evaporation processes, we refer the reader to Helling et al. (2008c) and Helling and Fomins (2013).

6.1.3 Gravitational settling

We now must consider the trajectories of the cloud particles along the atmosphere. Cloud particles that have just formed are small and light enough that they are frictionally coupled to the gas flow, moving like the molecules and atoms. However, as they grow larger they start decoupling from the gas because the gravitational force from the object dominates over the frictional forces. Due to this, the cloud particles gravitationally settle. Therefore, we must consider that the cloud particles are subjected to both (1) a frictional force which arises from collisions with the gas particles; (2) the object's gravitational force, which sinks the cloud particles down through its atmosphere. The radiation pressure force may also act on the cloud particles, however for non-irradiated substellar atmospheres, the radiation pressure force is orders of magnitude smaller compared to the gravitational force (e.g. Woitke and Helling, 2003). Disregarding the radiation pressure force, the equation of motion for a spherical cloud particle with radius a and a mass m_d is given by Newton's second law of motion, i.e.

$$m_d\, \ddot{\boldsymbol{x}} = \mathbf{F}_{\rm grav}(\boldsymbol{x}, a) + \mathbf{F}_{\rm fric}(\boldsymbol{x}, a, \boldsymbol{v}_{\rm drift}), \tag{6.6}$$

where $\boldsymbol{x}(t)$ is the particle's trajectory, $\mathbf{F}_{\rm grav}$ is the gravitational force, $\mathbf{F}_{\rm fric}$ is the frictional force exerted by the surrounding gas via collisions, and $\boldsymbol{v}_{\rm drift}$ is the relative velocity between the cloud particles and the gas (the drift velocity).

The gravitational force on the cloud particle is given by

$$\mathbf{F}_{\rm grav}(\boldsymbol{x}, a) = m_d\, \boldsymbol{g}(\boldsymbol{x}), \tag{6.7}$$

where $\boldsymbol{g}(\boldsymbol{x})$ is the gravitational acceleration. Substellar atmospheres of self-luminous objects have a small atmosphere extension compared to the radii of these objects. Therefore, we assume the gravitational acceleration is constant throughout the atmosphere.

Obtaining a unique description of the frictional force in substellar atmospheres is challenging. This complexity arises because the behaviour of the gas flow around

a moving cloud particle changes significantly with variations in cloud particle size, drift velocity, and the thermodynamic state of the gas. These changes can cause transitions from freely moving gas particles to a viscous flow, from subsonic to supersonic speeds, and from a smooth laminar flow to a turbulent flow. The physical conditions in substellar atmospheres are such that all these transitions can occur. For substellar atmospheres, we expect low enough gas densities and small enough cloud particle sizes to assume a subsonic, free molecular flow (e.g. Woitke and Helling, 2003). In this case, the frictional force is given by (Schaaf, 1963)

$$\mathbf{F}_{\rm fric} = -\frac{8\sqrt{\pi}}{3}\, a^2\, \rho_{\rm g}\, c_T\, \boldsymbol{v}_{\rm drift}, \tag{6.8}$$

where $\rho_{\rm g}$ is the gas density and c_T is the speed of sound at a temperature T.

Cloud particles are assumed to settle at the equilibrium drift velocity which is achieved through the balance of the gravitational and frictional forces acting on the particle (Woitke and Helling, 2003, 2004). Following this balance, we can solve Equation 6.6 for $\mathbf{F}_{\rm grav}(\boldsymbol{x}, a) + \mathbf{F}_{\rm fric}(\boldsymbol{x}, a, \boldsymbol{v}_{\rm drift}) = 0$. Writing the mass of a cloud particle m_d as $m_d = \frac{4}{3}\pi\, a^3\, \rho_d$, where ρ_d is the cloud particle density, we obtain that the equilibrium drift velocity $\mathring{\boldsymbol{v}}_{\rm drift}$ is given by

$$\mathring{\boldsymbol{v}}_{\rm drift} = \frac{\sqrt{\pi}}{2}\, \frac{a\, \rho_d}{c_T\, \rho_{\rm g}}\, \boldsymbol{g}. \tag{6.9}$$

The total velocity of the cloud particle is given by the sum of the drift velocity and the gas velocity, i.e. $\boldsymbol{v}_d = \boldsymbol{v}_{\rm drift} + \boldsymbol{v}_{\rm gas}$.

For more details on the equation of motion of the cloud particle, and the frictional forces under different assumptions, we refer the reader to Woitke and Helling (2003).

6.1.4 Conservation of elements

The gas-phase element abundances of the elements participating in the cloud formation processes change via depletion or replenishment, depending on the dominating process (nucleation, growth or evaporation) at a given point in the atmosphere. The gas element conservation equations as affected by nucleation, growth and evaporation are given by (Helling and Woitke, 2006)

$$\frac{\partial}{\partial t}(n_{\langle H\rangle}\, \epsilon_i) + \nabla\cdot(n_{\langle H\rangle}\, \epsilon_i\, \boldsymbol{v}_g) = \\ -\nu_{i,0}\, N_l\, J_\star(V_l) - \sqrt[3]{36\pi}\, \rho_g\, L_2 \sum_r \frac{\nu_{i,s} n_r^{\rm key} \upsilon_r^{\rm rel} \alpha_r}{\nu_r^{\rm key}} \left(1 - \frac{1}{S_r\, b_{\rm surf}^s}\right), \tag{6.10}$$

where $n_{\langle H\rangle}$ is the total number density of hydrogen nuclei, ϵ^i is the element abundance of element i normalised to hydrogen. $\tau_{\rm mix}$ is the mixing timescale. The first term on the r.h.s. of Equation 6.10 describes the element depletion by nucleation, where $\nu_{i,0}$ is the stoichiometric coefficient of the CCN and N_l is the number of

monomers in the CCN. The second term on the r.h.s. describes the element depletion/replenishment by growth/evaporation, where L_2 is the second dust moment (defined in the next section) and $\nu_{i,s}$ is the stoichiometric coefficient of element i in solid material s.

We note for the quasi-static case used in Chapter 8, $\boldsymbol{v}_g = \mathbf{0}$. For details on the derivation of the element conservation equations, we refer the reader to Helling and Woitke (2006).

6.1.5 The moment method

The physical and chemical processes described in the earlier sections occur simultaneously in the atmosphere and can be strongly coupled. A system of partial differential equations can be formulated to describe the evolution of the components of the cloud particles using the moments of their size distribution function. This approach was initially developed by Gail and Sedlmayr (1988) and later expanded by Dominik et al. (1993) to include core-mantle and dirty grains.

Considering a distribution of cloud particles $f(V)[\mathrm{cm}^{-6}]$, the master equation for cloud particles in the volume interval $[V, V + dV]$ is given by

$$\frac{\partial}{\partial t}(f(V)\,dV) + \nabla \cdot ([\boldsymbol{v}_{\rm gas} + \mathring{\boldsymbol{v}}_{\rm drift}(V)] f(V)\,dV) = \sum_k R_k\,dV, \tag{6.11}$$

where the r.h.s. of the equation describes the population and depopulation of the considered volume interval with cloud particles which are changing their size due to accretion or evaporation of molecules (Helling and Woitke, 2006; Helling et al., 2008c).

The dust volume moments $L_j(\boldsymbol{x}, t)$ $[\mathrm{cm}^j \mathrm{g}^{-1}]$ $(j = 0, 1, 2, 3)$ are defined as the local integrated cloud particle size distribution, weighted by a power of the particle's volume $V^{j/3}$ (Woitke and Helling, 2003, 2004; Helling and Woitke, 2006; Helling et al., 2008c), this is

$$\rho_{\rm g}\, L_j(\boldsymbol{x}, t) = \int_{V_l}^{\infty} f(V, \boldsymbol{x}, t)\, V^{j/3}\, dV, \tag{6.12}$$

where $f(V, \boldsymbol{x}, t)$ $[\mathrm{cm}^{-6}]$ is the distribution of particles in volume space and V_l is the volume of the CCN.

From Equations 6.11 and 6.12, we can derive the conservation equation of dust volume moments (see derivation details in Woitke and Helling, 2003) given by

$$\frac{\partial}{\partial t}(\rho_g\, L_j) + \nabla \cdot (\rho_g\, L_j\, \boldsymbol{v}_d) = V_l^{j/3}\, J_\star + \frac{j}{3}\, \chi^{\rm net}\, \rho_g\, L_{j-1}. \tag{6.13}$$

The composition of the cloud particles changes as a result of local chemical and thermodynamic conditions and the thermal stability of each cloud species in those conditions. The volume of a specific cloud species s depends on the growth/evaporation rate of that species. The volume of each species s can be described by

a separate moment conservation equation for the third dust moment L_3^s (Helling et al., 2008c), this is

$$\frac{\partial}{\partial t}(\rho_g\, L_3^s) + \nabla \cdot (\rho_g\, L_3^s\, \boldsymbol{v}_d) = V_l^s\, J_\star + \chi^{\mathrm{net},s}\, \rho_g\, L_2. \tag{6.14}$$

Equation 6.14 describes the evolution of the partial cloud volume of species s in space and time due to advection, nucleation, growth, evaporation and drift. It is then possible to compute V_s/V_{tot} from L_3^s by using the identities $L_3 = \sum_s L_3^s$ and $V_{\mathrm{tot}} = \sum_s V_s$ (Woitke and Helling, 2004; Helling et al., 2008c).

We can recover mean properties of the size distribution of the cloud particles from the dust moment solutions as integrated quantities. By using various ratios of the volume-integrated quantities, we can compute many local mean properties of the size distribution, each reflecting different physical characteristics.

The total cloud particle number density n_d is given by

$$n_d = \rho_g\, L_0. \tag{6.15}$$

The average cloud particle size $\langle a \rangle$ is given by

$$\langle a \rangle = \left(\frac{3}{4\pi}\right)^{1/3} \frac{L_1}{L_0}. \tag{6.16}$$

The average cloud particle area $\langle A \rangle$ is given by

$$\langle A \rangle = (36\pi)^{1/3}\, \frac{L_2}{L_0}. \tag{6.17}$$

The average cloud particle volume $\langle V \rangle$ is given by

$$\langle V \rangle = \frac{L_3}{L_0}. \tag{6.18}$$

6.2 Cloud opacity

In order to include the effects of cloud formation in the atmosphere model, we must take into consideration the gas-phase element abundance changes caused by the cloud formation, and we must consider the cloud opacity. The gas-phase element abundances for the elements participating in the cloud formation are a direct output of the `DRIFT` model. However, the cloud opacity is not and so we must compute it in order to include it in the `MARCS` model.

From the `DRIFT` model we obtain some of the necessary quantities to be able to compute the cloud opacity, namely the average cloud particle size and the volume fractions of the cloud species. However, we must further consider how each of the cloud species interacts with light. Different materials will transmit, scatter and absorb light differently. The information on how a material interacts with light is contained in the material's optical constants (n, k). Optical constants are

measured experimentally and the references for the ones used in this thesis for the cloud species considered are listed in Table 8.5 in Appendix 8.C. For a cloud species, we can define its complex refractive index m_λ, given by

$$m_\lambda = n_\lambda + i\, k_\lambda, \tag{6.19}$$

where the λ subscripts indicate the dependency of the optical constants on the wavelength of the light.

In this thesis we assume the cloud particles to be mixed-material, well mixed, spherical and compact. Because the particles are mixed-material, we need first to apply a method to find their effective complex refractive index, before we are able to apply Mie theory to compute the cloud opacity.

6.2.1 Effective Medium Theory (EMT)

We use effective medium theory (EMT) to compute the effective optical constants of the mixed-material cloud particles. We apply Bruggeman's method (Bruggeman, 1935) as described by Bosch et al. (2000) to numerically compute the effective optical constants. The Bruggeman method is given by

$$\sum_s \left(\frac{V_s}{V_{\rm tot}}\right) \frac{\epsilon_s - \epsilon_{\rm eff}}{\epsilon_s + 2\epsilon_{\rm eff}} = 0, \tag{6.20}$$

where $V_s/V_{\rm tot}$ is the volume fraction of cloud species s, ϵ_s is the dielectric function of cloud species s and $\epsilon_{\rm eff}$ is the effective dielectric function over the total cloud particle volume. Following Bosch et al. (2000), we can express Equation 6.20 in terms of the the complex refractive index by considering that $\epsilon = m^2$,

$$\sum_s \left(\frac{V_s}{V_{\rm tot}}\right) \frac{m_s^2 - m_{\rm eff}^2}{m_s^2 + 2m_{\rm eff}^2} = 0, \tag{6.21}$$

where m_s is the complex refractive index of species s and $m_{\rm eff}$ is the effective complex refractive index of the mixed cloud particle. We use a Newton-Raphson minimisation scheme to solve Equation 6.21 for $m_{\rm eff}$. The Bosch et al. (2000) method avoids ambiguities due to back and forth conversions between the dielectric functions and the complex refractive index.

In cases of rare non-convergence of the Bosch et al. (2000) method, towards longer wavelengths ($\lambda > 20\,\mu m$) where the optical constants values are more uncertain, we use the analytic Landau-Liftshitz-Looyenga (LLL) method (Looyenga, 1965) given by

$$\sqrt[3]{\epsilon_{\rm eff}^2} = \sum_s \left(\frac{V_s}{V_{\rm tot}}\right) \sqrt[3]{\epsilon_{\rm s}^2}. \tag{6.22}$$

6.2.2 Mie theory

After computing the effective complex refractive index of the cloud particles, we can apply Mie theory for spherical particles (Mie, 1908) to compute their scattering

and extinction cross sections. Following the Bohren and Huffman (1983) approach, the extinction cross section $C_{\rm ext}$ and the scattering cross section $C_{\rm sca}$ are given by

$$C_{\rm ext}(\lambda, a) = \frac{2\pi a^2}{x^2} \sum_{n=1}^{\infty} (2n+1)\, Re(a_{\rm n} + b_{\rm n}), \tag{6.23}$$

$$C_{\rm sca}(\lambda, a) = \frac{2\pi a^2}{x^2} \sum_{n=1}^{\infty} (2n+1)\, (|a_{\rm n}|^2 + |b_{\rm n}|^2), \tag{6.24}$$

where $x = 2\pi a/\lambda$ is the size parameter, and $a_{\rm n}$ and $b_{\rm n}$ are the scattering coefficients computed from the material optical k constant (see Bohren and Huffman, 1983, for details). The scattering and absorption efficiency factors are then given by

$$Q_{\rm sca}(\lambda, a) = \frac{C_{\rm sca}(\lambda, a)}{\pi a^2}, \tag{6.25}$$

$$Q_{\rm abs}(\lambda, a) = \frac{C_{\rm ext}(\lambda, a)}{\pi a^2} - Q_{\rm sca}(\lambda, a). \tag{6.26}$$

Finally we obtain the total absorption and scattering coefficients $\kappa\,[{\rm cm}^2\,{\rm g}^{-1}]$ by multiplying the efficiency factors with the area and occurrence rate of each cloud particle, this is

$$\kappa_{\rm sca}(\lambda, a) = Q_{\rm sca}(\lambda, a)\, \pi\, a^2\, \frac{n_d}{\rho_g} = Q_{\rm sca}(\lambda, a)\, \pi\, a^2\, L_0, \tag{6.27}$$

$$\kappa_{\rm abs}(\lambda, a) = Q_{\rm abs}(\lambda, a)\, \pi\, a^2\, \frac{n_d}{\rho_g} = Q_{\rm abs}(\lambda, a)\, \pi\, a^2\, L_0. \tag{6.28}$$

The total dust opacity κ_d is given by $\kappa_d = \kappa_{\rm sca} + \kappa_{\rm abs}$.

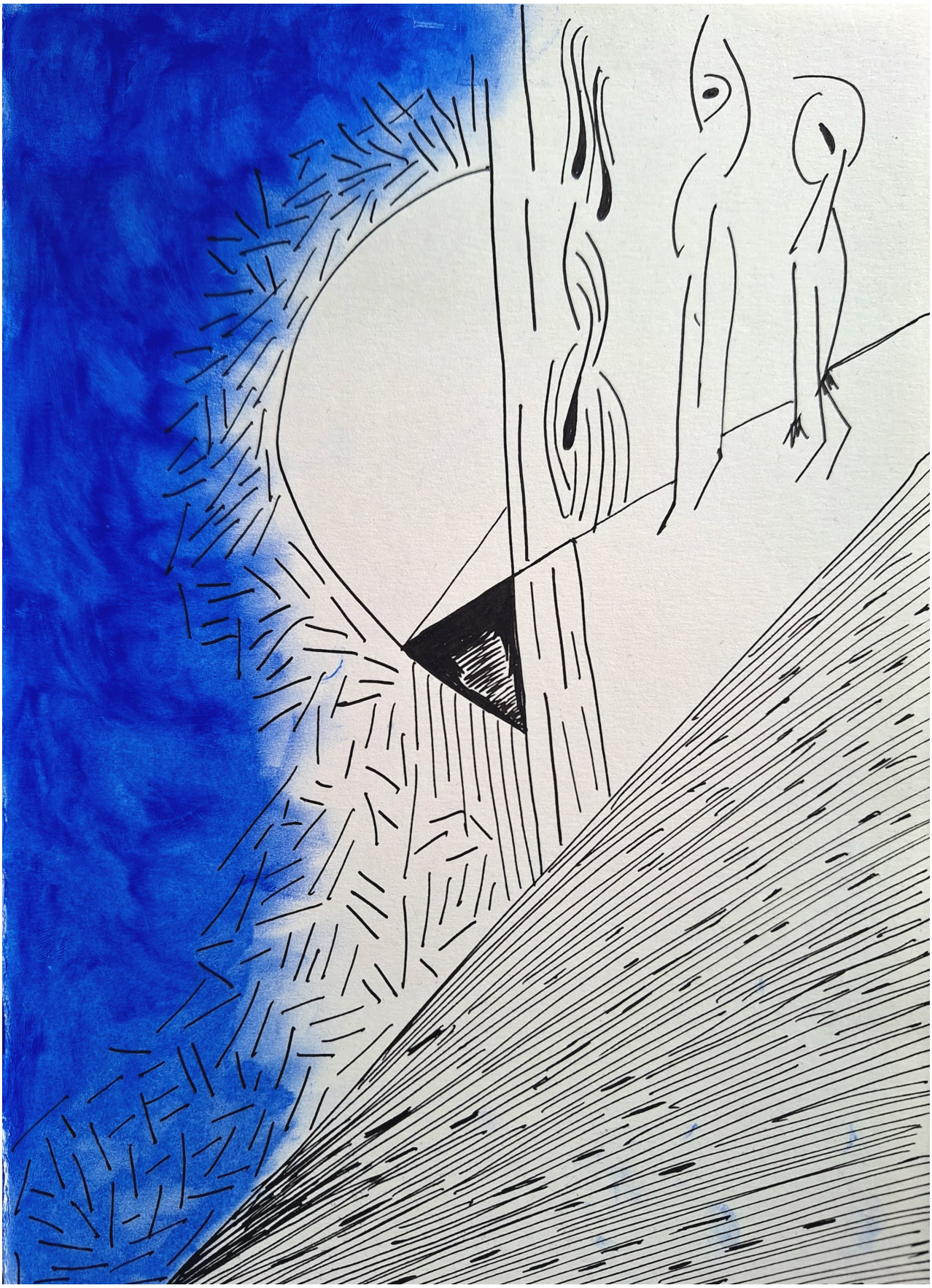

CHAPTER 7

The MSG model for cloudy substellar atmospheres: Research Summary

Yo soy muy mía, yo me transformo.
Una mariposa, yo me transformo.

— Rosalía, in *Saoko*

In this chapter we summarise the work later presented in Chapter 8, *The MSG model for cloudy substellar atmospheres: A grid of self-consistent substellar atmosphere models with microphysical cloud formation*, a manuscript that has been submitted to *Astronomy & Astrophysics*. We start by describing the research context and motivation in the context of the international state-of-art. Next, we present a summary of our methods and results. After, we give an overview of our discussion points in the context of the international state-of-the-art. Finally we present our conclusions and provide an outlook for future research in the topic.

7.1 Research context and motivation

Planetary atmospheres hold fingerprints of the still uncertain planet formation processes. Clouds present a challenge to atmospheric characterisation as they can often hide spectral features of the gaseous components of atmospheres (e.g. Sing et al., 2016; Powell et al., 2019; Wakeford et al., 2019). However, clouds are present in all Solar System bodies with atmospheres, and they are likely present in almost every exoplanet with an atmosphere (e.g. Helling, 2019). Therefore, to accurately characterise planetary atmospheres and robustly link them to a planet's

formation history, it is crucial to determine the composition and structure of a planet's clouds.

Mineral clouds in brown dwarf atmospheres were first proposed almost 40 years ago by Lunine et al. (1986), who concluded that such clouds should exist by comparing modelled temperature-pressure profiles with condensation curves of refractory materials. Over the years, various models have been developed to simulate these cloudy atmospheres, either using parameterised approaches or more complex kinetic treatments of cloud formation processes. Parameterised models typically calculate cloud particle compositions from thermochemical equilibrium and assume an average particle size or a specific size distribution (e.g. Ackerman and Marley, 2001; Cooper et al., 2003). On the other hand, microphysical models consider detailed processes like nucleation, condensation, evaporation, and transport, using methods such as the bin-method (e.g. Toon et al., 1979; Ohno and Okuzumi, 2017; Gao et al., 2018; Kawashima and Ikoma, 2018) or the dust moments method (e.g. Gail and Sedlmayr, 1988; Dominik et al., 1993; Woitke and Helling, 2003, 2004; Helling and Woitke, 2006).

Early evidence for silicate cloud features in L-dwarfs was reported by Cushing et al. (2006) from *Spitzer* mid-infrared observations. More recently, extensive analyses of *Spitzer* infrared spectra of M- to T-dwarfs by Suárez and Metchev (2022) found that silicate cloud absorption features are fairly common in L-dwarfs, though not universally present. The beginning of the JWST era has provided new insights, with the JWST/MIRI instrument enabling low- to medium-resolution spectroscopy in the mid-infrared. For instance, a silicate cloud absorption feature was detected in the planetary mass companion VHS 1256 b (Miles et al., 2023), and quartz clouds were confirmed in the atmospheres of hot Jupiter WASP-17 b (Grant et al., 2023) and warm Neptune WASP-107 b (Dyrek et al., 2024).

Following the discussion in Chapter 1, section 1.3, we call that brown dwarfs are analogues of directly imaged planets because these planets have large orbits (i.e., far from their host-star) and share similar temperatures, surface gravities, and ages with isolated brown dwarfs. Studying cloud formation in substellar atmospheres through brown dwarfs offers a significant benefit compared to irradiated planets: it eliminates the need to account for the host star's external radiation field, greatly simplifying any radiative-transfer calculations, and avoids the interference of the host star's brightness in observations. This approach will still enhance our comprehension of extrasolar giants planet's (EGP) atmospheres. In addition to this, there are still two major questions within brown dwarf science which remain unanswered: (1) What is the origin of the L-T dwarf transition? (2) What is the origin of the brown dwarfs spectroscopic variability? Mineral clouds are thought to be the major culprit of both these phenomena, and there is a need to unveil if this is the case via modelling and observations of substellar atmospheres.

Figure 7.1 shows a colour-magnitude diagram for field dwarfs and directly imaged companions. It is possible to see that field dwarfs and directly imaged companions share near-infrared colours and luminosities. Additionally, the figure shows

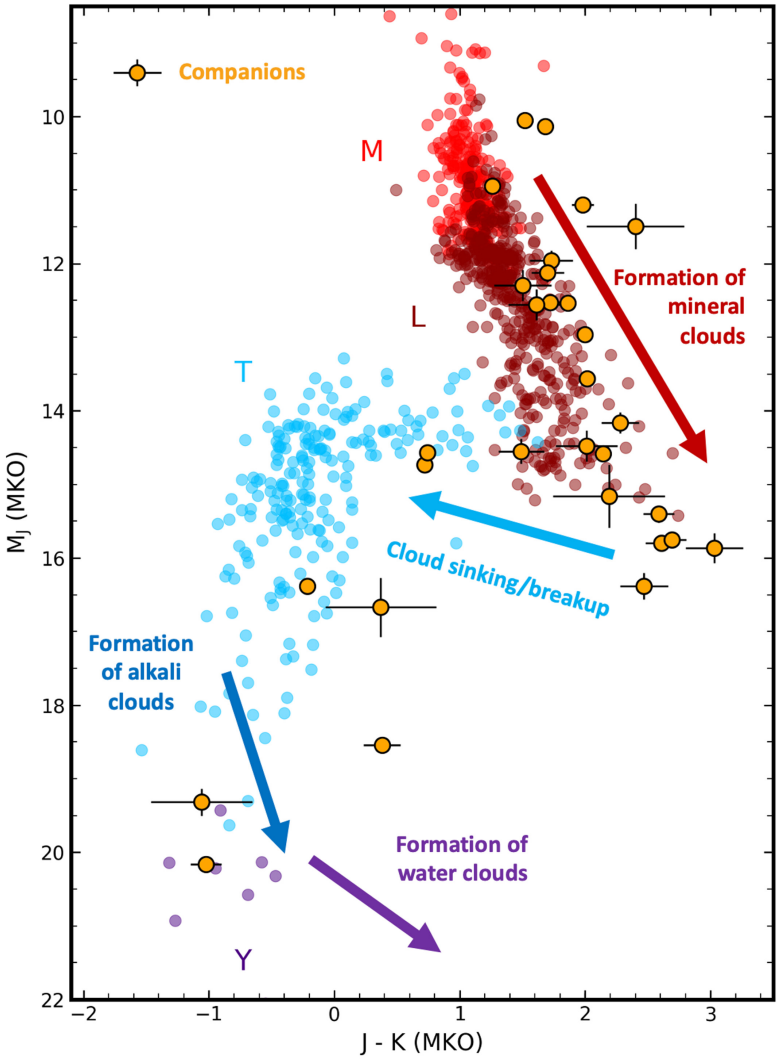

Figure 7.1: Colour-magnitude diagram of field dwarfs (M dwarfs: red; L dwarfs: dark red; T dwarf: blue; Y dwarfs: indigo) and directly imaged companions (orange). Only companions that may be exoplanets are included, following Best et al. (2021). The objects VHS J125601.92-125723.9 b and SDSSJ224953.46+004404.6A are also included. Data were taken directly from Best et al. (2021), which was compiled by Dupuy and Liu (2012); Dupuy and Kraus (2013); Liu et al. (2016); Best et al. (2018, 2020). Only objects with near-infrared photometry available in MKO magnitudes were included. Annotations indicate the current understanding of cloud evolution on brown dwarfs. Figure reproduced, and caption partially reproduced from Gao et al. (2021) under the Creative Commons Attribution 4.0 International License.

where we expect the near-infrared colours to be dominated by the formation and evolution of clouds as brown dwarfs age (Gao et al., 2021). The so-called L-T dwarf transition is this observed shift in the near-infrared colour from red to blue of these dwarfs. Large observational surveys have found high-amplitude spectroscopic variability to be common across the entire L-T spectral sequence (e.g. Metchev et al., 2015; Vos et al., 2019, 2022; Liu et al., 2024). Tan and Showman (2019) used a simplistic 1D model to show that radiative cloud feedback can drive spontaneous atmospheric variability in temperature and cloud structures in brown dwarfs and EGPs. They discovered that this variability, arising from a cloud cycle with varying cloud thickness, includes periods of cloud breaking and dissipation, potentially explaining the L-T dwarf transition.

To understand the implications of cloud formation in substellar atmospheres, we need self-consistent models that incorporate the radiative feedback of clouds and the resulting gas-phase element depletion due to cloud formation, while considering the microphysics of cloud formation. Recently, Petrus et al. (2024) have used various forward models to study the VHS 1256 b JWST data, but none have successfully reproduced the silicate cloud absorption feature observed. This highlights the need for an updated self-consistent grid of substellar atmosphere models with cloud microphysics.

Here we present the new `MSG` model grid for cloudy substellar atmospheres. For this grid we have combined the `MARCS` atmosphere model (e.g. Gustafsson et al., 2008), with the equilibrium chemistry model `GGchem` (Woitke et al., 2018), and the microphysical cloud formation model `DRIFT` (Woitke and Helling, 2003, 2004; Helling and Woitke, 2006; Helling et al., 2008c). Compared to a previous model grid with self-consistent microphysical cloud formation, `DRIFT-PHOENIX` (Witte et al., 2009), the new grid includes important updates in molecular and atomic line lists and includes additional cloud species. More importantly, we apply a new numerical algorithm based on control-theory to facilitate the convergence of cloudy substellar atmosphere models. In this work, we consider 12 cloud species: SiO[s], SiO_2[s], $MgSiO_3$[s], Mg_2SiO_4[s], TiO_2[s], $CaTiO_3$[s], Fe[s], FeO[s], FeS[s], Fe_2O_3[s], Al_2O_3[s] and MgO[s].

7.2 Methods summary

The `DRIFT` model (Woitke and Helling, 2003, 2004; Helling and Woitke, 2006; Helling et al., 2008c) starts by considering the nucleation of cloud condensation nuclei (CCN) via modified classical nucleation theory (Gail et al., 1984; Woitke and Helling, 2004), followed by considering their growth and evaporation. A system of dust moment and element conservation equations is solved, considering gravitational settling and the replenishment of elements (see sections 6.1.4 and 6.1.5). The cloud particles grow through gas-surface reactions, gravitationally settle, and encounter varying temperatures and gas densities, which change their composition. This dynamic interaction results in the continuous growth and eventual evaporation of cloud particles, thereby affecting local gas-phase element abundances. For

the cloud layers to persist, there must exist an element replenishment process, i.e. a source of fresh, non-depleted elements. In this case we consider convective overshooting to be the element replenishment mechanism.

For the atmosphere model we use the most recent version of MARCS, presented by Jørgensen et al. (2024). The model is a one-dimensional radiative-convective equilibrium model in LTE. The MARCS model uses a Feautrier-type method (Feautrier, 1964) to solve the radiative transfer equations over a Rosseland optical depth scale, iterating with a Newton-Raphson procedure. High-order angular dependencies are eliminated using the "variable Eddington factor" technique (Auer and Mihalas, 1970; Cannon, 1973). Convection is modelled with mixing length theory (e.g. Henyey et al., 1965; Nordlund, 1974; Gustafsson et al., 2008). By incorporating the GGchem code (Woitke et al., 2018), we compute gas-phase equilibrium chemistry, considering 20 elements and their molecular and ionic forms. The integration of GGchem with the MARCS model ensures accurate thermochemical computations across a wide temperature range.

To obtain the MSG cloudy substellar models, we couple the Jørgensen et al. (2024) MARCS version to DRIFT to create a self-consistent framework for studying cloudy substellar atmospheres. By iterating between MARCS and DRIFT, we ensure that our radiative transfer scheme incorporates cloud radiative feedback, adjusting for cloud opacity and gas-phase element depletion due to cloud formation. The cloud opacity is calculated using Mie theory (Mie, 1908) combined with effective medium theory (EMT) for mixed-material, spherical, and compact particles. We use the numerical Bruggeman method for effective optical constants (Bruggeman, 1935), resorting to the analytic Landau-Lifshitz-Looyenga method in cases of non-convergence (Looyenga, 1965). We run MARCS and DRIFT iteratively until we achieve convergence, guided by criteria such as changes in the pressure-temperature structure of the atmosphere, cloud opacity, and gas-phase element abundances. To manage the significant radiative feedback from clouds, we implement a control factor to stabilise iterations and reach a converged solution (based on control theory).

7.3 Results summary

The MSG cloudy model base grid consists of 11 models with effective temperatures between 2500 K and 1500 K, each with a surface gravity of $\log(g) = 4.0$. The models use undepleted solar element abundances and TiO_2 as the CCN. The pressure-temperature profiles indicate that the cloudy models are consistently warmer than their cloud-free counterparts, illustrating the blanketing effect of the clouds. As the effective temperature decreases, this divergence becomes more pronounced, resulting in a detached convective zone for models with $T_{\rm eff} \leq 1600$ K due to increased cloud opacity.

We analyse the cloud structure and properties, identifying four distinct cloud stages: nucleation and initial growth, drift, second growth, and evaporation. Initially, nucleation and growth lead to significant depletion of cloud-forming ele-

ments in the upper atmosphere. As the cloud particles fall and encounter higher gas densities, nucleation continues, producing many small particles and maintaining a constant average particle size over a certain pressure range. Further down, backwarming by the cloud particles causes a rapid temperature increase with increasing gas pressure, triggering the evaporation of the silicates and magnesium oxide, followed by iron and the metal oxides remaining, ultimately leading to the complete evaporation of cloud particles at the deeper atmospheric layers.

We compute synthetic spectra which reveal that the cloudy models exhibit significant reddening and reduced emergent flux in the near-infrared as the effective temperature decreases. This is an effect of the cloud opacity which diminishes the visibility of atomic absorption features, such as those of Na and K, and delays the emergence of CH_4 features seen in cloud-free spectra at the same effective temperature and surface gravity. At temperatures below 1600 K, the cloudy spectra become nearly flat at certain wavelengths, which differs notably from observed spectra, prompting us to investigate the roles of nucleation and mixing parameterisations.

We explored the effects of changing the CCN species from TiO_2 to SiO. Models with SiO nucleation show larger cloud particle number densities and smaller average particle sizes at pressures below 10^{-3} bar, compared to the TiO_2 nucleation models. As the nucleation rate drops, the average cloud particle size increases due to continued cloud species condensation on fewer particles. These variations in nucleation and growth rates significantly influence the cloud structure and observable spectra of substellar atmospheres. The spectra for models with SiO nucleation exhibit less reddening in the near-infrared and more distinct absorption features of Na and K, compared to models with TiO_2 nucleation. The presence of CH_4 features is also delayed, although not as significantly as in the TiO_2 nucleation models.

We further explore the effects of scaling the mixing timescale, making the mixing less efficient. Scaling the mixing timescale up, which reduces mixing efficiency, slows the replenishment of the upper atmosphere with cloud-forming elements. This decreased mixing efficiency results in fewer, larger cloud particles due to a reduced nucleation rate. Models with reduced mixing efficiency exhibit cooler pressure-temperature structures between approximately 0.001 bar and 1 bar. The cloud particle number density decreases, leading to an increased average particle size. This affects the cloud opacity, causing less reddening in the near-infrared and making absorption features of Na and K more prominent. Additionally, CH_4 and CO absorption features become more visible, suggesting that models with reduced mixing efficiency may better match observations.

7.4 Discussion overview

Here, we summarise the major discussions points of our study and present an outlook.

Convergence challenges of self-consistent substellar atmosphere models

In cloud-free MARCS models, we encounter convergence issues at effective temperatures between 1600 K and 1200 K due to "opacity cliffs" (e.g. Mukherjee et al., 2023), where the gas opacity changes rapidly with small temperature or pressure variations. These cliffs cause the models to oscillate between temperature corrections, making convergence difficult. The issue is further complicated in MSG cloudy models by sensitive cloud opacity changes with pressure, especially at lower effective temperatures.

We also face challenges in computing cloud opacities due to differences between the vertical scales of the MARCS and DRIFT models. DRIFT's variable pressure points and MARCS's fixed Rosseland optical depth scale lead to interpolation errors, exacerbated by the "opacity cliffs". This problem is more significant at lower temperatures, resulting in different interpolation points in consecutive iterations. Although the Rosseland optical depth scale works well for hotter objects, it is less suitable for cooler objects where the cloud opacity is fairly significant.

Detached convective zones, the L-T dwarf transition, and brown dwarf spectroscopic variability

In our study, we observed that detached convective zones form for effective temperatures below 1600 K due to the backwarming effect of clouds, consistent with other models that consider cloud formation (e.g. Morley et al., 2024). In our modelling approach, we overlook the full motion of the gas due to convection, which can accelerate the element replenishment at the TOA, and the drag of cloud particles by moving gas elements. Previous research by Witte et al. (2011) incorporated convective motion into the dust moment equations and found that convection significantly affects the movement and fate of cloud particles. They concluded that convection could drive cloud particles into higher or deeper atmospheric layers, leading to cycles of cloud destruction and growth, which affects cloud coverage and opacity.

Like previous models which consider cloud formation, our models show that clouds are a significant source of opacity in the near-infrared, influencing the colour and brightness of L dwarfs as they cool (e.g. Allard et al., 2001; Marley et al., 2002; Tsuji, 2002). Burgasser et al. (2002) and Burrows et al. (2006) discussed how cloud sinking or disruption at the L-T dwarf transition may be driven by convection. As mentioned earlier, clouds are also thought to be the origin of the spectroscopic variability observed across the L-T spectral sequence (e.g. Metchev et al., 2015; Vos et al., 2019, 2022; Liu et al., 2024). While clouds are a primary suspect for these variabilities, alternative theories, such as diabatic convection driven by chemical instabilities (Tremblin et al., 2015, 2019), also offer plausible explanations. Future observations, including those by the JWST, aim to disentangle these mechanisms (e.g. Biller et al., 2023).

Nucleation

The efficiency of nucleation to form CCN varies with the astrophysical environment and depends on the abundance of constituent elements and the binding energies of the clusters (e.g. Helling and Fomins, 2013). Various species have been proposed for nucleation in different environments, including warm to hot substellar atmospheres with species like TiO_2 (Jeong et al., 2000; Sindel et al., 2022), SiO (Gail et al., 2013; Bromley et al., 2016), Al_2O_3 (Lam et al., 2015; Gobrecht et al., 2022), and V_2O_5 (Lecoq-Molinos et al., 2024), and in colder exoplanet and brown dwarf atmospheres with species such as NaCl and KCl (Lee et al., 2018; Gao et al., 2018; Helling et al., 2021, 2023). Following previous works on hot Jupiter atmospheres (e.g. Helling and Woitke, 2006; Helling et al., 2019b, 2023), we chose TiO_2 and SiO as nucleating species in our study.

There are significant differences between classical and non-classical nucleation theories, particularly for species like TiO_2 and V_2O_5, where nucleation rates can differ by orders of magnitude (Sindel et al., 2022; Lecoq-Molinos et al., 2024). These findings highlight the sensitivity of nucleation rates to theoretical treatments and the need for laboratory data at relevant temperatures to improve computational models (e.g. Gao et al., 2018). Observational evidence of nucleation in substellar atmospheres is yet to be confirmed, but upcoming observations with the JWST/MIRI-LRS instrument aim to detect molecular clusters in ultra-hot Jupiters like WASP-76 b (Baeyens et al., 2024), potentially providing the first direct evidence of nucleation in these environments.

Mixing

Scaling of the mixing timescale in DRIFT has previously been applied in an attempt to improve the agreement with observation. Samra et al. (2023) predicted condensate clouds in WASP-96 b's atmosphere using `DRIFT`. However, their models were inconsistent with the VLT/FORS2 observations (Nikolov et al., 2018).

In our mixing prescription, we assume there is element replenishment at the TOA from a reservoir of undepleted elements in the deep atmosphere, transported by convective overshooting. This assumption implies that elements travel unchanged through the atmosphere. However, we do not consider that these elements could engage in cloud formation processes like nucleation or growth during their ascent. Ignoring these processes might lead us to overestimate the true efficiency of the mixing. Consequently, our models may assume a higher level of mixing than what actually occurs. This overestimation could explain why our models, with a scaled-up mixing timescale implying less efficient mixing, better match observations. We find more vigorous mixing supports a higher cloud deck, while less efficient mixing supports a lower cloud deck.

Other cloud models (e.g. Ackerman and Marley, 2001; Gao et al., 2018; Ormel and Min, 2019) assume vertical mixing is diffusive, parameterised by the eddy diffusion coefficient K_{zz}. K_{zz} encompasses various large-scale transport processes (e.g. convection, atmospheric circulation), making it difficult to pinpoint the exact

physics it represents. Woitke et al. (2020) combine the dust moment method of DRIFT with diffusive mixing but do not find a static solution to the problem. They solve time-dependent equations until a steady state is reached, resulting in fewer, larger cloud particles near the cloud base due to less efficient mixing. This causes particle growth at the base rather than transport to upper layers. Woitke et al. (2020) predict Mg_2SiO_4[s] as the dominant silicate, similar to our models, but favours SiO[s] and SiO_2[s] over $MgSiO_3$[s]. Recent JWST observations of WASP-17 b revealed crystalline SiO_2[s] (Grant et al., 2023), and (Dyrek et al., 2024) retrieved silicate-dominated clouds in WASP-107b. Combining such a time-dependent model with MARCS is computationally infeasible.

Silicate absorption feature

Silicate clouds in brown dwarf atmospheres are expected to show a significant absorption feature around 10 μm (e.g. Cushing et al., 2006; Suárez and Metchev, 2022; Miles et al., 2023). However, our models do not show this feature, likely due to not considering a particle size distribution function, as we only use the average particle size for cloud opacity calculations. Previous studies (e.g. Min et al., 2004; Powell et al., 2018; Luna and Morley, 2021) indicate that smaller particles ($\sim$0.1 - 1.0 μm) and crystallinity can significantly influence the silicate absorption feature.

7.5 Conclusions and outlook

Summarising our conclusions and outlook:

- We presented a new grid of MSG cloudy substellar model atmospheres with effective temperatures between 2500 K and 1500 K, at $\log(g) = 4.0$, with undepleted solar abundances and TiO_2 nucleation. We use a new convergence algorithm for coupling MARCS to DRIFT, which controls cloud opacity and gas-phase element abundances to avoid numerical oscillations.
- Our models include pressure-temperature profiles, cloud properties (composition and average particle sizes), and model spectra. Our models show significantly redder near-infrared spectra than the known substellar atmospheres.
- Changing the CCN from TiO_2 to SiO or reducing atmospheric mixing efficiency results in less red near-infrared spectra. However, our models still present a strong cloud continuum that does not match observations. Future models should consider more varied CCNs and improved mixing treatments.
- We identified detached convective zones in models with effective temperatures $\leq$ 1600 K due to backwarming by cloud particles. Current models do not consider the effect of convective motion on cloud particles, which can be important for understanding the L-T dwarf transition. Including convective motion in future models is crucial for accuracy.

- Our models lack the expected silicate absorption feature in the mid-infrared (~ 9 - $11\,\mu$m), likely because we do not consider a cloud particle size distribution. Future models should include a particle size distribution function and consider particle crystallinity to improve the representation of silicate absorption features.

CHAPTER 8

The MSG model for cloudy substellar atmospheres: A grid of self-consistent substellar atmosphere models with microphysical cloud formation

Beatriz Campos Estrada[a b c], David A. Lewis[b c], Christiane Helling[b c], Richard Booth[d], Francisco Ardévol Martínez[e f g h] & Uffe Gråe Jørgensen[a]

[a] Centre for ExoLife Sciences, Niels Bohr Institute, Copenhagen, Denmark
[b] Space Research Institute, Austrian Academy of Sciences, Graz, Austria
[c] TU Graz, Fakultät für Mathematik, Physik und Geodäsie, Graz, Austria
[d] School of Physics and Astronomy, University of Leeds, Leeds, UK
[e] Kapteyn Astronomical Institute, University of Groningen, Groningen, The Netherlands
[f] Netherlands Space Research Institute (SRON), Leiden, The Netherlands
[g] Centre for Exoplanet Science, University of Edinburgh, Edinburgh, UK
[h] School of GeoSciences, University of Edinburgh, Edinburgh, UK

Submitted to *Astronomy & Astrophysics*

Author contributions:
Beatriz Campos Estrada conducted the research, developed the new coupling between `DRIFT` and `MARCS`, ran the models and wrote the manuscript. All co-authors contributed to the interpretation of results and provided feedback on the manuscript. David A. Lewis contributed to the writing and editing of the manuscript. Richard Booth contributed to the development of the control algorithm presented. Christiane Helling and Uffe G. Jørgensen supervised Beatriz Campos Estrada.

Original Abstract

Context. State-of-the-art JWST observations are unveiling unprecedented views into the atmospheres of substellar objects in the infrared, further highlighting the importance of clouds. Current forward models struggle to fit the silicate clouds absorption feature at $\sim 10\,\mu$m observed in substellar atmospheres.

Aims. In the MSG model, we aim to couple the MARCS 1D radiative-convective equilibrium atmosphere model with the 1D kinetic, stationary, non-equilibrium, cloud formation model DRIFT, also known as StaticWeather, to create a new grid of self-consistent cloudy substellar atmosphere models with microphysical cloud formation. We aim to test if this new grid is able to reproduce the silicate cloud absorption feature at $\sim 10\,\mu$m.

Methods. We model substellar atmospheres with effective temperatures in the range $T_{\rm eff}$ = 1200-2500 K and with $\log(g) = 4.0$. We compute atmospheric structures that self-consistently account for condensate cloud opacities based on microphysical properties. We present an algorithm based on control theory to help converge such self-consistent models. Synthetic atmosphere spectra are computed for each model to explore the observable impact of the cloud microphysics. We additionally explore the impact of choosing different nucleation species (TiO_2 or SiO) and the effect of less efficient atmospheric mixing on these spectra.

Results. The new MSG cloudy grid using TiO_2 nucleation shows spectra which are redder in the near-infrared compared to the currently known population of substellar atmospheres. We find the models with SiO nucleation, and models with reduced mixing efficiency are less red in the near-infrared. We find detached convective zones arise at effective temperatures $T_{\rm eff} \leq 1600$ due to a backwarming effect by the clouds.

Conclusions. We present a new grid of MSG models for cloudy substellar atmospheres that include cloud-radiative feedback from microphysical clouds. The grid is unable to reproduce the silicate features similar to those found in recent JWST observations and *Spitzer* archival data. We thoroughly discuss further work that may better approximate the impact of convection in cloud-forming regions and steps that may help resolve the silicate cloud feature.

8.1 Introduction

Mineral clouds in brown dwarf atmospheres were first proposed almost 40 years ago by Lunine et al. (1986). By comparing modelled temperature-pressure profiles, with the condensation curves of some refractory materials, Lunine et al. (1986) reached the conclusion that mineral clouds should exist in substellar atmospheres.

During these past 40 years, several different models have been developed and used to model these cloudy atmospheres. Cloud models used in the present day tend

to either be based on a parameterised approach or in a more complex approach which treats cloud formation microphysical processes kinetically. The parameterised approaches generally handle cloud particle compositions calculated from thermochemical equilibrium and either assume an average cloud particle size or define a specific size distribution for the cloud particles. This allows for a determination of the cloud optical properties based on Mie theory (Mie, 1908). The differences between parameterised models arise from the different manner in which they parameterise microphysical processes. For example, the Ackerman and Marley (2001) approach is based on determining cloud distributions by balancing particle sedimentation with vertical mixing, with the vertical extent of the clouds being controlled by a sedimentation efficiency parameter. On the other hand, the Cooper et al. (2003) approach obtains the average cloud particle size by balancing the timescales of microphysical processes following Rossow (1978). The microphysical approach considers complex processes that lead to cloud formation, such as nucleation, condensation, evaporation, and transport. Within the microphysical approach, there are two major modelling methods, the bin-method (e.g. Toon et al., 1979; Gao et al., 2018; Ohno and Okuzumi, 2017; Kawashima and Ikoma, 2018) and the dust moments method (e.g. Gail and Sedlmayr, 1988; Dominik et al., 1993; Woitke and Helling, 2003, 2004; Helling and Woitke, 2006). For a comparison and a review of the different cloud modelling methodologies and their advantages and disadvantages see Helling et al. (2008a) and Gao et al. (2021).

To consider the effect of the cloud's radiative feedback onto substellar atmospheres, we must employ self-consistent models which take into consideration the effects of the cloud opacity and gas-phase element depletion caused by the cloud formation onto the atmospheric structure. Using brown dwarfs to assess the implications of cloud formation in substellar atmospheres has a major advantage over using irradiated planets: one does not need to model the external radiation field of a host-star, which immensely simplifies the radiative-transfer problem, and there is no brightness from a host hindering the observations. Modelling and observing brown dwarf atmospheres will still increase our understanding of extrasolar giant planet (EGP) atmospheres. This is because L- and T- dwarfs are analogues of EGPs as they share temperatures, surface gravities and ages.

Cushing et al. (2006) reported what can be seen as the very first evidence for silicate cloud features from *Spitzer* mid-infrared observations of several L-dwarfs. More recently, Suárez and Metchev (2022) analysed hundreds of M- to T- dwarfs *Spitzer* infrared spectra. They found the silicate cloud absorption feature to be fairly common in L-dwarfs. However, not all of the L-dwarf spectra showed silicate absorption features.

We have now entered the JWST era which has provided us with a new view of substellar atmospheres. The JWST/MIRI instrument allows for medium resolution (R$\sim$1,000 - 10,000) spectroscopy measurements in the mid-infrared. A silicate cloud absorption feature was detected with JWST/MIRI in the planetary mass companion VHS 1256 b, between 9 and 11 μm by Miles et al. (2023). In addition to this, we have had the first confirmation of the presence of quartz clouds in a hot

Jupiter, WASP-17 b (Grant et al., 2023), and in a warm Neptune, WASP-107 b (Dyrek et al., 2024).

Petrus et al. (2024) have presented an analysis of the VHS 1256 b data using 5 different forward-models: ATMO (Tremblin et al., 2015), Exo-REM (Charnay et al., 2018), Sonora Diamondback (Morley et al., 2024), BT-Settl (Allard et al., 2012) and DRIFT-PHOENIX (Helling et al., 2008b; Witte et al., 2009, 2011). Out of the five models, ATMO is the only that is cloudless. BT-Settl and DRIFT-PHOENIX consider cloud microphysics self-consistently, although based on different modelling approaches. Exo-REM makes a parameterisation of the cloud microphysics processes, in a self-consistent manner. Sonora Diamond is self-consistent; however, it does not use cloud microphysics and instead uses the Ackerman and Marley (2001) approach to consider the presence of clouds in the atmosphere. None of the five models can reproduce the silicate cloud absorption feature of VHS 1256 b (Petrus et al., 2024).

There is a need for an updated self-consistent grid with cloud microphysics. Since the publication of the DRIFT-PHOENIX grid over 10 years ago, a considerable number of important molecules and atoms, such as CH_4 (Yurchenko et al., 2017), NH_3 (Coles et al., 2019), TiO (McKemmish et al., 2019), VO (McKemmish et al., 2016), Na (Allard et al., 2019), K (Allard et al., 2019), have had their line-lists updated. In addition to this, equilibrium chemistry models have become more complex but also computationally faster. In this new MSG grid, we include five more cloud species (SiO[s], $CaTiO_3$[s], FeO[s], FeS[s] and Fe_2O_3[s]) than those considered in DRIFT-PHOENIX (TiO_2[s], Al_2O_3[s], Fe[s], SiO_2[s], MgO[s], $MgSiO_3$[s] and Mg_2SiO_4[s]). The formulation used to treat atmospheric mixing has also been updated and is explained in detail in Section 8.2. MSG grid combines the MARCS atmosphere model, with the equilibrium chemistry model GGchem and the DRIFT cloud formation model. Here, we have coupled MARCS to DRIFT using a new algorithm which ensures convergence of the cloud opacity and gas-phase element depletion caused by the cloud formation along the atmosphere.

MARCS was originally written to model the atmospheres of solar-type stars (Gustafsson et al., 1975) and has since been extended to model stellar atmospheres ranging from late A-type to early M-type stars (e.g. Lambert et al., 1986; Jørgensen et al., 1992; Gustafsson et al., 2008). MARCS has been used for multiple purposes from abundance analyses (e.g. Blackwell et al., 1995; Siqueira-Mello et al., 2016), to H_2O detections (Ryde et al., 2002; Aringer et al., 2002), to modelling carbon stars and white dwarf atmospheres (Jørgensen et al., 1992, 2000) and instrument calibrations (Decin et al., 2003; Decin and Eriksson, 2007). MARCS stellar atmosphere models are being used to compute stellar parameters of PLATO targets (Gent et al., 2022; Morello et al., 2022). A summary of the development of MARCS can be found in Gustafsson et al. (2008).

More recently, MARCS has been expanded to model the cloudy atmospheres of late-type M-dwarfs and early-type L-dwarfs (Juncher et al., 2017). However, this extension was limited to effective temperatures down to 2000 K due to convergence

complications. The convergence issues primarily arose from MARCS using the electron pressure as an independent variable (instead of the gas pressure as it is commonly used in other models). Addressing this challenge, Jørgensen et al. (2024) have adapted the MARCS framework to account for the extremely low abundance of free electrons at cooler temperatures, successfully resolving these convergence issues. In this work, following the new MSG grid (based on MARCS) presented in Jørgensen et al. (2024), we expand the MSG grid of cloudy substellar objects down to effective temperatures of 1200 K.

DRIFT, also known as StaticWeather, is a 1D non-equilibrium, stationary, microphysical model which kinetically treats cloud formation (Woitke and Helling, 2003, 2004; Helling and Woitke, 2006; Helling et al., 2008c). DRIFT models several key cloud formation processes, including nucleation, bulk growth, evaporation, gravitational settling of cloud particles, and the depletion of gas-phase element abundances. The model further employs a parameterised scheme for atmospheric mixing that acts to replenish depleted element abundances and counteract the gravitational settling of the cloud particles. The gas-phase composition is computed with the equilibrium chemistry code GGchem (Woitke et al., 2018). DRIFT has been applied across a broad range of substellar atmospheres (Helling and Woitke, 2006; Helling et al., 2008a) and has previously been coupled to the PHOENIX code (Hauschildt and Baron, 1999) to produce the DRIFT-PHOENIX atmosphere model grid and synthetic spectra (Helling et al., 2008b; Witte et al., 2009, 2011). Recent works have explored cloud formation in exoplanet atmospheres utilising a hierarchical modelling approach of post-processing DRIFT onto 3D cloud-free General Circulation Models (GCMs). This has been applied to hot and ultra-hot Jupiter atmospheres such as WASP-18 b (Helling et al., 2019a), WASP-43 b (Helling et al., 2020, 2021), HAT-P-7 b (Helling et al., 2019b, 2021), and WASP-96 b (Samra et al., 2023), as well as to a grid of model exoplanet atmospheres spanning a wide physical parameter space (Helling et al., 2023).

We start by describing cloud formation and the DRIFT model in Section 8.2. Next, we describe atmosphere modelling with MARCS in Section 8.3. In Section 8.4 we describe how we couple MARCS to DRIFT, in order to compute the new MSG model grid. In Section 8.5 we present our results. We start by presenting an overview of the grid. This includes an overview of the pressure-temperature profiles, the cloud properties and the model spectra. In Section 8.5.4 we explore the effect of changing the cloud condensation nuclei (CCN) from TiO_2 to SiO. We investigate the effect of scaling down the mixing efficiency in Section 8.5.5. Section 8.6 discusses our results, including our prospects for future cloudy models using the MSG grid.

8.2 Cloud formation and the DRIFT model

The DRIFT model addresses cloud formation by considering the formation of cloud condensation nuclei (CCN), i.e. nucleation, followed by their growth and evaporation. This involves solving a system of dust moment and element conservation equations. Additionally, the model accounts for gravitational settling and element

replenishment through convective overshooting.

Cloud formation starts with the emergence of CCN, on which all thermally stable cloud species may grow through gas-surface reactions (e.g. Helling, 2019). In DRIFT, the nucleation rate of CCN is considered by applying the modified classical nucleation theory of Gail et al. (1984), as described in Woitke and Helling (2004). Dust growth of mixed-material cloud particles is computed following Woitke and Helling (2003), Helling and Woitke (2006) and Helling et al. (2008c). The cloud particles will gravitationally settle and, as the cloud particles fall, they will encounter different temperatures and gas densities, which causes their composition to change due to the changing thermal stability of the cloud species. The cloud particles continue to grow as they fall until the temperature is so high that all considered cloud species begin to evaporate. The growth and evaporation processes change the local gas-phase element abundances because elements which participate in the cloud formation are depleted. An element replenishment mechanism must exist for a cloud layer to persist (i.e., a source of fresh, non-depleted elements must exist). Here, the replenishment of elements is considered via convective overshooting, which is described in more detail later in this section.

In this work, we model plane-parallel, quasi-static substellar atmospheres. Following this, the evolution of the cloud particles can be described by a series of moment equations for mixed-material cloud particles (Gail and Sedlmayr, 1988; Dominik et al., 1993; Woitke and Helling, 2003; Helling and Woitke, 2006), these are

$$-\frac{d}{dz}\left(\frac{\rho_d}{c_{\rm T}}L_{j+1}\right) = \frac{1}{\xi_{\rm 1Kn}}\left(-\frac{\rho L_j}{\tau_{\rm mix}} + V_\ell^{j/3}\,J_\star + \frac{j}{3}\,\chi_{\rm net}\,\rho L_{j-1}\right) \tag{8.1}$$

for j=(0, 1, 2), where V_ℓ is the minimum volume of a cluster to be considered a cloud particle, ρ is the gas mass density, ρ_d is the cloud mass density, $J_\star[\mathrm{cm^{-3}s^{-1}}]$ is the total nucleation rate, $\chi_{\rm net}[\mathrm{cm\,s^{-1}}]$ is the net growth velocity, $\xi_{\rm 1Kn}[\mathrm{dyn\,cm^{-3}}]$ is the drag force density, $c_{\rm T}$ is a mean thermal velocity and $\tau_{\rm mix}$ is a mixing timescale. For more details on Equation 8.1 see Woitke and Helling (2003, 2004) and Helling et al. (2008c). The moments $L_j\,[\mathrm{cm^j/g}]$ of the cloud particle volume distribution function $f(V)\,[\mathrm{cm^{-6}}]$ are defined as

$$\rho\,L_j = \int_{V_\ell}^{\infty} f(V)\,V^{j/3}\,dV. \tag{8.2}$$

The total cloud particle volume per $\mathrm{cm^3}$ of total matter is determined by the 3$^{\rm rd}$ dust moment, L_3, as

$$\rho\,L_3 = \int_{V_\ell}^{\infty} f(V)\,V\,dV = V_{\rm tot}\ [\mathrm{cm^3 cm^{-3}}] \tag{8.3}$$

where V is the volume of an individual dust particle, and V_ℓ is the lower integration boundary. Similarly, we can define the volume V_s of a certain cloud species s by

$$\rho\,L_3^s = \int_{V_\ell}^{\infty} f(V)\,V^s\,dV = V_s\ [\mathrm{cm^3 cm^{-3}}] \tag{8.4}$$

where V^s is the sum of island volumes of cloud species s in an individual dust particle, $V_{\rm tot} = \sum V_s$, and $L_3 = \sum L_3^s$. Because we consider multiple cloud species, we must use a set of equations for mixed-material cloud particles, i.e. the third dust moment equations for all volume contributions (one for each cloud species s). Following equations 8.1 and 8.4, one finds

$$-\frac{d}{dz}\left(\frac{\rho_d}{c_{\rm T}} L_4^s\right) = \frac{1}{\xi_{\rm 1Kn}}\left(-\frac{\rho L_3^s}{\tau_{\rm mix}} + V_\ell^s\, J_\star + \frac{j}{3}\,\chi_{\rm net}^s \rho L_2\right), \tag{8.5}$$

where L_4^s is defined as $L_4^s = L_4\, V_s / V_{\rm tot}$. For the full derivation of Equation 8.5 see Helling et al. (2008c).

Equations 8.1 for $j \in (0, 1, 2)$ and equations 8.5 for $s \in (0, 1, 2, ..., S)$, where S is the number of cloud species considered, form a system of $(S + 3)$ ordinary differential equations (ODEs) for the unknowns (L_1, L_2, L_3^s, L_4^s).

The gas-phase element abundance conservation as affected by nucleation, growth and evaporation is given by (Woitke and Helling, 2004; Helling et al., 2008c),

$$\frac{n_{\langle H\rangle}\,(\epsilon_i^0 - \epsilon_i)}{\tau_{\rm mix}} = \nu_{i,0}\, N_\ell\, J_* + \sqrt[3]{36\pi}\,\rho_g\, L_2 \sum_{r=1}^{R} \frac{\nu_{i,s} n_r^{\rm key} \upsilon_r^{\rm rel} \alpha_r}{\nu_r^{\rm key}} \left(1 - \frac{1}{S_r\, b_{\rm surf}^s}\right). \tag{8.6}$$

The term on the l.h.s. describes the gas-phase element replenishment through atmospheric mixing, where $n_{\langle H\rangle}$ is the total hydrogen nuclei density, and ϵ_i^0 and ϵ_i are the initial and depleted element abundances of element i normalised to hydrogen, respectively. The first term on the r.h.s. describes the element depletion by nucleation, where $\nu_{i,0}$ is the stoichiometric coefficient of the CCN and N_ℓ is the number of monomers in the CCN. The second term on the r.h.s. describes the element depletion by evaporation/growth, where ρ is the gas mass density, L_2 is the $2^{\rm nd}$ dust moment as defined in Equation 8.2, r is the index for the chemical surface reaction, $\nu_{i,s}$ is the stoichiometric coefficient of element i in solid material s, $n_r^{\rm key}$ is the particle number density of the key reactant in the gas-phase, $\upsilon_r^{\rm rel}$ is the relative thermal velocity of the gas species taking part in reaction r, α_r is the sticking coefficient of reaction r, $\nu_r^{\rm key}$ is the stoichiometric factor of the key reactant in reaction r, S_r is the reaction's supersaturation ratio and $1/b_{\rm surf}^s = V_s/V_{\rm tot}$ is the volume ratio of solid s to the total cloud particle volume $V_{\rm tot}$. For more details on Equation 8.6 see Woitke and Helling (2004) and Helling et al. (2008c). In this work $N_l = 1000$ and $\alpha_r = 1$ for all reactions.

The element conservation equations 8.6 provide algebraic auxiliary conditions for the ODE system (Equations 8.1 and 8.5). First, the system of non-linear algebraic equations 8.6 has to be solved for ϵ_i at given (L_2, L_4^s) before the r.h.s of the ODEs can be computed. The dust volume composition $b_{\rm surf}^s$ is obtained from $L_4^s = L_4/b_{\rm surf}^s$. The abundance ϵ_i is strongly dependent on $J_\star$, $n_r^{\rm key}$ and S_r and therefore an intricate iterative procedure is required to solve the equations. L_0 is set by a closure condition (see Appendix A in Helling et al., 2008c), $L_{1,2,3}$ are determined by solving for L_j in Equation 8.2 (see Woitke and Helling (2003) for

details), and L_4 is solved by using L_3. The numerical methods and iterative processes used in DRIFT are described in detail in Woitke and Helling (2004).

The cloud particle number density, n_d [cm^{-3}], and the average cloud particle size, $\langle a \rangle$ [cm], can be calculated from the moments (Helling and Fomins, 2013) by

$$n_d = \rho\, L_0, \tag{8.7}$$

$$\langle a \rangle = \left(\frac{3}{4\pi}\right)^{1/3} \frac{L_1}{L_0}, \tag{8.8}$$

respectively.

Atmospheric mixing is parameterised within the model using a mixing timescale, $\tau_{\rm mix}$. This timescale is introduced by Woitke and Helling (2004) as the atmosphere would remain cloud-free in the truly static case. This approach is simplified and assumes the gas/cloud particles mix at a height z is exchanged by cloud-free gas from the deep atmosphere with element abundances ϵ_i^0 on a mixing timescale $\tau_{\rm mix}(z)$ (overshooting). Similar to previous works (e.g. Helling et al., 2008c; Witte et al., 2009) we parameterise $\tau_{\rm mix}$ following the convective mixing and overshooting assumption. In the deepest, convective, atmospheric layers (i.e. the bottom of the atmosphere) we compute τ_{mix}, as

$$\tau_{\rm mix} = \frac{\alpha\, H_p}{v_{\rm conv}}, \tag{8.9}$$

where α and $v_{\rm conv}$ are the mixing length parameter and the convective velocity respectively, as defined in Gustafsson et al. (2008). H_p is the atmospheric layer's scale height given by

$$H_p = \frac{k_B\, T}{m_u\, u\, g}, \tag{8.10}$$

where k_B is the Boltzmann's constant, T is the atmospheric layer's temperature, m_u is the mean molecular mass in atomic mass units, u is an atomic mass unit and g is the acceleration of gravity. If a detached convective layer exists higher in the atmosphere, $\tau_{\rm mix}$ is set to constant to the value at the top of the radiative zone just below. We discuss the validity of this assumption in Section 8.6.2.

In the radiative zone(s), the convective velocity is zero, and therefore, we must parameterise the mixing timescale differently. At each layer, we calculate β, defined as

$$\beta = \frac{\log \tau_{\rm mix}^{\rm i+1} - \log \tau_{\rm mix}^{\rm i}}{\log {\rm P_i} - \log {\rm P_{i+1}}}. \tag{8.11}$$

When the calculated β exceeds a critical value $\beta_{\rm cr}$, we set $\beta = \beta_{\rm cr}$. The mixing timescale is then calculated as

$$\log \tau_{\rm mix}^{\rm i} = \log \tau_{\rm mix}^{\rm i+1} - \beta_{\rm cr}\, (\log {\rm P_i} - \log {\rm P_{i+1}}), \tag{8.12}$$

where $\tau_{\rm mix}^{i}$ is the mixing timescale at layer i of the atmosphere, $\tau_{\rm mix}^{i+1}$ is the mixing timescale at layer $i+1$ of the atmosphere, which is one layer deeper than i,

$P_{i,i+1}$ are the atmospheric pressures at layer i and layer $i+1$ respectively. The parameterisation in Equation 8.12 has its origin in the numerical simulations of surface convection in late M-dwarfs by Ludwig et al. (2002), as described in Woitke and Helling (2004). In this work we set $\beta_{\rm cr} = 2.2$ following Ludwig et al. (2002).

All the chemical surface reactions considered by DRIFT are listed in Table 8.3 in Appendix 8.B.

8.3 Atmosphere modelling with MARCS

MARCS is a one-dimensional, stratified, cloud-free, radiative-convective equilibrium atmospheric model in local thermodynamic equilibrium (LTE). MARCS models are computed with a Feautrier (1964) type method, over a Rosseland optical depth scale and solved iteratively using a Newton-Raphson procedure (e.g. Nordlund, 1974; Gustafsson et al., 1975). The radiative transfer scheme in MARCS uses a method of the type given by Rybicki (1971), as described in Gustafsson and Nissen (1972). High-order angular dependencies are eliminated using the "variable Eddington factor" technique (Auer and Mihalas, 1970) as described in Cannon (1973). Convection is modelled with mixing length theory as described in Nordlund (1974) and Gustafsson et al. (2008). In this work, we use the most recent version of MARCS (Jørgensen et al., 2024), which is able to model plane-parallel cloud-free substellar atmospheres down to the effective temperatures of the coldest T-dwarfs ($\approx 500\,$K).

8.3.1 Gas-phase equilibrium chemistry

In Jørgensen et al. (2024), MARCS was updated to use GGchem (Woitke et al., 2018), a thermochemical equilibrium code which is used to compute the gas-phase equilibrium chemistry in MARCS. GGchem functions by minimising the total Gibbs free energy, and is applicable across a wide temperature range, from 100 K up to 6000 K. GGchem computes the gas-phase equilibrium chemistry in each atmospheric layer from the local temperature, the gas pressure and the gas-phase element abundances.

The models presented here include 20 elements (H, He, C, N, O, Ne, Na, Mg, Al, Si, S, K, Ca, Cr, Fe, Ni, Li, Cl, Ti and V), each capable of existing as neutral atoms or singly charged ions. Following this choice of elements, GGchem considers 334 molecules, molecular ions and cations in the gas-phase equilibrium chemistry computations. Details on the thermochemical data and the methods used by GGchem can be found in Woitke et al. (2018).

8.3.2 Gas and continuum opacities

We include the same continuum opacities as in Juncher et al. (2017). We compute the continuum absorption for 12 ions, electron scattering and Rayleigh scattering by H_2. The references for the continuum opacities data are listed in Table 8.1 in

Appendix 8.A. In this work, we include the line opacities of 34 molecules and 2 atoms (Na and K). We sample the line opacities using the Opacity Sampling (OS) method as described in, for example, Jørgensen (1992). All the models presented here use a sampling density of $R = \lambda/\Delta\lambda = 15000$, where each 3$^{\text{rd}}$ point is sampled for the radiative transfer calculation. Specifically, the TauREx (Al-Refaie et al., 2021) OS files from the ExoMol database as compiled by Chubb et al. (2021) were modified by Jørgensen et al. (2024) as necessary to be read and used by MARCS. All the references of the line lists of the molecules and atoms considered are presented in Table 8.2 in Appendix 8.A.

8.4 The MSG model algorithm for cloudy substellar atmospheres

We have coupled MARCS to DRIFT in a self-consistent manner to study the effects of microphysical cloud formation in substellar atmospheres. This implies that the radiative transfer scheme accounts for the cloud radiative feedback. The cloud radiative effect is added to the radiative transfer by considering the cloud's opacity contribution and through the change in the local gas opacity due to the depletion of cloud-forming elements.

We run MARCS and DRIFT iteratively until we find a converged solution (the convergence criteria are defined in Section 8.4.1). Fig. 8.1 shows a diagram of the MSG workflow. To run MARCS, the user is required to provide an effective temperature of the object (T_{eff}), the gravitational acceleration of the object ($\log(g)$), the gas-phase element abundances, and an initial guess of the pressure-temperature structure of the atmosphere (typically from a previous MARCS model). The closer the initial pressure-temperature structure is to the solution, the faster the model converges. When running a grid of MSG models, it is best to start from a cloud-free model at a high T_{eff} ($\geq$ 2500 K), where we expect fewer clouds to form. This is because the clouds have a blanketing effect and heat up the atmosphere considerably compared to cloud-free models. As the T_{eff} decreases, the pressure-temperature structure of the cloudy atmosphere diverges more and more from that of a cloud-free atmosphere at the same T_{eff} and $\log(g)$. DRIFT requires as inputs from MARCS the pressure-temperature structure, the gas density, the scale height and the convective velocity, all as a function of atmospheric height. When starting a new run of MSG, these inputs are taken from a previous cloudy MARCS model at a similar T_{eff} and $\log(g)$. The initial gas element abundances are set by the user and must be consistent between the two models. In DRIFT, the initial abundances are always the abundances before any element depletion by cloud formation has occurred. The computation of the mixing timescale (Equation 8.9) is done within the DRIFT framework. DRIFT then kinetically models the cloud formation considering the processes described in Section 8.2. The numerical methods are described in detail in Woitke and Helling (2004).

Once DRIFT has computed the cloud structure, we run MARCS taking as inputs

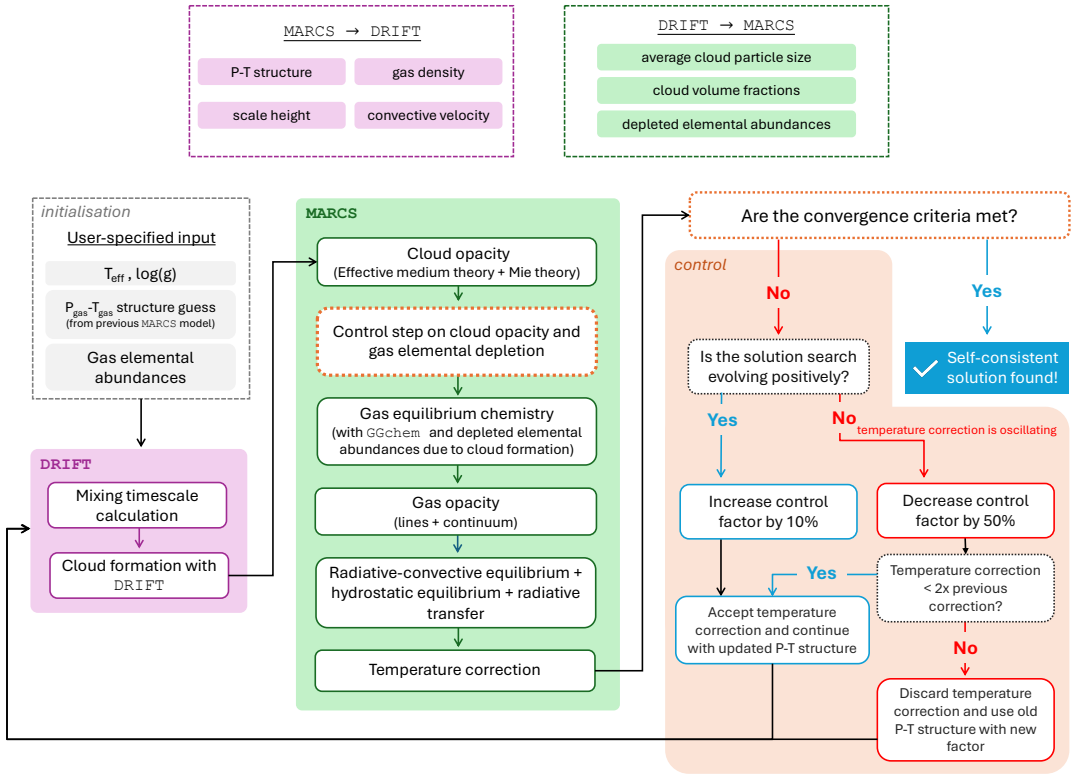

Figure 8.1: Diagram of the MSG model algorithm for cloudy substellar atmospheres. The boxes with a dashed outline indicate parameters that are inputs to the model. The boxes with a dotted outline indicate control processes within the workflow. For a detailed explanation of the cloud formation process, see Section 8.2. For a detailed explanation of the control process, see Section 8.4.3. For the convergence criteria considered under the control process see Section 8.4.1.

from DRIFT the average cloud particle size, the cloud particle condensate volume fractions, and the depleted gas-phase element abundances, all as a function of atmospheric height. The cloud opacity is calculated using effective medium theory (EMT) and Mie theory (see Section 8.4.2). The change in the cloud opacity and in the gas-phase element abundances between two consecutive MSG iterations is controlled as described in the coming Section 8.4.3. MARCS then proceeds to use GGchem to compute the gas-phase equilibrium chemistry. The gas opacities are calculated after obtaining the number densities for each gas-phase species from GGchem. The radiative-transfer equation is then solved using a Feautrier (1964) type method, assuming radiative-convective equilibrium and hydrostatic equilibrium. The numerical methods are described in detail in Nordlund (1974) and Gustafsson et al. (1975). Finally, we obtain a temperature correction that is applied to the old $P_{\rm gas} - T_{\rm gas}$ structure to produce the new atmospheric structure. We check if the solution meets the convergence criteria. If the convergence criteria are not met, we enter a control process to handle the cloud opacity and the depleted gas-phase element abundances in order to avoid oscillations in the temperature

corrections and reach convergence. This control process is explained in detail in Section 8.4.3. The cycle described above is repeated until a converged solution is found.

8.4.1 Convergence criteria

The convergence criteria for a MSG cloudy model are the following:

1. The change in the $P_{\rm gas} - T_{\rm gas}$ structure between the previous and current iteration must be smaller than 5 K;
2. The relative difference in the cloud opacity and the gas-phase element abundances between the current and the previous iteration must be smaller than 10%;
3. The relative difference in the wavelength-dependent emergent flux between the current and previous iteration must be smaller than 1%. Generally, when the wavelength-dependent emergent flux has converged, $|F_i^\lambda - F_{i-1}^\lambda|/F_i^\lambda < 1\%$, all the other convergence criteria have also been met.

8.4.2 Cloud opacity

We consider the cloud particles to be mixed-material, well-mixed, spherical, and compact. As presented in Lee et al. (2016), we calculate the cloud opacity with spherical particle Mie theory (Mie, 1908) combined with effective medium theory (EMT).

The effective optical constants for the material mixtures are calculated with EMT. We generally use the numerical Bruggeman method (Bruggeman, 1935) except for rare cases where we find non-convergence and therefore use the analytic Landau-Lifshitz-Looyenga [LLL] method (Looyenga, 1965) (see Section 2.4. of Lee et al. (2016) for more details). The cloud particle extinction and scattering coefficients are computed with Mie theory using the routine developed by Wolf and Voshchinnikov (2004), which is based on the widely used Bohren and Huffman (1983) routine.

We use the data tables compiled by Kitzmann and Heng (2018) for the cloud particle optical constants. Table 4.1 in Appendix 8.C lists all the references for the cloud particle optical constants.

8.4.3 Controlling the cloud opacity and the depleted gas element abundances

One of the biggest challenges in modelling cloudy atmospheres self-consistently is handling the significant radiative feedback of the cloud. At effective temperatures of less than 2200 K, if we start a MSG run from a cloud-free model, the atmosphere is significantly heated up at the second iteration due to the cloud radiative feedback. When we run the cloud formation model with this heated-up atmosphere as an

input, much of the condensed material is no longer thermally stable because the atmosphere is significantly hotter, and therefore evaporates. This leads to an atmosphere that is now significantly cooler than the one obtained in the previous iteration. The solution may thus enter an oscillating cycle without ever converging.

We introduce a control factor f in our modelling to avoid these oscillations. The factor can take a value between 0 and 1, and it controls the change in cloud opacity and in element abundances between two iterations. We define the cloud opacity $\kappa^{\rm cloud}$ at iteration j as

$$\kappa_j^{\rm cloud} = f\,\kappa_{j/2}^{\rm cloud} + (1-f)\,\kappa_{j-1}^{\rm cloud}, \tag{8.13}$$

where $\kappa_{j-1}^{\rm cloud}$ is the cloud opacity used in the previous iteration and $\kappa_{j/2}^{\rm cloud}$ is the true cloud opacity calculated after the `DRIFT` run (first step within `MARCS` as shown in the diagram in Fig. 8.1). We update the gas-phase element abundances in the same manner. The gas-phase element abundance ϵ_i of element i at iteration j is therefore given by

$$\epsilon_i^j = f\,\epsilon_i^{j/2} + (1-f)\,\epsilon_i^{j-1}, \tag{8.14}$$

where ϵ_i^{j-1} is the element abundance used in the previous iteration and $\epsilon_i^{j/2}$ is the true element abundance computed after the `DRIFT` run.

The factor f is updated depending on the evolution of the solution search. The solution search is evolving positively if the atmosphere is consecutively heating up or cooling down. This is checked by considering the ratio between the maximum temperature corrections obtained in the current and previous iterations, i.e.

$$R = \frac{\Delta T_j^{\rm max}}{\Delta T_{j-1}^{\rm max}}, \tag{8.15}$$

where $\Delta T_{j,j-1}^{\rm max}$ are the maximum temperature corrections in the current and previous iterations respectively. If the ratio R is positive, the atmosphere has either heated up consecutively between the two iterations or cooled down consecutively between the two iterations. This means the solution is evolving positively and we accept the temperature correction and increase the factor f by 10%. If the ratio R is negative, we are within an oscillation and decrease f by 50%. These percentages were chosen after we performed testing on a toy model and concluded they tend to minimise the number of iterations needed for convergence. If the current temperature correction exceeds double the previous temperature correction, we discard the current temperature correction and re-run the model with the new f. Otherwise, we accept the temperature correction but still use the new f in the next iteration. These steps are illustrated in the area denominated "control" in the diagram shown in Fig. 8.1.

We note the maximum value f can have is 1 and f can never be 0. At effective temperatures above 1800 K, we start the model run with $f = 1$. However, at lower effective temperatures we have found it favourable to start with a lower value of f. We typically use $f = 0.1$. For the 0^{th} iteration, $j = 0$, $\kappa_{-1}^{\rm cloud}$ is the cloud opacity used in the last iteration of the input model. If the input model is cloud-free then

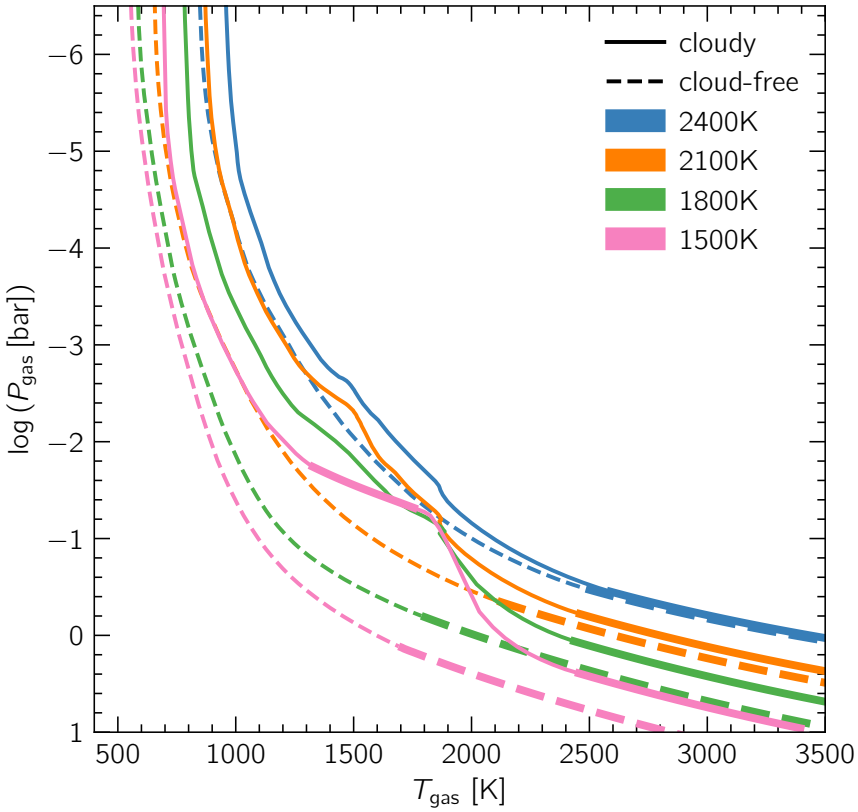

Figure 8.2: Pressure-temperature profiles for cloud-free MARCS models (dashed curves) and cloudy MSG models with TiO_2 nucleation (solid curves), at different effective temperatures and $\log(g) = 4.0$. Convective zones are plotted with thicker lines while radiative zones are plotted with thinner lines. We note the cloudy profile at 1500 K has a detached convective zone.

$\kappa_{-1}^{\rm cloud} = 0$ and f is set to 1. The cloud opacity is converged if $|\kappa_{i/2}^{\rm cloud} - \kappa_{i}^{\rm cloud}|/\kappa_{i/2}^{\rm cloud}$ is less than 10%. The same principles apply to the control of each of the gas-phase element abundances.

8.5 Results

The base grid of models consists of 11 models at effective temperatures between 2500 K and 1500 K, in steps of 100 K, at $\log(g) = 4.0$, with undepleted solar element abundances and C/O ratio, and TiO_2 CCN. In Sections 8.5.1, 8.5.2 and 8.5.3 we present $P_{\rm gas} - T_{\rm gas}$ profiles, cloud structures and properties, and model spectra for some selected models. In Section 8.5.4, we explore the effect of changing the CCN species to SiO. In Section 8.5.5 we explore the effect of scaling up the mixing timescale, making the mixing less efficient.

8.5.1 $P_{\rm gas} - T_{\rm gas}$ profiles

Fig. 8.2 shows the $P_{\rm gas} - T_{\rm gas}$ profiles of MSG cloudy models (solid curves) and MARCS cloud-free models (dashed curves), at the effective temperatures of 2400 K, 2100 K, 1800 K and 1500 K, and $\log(g) = 4.0$. The cloudy models are consistently warmer than the cloud-free models at the same effective temperature, indicating the clouds have a blanketing effect over the atmosphere. This effect is generally seen in L dwarf models (e.g. Morley et al., 2024). The radiative regions of the atmosphere are plotted with a thinner line width, while the convective regions are plotted with a thicker line width.

In the cloudy models, a detached convective zone emerges at $T_{\rm eff} \leq 1600$ K due to the increasing cloud opacity. This is also seen in other L dwarf model grids (e.g. Burrows et al., 2006; Witte et al., 2011; Morley et al., 2024). In Section 8.6.2 we discuss the implications of detached convective zones in more detail.

8.5.2 Cloud structure and properties

Fig. 8.3 shows the average cloud particle size (left), the cloud particle number density (middle) and the nucleation rate (right) in the atmosphere for the MSG models shown in Fig. 8.2. Fig. 8.4 shows the cloud particle composition and the relative gas-phase elemental depletion along the atmosphere for the model at 1500 K.

We can identify four different cloud stages where different processes take place and dominate the cloud structure. The first region we identify is the region of the *nucleation* and *first growth* stage, visible in Fig. 8.3 (left) between $\sim 10^{-7}$ to 10^{-5} bar. As the cloud particles fall inwards, the increasing gas density and the element replenishment allow for the collision rate between the gas and the dust particles to increase, allowing for a growing number of surface reactions. This leads to the cloud particles growing in size and the cloud-forming elements depleting significantly (see Fig. 8.4 right). Particularly, we see Ti highly depleted at the very top of the atmosphere (TOA) due to the *nucleation* process. Although O is also depleted, this is not as visible because O is highly abundant compared to Ti. Throughout this stage, the nucleation rate continues to increase, however the growth process is dominant on the average cloud particle size.

We then reach the *drift* stage, between $\sim 10^{-5}$ to 10^{-3} bar (dependent on the effective temperature). During this stage, the nucleation rate is increasing. This results in the formation of many new, small cloud particles, efficiently consuming elements from the gas-phase. Consequently, the available material for the growth of cloud particles is reduced, and the net growth rate of the particles decreases. The creation of new particles and the reduction in the net growth rate ultimately act to keep the average particle size constant over this pressure region. The maximum gas-phase depletion is reached at about the same pressure at which the nucleation rate peaks (Fig. 8.4 right).

When the nucleation rate drops, the increasing grain size is no longer balanced by

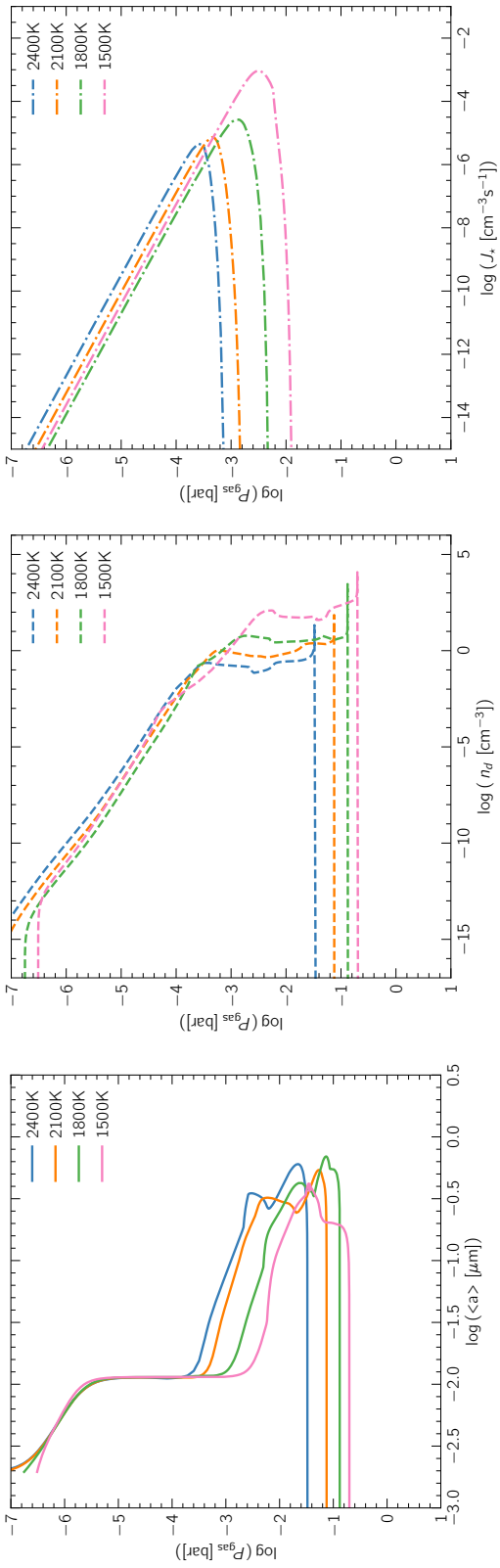

Figure 8.3: The average cloud particle size $\langle a \rangle$ (left), the cloud particle number density n_d (middle) and the nucleation rate $J_\star$ (right) along the atmosphere for models with TiO_2 nucleation at $T_{\rm eff} = 2400\,{\rm K}$, 2100 K, 1800 K and 1500 K and $\log(g) = 4.0$. The corresponding $P_{\rm gas} - T_{\rm gas}$ profiles are shown in Fig. 8.2.

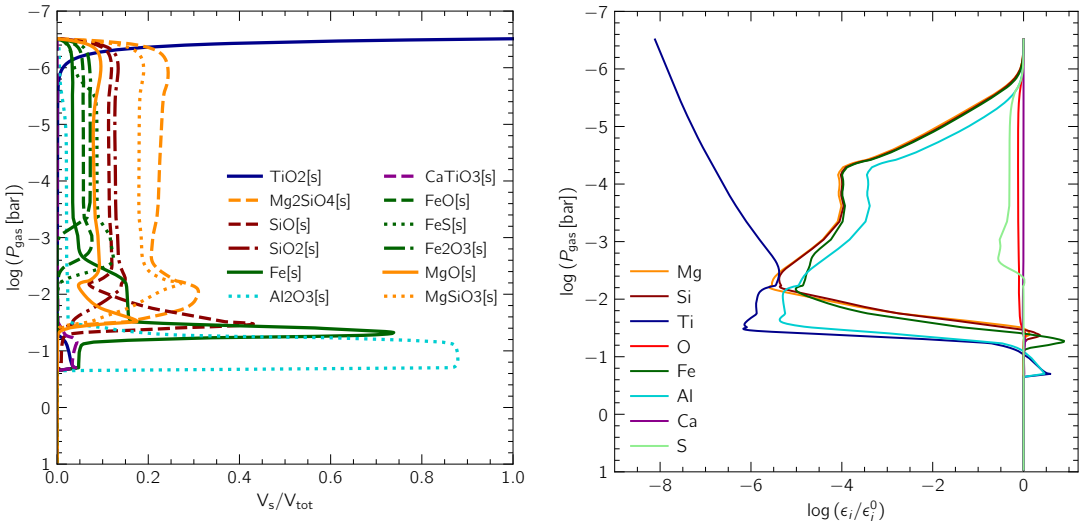

Figure 8.4: Composition of the cloud particles in units of volume fractions $V_s/V_{\rm tot}$ (left) and the relative gas-phase element depletions ϵ_i/ϵ_i^0 (right) for a MSG model with TiO_2 nucleation, at 1500 K and $\log(g) = 4.0$.

the formation of new CCN, and therefore we reach the *second growth* stage, between $\sim 10^{-3}$ to 10^{-1} bar (dependent on the effective temperature). At this point, due to backwarming by the cloud particles, the temperature increases rapidly with increasing gas pressure (see Fig. 8.2). The silicate species and magnesium oxide are the first to react to this. Over a small pressure interval, dissociation begins to be the favoured chemical path. We enter the stage of *evaporation*. The average particle size drops slightly, which creates a local maximum in the average cloud particle size (Fig. 8.3 left). For example, for the model at 1500 K, we can see from Fig. 8.4 (left) that the first local maximum in cloud particle size occurs just before the cloud volume fraction of SiO[s], SiO_2[s], Mg_2SiO_4[s], $MgSiO_3$[s] and MgO[s] drop to zero (between 0.01 and 0.1 bar). This is also seen in Fig. 8.4 (left), where the relative element abundance of Si and Mg are replenished due to the evaporation.

Once the silicates evaporate, Fe[s] and AlO_3[s] dominate the growth process. Fe[s] quickly becomes the species with the largest cloud volume fraction, increasing the cloud opacity in the optical and near-infrared. Due to the increased cloud opacity, the cloud particles heat extremely fast, and Fe[s] quickly evaporates, followed by AlO_3[s], $CaTiO_3$[s] and TiO_2[s]. A local maximum in average cloud particle size is also visible for the evaporation of Fe[s] and AlO_3[s]. The cloud ends when all the cloud species have evaporated. Within the evaporation regions of individual solids, cloud-forming elements can be enriched due to their rain out in cloud particles (Fig. 8.4 left).

The maximum average cloud particle size is similar at all effective temperatures modelled. However, at the same pressure, the average cloud particle size is smaller for decreasing effective temperature. There is a shift with effective temperature in the pressure at which the *second growth* starts. The *second growth* starts at higher

pressures for smaller effective temperatures (Fig. 8.3 left). This is expected as the nucleation rate peaks at higher pressures with decreasing effective temperature (Fig. 8.3 right). The cloud particle number density increases slightly with effective temperature due to the reduction in the average cloud particle size (Fig. 8.3 middle).

8.5.3 Synthetic spectra

Synthetic spectra allow us to compare models to observations. In this section, we show the spectra of the MSG models presented in Fig. 8.2 at selected wavelength ranges. All the spectra shown have been re-binned to have a resolution of $R = 1000$. The spectra inform us about the observable atmosphere of the object. The observable atmosphere of the object goes down to where the optical depth (τ) is equal to unity. Anything below $\tau = 1$ is not observable.

Fig. 8.5 shows MSG cloudy and MARCS cloud-free spectra at different wavelength ranges, for the models shown in Fig. 8.2. At the highest effective temperatures (2100 K and 2400 K in the plots), the cloudy spectra are similar to the cloud-free spectra. They are majorly defined by the absorption features of atoms Na and K, metal oxides such as TiO and VO, and the metal hydride FeH, in the optical and near-infrared (Fig. 8.5, top right). In the mid-infrared, H_2O and CO dominate the shape of the spectra (Fig. 8.5, bottom left).

Towards lower effective temperatures, the effects of the cloud opacity are significant in all wavelength bands. The spectra redden significantly in the near-infrared wavelengths, and the emergent flux is considerably reduced (Fig. 8.5, top left). For example, although the abundances of Na and K are never depleted due to cloud formation, the absorption features of both these atoms shrink with decreasing effective temperature (Fig. 8.5 top right). At 1500 K the Na and K features are no longer visible due to the cloud continuum. Another striking difference between the cloud-free and cloudy spectra is the effective temperature at which CH_4 emerges. For the cloud-free models, the CH_4 feature at $\sim 3.3\,\mu$m emerges at approximately 1900 K. Due to the warming of the $P_{\rm gas} - T_{\rm gas}$ structure by the cloud radiative feedback, CH_4 never emerges as prominently in the spectra within the models shown in Fig. 8.5 (bottom right).

In the models presented in this section, the cloud opacity has the extreme effect of making the spectra nearly flat at certain wavelengths for effective temperatures below 1600 K. This is extremely different compared to observed spectra (e.g. Cushing et al., 2005, 2008; Stephens et al., 2009; Suárez and Metchev, 2022; Miles et al., 2023), where although a cloud continuum is generally seen, the spectra are not flat. This is the major discrepancy between our model grid and the observations. Therefore, in the next two sections, we explore nucleation and mixing parameterisations to unravel the potential origin of our extremely flat spectra.

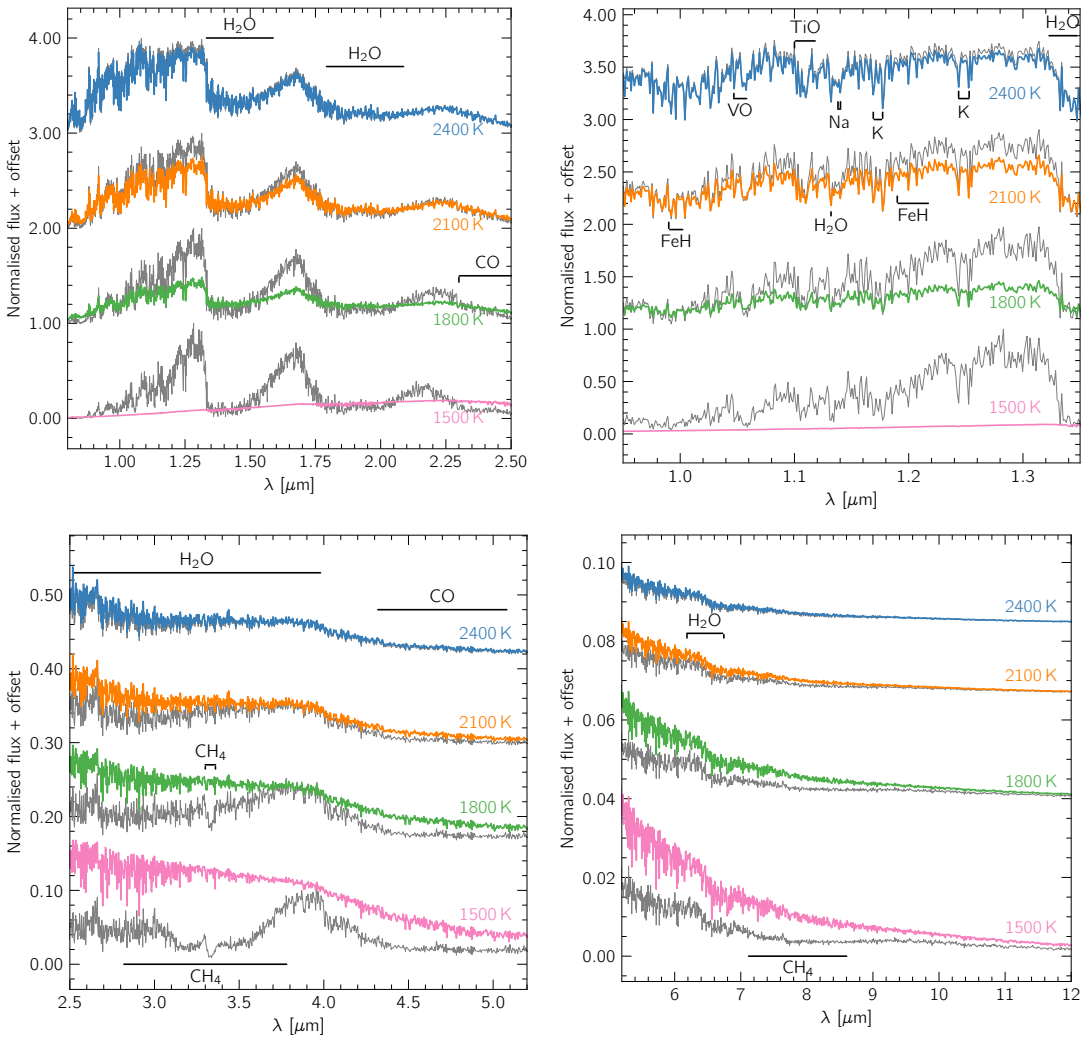

Figure 8.5: Synthetic spectra of MSG models with TiO_2 nucleation at $T_{\rm eff} = 2400\,{\rm K}$ (blue), 2100 K (orange), 1800 K (green) and 1500 K (pink), with $\log(g) = 4.0$, and the respective cloud-free spectra at the same $T_{\rm eff}$ and $\log(g)$ in grey. The emergent fluxes are normalised with respect to the cloud-free MARCS spectra, i.e. $F_{\rm norm}(\lambda) = (F_{\rm cloudy}(\lambda) - F^{\rm min}_{\rm cloud-free})/(F^{\rm max}_{\rm cloud-free} - F^{\rm min}_{\rm cloud-free})$, where $F_{\rm norm}$ is the normalised flux, $F_{\rm cloudy}$ the flux from the cloudy model, and $F^{\rm max,min}_{\rm cloud-free}$ the maximum and minimum fluxes from the cloud-free model within the full wavelength range considered ($\sim 0.4\,\mu$m - $20.0\,\mu$m). An arbitrary offset is added for clarity. In the top-left plots we show the near-infrared range, in the top-right the Y and J bands, in the bottom-left the mid-infrared and the bottom-right the thermal infrared. Important absorbers are respectively labelled.

8.5.4 Models with SiO nucleation

In this section, we investigate the effect of changing the CCN from TiO_2 to SiO in our self-consistent models. An in-depth investigation comparing TiO_2 to SiO nucleation with the DRIFT model was previously conducted by Lee et al. (2015). However, Lee et al. (2015) do this comparison by post-processing DRIFT on DRIFT-PHOENIX models (Witte et al., 2009). Here, we make this comparison using our full self-consistent algorithm and investigate the impact a different CCN has on the atmospheric $P_{\rm gas} - T_{\rm gas}$ structure, the cloud structure and the observables (spectra).

Fig. 8.6 (left) shows a comparison between the $P_{\rm gas} - T_{\rm gas}$ profile of a MSG cloudy model with TiO_2 nucleation (blue dashed curve) and one with SiO nucleation (orange solid curve), both at $T_{\rm eff}$=1500 K and $\log(g) = 4.0$. Similarly to the model with TiO_2 nucleation, there is a detached convective zone, which has its origin in the cloud's backwarming effect. Fig. 8.6 (middle) shows the average cloud particle size (solid curves) and the cloud particle number density (dashed curves) for the models shown in Fig. 8.6 (left). For the $P_{\rm gas} - T_{\rm gas}$ structures and cloud properties of models with SiO nucleation at other $T_{\rm eff}$'s, see Appendix 8.D.

If only nucleation processes are taken into account, SiO nucleation is more efficient than TiO_2 nucleation (Lee et al., 2015), and would therefore form more CCN overall. However, as discussed by Lee et al. (2015), we must consider other cloud formation processes, namely growth. This is because the elements Si and O are part of many silicate materials (e.g., SiO_2[s], $MgSiO_3$[s], Mg_2SiO_4[s]) that are already thermally stable and therefore grow efficiently as soon as the CCN form from the gas-phase. At pressures between $\sim 10^{-7}$ to 10^{-4} bar, the SiO nucleation is more efficient than the TiO_2 nucleation (see Fig. 8.6, right). However, as soon as other Si-bearing cloud species start growing, the growth processes dominate over the nucleation, and the nucleation rate drops drastically. On the other hand, when TiO_2 nucleation is considered, the nucleation process is fairly efficient, and the growth of the Ti-bearing cloud species never dominates over nucleation. The SiO nucleation model shows a larger cloud particle number density and smaller average cloud particle size than the TiO_2 nucleation model for pressures less than 10^{-3} bar where the SiO nucleation rate is higher than in the TiO_2 case (see Fig. 8.6, middle). Once the SiO nucleation rate drops, at pressures higher than $10^{-3.5}$ bar, the cloud particle number density becomes approximately constant as no new particles are created. In comparison, at 10^{-3} bar the cloud particle number density for the TiO_2 nucleation case becomes larger than the SiO case as the nucleation persists to deeper in the atmosphere. Consequently, the average cloud particle size increases in the SiO model compared to the TiO_2 nucleation model at these pressures. [1] This follows the principle of mass conservation: although there is less surface available for growth, the same amount of material condenses, and therefore, it must continue growing on top of the available surface, leading to larger cloud particles and smaller cloud particle number densities.

[1] We note the average cloud particle sizes obtained here are not comparable to those in Lee et al. (2015) as MSG is fully self-consistent, while Lee et al. (2015) do a post-processing.

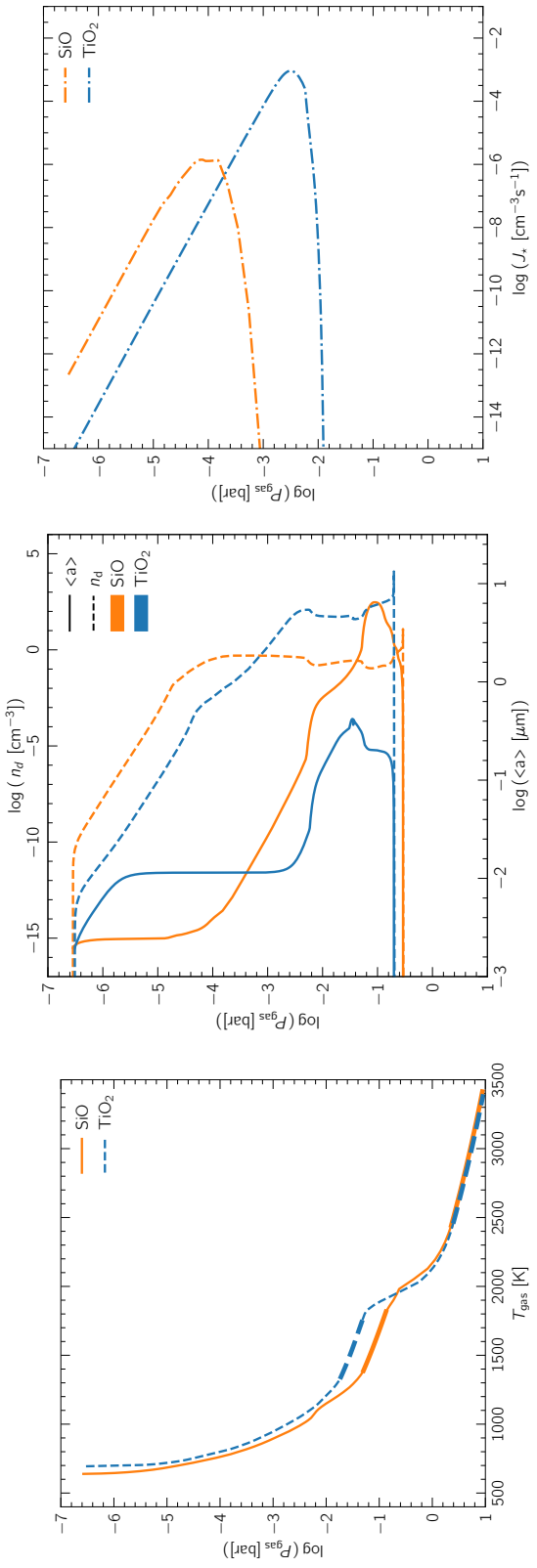

Figure 8.6: **Left:** Pressure-temperature profiles for MSG models at $T_{\rm eff}$= 1500 K and $\log(g) = 4.0$ with TiO_2 nucleation (blue dashed curve) and SiO nucleation (orange solid curve). Convective zones are plotted with thicker lines while radiative zones are plotted with thinner lines. **Middle:** The average cloud particle size (solid curves) and the cloud particle number density (dashed curves) for the models shown on the left. **Right:** The nucleation rates for MSG models at $T_{\rm eff}$ = 1500 K and $\log(g) = 4.0$ with TiO_2 nucleation (blue curve) and SiO nucleation (orange curve).

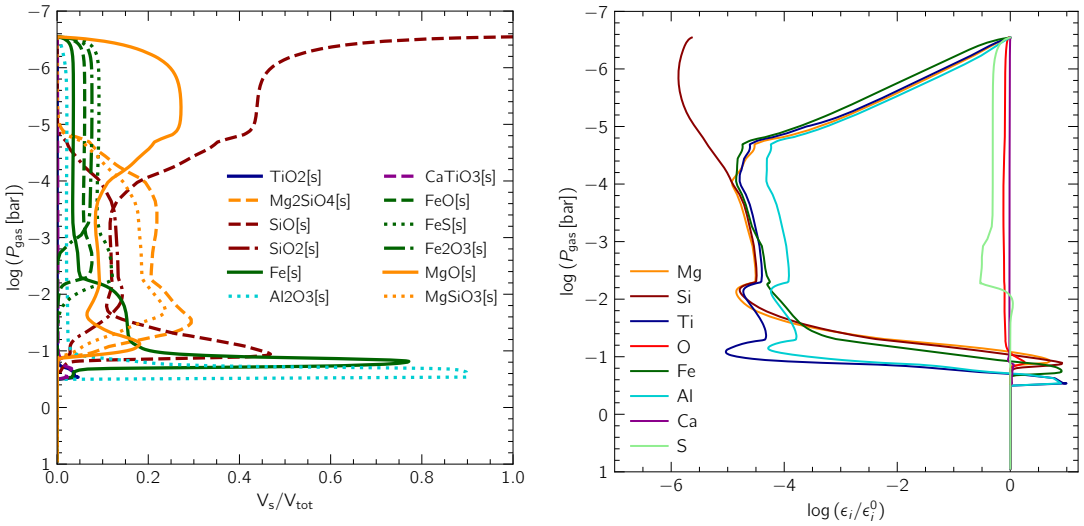

Figure 8.7: Composition of the cloud particles in units of volume fractions $V_s/V_{\rm tot}$ (left) and the relative gas-phase element depletions ϵ_i/ϵ_i^0 (right) for a MSG model with SiO nucleation, at 1500 K and $\log(g) = 4.0$.

Fig. 8.7 shows the cloud composition and the relative gas-phase element depletion along the atmosphere for the model with SiO nucleation at $T_{\rm eff} = 1500$ K and $\log(g) = 4.0$. The TOA has the largest difference in cloud composition between the TiO_2 nucleation models and the SiO nucleation models. In the TiO_2 models, right after TiO_2 nucleates at the TOA, other cloud species start growing and quickly the silicates dominate the cloud volume fraction from the very top down to approximately 0.05 bar where Fe_2O_3[s] and Al_2O_3[s] become the dominant cloud species (Fig. 8.4 left). In the SiO models, at the TOA, SiO[s] and MgO[s] are the dominant cloud species down until the growth of magnesium-silicates and SiO_2 starts dominating over nucleation at $\sim 10^{-4}$ bar. Between $\sim 10^{-4}$ bar and 0.1 bar, the silicates dominate the cloud volume fraction, down until Fe[s] and Al_2O_3[s] become the dominant species at the very cloud bottom (Fig. 8.7 left). Fig. 8.8 shows MSG cloudy and MARCS cloud-free spectra at different wavelength ranges, for the models with SiO nucleation, at $T_{\rm eff} = 1800$ K, 1500 K and 1200 K ($P_{\rm gas} - T_{\rm gas}$ profiles shown shown in Fig. 8.2). The spectra show visible differences from the TiO_2 nucleation model spectra (shown in Fig. 8.5) in all the wavelength regimes investigated. The SiO nucleation spectra are less red in the near-infrared (Fig. 8.8 top row). For example, although small at 1500 K, the absorption features of K and H_2O are still noticeable. In the mid-infrared (Fig. 8.8 bottom left), the emergent flux in the cloud-free spectra is stronger at around 4.0 μm than the emergent flux of the cloudy spectra.

As mentioned before, the SiO nucleation models have a larger average cloud particle size than the TiO_2 nucleation models. We expect the emission cross-section for magnesium-silicates to be larger for larger dust grain sizes (e.g. Min et al., 2004). This, combined with the reduced cloud particle number density, results in a different cloud opacity, which gives rise to the observed spectral changes, and

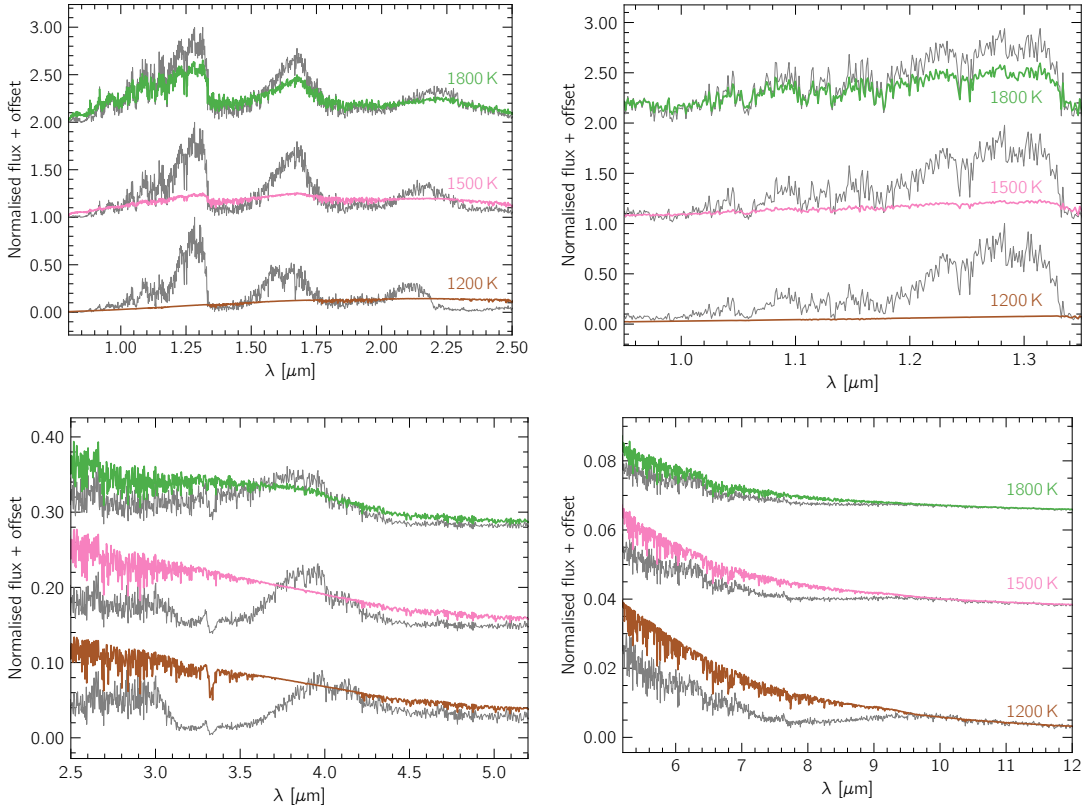

Figure 8.8: Synthetic spectra of MSG models with SiO nucleation at $T_{\rm eff} = 1800\,{\rm K}$ (green) and 1500 K (pink) and 1200 K (brown), with $\log(g) = 4.0$, and the respective cloud-free spectra at the same effective temperatures and $\log(g)$ in grey. The emergent fluxes are normalised with respect to the cloud-free MARCS spectra, and an arbitrary offset is added for clarity. In the top-left plots we show the near-infrared range, in the top-right the Y and J bands, in the bottom-left the mid-infrared and the bottom-right the thermal infrared. For a reference on the location of important absorbers see Fig. 8.5.

different $P_{\rm gas} - T_{\rm gas}$ structures (see Fig. 8.6, left). This is better visualised when we look at the location where the optical depth is equal to unity for each of the cases (see Fig. 8.9). In the near-infrared, the cloud continuum sits at lower pressures in the TiO_2 nucleation spectra (Fig. 8.9 top) compared to the SiO nucleation spectra (Fig. 8.9 bottom). In the mid-infrared, between $\sim 6\,\mu$m and $\sim 10\,\mu$m, there is a window with no cloud continuum in the TiO_2 nucleation spectra, while there is no window in the SiO nucleation spectra. This justifies the spectral differences we note between Fig. 8.5 and Fig. 8.8.

8.5.5 Mixing: the effect of decreasing the mixing efficiency

We explore our assumption and parameterisation of the mixing timescale (see Section 8.2, equations 8.9 and 8.12) by scaling the mixing timescale up, this is reducing the efficiency of the mixing. This means the replenishment of the upper atmosphere with the cloud-forming elements happens on a slower timescale. This parameterisation breaks the self-consistency, however we find this to be the most

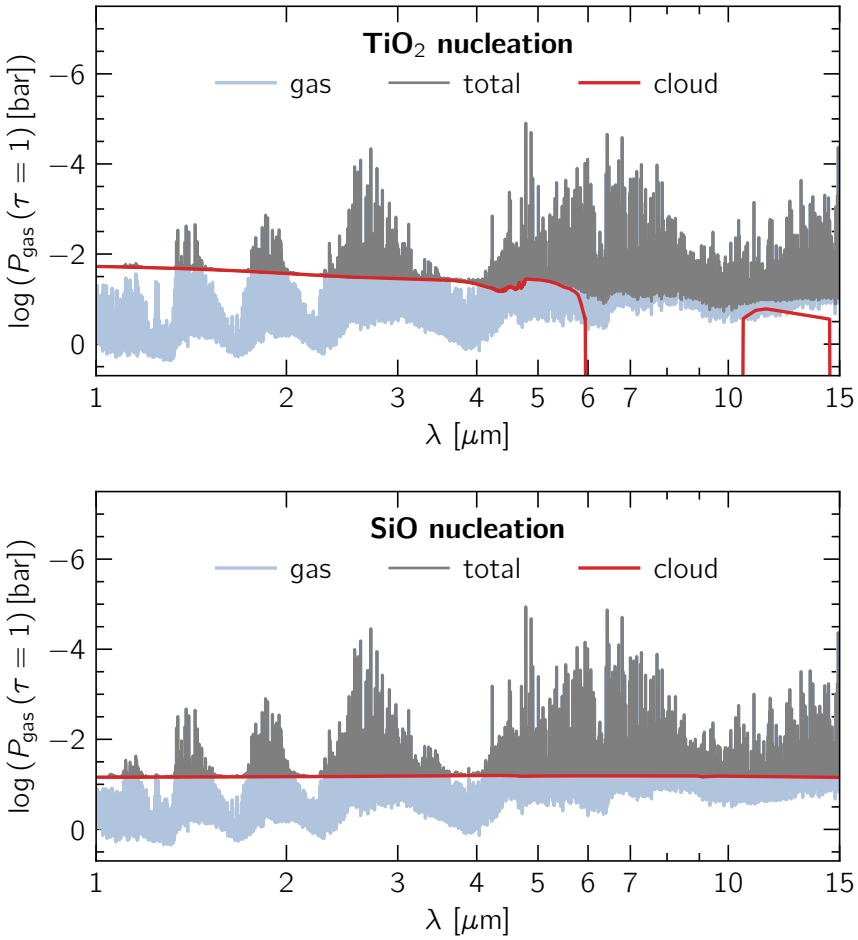

Figure 8.9: Gas pressure at optical depth of unity at different wavelengths, considering the gas opacity (light blue-grey curves), the cloud opacity (red curves) and the total contribution (gas+cloud, grey curves), for MSG models at $T_{\rm eff} = 1500\,{\rm K}$ and $\log(g) = 4.0$ with TiO_2 nucleation (top) and SiO nucleation (bottom).

reasonable manner to test our assumptions and see how a less efficient mixing would affect the atmosphere. Here we present the results for the models with SiO nucleation, however we note that the models with TiO_2 nucleation show the same trends and can be found in Appendix 8.F.

Fig. 8.10 shows the $P_{\rm gas} - T_{\rm gas}$ structures for the models with the less efficient mixing. Fig. 8.11 shows the average cloud particle size, the cloud particle number density and the nucleation rate with the different mixing efficiency scalings, at $T_{\rm eff} = 1500\,{\rm K}$ and $\log(g) = 4.0$. The nucleation rate was slower in the SiO nucleation models than in the TiO_2 models. Scaling the mixing efficiency down makes the nucleation less efficient, resulting in similar behaviour to the one seen in the SiO nucleation models compared to the TiO_2 nucleation ones (Section 8.5.4). At the TOA, the average cloud particle size is similar in all models with different mixing efficiencies. However, the nucleation rate is slower for the decreased mixing efficiencies, and therefore, the cloud particle number density is lower. Once

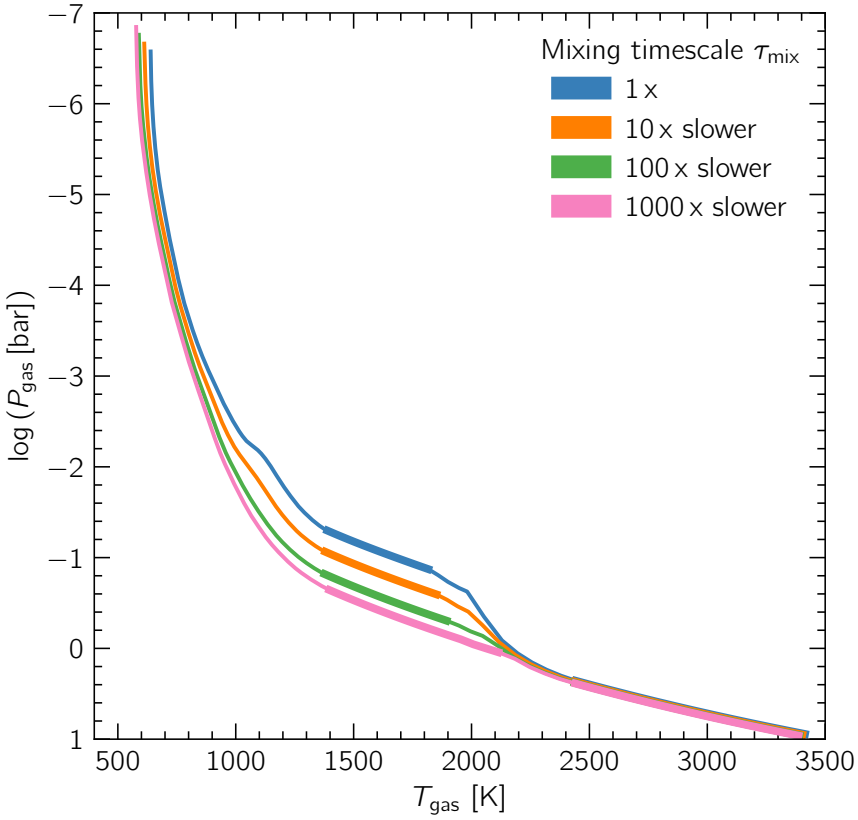

Figure 8.10: Pressure-temperature profiles for MSG models with SiO nucleation, at $T_{\rm eff} = 1500\,{\rm K}$ and $\log(g) = 4.0$, and different mixing timescale scalings (1x, 10x slower, 100x slower, 1000x slower). Convective zones are plotted with thicker lines while radiative zones are plotted with thinner lines.

growth processes start dominating, i.e. when the nucleation rate drops, the average cloud particle size increases. As there are fewer CCN available for the reduced mixing efficiency cases, the cloud particles grow to slightly larger sizes. For more efficient mixing, the point of stronger growth onset is higher in the atmosphere than for the less efficient mixing cases (see Fig. 8.11, left). As previously shown by Samra et al. (2023), more efficient mixing supports a higher cloud deck. The location of the cloud deck is also a consequence of the $P_{\rm gas} - T_{\rm gas}$ structure (see Fig. 8.10), which is hotter for more efficient mixing due to the different cloud and gas opacities (with the differences being caused by the change in average cloud particle size, cloud composition and gas-phase element abundances). For detailed figures of the average cloud composition and gas-phase element abundances see Appendix 8.E.

The effect of the scaling on the $P_{\rm gas} - T_{\rm gas}$ structure is similar to that of SiO nucleation models compared to the TiO_2 nucleation models (see Fig. 8.6 left). Between approximately 0.001 bar and 1 bar, the models with less efficient mixing are cooler overall.

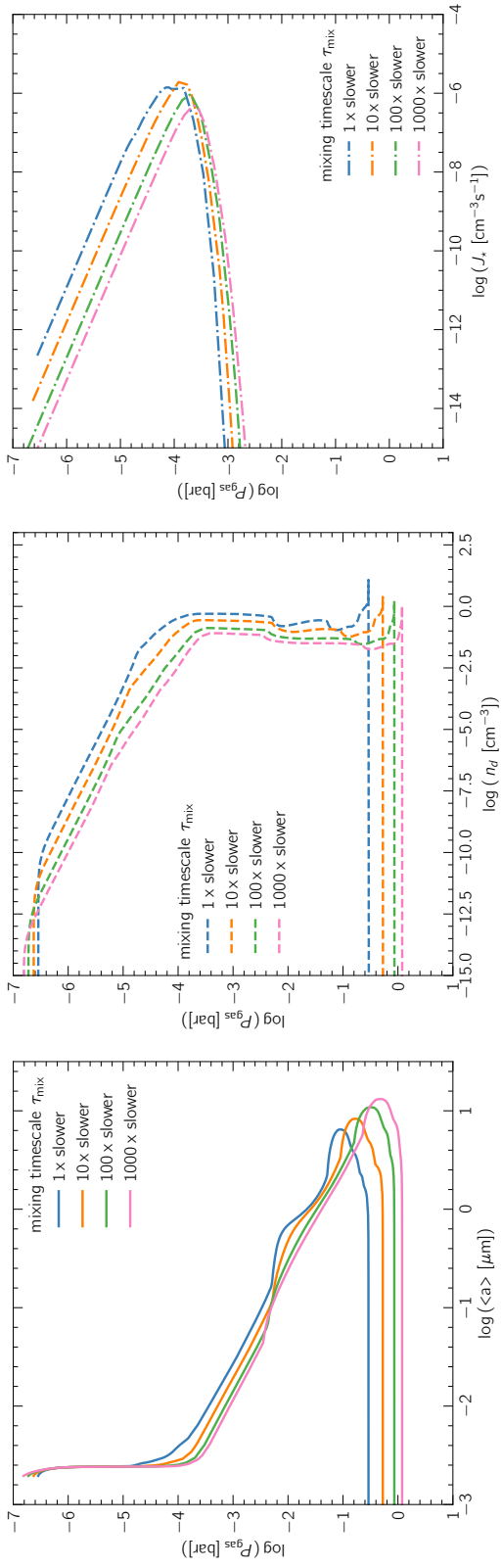

Figure 8.11: The average cloud particle size $\langle a \rangle$ (left), the cloud particle number density n_d (middle) and the nucleation rate $J_\star$ (right) along the atmosphere for models with SiO nucleation at $T_{\rm eff} = 1500\,$K and $\log(g) = 4.0$, and different mixing timescale scalings (1x, 10x slower, 100x slower, 1000x slower).

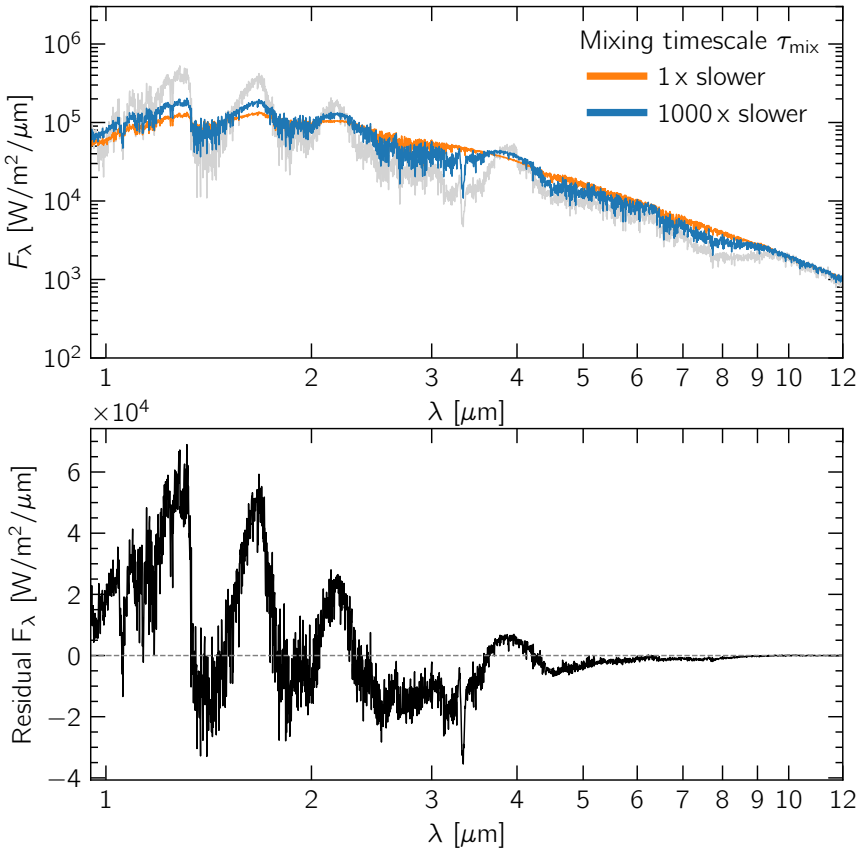

Figure 8.12: **Top:** Synthetic spectra of MSG cloudy models with SiO nucleation, at $T_{\rm eff} = 1500\,$K and $\log(g) = 4.0$. The orange spectrum shows the spectrum for a fully self-consistent MSG cloudy model. The blue spectrum shows the spectrum for a model where the mixing efficiency was scaled down by 1000 times. The spectrum in grey is that of a cloud-free MARCS model at the same $T_{\rm eff}$ and $\log(g)$. **Bottom:** The flux residual between the model with the mixing efficiency scaled down by 1000 times (blue) and the self-consistent model with no scaling (orange).

Fig. 8.12 (top) shows the spectrum resulting from scaling the mixing timescale up by 1000 times (blue), compared to the spectrum with no scaling (orange), and the spectrum of a MARCS cloud-free model at the same effective temperature and surface gravity (grey). We compute the residual flux between the scaled and the self-consistent model to better visualise the major spectral differences (Fig. 8.12 bottom).

Due to the increased average cloud particle size and the decreased cloud particle number density, the cloud opacity changes give rise to a less red spectrum in the near-infrared. This allows for the absorption by the alkali metals, Na and K, to be more prominent. Na and K have been regularly observed in brown dwarf atmospheres, and are important features to estimate a brown dwarf's surface gravity (e.g. McGovern et al., 2004; Allers and Liu, 2013; Martin et al., 2017). In addition to this, there is a significant difference in the mid-infrared, where CH_4 ($\sim 3.3\,\mu$m) and CO ($\sim 4.6\,\mu$m) absorption become visible compared to the

not scaled spectrum. Both CH_4 and CO have been consistently detected in L-dwarfs (e.g. Noll et al., 2000; Cushing et al., 2005; Beiler et al., 2023; Manjavacas et al., 2024; Biller et al., 2024). Therefore, the model with the increased mixing timescale will likely be a better match to observations. This also indicates that our understanding of the mixing is incomplete and we discuss the mixing treatment in more depth in Section 8.6.4.

8.6 Discussion

8.6.1 Convergence challenges of self-consistent brown dwarf models

Besides the convergence challenges we face when considering the cloud opacity in a self-consistent scheme (see Section 8.4.3), there are a number of other convergence challenges in our models.

In cloud-free MARCS models, we face challenges with convergence at effective temperatures between 1600 K and 1200 K due to so called "opacity cliffs" (Mukherjee et al., 2023). "Opacity cliffs" are regions where the gas opacity changes quickly with small changes in temperature or pressure. These cliffs are also seen in Rosseland mean opacities (Figure 2 in Freedman et al. (2008); Figure 3 in Freedman et al. (2014)). We note MARCS models are computed over a Rosseland optical depth scale. The cloud-free models at effective temperatures between 1600 K and 1200 K often end up oscillating between two temperature corrections of the same amplitude but with different signs. For these cloud-free cases, a given model is more likely to reach convergence if the applied temperature correction is both smaller than the current temperature oscillation, and larger than the convergence criteria applied. This works by introducing a temperature correction which breaks out of the oscillation. However, this does not seem to help in the MSG cloudy models case. Besides an "opacity cliff" due to the gas opacity, the cloud opacity also contributes to the cliff as it changes rapidly with pressure, especially at lower effective temperatures.

In addition, we face a challenge when computing the cloud opacities as the vertical scale in MARCS is different from that of DRIFT. Unless the input values are exactly the same, DRIFT never outputs the same pressure points because it computes the necessary atmospheric height steps within its numerical methods, meaning the number of atmospheric layers out of a DRIFT run is variable. On the other hand, the number of atmospheric layers in MARCS is fixed and defined on a Rosseland optical depth scale. This introduces non-ideal interpolation errors when interpolating the necessary DRIFT outputs to perform the Mie theory and EMT calculations. The major problem is rooted in the fact that due to the "opacity cliffs" mentioned above, a small change in pressure leads to a large change in the Rosseland optical depth. This is exacerbated at lower effective temperatures. Following this, the chosen points for the interpolation are almost always different in consecutive iterations. Although a Rosseland optical depth scale works well for hotter objects,

it is not the best choice for cooler objects where the cloud opacity has a large influence. In the future, it might be beneficial to switch this treatment in MARCS to use a scale in gas pressure, or use an already existent atmospheric model with the scale in gas pressure.

8.6.2 Detached convective zones, the L-T dwarf transition and brown dwarf spectroscopic variability

In both models with TiO_2 nucleation and SiO nucleation, detached convective zones appear for effective temperatures below 1600 K due to the cloud's back-warming effect. This is also observed in other model grids which consider cloud formation (e.g. Morley et al., 2024). In this work, as described at the end of Section 8.2, we set the mixing timescale $\tau_{\rm mix}$ at the detached convective layer to the value of $\tau_{\rm mix}$ at the top of the radiative zone just below. This assumption misses two important considerations: (1) we fail to consider the full motion of the gas due to convection, which can accelerate the element replenishment at the TOA; (2) we do not consider the cloud particles will be dragged by the moving gas elements.

Witte et al. (2011) test the addition of a convective motion term to the dust moment equations in some DRIFT-PHOENIX models. Essentially, they change the $\rho\, L_j/\tau_{\rm mix}$ term in Equation 8.1 to a term which allows for the consideration of the convective motion. Witte et al. (2011) find the resulting gas velocities exceed the typical settling velocity of cloud particles by several orders of magnitude. Following this, they expect that, at the cloud base, convection drives approximately half of the local cloud particles into the higher atmosphere, destroying the local cloud layer, while the remaining cloud particles are pushed into the deeper atmosphere, accelerating their evaporation process. In addition, the cloud particles driven into the upper atmosphere will continue to grow, reducing their settling timescale and returning to their initial altitude. Once they return to their initial altitude, if convection is still at play, the cycle repeats, leaving a 50% chance of pushing the cloud particles into the deeper atmosphere or driving them into the upper atmosphere. Due to this cycle, convection is thought to partially destroy the cloud. Comparing the DRIFT-PHOENIX models which consider the detached convective zone appropriately (Witte, 2011), versus the ones that ignore it (grid presented in Witte et al., 2009), the authors report a drop in the number of cloud particles in the detached convective zone models which stops a trend of reddening in the near-infrared. However, from effective temperatures below 1400 K, they find strong numerical oscillations in the model and struggle to find convergence.

As seen in the models presented in this work, clouds are a major source of opacity in the near-infrared. L dwarfs become redder as they cool to later spectral types likely due to the increasing cloud optical depth with lower effective temperatures (e.g. Allard et al., 2001; Marley et al., 2002; Tsuji, 2002).However, at the so-called L-T dwarf transition, at about effective temperatures of $\sim$ 1400 K, a major shift is observed in the near-infrared colour of brown dwarfs. The near-infrared colour quickly shifts from red to blue, and a significant brightening is observed in

the J band of early T dwarfs (e.g. Kirkpatrick, 2005). The physical mechanism which gives rise to this L-T transition is still highly debated. The sinking or disruption of clouds at the effective temperatures of this transition are two of the major mechanisms suggested in the literature. Burgasser et al. (2002) and Burrows et al. (2006) discussed convection as a potential disruption mechanism of clouds in brown dwarfs, and as the possible mechanism that gives rise to the L-T transition.

In addition to the L-T dwarf transition, large observational surveys have found high-amplitude spectroscopic variability to be ubiquitous across the entire L-T spectral sequence (Metchev et al., 2015; Vos et al., 2019, 2022; Liu et al., 2024). Clouds are also thought to be the primary cause of these observed variabilities. Tan and Showman (2019) investigated the short-time evolution of clouds and thermal structures driven by radiative cloud feedback in brown dwarfs and extrasolar giant planets with a simple time-dependent, self-consistent, 1D model. They find the radiative cloud feedback is able to drive spontaneous atmospheric variability in the temperature and cloud structures. The variability arises from a cloud cycle where the cloud thickness varies over time. They also find that cloud dissipation naturally arises from the cycle and that a detached convective layer generally exists at the cloud layer. This cloud-cycle found by Tan and Showman (2019) includes a period of cloud breaking, which as mentioned before, has been proposed as the potential mechanism for the origin of the L-T transition.

Other mechanisms that do not involve clouds have been proposed to explain the L-T transition and the observed variability. Tremblin et al. (2016, 2019) have proposed diabatic convection due to the instability of carbon chemistry in brown dwarf atmospheres as a potential mechanism which drives the L-T transition. Tremblin et al. (2020) find the spectroscopic variability from cloud opacity and temperature variations (driven by chemical instabilities) are degenerate. Several JWST proposals have been accepted to do follow-up observations on variable brown dwarfs to determine if the variability's origin is the clouds, chemical instabilities, or both (e.g. PI: Biller, B. Program ID: 2965; Biller et al., 2023).

In future work, we find it crucial to include the convective motion consideration in the dust moments equation in order to investigate if it is a plausible mechanism for the origin of the L-T transition in our model framework. It is necessary to understand if our control factor treatment of the cloud opacity (Section 8.4.3) would give rise to the same numerical oscillations found by Witte et al. (2011), or if there is a static solution, and if we are able to replicate the bluer near-infrared colours of early T-dwarfs. Although challenging, exploring the combined effect of chemical instabilities and microphysical cloud formation would be interesting.

8.6.3 Nucleation

The nucleation process is the first stage of cloud formation in a gas atmosphere. The process involves the formation of clusters of molecules growing through gas-gas reactions (Gail et al., 1984; Helling and Fomins, 2013). It is not always entirely

clear which species will nucleate efficiently to form CCN in a given astrophysical environment. Helling and Fomins (2013) describe that for an ideal candidate species, there is a balance between how abundant the constituent elements are, and the binding energies of the clusters. Several species have been proposed as possible nucleation species in astrophysical environments, including warm to hot substellar atmospheres. Some examples of the proposed nucleation species are TiO_2 (Jeong et al., 2000; Sindel et al., 2022), SiO (Gail et al., 2013; Bromley et al., 2016), Al_2O_3 (Lam et al., 2015; Gobrecht et al., 2022), and more recently vanadium oxides such as VO, VO_2, and V_2O_5 (Lecoq-Molinos et al., 2024). In colder exoplanet and brown dwarf atmospheres, other species such as salts (e.g. NaCl and KCl) or metal sulphides (e.g. ZnS) may nucleate (Lee et al., 2018; Gao and Benneke, 2018; Helling et al., 2021, 2023). Here we follow several previous works for hot Jupiter atmospheres (e.g. Helling and Woitke, 2006; Helling et al., 2019b, 2023) by choosing TiO_2 and SiO to act as nucleating species. We note the `DRIFT-PHOENIX` models (Helling et al., 2008b; Witte et al., 2009, 2011) use TiO_2 CCN.

While beyond the scope of this paper, Sindel et al. (2022) and Lecoq-Molinos et al. (2024) compare the difference between applying classical nucleation theory to non-classical nucleation theory for TiO_2 and V_2O_5, respectively. The differences between these methods are described within the studies (and references therein), and they show the nucleation rates differ by approximately 2 orders of magnitude for TiO_2 and approximately 15 orders of magnitude for V_2O_5. While these results do not include the competing growth process, which would limit the available elements for nucleation, they show that the result may be strongly sensitive to the treatment of nucleation, and that each nucleation species will have different behaviours. In addition to this, there is a lack of laboratory data at the temperatures of L/T dwarfs and hot Jupiters, data which is crucial for the computation of nucleation and growth rates, such as the surface energies of cloud species (e.g. Gao et al., 2018).

Therefore, there are a number of uncertainties in the modelling of nucleation processes in substellar atmospheres. So far, nucleation has not been observed in substellar atmospheres. However, spectral features of molecular clusters that may provide observational evidence of nucleation, are expected to be within the JWST/MIRI-LRS wavelength range (Sindel et al., 2023; Lecoq-Molinos et al., 2024). An observation of the ultra-hot Jupiter WASP-76 b to look for $(Al_2O_3)_N$ and $(TiO_2)_N$ clusters is currently scheduled as part of JWST Cycle 3 (PI: Baeyens, R. Program ID: 6045; Baeyens et al., 2024).

8.6.4 Mixing

Scaling of the mixing timescale in `DRIFT` has previously been applied in an attempt to improve the agreement with observations. Pre-JWST observations of the warm Saturn exoplanet WASP-96 b with VLT/FORS2 (Nikolov et al., 2018) revealed the Na I line at $\sim 0.6\,\mu$m with broad wings leading the authors to conclude they observe a cloud-free atmosphere. WASP-96 b is a JWST ERO target and

was observed with JWST NIRISS/SOSS (Pontoppidan et al., 2022; Radica et al., 2023; Taylor et al., 2023). Radica et al. (2023) and Taylor et al. (2023) find they do not require a grey cloud deck in their retrievals to match the observations. However, they have to include a Rayleigh scattering slope. Samra et al. (2023) predict condensate clouds in the atmosphere of WASP-96 b and find their DRIFT models predict a cloud top, which is inconsistent with the broadened Na I line seen in the VLT/FORS2 observations. To address this, Samra et al. (2023) scaled the mixing timescale, finding that increasing the mixing timescale by a factor of 100× shifts the cloud top to higher pressures of 0.01 bar, which is more consistent with observations.

In our mixing prescription, we assume there is element replenishment at the TOA from a reservoir in the deep atmosphere. We assume the elements are transported from this reservoir by convective mixing (see Section 8.2). However, we do not consider that these elements could take part in other cloud formation processes as they travel up the atmosphere (e.g. nucleation or growth). We could be overestimating the true mixing efficiency by not considering the possibility of these other processes happening. This is perhaps why our models with a scaled-up mixing timescale, and therefore less mixing efficiency, tend improve the agreement with observations.

Several other cloud models (e.g. Ackerman and Marley, 2001; Gao et al., 2018; Ormel and Min, 2019) assume the vertical mixing to be diffusive. This diffusive mixing is parameterised by the eddy diffusion coefficient K_{zz}, a coefficient which approximately encompasses a number of large-scale transport processes in substellar atmospheres, such as convection and atmospheric circulation. The estimation of K_{zz} often depends on the type of object being modelled. For example, in Morley et al. (2024) (following Ackerman and Marley, 2001), K_{zz} is calculated using mixing length theory while also considering the energy transported by radiation. Overall, K_{zz} is often used to describe different types of transport, and it can be difficult to pinpoint the physics that it truly probes.

Woitke et al. (2020) combine the dust moment method with diffusive mixing (the DIFFU_DRIFT model). However, they do not find a static solution for the system of equations to be solved. They solve the time-dependent equations until the model relaxes towards a time-independent solution. Woitke et al. (2020) find fewer and larger cloud particles, with a higher concentration of cloud particles closer to the cloud base, are expected within this framework compared to DRIFT. They reason that this occurs as diffusive mixing is less efficient at transporting elements to the upper atmosphere layers compared to the relaxation scheme used in DRIFT. Consequently, the elements interact at the cloud base causing particle growth, rather than being transported unhindered to the upper layers. Furthermore, Woitke et al. (2020) find that Mg_2SiO_4[s] is the dominant condensed silicate in the deep silicate cloud layer. This is similar to the models presented here which show Mg_2SiO_4[s] as the major silicate (see Figs. 8.4 and 8.7). However, Woitke et al. (2020) show that $MgSiO_3$[s] is not the next dominant Si-bearing species; instead, the formation of SiO[s] and SiO_2[s] is favoured. Recent transmission observations with JWST

of the exoplanet WASP-17 b (Grant et al., 2023) have indicated the presence of crystalline SiO_2[s] through the detection of the $\sim 10\,\mu$m silicate features. Additionally, Dyrek et al. (2024) used the ARCiS framework (Ormel and Min, 2019; Min et al., 2020) to retrieve silicate dominated clouds (including SiO[s], SiO_2[s], and $MgSiO_3$[s]) to be present in the atmosphere of WASP-107 b. Unfortunately, it is not computationally feasible to self-consistently combine such a time-dependent model with MARCS.

Overall, whether one uses the mixing prescription of DRIFT or K_{zz}, it is difficult to constrain the physics of the mixing, and this will likely remain an uncertain parameter within 1D self-consistent cloudy models like the ones presented here.

8.6.5 Silicate cloud features

If silicate clouds are present in brown dwarf atmospheres, they are expected to show a significant absorption feature at about $10\,\mu$m. Suárez and Metchev (2022) presented an analysis of *Spitzer* mid-infrared spectra of 113 field M5-T9 dwarfs. They find silicate absorption starts to appear at the L2 spectral type, is strongest in L4-L6 dwarfs, and disappears past L8 dwarfs. Nevertheless, the silicate absorption feature is not ubiquitous and can be missing at any L sub-type. More recently, a silicate absorption feature was detected in the planetary mass companion VHS 1256 b with JWST/MIRI-MRS (Miles et al., 2023; Petrus et al., 2024).

In the models presented here, we do not see a silicate absorption feature at $10\,\mu$m. We argue that a possible reason for this is that we do not consider a particle size distribution function. We currently only use the average cloud particle size in the cloud opacity calculation. This misses any potential particle size distribution, which could change the spectral feature of the silicate absorption (e.g. Powell et al., 2018). Min et al. (2004), and more recently Luna and Morley (2021), show how smaller cloud particles ($\sim 0.1-1.0\,\mu m$) have a more outstanding silicate absorption feature around $10\,\mu$m. Luna and Morley (2021) also found the crystallinity of the cloud particles can highly influence the shape of the silicate absorption feature. In this paper, we assume Mg_2SiO_4[s], $MgSiO_3$[s] and SiO_2[s] to be amorphous. However, MSG models considering these condensates to be crystalline should be computed in the future to make a comparison of their spectral in-print.

Using the microphysical cloud model CARMA, which is based on a bin-scheme, Powell et al. (2018) find the particle size distributions in hot Jupiters are often bimodal. In the future, different particle size distribution functions should be considered in the MSG framework when computing the cloud opacity to evaluate if the silicate feature can be replicated in this manner.

8.7 Summary

We have presented a new grid of MSG cloudy substellar model atmospheres at effective temperatures between 2500 K and 1200 K and at a surface gravity of $\log(g) = 4.0$. We have presented a new convergence algorithm for the coupling of

MARCS to DRIFT in comparison to the grid presented in Juncher et al. (2017). The new algorithm is based on a control factor that controls the change in cloud opacity and the gas-phase element abundances to avoid unwanted numerical oscillations. We present pressure-temperature profiles, cloud properties including the cloud composition along the atmosphere and the average cloud particle sizes, and model spectra.

Our models, which consider TiO_2 nucleation, show spectra that are significantly redder in the near-infrared than the currently known population of substellar atmospheres. We have explored the effect of changing the CCN from TiO_2 to SiO. Changing the CCN to SiO makes the spectra appear less red in the near-infrared. Additionally, we investigated the effect of making the atmospheric mixing less efficient. The models with reduced mixing also appear less red in the near-infrared. Overall, our models present a strong cloud continuum which does not match observations.

We find detached convective zones in models at effective temperatures below or equal to 1600 K. The detached convective zone originates from the backwarming effect by the cloud particles. The mixing treatment we use does not consider the effect of the convection motion on the cloud particles. We propose that it is crucial to consider the convective motion in future work. This is because it has been argued the L-T transition can have its origin in cloud clearing caused by such a convective motion (Burgasser et al., 2002; Burrows et al., 2006).

Our models do not present the expected silicate absorption feature in the mid-infrared between 9 and 11 μm. We argue this is because we do not take into consideration a cloud particle size distribution. It has been shown that smaller cloud particles present a more prominent silicate absorption feature (Min et al., 2004; Luna and Morley, 2021). The crystallinity of the particles can also have an influence on their absorption spectra (Luna and Morley, 2021). We propose that it is necessary to include a particle size distribution function in future MDG cloudy model grids.

Acknowledgements

We are grateful to Peter Woitke, Dominic Samra and Helena Lecoq-Molinos for interesting discussions. BCE, ChH, FAM and UGJ are part of the CHAMELEON MC ITN EJD which received funding from the European Union's Horizon 2020 research and innovation programme under the Marie Sklodowska-Curie grant agreement no. 860470. DAL acknowledges financial support from the Austrian Academy of Sciences. UGJ acknowledges funding from the Novo Nordisk Foundation Interdisciplinary Synergy Programme grant no.1716 NNF19OC0057374. The Tycho supercomputer hosted at the SCIENCE HPC center at the University of Copenhagen was used for supporting this work.

8.A Continuum opacity sources and molecular & atomic line lists references

Table 8.1: Continuum opacity data sources.

Ion	Process	Reference
H^-	b-f	Doughty et al. (1966)
H^-	f-f	Doughty and Fraser (1966)
H I	b-f, f-f	Karzas and Latter (1961)
H I+H I	CIA	Doyle (1968)
H_2^-	f-f	Somerville (1964)
H_2^+	f-f	Mihalas (1965)
He^-	f-f	Somerville (1965), John (1967)
He I	f-f	Peach (1970)
C I	f-f	Peach (1970)
Mg I	f-f	Peach (1970)
Al I	f-f	Peach (1970)
Si I	f-f	Peach (1970)
e^-	scattering	Mihalas (1978)
H_2	scattering	Dalgarno and Williams (1962)

Bound-free processes are denoted by b-f. Free-free processes are denoted by f-f. Collision induced absorption processes are denoted by CIA.

Table 8.2: Molecular and atomic line lists data sources.

Molecule/atom	Reference	Molecule/atom	Reference
AlCl	Yousefi and Bernath (2018)	MgH	GharibNezhad et al. (2013)
AlH	Yurchenko et al. (2018d)	NaCl	Barton et al. (2014)
AlO	Patrascu et al. (2015)	NaH	Rivlin et al. (2015)
C_2	Yurchenko et al. (2018c)	NH	Brooke et al. (2014a, 2015); Fernando et al. (2018)
CaH	Owens et al. (2022)	NH_3	Coles et al. (2019)
CH	Masseron et al. (2014)	NO	Hargreaves et al. (2019)
CH_4	Yurchenko et al. (2017)	NS	Yurchenko et al. (2018a)
CN	Brooke et al. (2014b)	OH	Brooke et al. (2016); Yousefi et al. (2018)
CO	Li et al. (2015)	SiH	Yurchenko et al. (2018b)
CO_2	Yurchenko et al. (2020)	SiO	Yurchenko et al. (2022)
CS	Paulose et al. (2015)	SiS	Upadhyay et al. (2018)
FeH	Wende et al. (2010)	SH	Gorman et al. (2019)
H_2CO	Al-Refaie et al. (2015)	SO_2	Underwood et al. (2016)
H_2O	Polyansky et al. (2018)	TiH	Burrows et al. (2005)
HCN	Barber et al. (2014)	TiO	McKemmish et al. (2019)
KCl	Barton et al. (2014)	VO	McKemmish et al. (2016)
LiCl	Bittner and Bernath (2018)	Na	Allard et al. (2019)
LiH	Coppola et al. (2011)	K	Allard et al. (2019)

8.B Chemical surface reactions assumed to form the cloud particles

Table 8.3: Chemical surface reactions r assumed to form the solid materials s.

Index r	Solid s	Surface reaction	Key species
1	TiO_2[s]	$TiO_2 \longrightarrow TiO_2$[s]	TiO_2
2	rutile	$Ti + 2\ H_2O \longrightarrow TiO_2$[s] $+ 2\ H_2$	Ti
3	(1)	$TiO + H_2O \longrightarrow TiO_2$[s] $+ H_2$	TiO
4		$TiS + 2\ H_2O \longrightarrow TiO_2$[s] $+ H_2S + H_2$	TiS
5	SiO_2[s]	$SiH + 2\ H_2O \longrightarrow SiO_2$[s] $+ 2\ H_2 + H$	SiH
6	silica	$SiO + H_2O \longrightarrow SiO_2$[s] $+ H_2$	SiO
7	(3)	$SiS + 2\ H_2O \longrightarrow SiO_2$[s] $+ H_2S + H_2$	SiS
8	SiO[s]	$SiO \longrightarrow$ SiO[s]	SiO
9	silicon mono-oxide	$2\ SiH + 2\ H_2O \longrightarrow 2$ SiO[s] $+ 3\ H_2$	SiH
10	(2)	$SiS + H_2O \longrightarrow$ SiO[s] $+ H_2S$	SiS
11	Fe[s]	$Fe \longrightarrow$ Fe[s]	Fe
12	solid iron	$FeO + H_2 \longrightarrow$ Fe[s] $+ H_2O$	FeO
13	(1)	$FeS + H_2 \longrightarrow$ Fe[s] $+ H_2S$	FeS
14		$Fe(OH)_2 + H_2 \longrightarrow$ Fe[s] $+ 2\ H_2O$	$Fe(OH)_2$
15		$2\ FeH \longrightarrow 2$ Fe[s] $+ H_2$	FeH
16	FeO[s]	$FeO \longrightarrow$ FeO[s]	FeO
17	iron (II) oxide	$Fe + H_2O \longrightarrow$ FeO[s] $+ H_2$	Fe
18	(3)	$FeS + H_2O \longrightarrow$ FeO[s] $+ H_2S$	FeS
19		$Fe(OH)_2 \longrightarrow$ FeO[s] $+ H_2$	$Fe(OH)_2$
20		$2\ FeH + 2\ H_2O \longrightarrow 2$ FeO[s] $+ 3\ H_2$	FeH
21	FeS[s]	$FeS \longrightarrow$ FeS[s]	FeS
22	iron sulphide	$Fe + H_2S \longrightarrow$ FeS[s] $+ H_2$	Fe
23	(3)	$FeO + H_2S \longrightarrow$ FeS[s] $+ H_2O$	min{FeO, H_2S}
24		$Fe(OH)_2 + H_2S \longrightarrow$ FeS[s] $+ 2\ H_2O$	min{$Fe(OH)_2$, H_2S}
25		$2\ FeH + 2\ H_2S \longrightarrow 2$ FeS[s] $+ 3\ H_2$	min{FeH, H_2S}
26	Fe_2O_3[s]	$2\ Fe + 3\ H_2O \longrightarrow Fe_2O_3$[s] $+ 3\ H_2$	$\frac{1}{2}$Fe
27	iron (III) oxide	$2\ FeO + H_2O \longrightarrow Fe_2O_3$[s] $+ H_2$	$\frac{1}{2}$FeO
28	(3)	$2\ FeS + 3\ H_2O \longrightarrow Fe_2O_3$[s] $+ 2\ H_2S + H_2$	$\frac{1}{2}$FeS
29		$2\ Fe(OH)_2 \longrightarrow Fe_2O_3$[s] $+ H_2O + H_2$	$\frac{1}{2}Fe(OH)_2$
30		$2\ FeH + 3\ H_2O \longrightarrow Fe_2O_3$[s] $+ 4\ H_2$	$\frac{1}{2}$FeH
31	MgO[s]	$Mg + H_2O \longrightarrow$ MgO[s] $+ H_2$	Mg
32	periclase	$2\ MgH + 2\ H_2O \longrightarrow 2$ MgO[s] $+ 3\ H_2$	$\frac{1}{2}$MgH
33	(3)	$2\ MgOH \longrightarrow 2$ MgO[s] $+ H_2$	$\frac{1}{2}$MgOH
34		$Mg(OH)_2 \longrightarrow$ MgO[s] $+ H_2O$	$Mg(OH)_2$

The efficiency of the reaction is limited by the collision rate of the key species, which has the lowest abundance among the reactants. The notation $\frac{1}{2}$ in the r.h.s. column means that only every second collision (and sticking) event initiates one reaction. Data sources for the supersaturation ratios (and saturation vapor pressures): (1) Helling and Woitke (2006); (2) Nuth and Ferguson (2006); (3) Sharp and Huebner (1990).

Table 8.4: Table 8.3 continued

Index r	Solid s	Surface reaction	Key species
35	$MgSiO_3$[s]	$Mg + SiO + 2\ H_2O \longrightarrow MgSiO_3$[s] $+ H_2$	min{Mg, SiO}
36	enstatite	$Mg + SiS + 3\ H_2O \longrightarrow MgSiO_3$[s] $+ H_2S + 2\ H_2$	min{Mg, SiS}
37	(3)	$2\ Mg + 2\ SiH + 6\ H_2O \longrightarrow 2\ MgSiO_3$[s] $+ 7\ H_2$	min{Mg, SiH}
38		$2\ MgOH + 2\ SiO + 2\ H_2O \longrightarrow 2\ MgSiO_3$[s] $+ 3\ H_2$	min{$\frac{1}{2}$MgOH, $\frac{1}{2}$SiO}
39		$2\ MgOH + 2\ SiS + 4\ H_2O \longrightarrow 2\ MgSiO_3$[s] $+ 2\ H_2S + 3\ H_2$	min{$\frac{1}{2}$MgOH, $\frac{1}{2}$SiS}
40		$MgOH + SiH + 2\ H_2O \longrightarrow MgSiO_3$[s] $+ 3\ H_2$	min{$\frac{1}{2}$MgOH, $\frac{1}{2}$SiH}
41		$Mg(OH)_2 + SiO \longrightarrow 2\ MgSiO_3$[s] $+ H_2$	min{$Mg(OH)_2$, SiO}
42		$Mg(OH)_2 + SiS + H_2O \longrightarrow MgSiO_3$[s] $+ H_2S + H_2$	min{$Mg(OH)_2$, SiS}
43		$2\ Mg(OH)_2 + 2\ SiH + 2\ H_2O \longrightarrow 2\ MgSiO_3$[s] $+ 5\ H_2$	min{$Mg(OH)_2$, SiH}
44		$2\ MgH + 2\ SiO + 4\ H_2O \longrightarrow 2\ MgSiO_3$[s] $+ 5\ H_2$	min{MgH, SiO}
45		$2\ MgH + 2\ SiS + 6\ H_2O \longrightarrow 2\ MgSiO_3$[s] $+ 2\ H_2S + 5\ H_2$	min{MgH, SiS}
46		$MgH + SiH + 3\ H_2O \longrightarrow MgSiO_3$[s] $+ 4\ H_2$	min{MgH, SiH}
47	Mg_2SiO_4[s]	$2\ Mg + SiO + 3\ H_2O \longrightarrow Mg_2SiO_4$[s] $+ 3\ H_2$	min{$\frac{1}{2}$Mg, SiO}
48	forsterite	$2\ MgOH + SiO + H_2O \longrightarrow Mg_2SiO_4$[s] $+ 2\ H_2$	min{$\frac{1}{2}$MgOH, SiO}
49	(3)	$2\ Mg(OH)_2 + SiO \longrightarrow Mg_2SiO_4$[s] $+ H_2O + H_2$	min{$\frac{1}{2}$$Mg(OH)_2$, SiO}
50		$2\ MgH + SiO + 3\ H_2O \longrightarrow Mg_2SiO_4$[s] $+ 4\ H_2$	min{$\frac{1}{2}$MgH, SiO}
51		$2\ Mg + SiS + 4\ H_2O \longrightarrow Mg_2SiO_4$[s] $+ H_2S + 3\ H_2$	min{$\frac{1}{2}$Mg, SiS}
52		$2\ MgOH + SiS + 2\ H_2O \longrightarrow Mg_2SiO_4$[s] $+ H_2S + 2\ H_2$	min{$\frac{1}{2}$MgOH, SiS}
53		$2\ Mg(OH)_2 + SiS \longrightarrow Mg_2SiO_4$[s] $+ H_2 + H_2S$	min{$\frac{1}{2}$$Mg(OH)_2$, SiS}
54		$2\ MgH + SiS + 4\ H_2O \longrightarrow Mg_2SiO_4$[s] $+ H_2S + 4\ H_2$	min{$\frac{1}{2}$MgH, SiS}
55		$4\ Mg + 2\ SiH + 8\ H_2O \longrightarrow 2\ Mg_2SiO_4$[s] $+ 9\ H_2$	min{$\frac{1}{2}$Mg, SiH}
56		$4\ MgOH + 2\ SiH + 4\ H_2O \longrightarrow 2\ Mg_2SiO_4$[s] $+ 7\ H_2$	min{$\frac{1}{2}$MgOH, SiH}
57		$4\ Mg(OH)_2 + 2\ SiH \longrightarrow 2\ Mg_2SiO_4$[s] $+ 5\ H_2$	min{$\frac{1}{2}$$Mg(OH)_2$, SiH}
58		$4\ MgH + 2\ SiH + 8\ H_2O \longrightarrow 2\ Mg_2SiO_4$[s] $+ 11\ H_2$	min{$\frac{1}{2}$MgH, SiS}
59	Al_2O_3[s]	$2\ Al + 3\ H_2O \longrightarrow Al_2O_3$[s] $+ 3\ H_2$	$\frac{1}{2}$Al
60	aluminia	$2\ AlOH + H_2O \longrightarrow Al_2O_3$[s] $+ 2\ H_2$	$\frac{1}{2}$AlOH
61	(3)	$2\ AlH + 3\ H_2O \longrightarrow Al_2O_3$[s] $+ 4\ H_2$	$\frac{1}{2}$AlH
62		$Al_2O + 2\ H_2O \longrightarrow Al_2O_3$[s] $+ 2\ H_2$	Al_2O
63		$2\ AlO_2H \longrightarrow Al_2O_3$[s] $+ H_2O$	$\frac{1}{2}$$AlO_2H$
64	$CaTiO_3$[s]	$Ca + Ti + 3\ H_2O \longrightarrow CaTiO_3$[s] $+ 3\ H_2$	min{Ca, Ti}
65	perovskite	$Ca + TiO + 2\ H_2O \longrightarrow CaTiO_3$[s] $+ 2\ H_2$	min{Ca, TiO}
66	(3)	$Ca + TiO_2 + H_2O \longrightarrow CaTiO_3$[s] $+ H_2$	min{Ca, TiO_2}
67		$Ca + TiS + 3\ H_2O \longrightarrow CaTiO_3$[s] $+ H_2S + 2\ H_2$	min{Ca, TiS}
68		$CaO + Ti + 2\ H_2O \longrightarrow CaTiO_3$[s] $+ 2\ H_2$	min{CaO, Ti}
69		$CaO + TiO + H_2O \longrightarrow CaTiO_3$[s] $+ H_2$	min{CaO, TiO}
70		$CaO + TiO_2 \longrightarrow CaTiO_3$[s]	min{CaO, TiO_2}
71		$CaO + TiS + 2\ H_2O \longrightarrow CaTiO_3$[s] $+ H_2S + H_2$	min{CaO, TiO}
72		$CaS + Ti + 3\ H_2O \longrightarrow CaTiO_3$[s] $+ H_2S + H_2$	min{CaS, Ti}
73		$CaS + TiO + 2\ H_2O \longrightarrow CaTiO_3$[s] $+ H_2S + 2\ H_2$	min{CaS, TiO}
74		$CaS + TiO_2 + H_2O \longrightarrow CaTiO_3$[s] $+ H_2S$	min{CaS, TiO_2}
75		$CaS + TiS + 3\ H_2O \longrightarrow CaTiO_3$[s] $+ 2\ H_2S + H_2$	min{CaS, TiO}
76		$Ca(OH)_2 + Ti + H_2O \longrightarrow CaTiO_3$[s] $+ 2\ H_2$	min{$Ca(OH)_2$, Ti}
77		$Ca(OH)_2 + TiO \longrightarrow CaTiO_3$[s] $+ H_2$	min{$Ca(OH)_2$, TiO}
78		$Ca(OH)_2 + TiO_2 \longrightarrow CaTiO_3$[s] $+ H_2O$	min{$Ca(OH)_2$, TiO_2}
79		$Ca(OH)_2 + TiS + H_2O \longrightarrow CaTiO_3$[s] $+ H_2S + H_2$	min{$Ca(OH)_2$, TiO}
80		$2\ CaH + 2\ Ti + 6\ H_2O \longrightarrow 2\ CaTiO_3$[s] $+ 7\ H_2$	min{CaH, Ti}
81		$2\ CaH + 2\ TiO + 4\ H_2O \longrightarrow 2\ CaTiO_3$[s] $+ 5\ H_2$	min{CaH, TiO}
82		$2\ CaH + 2\ TiO_2 + 2\ H_2O \longrightarrow 2\ CaTiO_3$[s] $+ 3\ H_2$	min{CaH, TiO_2 }
83		$2\ CaH + 2\ TiS + 6\ H_2O \longrightarrow 2\ CaTiO_3$[s] $+ 2\ H_2S + 5\ H_2$	min{CaH, TiS}
84		$2\ CaOH + 2\ Ti + 4\ H_2O \longrightarrow 2\ CaTiO_3$[s] $+ 5\ H_2$	min{CaOH, Ti}
85		$2\ CaOH + 2\ TiO + 2\ H_2O \longrightarrow 2\ CaTiO_3$[s] $+ 3\ H_2$	min{CaOH, TiO}
86		$2\ CaOH + 2\ TiO_2 \longrightarrow 2\ CaTiO_3$[s] $+ H_2$	min{CaOH, TiO_2 }
87		$2\ CaOH + 2\ TiS + 4\ H_2O \longrightarrow 2\ CaTiO_3$[s] $+ 2\ H_2S + 3\ H_2$	min{CaOH, TiS}

8.C Dust optical constants data references

Table 8.5: Dust optical data sources. For details on the wavelength ranges please refer to Table 1 in Kitzmann and Heng (2018).

Condensate	Reference
Al_2O_3 [s]	Begemann et al. (1997)^{*t}; Koike et al. (1995b)^{t}
$CaTiO_3$[s]	Posch et al. (2003)^{t}; Ueda et al. (1998)^{f}
Fe[s]	Lynch & Hunter in Palik (1991)^{t}
Fe_2O_3[s]	A.H.M.J. Triaud^{*t}
FeO[s]	Henning et al. (1995)^{*t}
FeS[s]	Pollack et al. (1994)^{t}; Henning and Mutschke (1997)^{t}
Mg_2SiO_4[s]	Jäger et al. (2003)^{*t}
$MgSiO_3$[s]	Jäger et al. (2003)^{*t}
MgO[s]	Roessler & Huffman in Palik (1991)^{t}
SiO[s]	Philipp in Palik (1985)^{t}
SiO_2 [s]	Henning and Mutschke (1997)^{*t}; Philipp in Palik (1985)^{t}
TiO_2 [s]	Zeidler et al. (2011b)^{*t}; Posch et al. (2003)^{*t}

We note we use the amorphous (sol-gel) data for Mg_2SiO_4[s] and $MgSiO_3$[s], and the amorphous data for SiO_2[s].
*Data from the Database of Optical Constants for Cosmic Dust, Laboratory Astrophysics Group of the AIU Jena.
^{t}Data from a printed or digital table.
^{f}Data from a figure.

8.D Models with SiO nucleation

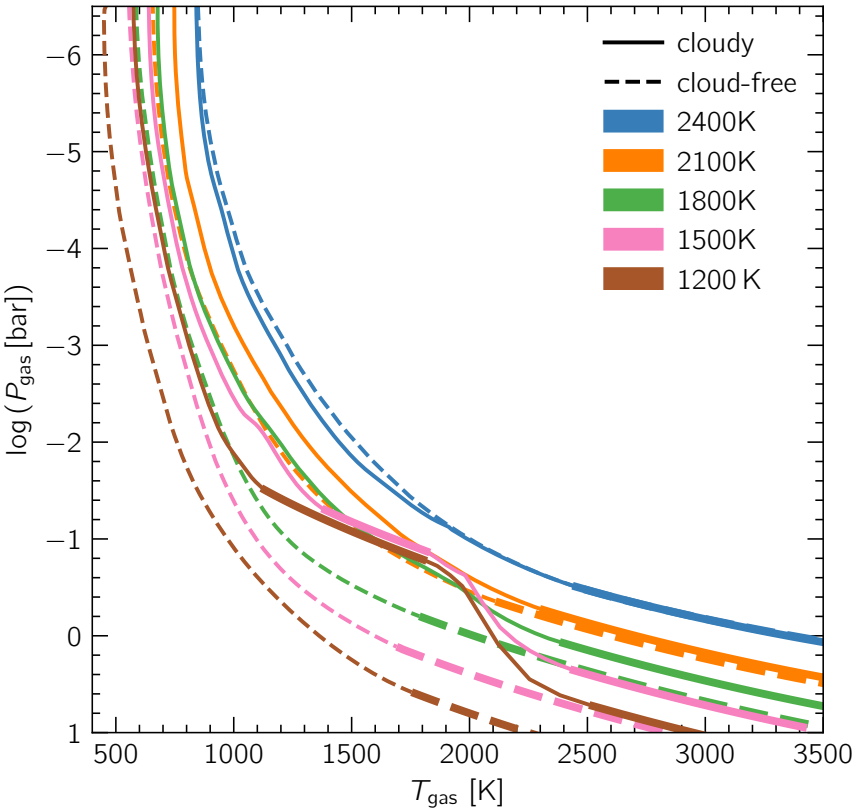

Figure 8.13: Pressure-temperature profiles for cloud-free MARCS models (dashed curves) and cloudy MSG models with SiO nucleation (solid curves), at different effective temperatures and $\log(g) = 4.0$. Convective zones are plotted with thicker lines while radiative zones are plotted with thinner lines.

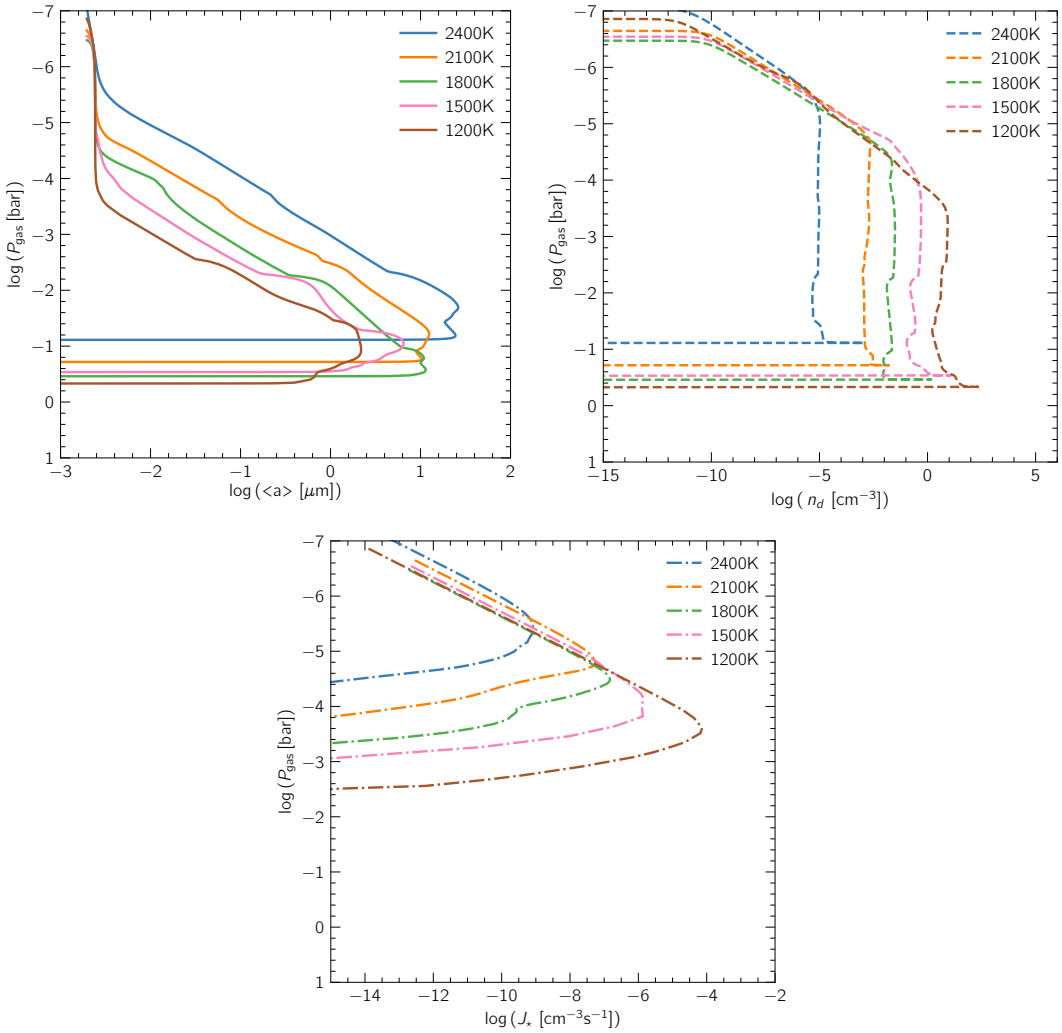

Figure 8.14: The average cloud particle size $\langle a \rangle$ (top left), the cloud particle number density n_d (top right) and the nucleation rate $J_\star$ (bottom) along the atmosphere for models with SiO nucleation at $T_{\rm eff}$ = 2400 K, 2100 K, 1800 K, 1500 K and 1200 K and $\log(g) = 4.0$. The corresponding $P_{\rm gas} - T_{\rm gas}$ profiles are shown in Fig. 8.13.

8.E The effect of decreasing the mixing efficiency - models with SiO nucleation

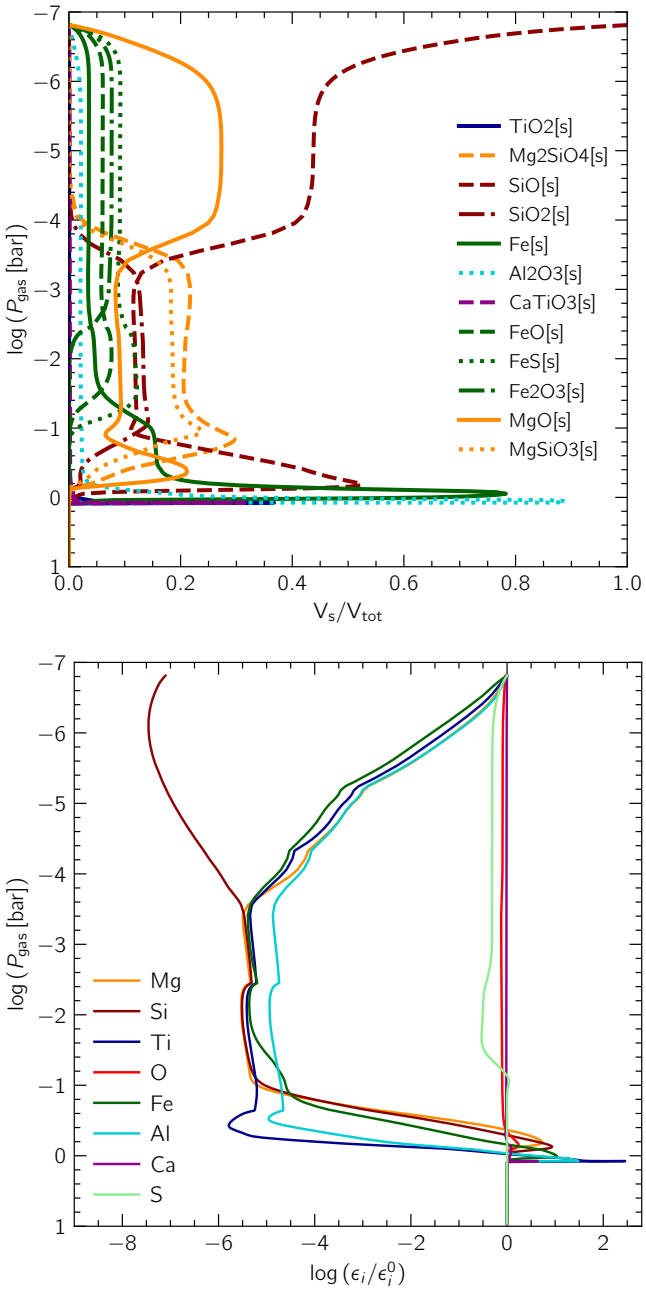

Figure 8.15: Composition of the cloud particles in units of volume fractions $V_s/V_{\rm tot}$ (top) and the relative gas-phase element depletions ϵ_i/ϵ_i^0 (bottom) for a MSG model with SiO nucleation, at $T_{\rm eff} = 1500\,{\rm K}$ and $\log(g) = 4.0$ and with a 1000 times slower mixing timescale.

8.F The effect of decreasing the mixing efficiency - models with TiO_2 nucleation

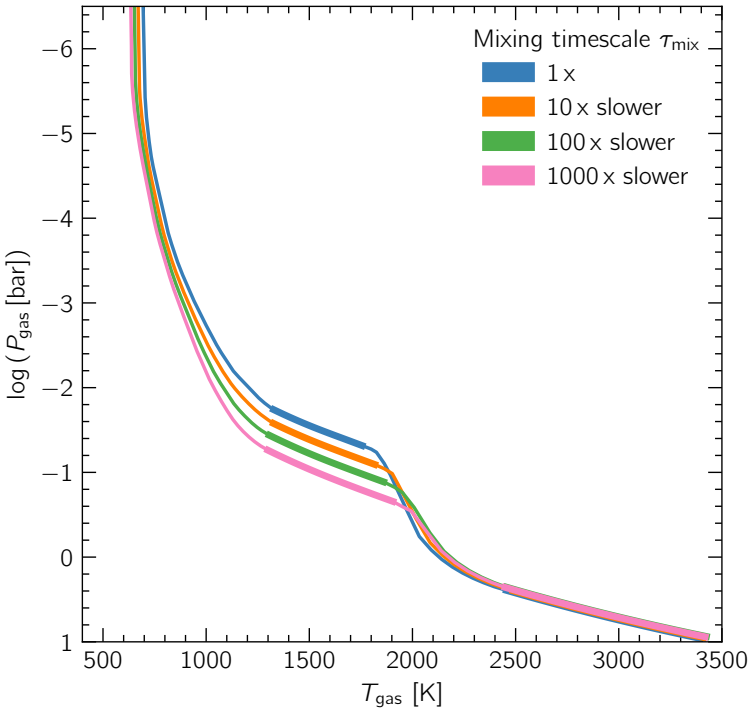

Figure 8.16: Pressure-temperature profiles for MSG models with TiO_2 nucleation, at $T_{\rm eff} = 1500\,{\rm K}$ and $\log(g) = 4.0$, and different mixing timescale scalings (1x, 10x slower, 100x slower, 1000x slower). Convective zones are plotted with thicker lines while radiative zones are plotted with thinner lines.

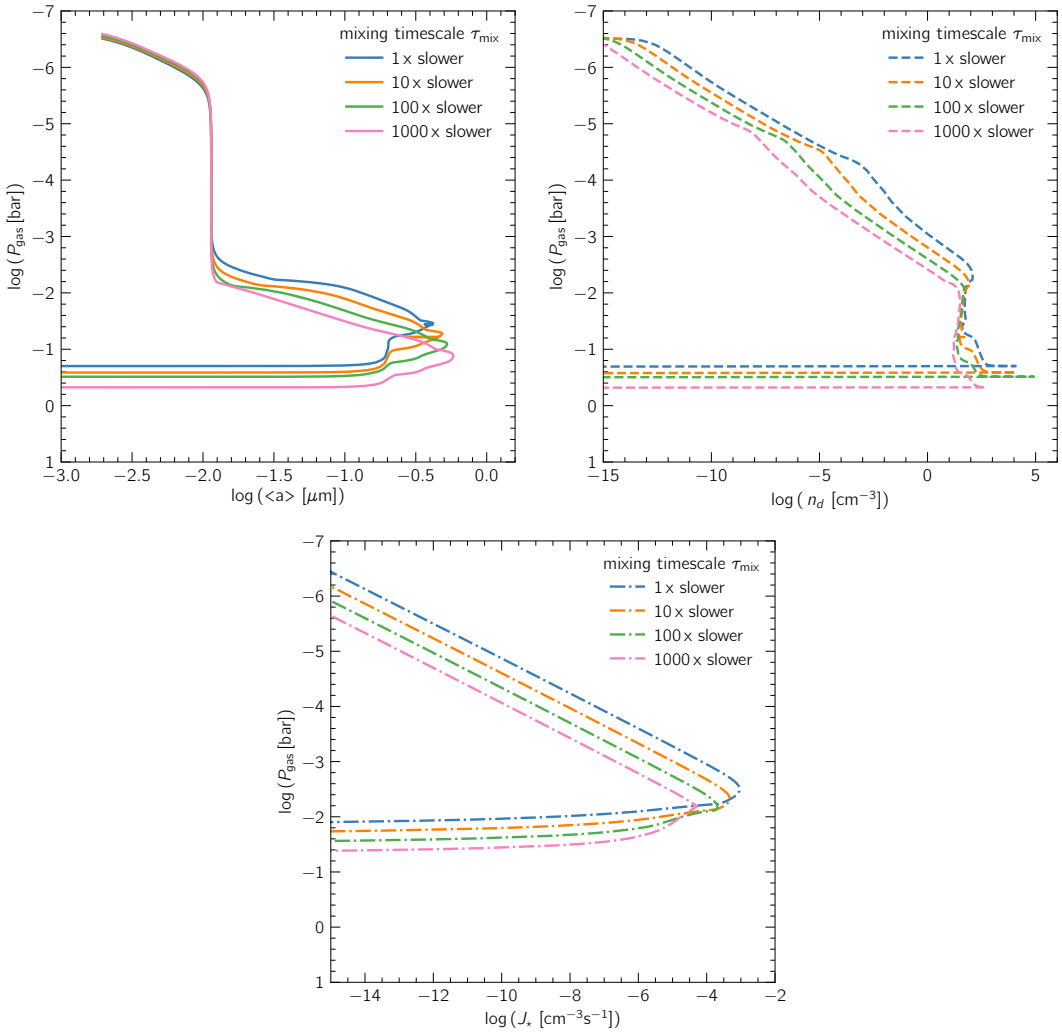

Figure 8.17: The average cloud particle size $\langle a \rangle$ (left), the cloud particle number density n_d (middle) and the nucleation rate $J_\star$ (right) along the atmosphere for models with TiO_2 nucleation at $T_{\rm eff} = 1500\,{\rm K}$ and $\log(g) = 4.0$, and different mixing timescale scalings (1x, 10x slower, 100x slower, 1000x slower).

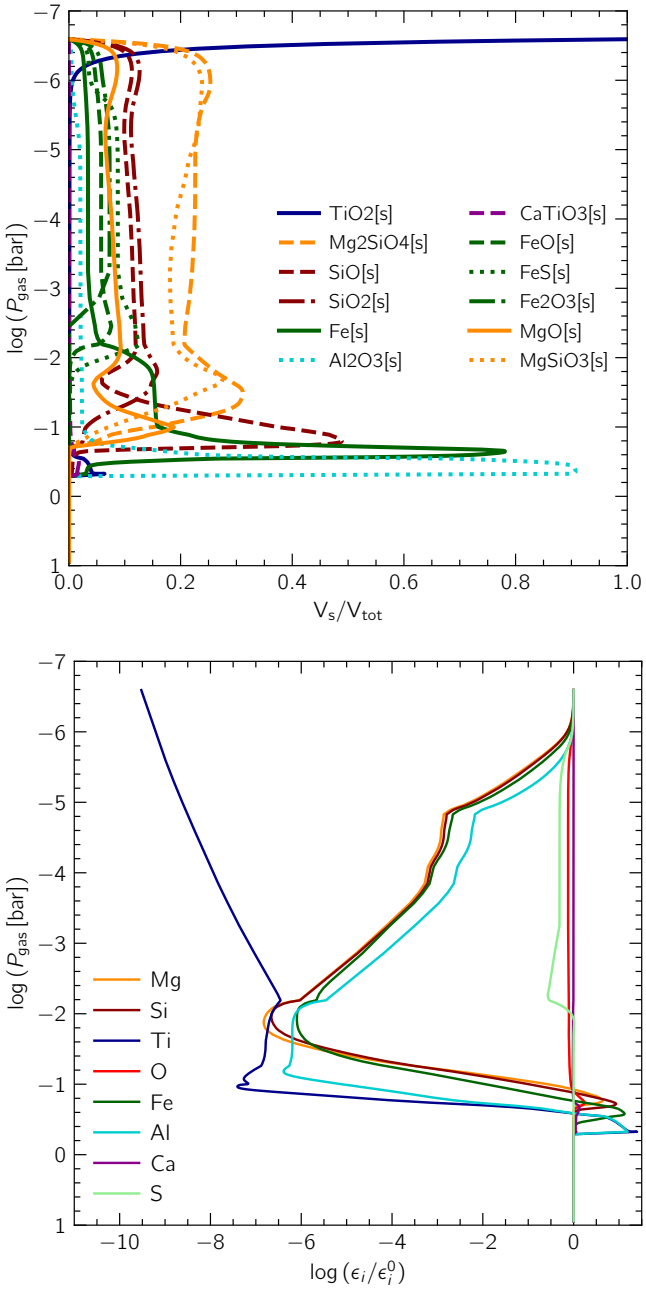

Figure 8.18: Composition of the cloud particles in units of volume fractions $V_s/V_{\rm tot}$ (left) and the relative gas-phase element depletions ϵ_i/ϵ_i^0 (right) for a MSG model with TiO_2 nucleation, at $T_{\rm eff} = 1500\,{\rm K}$ and $\log(g) = 4.0$ and with a 1000 times slower mixing timescale.

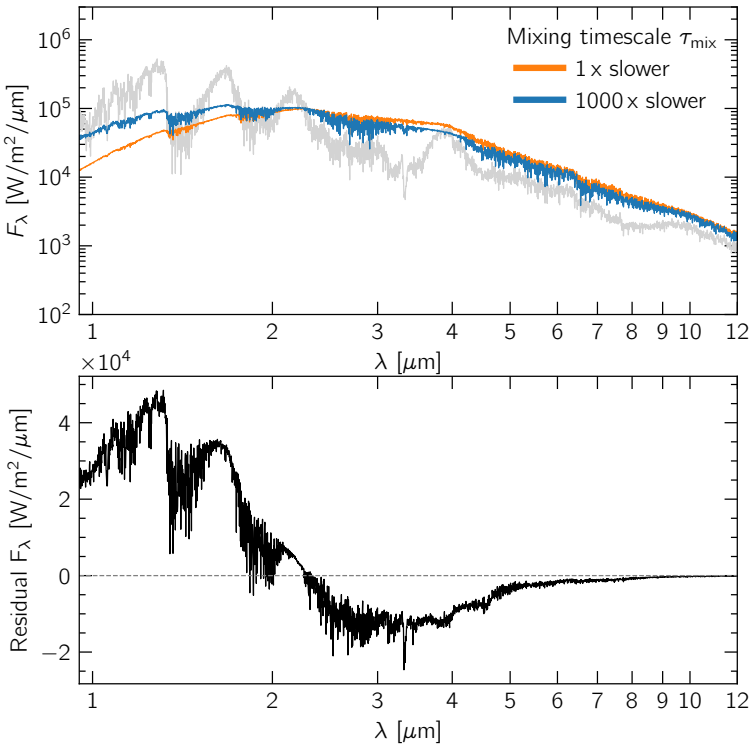

Figure 8.19: **Top:** Synthetic spectra of MSG cloudy models with TiO_2 nucleation, at 1500 K and $\log(g) = 4.0$. The orange spectrum shows the spectrum for a fully self-consistent MSG cloudy model. The blue spectrum shows the spectrum for a model where the mixing timescale was scaled up by 1000 times. The spectrum in grey is that of a cloud-free MARCS model at the same effective temperature and surface gravity. **Bottom:** The flux residual between the model with the mixing timescale scaled up by 1000 times (blue) and the self-consistent model with no scaling (orange).

Bibliography

Abrams, P. A. (2000). The evolution of predator-prey interactions: Theory and evidence. *Annual Review of Ecology, Evolution, and Systematics*, 31(Volume 31, 2000):79–105.

Ackerman, A. S. and Marley, M. S. (2001). Precipitating Condensation Clouds in Substellar Atmospheres. ApJ, 556(2):872–884.

Al-Refaie, A. F., Changeat, Q., Waldmann, I. P., and Tinetti, G. (2021). TauREx 3: A Fast, Dynamic, and Extendable Framework for Retrievals. ApJ, 917(1):37.

Al-Refaie, A. F., Yachmenev, A., Tennyson, J., and Yurchenko, S. N. (2015). ExoMol line lists - VIII. A variationally computed line list for hot formaldehyde. MNRAS, 448(2):1704–1714.

Allard, F., Hauschildt, P. H., Alexander, D. R., Tamanai, A., and Schweitzer, A. (2001). The Limiting Effects of Dust in Brown Dwarf Model Atmospheres. ApJ, 556(1):357–372.

Allard, F., Homeier, D., and Freytag, B. (2012). Models of very-low-mass stars, brown dwarfs and exoplanets. *Philosophical Transactions of the Royal Society of London Series A*, 370(1968):2765–2777.

Allard, N. F., Spiegelman, F., Leininger, T., and Molliere, P. (2019). New study of the line profiles of sodium perturbed by H_2. A&A, 628:A120.

Allers, K. N. and Liu, M. C. (2013). A Near-infrared Spectroscopic Study of Young Field Ultracool Dwarfs. ApJ, 772(2):79.

Anderson, D. R., Collier Cameron, A., Delrez, L., Doyle, A. P., Gillon, M., Hellier, C., Jehin, E., Lendl, M., Maxted, P. F. L., Madhusudhan, N., Pepe, F., Pollacco, D., Queloz, D., Ségransan, D., Smalley, B., Smith, A. M. S., Triaud, A. H. M. J., Turner, O. D., Udry, S., and West, R. G. (2017). The discoveries of WASP-91b,

WASP-105b and WASP-107b: Two warm Jupiters and a planet in the transition region between ice giants and gas giants. A&A, 604:A110.

Aringer, B., Kerschbaum, F., and Jörgensen, U. G. (2002). H_2O in stellar atmospheres. II. ISO spectra of cool red giants and hydrostatic models. A&A, 395:915–927.

Auer, L. H. and Mihalas, D. (1970). On the use of variable Eddington factors in non-LTE stellar atmospheres computations. MNRAS, 149:65.

Baeyens, R., Barat, S., Decin, L., Desert, J.-M., Gobrecht, D., Helling, C., Lecoq-Molinos, H., Savel, A. B., Shivkumar, H., Sikora, J., and Sindel, J. P. (2024). Detecting ongoing gas-to-solid nucleation on the ultra-hot planet WASP-76 b. JWST Proposal. Cycle 3, ID. #6045.

Bakos, G. Á., Lázár, J., Papp, I., Sári, P., and Green, E. M. (2002). System Description and First Light Curves of the Hungarian Automated Telescope, an Autonomous Observatory for Variability Search. PASP, 114(799):974–987.

Baraffe, I., Chabrier, G., and Barman, T. (2008). Structure and evolution of super-Earth to super-Jupiter exoplanets. I. Heavy element enrichment in the interior. A&A, 482(1):315–332.

Barber, R. J., Strange, J. K., Hill, C., Polyansky, O. L., Mellau, G. C., Yurchenko, S. N., and Tennyson, J. (2014). ExoMol line lists - III. An improved hot rotation-vibration line list for HCN and HNC. MNRAS, 437(2):1828–1835.

Barton, E. J., Chiu, C., Golpayegani, S., Yurchenko, S. N., Tennyson, J., Frohman, D. J., and Bernath, P. F. (2014). ExoMol molecular line lists V: the ro-vibrational spectra of NaCl and KCl. MNRAS, 442(2):1821–1829.

Bean, J. L., Raymond, S. N., and Owen, J. E. (2021). The Nature and Origins of Sub-Neptune Size Planets. *Journal of Geophysical Research (Planets)*, 126(1):e06639.

Begemann, B., Dorschner, J., Henning, T., Mutschke, H., Gürtler, J., Kömpe, C., and Nass, R. (1997). Aluminum Oxide and the Opacity of Oxygen-rich Circumstellar Dust in the 12-17 Micron Range. ApJ, 476(1):199–208.

Beiler, S. A., Allers, K. N., Cushing, M., Faherty, J., Marley, M., and Skemer, A. (2023). L-band spectroscopy of young brown dwarfs. MNRAS, 518(4):4870–4894.

Bell, T. J., Welbanks, L., Schlawin, E., Line, M. R., Fortney, J. J., Greene, T. P., Ohno, K., Parmentier, V., Rauscher, E., Beatty, T. G., Mukherjee, S., Wiser, L. S., Boyer, M. L., Rieke, M. J., and Stansberry, J. A. (2023). Methane throughout the atmosphere of the warm exoplanet WASP-80b. Nature, 623(7988):709–712.

Benneke, B., Roy, P.-A., Coulombe, L.-P., Radica, M., Piaulet, C., Ahrer, E.-M., Pierrehumbert, R., Krissansen-Totton, J., Schlichting, H. E., Hu, R., Yang, J.,

Christie, D., Thorngren, D., Young, E. D., Pelletier, S., Knutson, H. A., Miguel, Y., Evans-Soma, T. M., Dorn, C., Gagnebin, A., Fortney, J. J., Komacek, T., MacDonald, R., Raul, E., Cloutier, R., Acuna, L., Lafrenière, D., Cadieux, C., Doyon, R., Welbanks, L., and Allart, R. (2024). JWST Reveals CH_4, CO_2, and H_2O in a Metal-rich Miscible Atmosphere on a Two-Earth-Radius Exoplanet. *arXiv e-prints*, page arXiv:2403.03325.

Best, W. M. J., Liu, M. C., Magnier, E. A., and Dupuy, T. J. (2020). The Hawaii Infrared Parallax Program. IV. A Comprehensive Parallax Survey of L0-T8 Dwarfs with UKIRT. AJ, 159(6):257.

Best, W. M. J., Liu, M. C., Magnier, E. A., and Dupuy, T. J. (2021). A Volume-limited Sample of Ultracool Dwarfs. I. Construction, Space Density, and a Gap in the L/T Transition. AJ, 161(1):42.

Best, W. M. J., Magnier, E. A., Liu, M. C., Aller, K. M., Zhang, Z., Burgett, W. S., Chambers, K. C., Draper, P., Flewelling, H., Kaiser, N., Kudritzki, R. P., Metcalfe, N., Tonry, J. L., Wainscoat, R. J., and Waters, C. (2018). Photometry and Proper Motions of M, L, and T Dwarfs from the Pan-STARRS1 3π Survey. ApJS, 234(1):1.

Biller, B., Chen, X., Crossfield, I., Crouzet, N. M., Dupuy, T. J., Faherty, J. K., Henning, T. K., Kataria, T., Liu, P., Mace, G. N., Manjavacas, E., Molliere, P., Suarez, G., Sutlieff, B., Tan, X., Tremblin, P., Vos, J., and Whiteford, N. (2023). Clouds or Chemistry?: Pinpointing the drivers of variability across the L/T transition via the benchmark L/T binary WISE 1049AB. JWST Proposal. Cycle 2, ID. #2965.

Biller, B. A., Vos, J. M., Zhou, Y., McCarthy, A. M., Tan, X., Crossfield, I. J. M., Whiteford, N., Suarez, G., Faherty, J., Manjavacas, E., Chen, X., Liu, P., Sutlieff, B. J., Limbach, M. A., Molliere, P., Dupuy, T. J., Oliveros-Gomez, N., Muirhead, P. S., Henning, T., Mace, G., Crouzet, N., Karalidi, T., Morley, C. V., Tremblin, P., and Kataria, T. (2024). The JWST Weather Report from the Nearest Brown Dwarfs I: multi-period JWST NIRSpec + MIRI monitoring of the benchmark binary brown dwarf WISE 1049AB. *arXiv e-prints*, page arXiv:2407.09194.

Birdsall, C. K. and Fuss, D. (1969). Clouds-in-clouds, clouds-in-cells physics for many-body plasma simulation. *Journal of Computational Physics*, 3(4):494–511.

Bitsch, B., Raymond, S. N., Buchhave, L. A., Bello-Arufe, A., Rathcke, A. D., and Schneider, A. D. (2021). Dry or water world? How the water contents of inner sub-Neptunes constrain giant planet formation and the location of the water ice line. A&A, 649:L5.

Bittner, D. M. and Bernath, P. F. (2018). Line Lists for LiF and LiCl in the X $^1\Sigma^+$ Ground State. ApJS, 235(1):8.

Blackwell, D. E., Lynas-Gray, A. E., and Smith, G. (1995). On the determination of the solar iron abundance using Fe I lines. A&A, 296:217.

Boccaletti, A., Mâlin, M., Baudoz, P., Tremblin, P., Perrot, C., Rouan, D., Lagage, P.-O., Whiteford, N., Mollière, P., Waters, R., Henning, T., Decin, L., Güdel, M., Vandenbussche, B., Absil, O., Argyriou, I., Bouwman, J., Cossou, C., Coulais, A., Gastaud, R., Glasse, A., Glauser, A. M., Kamp, I., Kendrew, S., Krause, O., Lahuis, F., Mueller, M., Olofsson, G., Patapis, P., Pye, J., Royer, P., Serabyn, E., Scheithauer, S., Colina, L., van Dishoeck, E. F., Ostlin, G., Ray, T. P., and Wright, G. (2024). Imaging detection of the inner dust belt and the four exoplanets in the HR 8799 system with JWST's MIRI coronagraph. A&A, 686:A33.

Bochinski, J. J., Haswell, C. A., Marsh, T. R., Dhillon, V. S., and Littlefair, S. P. (2015). Direct Evidence for an Evolving Dust Cloud from the Exoplanet KIC 12557548 b. ApJ, 800(2):L21.

Bodenheimer, P., D'Angelo, G., Lissauer, J. J., Fortney, J. J., and Saumon, D. (2013). Deuterium Burning in Massive Giant Planets and Low-mass Brown Dwarfs Formed by Core-nucleated Accretion. ApJ, 770(2):120.

Bodman, E. H. L., Wright, J. T., Desch, S. J., and Lisse, C. M. (2018). Inferring the Composition of Disintegrating Planet Interiors from Dust Tails with Future James Webb Space Telescope Observations. AJ, 156(4):173.

Böhm-Vitense, E. (1958). Über die Wasserstoffkonvektionszone in Sternen verschiedener Effektivtemperaturen und Leuchtkräfte. Mit 5 Textabbildungen. ZAp, 46:108.

Bohren, C. F. and Huffman, D. R. (1983). Absorption and scattering of light by small particles. Research supported by the University of Arizona and Institute of Occupational and Environmental Health. New York, Wiley-Interscience, 1983, 541 p.

Boltzmann, L. (1884). Ableitung des Stefan'schen Gesetzes, betreffend die Abhängigkeit der Wärmestrahlung von der Temperatur aus der electromagnetischen Lichttheorie. *Annalen der Physik*, 258(6):291–294.

Bonfils, X., Delfosse, X., Udry, S., Forveille, T., Mayor, M., Perrier, C., Bouchy, F., Gillon, M., Lovis, C., Pepe, F., Queloz, D., Santos, N. C., Ségransan, D., and Bertaux, J. L. (2013). The HARPS search for southern extra-solar planets. XXXI. The M-dwarf sample. A&A, 549:A109.

Bonsor, A., Carter, P. J., Hollands, M., Gänsicke, B. T., Leinhardt, Z., and Harrison, J. H. D. (2020). Are exoplanetesimals differentiated? MNRAS, 492(2):2683–2697.

Booth, R. A., Clarke, C. J., Madhusudhan, N., and Ilee, J. D. (2017). Chemical enrichment of giant planets and discs due to pebble drift. MNRAS, 469(4):3994–4011.

Booth, R. A., Owen, J. E., and Schulik, M. (2023). Dust formation in the outflows of catastrophically evaporating planets. MNRAS, 518(2):1761–1775.

Borucki, W. J., Koch, D., Basri, G., Batalha, N., Brown, T., Caldwell, D., Caldwell, J., Christensen-Dalsgaard, J., Cochran, W. D., DeVore, E., Dunham, E. W., Dupree, A. K., Gautier, T. N., Geary, J. C., Gilliland, R., Gould, A., Howell, S. B., Jenkins, J. M., Kondo, Y., Latham, D. W., Marcy, G. W., Meibom, S., Kjeldsen, H., Lissauer, J. J., Monet, D. G., Morrison, D., Sasselov, D., Tarter, J., Boss, A., Brownlee, D., Owen, T., Buzasi, D., Charbonneau, D., Doyle, L., Fortney, J., Ford, E. B., Holman, M. J., Seager, S., Steffen, J. H., Welsh, W. F., Rowe, J., Anderson, H., Buchhave, L., Ciardi, D., Walkowicz, L., Sherry, W., Horch, E., Isaacson, H., Everett, M. E., Fischer, D., Torres, G., Johnson, J. A., Endl, M., MacQueen, P., Bryson, S. T., Dotson, J., Haas, M., Kolodziejczak, J., Van Cleve, J., Chandrasekaran, H., Twicken, J. D., Quintana, E. V., Clarke, B. D., Allen, C., Li, J., Wu, H., Tenenbaum, P., Verner, E., Bruhweiler, F., Barnes, J., and Prsa, A. (2010). Kepler Planet-Detection Mission: Introduction and First Results. *Science*, 327(5968):977.

Bosch, S., Ferré-Borrull, J., Leinfellner, N., and Canillas, A. (2000). Effective dielectric function of mixtures of three or more materials: a numerical procedure for computations. *Surface Science*, 453(1):9–17.

Brent, R. P. (1973). Some Efficient Algorithms for Solving Systems of Nonlinear Equations. *SIAM Journal on Numerical Analysis*, 10(2):327–344.

Brogi, M., Keller, C. U., de Juan Ovelar, M., Kenworthy, M. A., de Kok, R. J., Min, M., and Snellen, I. A. G. (2012). Evidence for the disintegration of KIC 12557548 b. A&A, 545:L5.

Bromley, J. and Chiang, E. (2023). Chaotic winds from a dying world: a one-dimensional map for evolving atmospheres. MNRAS, 521(4):5746–5759.

Bromley, S. T., Gómez Martín, J. C., and Plane, J. M. C. (2016). Under what conditions does (SiO)Nnucleation occur? A bottom-up kinetic modelling evaluation. *Physical Chemistry Chemical Physics (Incorporating Faraday Transactions)*, 18(38):26913–26922.

Brooke, J. S. A., Bernath, P. F., and Western, C. M. (2015). Note: Improved line strengths of rovibrational and rotational transitions within the $X^3\Sigma^-$ ground state of NH. J. Chem. Phys., 143(2):026101.

Brooke, J. S. A., Bernath, P. F., Western, C. M., Sneden, C., Afşar, M., Li, G., and Gordon, I. E. (2016). Line strengths of rovibrational and rotational transitions in the X^2 Π ground state of OH. J. Quant. Spec. Radiat. Transf., 168:142–157.

Brooke, J. S. A., Bernath, P. F., Western, C. M., van Hemert, M. C., and Groenenboom, G. C. (2014a). Line strengths of rovibrational and rotational transitions within the X$\hat{3}\Sigma$ {$\hat{}$} ground state of NH. J. Chem. Phys., 141(5):054310.

Brooke, J. S. A., Ram, R. S., Western, C. M., Li, G., Schwenke, D. W., and Bernath, P. F. (2014b). Einstein A Coefficients and Oscillator Strengths for the A $^2\Pi$-X $^2\Sigma^+$ (Red) and $B^2\Sigma^+$-$X^2\Sigma^+$ (Violet) Systems and Rovibrational Transitions in the X $^2\Sigma^+$ State of CN. ApJS, 210(2):23.

Brouwers, M. G., Bonsor, A., and Malamud, U. (2023). Asynchronous accretion can mimic diverse white dwarf pollutants I: core and mantle fragments. MNRAS, 519(2):2646–2662.

Bruggeman, D. A. G. (1935). Berechnung verschiedener physikalischer Konstanten von heterogenen Substanzen. I. Dielektrizitätskonstanten und Leitfähigkeiten der Mischkörper aus isotropen Substanzen. *Annalen der Physik*, 416(7):636–664.

Bryant, E. M., Bayliss, D., and Van Eylen, V. (2023). The occurrence rate of giant planets orbiting low-mass stars with TESS. MNRAS, 521(3):3663–3681.

Buchan, A. M., Bonsor, A., Shorttle, O., Wade, J., Harrison, J., Noack, L., and Koester, D. (2022). Planets or asteroids? A geochemical method to constrain the masses of White Dwarf pollutants. MNRAS, 510(3):3512–3530.

Budaj, J. (2013). Light-curve analysis of KIC 12557548b: an extrasolar planet with a comet-like tail. A&A, 557:A72.

Burgasser, A. J., Marley, M. S., Ackerman, A. S., Saumon, D., Lodders, K., Dahn, C. C., Harris, H. C., and Kirkpatrick, J. D. (2002). Evidence of Cloud Disruption in the L/T Dwarf Transition. ApJ, 571(2):L151–L154.

Burn, R., Mordasini, C., Mishra, L., Haldemann, J., Venturini, J., Emsenhuber, A., and Henning, T. (2024). A radius valley between migrated steam worlds and evaporated rocky cores. *Nature Astronomy*, 8:463–471.

Burns, J. A., Lamy, P. L., and Soter, S. (1979). Radiation forces on small particles in the solar system. Icarus, 40(1):1–48.

Burrows, A., Dulick, M., Bauschlicher, C. W., J., Bernath, P. F., Ram, R. S., Sharp, C. M., and Milsom, J. A. (2005). Spectroscopic Constants, Abundances, and Opacities of the TiH Molecule. ApJ, 624(2):988–1002.

Burrows, A., Sudarsky, D., and Hubeny, I. (2006). L and T Dwarf Models and the L to T Transition. ApJ, 640(2):1063–1077.

Campos Estrada, B., Owen, J. E., Jankovic, M. R., Wilson, A., and Helling, C. (2024). On the likely magnesium-iron silicate dusty tails of catastrophically evaporating rocky planets. MNRAS, 528(2):1249–1263.

Cannon, C. J. (1973). Frequency-Quadrature Perturbations in Radiative-Transfer Theory. ApJ, 185:621–630.

Carrión-González, Ó., García Muñoz, A., Cabrera, J., Csizmadia, S., Santos, N. C., and Rauer, H. (2020). Directly imaged exoplanets in reflected starlight: the importance of knowing the planet radius. A&A, 640:A136.

Carrión-González, Ó., García Muñoz, A., Santos, N. C., Cabrera, J., Csizmadia, S., and Rauer, H. (2021). Catalogue of exoplanets accessible in reflected starlight to the Nancy Grace Roman Space Telescope. Population study and prospects for phase-curve measurements. A&A, 651:A7.

Cassan, A., Kubas, D., Beaulieu, J. P., Dominik, M., Horne, K., Greenhill, J., Wambsganss, J., Menzies, J., Williams, A., Jørgensen, U. G., Udalski, A., Bennett, D. P., Albrow, M. D., Batista, V., Brillant, S., Caldwell, J. A. R., Cole, A., Coutures, C., Cook, K. H., Dieters, S., Dominis Prester, D., Donatowicz, J., Fouqué, P., Hill, K., Kains, N., Kane, S., Marquette, J. B., Martin, R., Pollard, K. R., Sahu, K. C., Vinter, C., Warren, D., Watson, B., Zub, M., Sumi, T., Szymański, M. K., Kubiak, M., Poleski, R., Soszynski, I., Ulaczyk, K., Pietrzyński, G., and Wyrzykowski, Ł. (2012). One or more bound planets per Milky Way star from microlensing observations. Nature, 481(7380):167–169.

Chabrier, G. (2003). Galactic Stellar and Substellar Initial Mass Function. PASP, 115(809):763–795.

Chabrier, G., Baraffe, I., Selsis, F., Barman, T. S., Hennebelle, P., and Alibert, Y. (2007). Gaseous Planets, Protostars, and Young Brown Dwarfs: Birth and Fate. In Reipurth, B., Jewitt, D., and Keil, K., editors, *Protostars and Planets V*, page 623.

Chabrier, G., Johansen, A., Janson, M., and Rafikov, R. (2014). Giant Planet and Brown Dwarf Formation. In Beuther, H., Klessen, R. S., Dullemond, C. P., and Henning, T., editors, *Protostars and Planets VI*, pages 619–642.

Charbonneau, D., Brown, T. M., Latham, D. W., and Mayor, M. (2000). Detection of Planetary Transits Across a Sun-like Star. ApJ, 529(1):L45–L48.

Charbonneau, D., Brown, T. M., Noyes, R. W., and Gilliland, R. L. (2002). Detection of an Extrasolar Planet Atmosphere. ApJ, 568(1):377–384.

Charnay, B., Bézard, B., Baudino, J. L., Bonnefoy, M., Boccaletti, A., and Galicher, R. (2018). A Self-consistent Cloud Model for Brown Dwarfs and Young Giant Exoplanets: Comparison with Photometric and Spectroscopic Observations. ApJ, 854(2):172.

Chauvin, G., Lagrange, A. M., Dumas, C., Zuckerman, B., Mouillet, D., Song, I., Beuzit, J. L., and Lowrance, P. (2005). Giant planet companion to 2MASSW J1207334-393254. A&A, 438(2):L25–L28.

Chiang, E. and Laughlin, G. (2013). The minimum-mass extrasolar nebula: in situ formation of close-in super-Earths. MNRAS, 431(4):3444–3455.

Chubb, K. L., Rocchetto, M., Yurchenko, S. N., Min, M., Waldmann, I., Barstow, J. K., Mollière, P., Al-Refaie, A. F., Phillips, M. W., and Tennyson, J. (2021). The ExoMolOP database: Cross sections and k-tables for molecules of interest in high-temperature exoplanet atmospheres. A&A, 646:A21.

Coles, P. A., Yurchenko, S. N., and Tennyson, J. (2019). ExoMol molecular line lists - XXXV. A rotation-vibration line list for hot ammonia. MNRAS, 490(4):4638–4647.

Cooper, C. S., Sudarsky, D., Milsom, J. A., Lunine, J. I., and Burrows, A.

(2003). Modeling the Formation of Clouds in Brown Dwarf Atmospheres. ApJ, 586(2):1320–1337.

Coppola, C. M., Lodi, L., and Tennyson, J. (2011). Radiative cooling functions for primordial molecules. MNRAS, 415(1):487–493.

Costa, G. C. C., Jacobson, N. S., and Fegley, Bruce, J. (2017). Vaporization and thermodynamics of forsterite-rich olivine and some implications for silicate atmospheres of hot rocky exoplanets. Icarus, 289:42–55.

Croll, B., Rappaport, S., DeVore, J., Gilliland , R. L., Crepp, J. R., Howard, A. W., Star, K. M., Chiang, E., Levine, A. M., Jenkins, J. M., Albert, L., Bonomo, A. S., Fortney, J. J., and Isaacson, H. (2014). Multiwavelength Observations of the Candidate Disintegrating Sub-Mercury KIC 12557548b. ApJ, 786(2):100.

Croll, B., Rappaport, S., and Levine, A. M. (2015). The relation between the transit depths of KIC 12557548b and the stellar rotation period. MNRAS, 449(2):1408–1421.

Crossfield, I. J. M., Malik, M., Hill, M. L., Kane, S. R., Foley, B., Polanski, A. S., Coria, D., Brande, J., Zhang, Y., Wienke, K., Kreidberg, L., Cowan, N. B., Dragomir, D., Gorjian, V., Mikal-Evans, T., Benneke, B., Christiansen, J. L., Deming, D., and Morales, F. Y. (2022). GJ 1252b: A Hot Terrestrial Super-Earth with No Atmosphere. ApJ, 937(1):L17.

Currie, T., Lawson, K., Schneider, G., Lyra, W., Wisniewski, J., Grady, C., Guyon, O., Tamura, M., Kotani, T., Kawahara, H., Brandt, T., Uyama, T., Muto, T., Dong, R., Kudo, T., Hashimoto, J., Fukagawa, M., Wagner, K., Lozi, J., Chilcote, J., Tobin, T., Groff, T., Ward-Duong, K., Januszewski, W., Norris, B., Tuthill, P., van der Marel, N., Sitko, M., Deo, V., Vievard, S., Jovanovic, N., Martinache, F., and Skaf, N. (2022). Images of embedded Jovian planet formation at a wide separation around AB Aurigae. *Nature Astronomy*, 6:751–759.

Curry, A., Booth, R., Owen, J. E., and Mohanty, S. (2023). The evolution of catastrophically evaporating rocky planets. *arXiv e-prints*, page arXiv:2303.15200.

Cushing, M. C., Marley, M. S., Saumon, D., Kelly, B. C., Vacca, W. D., Rayner, J. T., Freedman, R. S., Lodders, K., and Roellig, T. L. (2008). Atmospheric Parameters of Field L and T Dwarfs. ApJ, 678(2):1372–1395.

Cushing, M. C., Rayner, J. T., and Vacca, W. D. (2005). An Infrared Spectroscopic Sequence of M, L, and T Dwarfs. ApJ, 623(2):1115–1140.

Cushing, M. C., Roellig, T. L., Marley, M. S., Saumon, D., Leggett, S. K., Kirkpatrick, J. D., Wilson, J. C., Sloan, G. C., Mainzer, A. K., Van Cleve, J. E., and Houck, J. R. (2006). A Spitzer Infrared Spectrograph Spectral Sequence of M, L, and T Dwarfs. ApJ, 648(1):614–628.

Dalgarno, A. and Williams, D. A. (1962). Rayleigh Scattering by Molecular Hydrogen. ApJ, 136:690–692.

Decin, L. and Eriksson, K. (2007). Theoretical model atmosphere spectra used for the calibration of infrared instruments. A&A, 472(3):1041–1053.

Decin, L., Vandenbussche, B., Waelkens, C., Decin, G., Eriksson, K., Gustafsson, B., Plez, B., and Sauval, A. J. (2003). ISO-SWS calibration and the accurate modelling of cool-star atmospheres. IV. G9 to M2 stars. A&A, 400:709–727.

Deeg, H. J. and Alonso, R. (2018). *Transit Photometry as an Exoplanet Discovery Method*, pages 633–657. Springer International Publishing, Cham.

Deeg, H. J. and Belmonte, J. A. (2018). *Handbook of Exoplanets*. Springer International Publishing, Cham, 1st ed. 2018. edition.

Deming, D., Wilkins, A., McCullough, P., Burrows, A., Fortney, J. J., Agol, E., Dobbs-Dixon, I., Madhusudhan, N., Crouzet, N., Desert, J.-M., Gilliland, R. L., Haynes, K., Knutson, H. A., Line, M., Magic, Z., Mandell, A. M., Ranjan, S., Charbonneau, D., Clampin, M., Seager, S., and Showman, A. P. (2013). Infrared Transmission Spectroscopy of the Exoplanets HD 209458b and XO-1b Using the Wide Field Camera-3 on the Hubble Space Telescope. ApJ, 774(2):95.

Demory, B.-O., Gillon, M., Seager, S., Benneke, B., Deming, D., and Jackson, B. (2012). Detection of Thermal Emission from a Super-Earth. ApJ, 751(2):L28.

Dominik, C., Sedlmayr, E., and Gail, H. P. (1993). Dust formation in stellar winds. VI. Moment equations for the formation of heterogeneous and core-mantle grains. A&A, 277:578.

Dormand, J. and Prince, P. (1980). A family of embedded runge-kutta formulae. *Journal of Computational and Applied Mathematics*, 6(1):19 – 26.

Dorn, C., Harrison, J. H. D., Bonsor, A., and Hands, T. O. (2019). A new class of Super-Earths formed from high-temperature condensates: HD219134 b, 55 Cnc e, WASP-47 e. MNRAS, 484(1):712–727.

Dorn, C., Hinkel, N. R., and Venturini, J. (2017a). Bayesian analysis of interiors of HD 219134b, Kepler-10b, Kepler-93b, CoRoT-7b, 55 Cnc e, and HD 97658b using stellar abundance proxies. A&A, 597:A38.

Dorn, C., Venturini, J., Khan, A., Heng, K., Alibert, Y., Helled, R., Rivoldini, A., and Benz, W. (2017b). A generalized Bayesian inference method for constraining the interiors of super Earths and sub-Neptunes. A&A, 597:A37.

Dorschner, J., Begemann, B., Henning, T., Jaeger, C., and Mutschke, H. (1995). Steps toward interstellar silicate mineralogy. II. Study of Mg-Fe-silicate glasses of variable composition. A&A, 300:503.

Doughty, N. A. and Fraser, P. A. (1966). The free-free absorption coefficient of the negative hydrogen ion. MNRAS, 132:267.

Doughty, N. A., Fraser, P. A., and McEachran, R. P. (1966). The bound-free absorption coefficient of the negative hydrogen ion. MNRAS, 132:255.

Doyle, L. R., Carter, J. A., Fabrycky, D. C., Slawson, R. W., Howell, S. B., Winn, J. N., Orosz, J. A., Přsa, A., Welsh, W. F., Quinn, S. N., Latham, D., Torres, G., Buchhave, L. A., Marcy, G. W., Fortney, J. J., Shporer, A., Ford, E. B., Lissauer, J. J., Ragozzine, D., Rucker, M., Batalha, N., Jenkins, J. M., Borucki, W. J., Koch, D., Middour, C. K., Hall, J. R., McCauliff, S., Fanelli, M. N., Quintana, E. V., Holman, M. J., Caldwell, D. A., Still, M., Stefanik, R. P., Brown, W. R., Esquerdo, G. A., Tang, S., Furesz, G., Geary, J. C., Berlind, P., Calkins, M. L., Short, D. R., Steffen, J. H., Sasselov, D., Dunham, E. W., Cochran, W. D., Boss, A., Haas, M. R., Buzasi, D., and Fischer, D. (2011). Kepler-16: A Transiting Circumbinary Planet. *Science*, 333(6049):1602.

Doyle, R. O. (1968). The Astrophysical Significance of the Continuous Spectrum of the Hydrogen Quasi-Molecule. ApJ, 153:987.

Dressing, C. D., Charbonneau, D., Dumusque, X., Gettel, S., Pepe, F., Collier Cameron, A., Latham, D. W., Molinari, E., Udry, S., and Affer, L. (2015). The Mass of Kepler-93b and The Composition of Terrestrial Planets. ApJ, 800(2):135.

Drążkowska, J., Bitsch, B., Lambrechts, M., Mulders, G. D., Harsono, D., Vazan, A., Liu, B., Ormel, C. W., Kretke, K., and Morbidelli, A. (2023). Planet Formation Theory in the Era of ALMA and Kepler: from Pebbles to Exoplanets. In Inutsuka, S., Aikawa, Y., Muto, T., Tomida, K., and Tamura, M., editors, *Protostars and Planets VII*, volume 534 of *Astronomical Society of the Pacific Conference Series*, page 717.

Dupuy, T. J. and Kraus, A. L. (2013). Distances, Luminosities, and Temperatures of the Coldest Known Substellar Objects. *Science*, 341(6153):1492–1495.

Dupuy, T. J. and Liu, M. C. (2012). The Hawaii Infrared Parallax Program. I. Ultracool Binaries and the L/T Transition. ApJS, 201(2):19.

Dyrek, A., Min, M., Decin, L., Bouwman, J., Crouzet, N., Mollière, P., Lagage, P.-O., Konings, T., Tremblin, P., Güdel, M., Pye, J., Waters, R., Henning, T., Vandenbussche, B., Ardevol Martinez, F., Argyriou, I., Ducrot, E., Heinke, L., van Looveren, G., Absil, O., Barrado, D., Baudoz, P., Boccaletti, A., Cossou, C., Coulais, A., Edwards, B., Gastaud, R., Glasse, A., Glauser, A., Greene, T. P., Kendrew, S., Krause, O., Lahuis, F., Mueller, M., Olofsson, G., Patapis, P., Rouan, D., Royer, P., Scheithauer, S., Waldmann, I., Whiteford, N., Colina, L., van Dishoeck, E. F., Östlin, G., Ray, T. P., and Wright, G. (2024). SO_2, silicate clouds, but no CH_4 detected in a warm Neptune. Nature, 625(7993):51–54.

Eistrup, C., Walsh, C., and van Dishoeck, E. F. (2016). Setting the volatile composition of (exo)planet-building material. Does chemical evolution in disk midplanes matter? A&A, 595:A83.

Elachi, C., Angel, R., Beichman, C. A., Boss, A., Brown, R., Dressler, A., Dyson, F., Fanson, J., Ftaclas, C., Goad, L., Klein, M., Leger, A., Lillie, C., Peale, S., Peterson, D., Reasenberg, B., Sandler, D., Shao, M., Simon, R., and Tenerelli,

D. (1996). A Road Map for the Exploration of Neighboring Planetary Systems (ExNPS). Technical Report, Jet Propulsion Lab., California Inst. of Tech. Pasadena, CA United States.

Fabian, D., Henning, T., Jäger, C., Mutschke, H., Dorschner, J., and Wehrhan, O. (2001). Steps toward interstellar silicate mineralogy. VI. Dependence of crystalline olivine IR spectra on iron content and particle shape. A&A, 378:228–238.

Faherty, J. K. (2018). Spectral Properties of Brown Dwarfs and Unbound Planetary Mass Objects. In Deeg, H. J. and Belmonte, J. A., editors, *Handbook of Exoplanets*, page 188.

Faherty, J. K., Gagné, J., Popinchalk, M., Vos, J. M., Burgasser, A. J., Schümann, J., Schneider, A. C., Kirkpatrick, J. D., Meisner, A. M., Kuchner, M. J., Bardalez Gagliuffi, D. C., Marocco, F., Caselden, D., Gonzales, E. C., Rothermich, A., Casewell, S. L., Debes, J. H., Aganze, C., Ayala, A., Hsu, C.-C., Cooper, W. J., Smart, R. L., Gerasimov, R., Theissen, C. A., and Backyard Worlds: Planet 9 Collaboration (2021). A Wide Planetary Mass Companion Discovered through the Citizen Science Project Backyard Worlds: Planet 9. ApJ, 923(1):48.

Farihi, J., Koester, D., Zuckerman, B., Vican, L., Gänsicke, B. T., Smith, N., Walth, G., and Breedt, E. (2016). Solar abundances of rock-forming elements, extreme oxygen and hydrogen in a young polluted white dwarf. MNRAS, 463(3):3186–3192.

Feautrier, P. (1964). Sur la resolution numerique de l'equation de transfert. *Comptes Rendus Academie des Sciences (serie non specifiee)*, 258:3189.

Fegley, B. and Osborne, R. (2013). *Practical chemical thermodynamics for geoscientists*. Academic Press, Waltham, Mass.

Fernando, A. M., Bernath, P. F., Hodges, J. N., and Masseron, T. (2018). A new linelist for the $A^3\Pi$-$X^3\Sigma^-$ transition of the NH free radical. J. Quant. Spec. Radiat. Transf., 217:29–34.

Fortney, J. J., Marley, M. S., and Barnes, J. W. (2007). Planetary Radii across Five Orders of Magnitude in Mass and Stellar Insolation: Application to Transits. ApJ, 659(2):1661–1672.

Freedman, R. S., Lustig-Yaeger, J., Fortney, J. J., Lupu, R. E., Marley, M. S., and Lodders, K. (2014). Gaseous Mean Opacities for Giant Planet and Ultracool Dwarf Atmospheres over a Range of Metallicities and Temperatures. ApJS, 214(2):25.

Freedman, R. S., Marley, M. S., and Lodders, K. (2008). Line and Mean Opacities for Ultracool Dwarfs and Extrasolar Planets. ApJS, 174(2):504–513.

Fressin, F., Torres, G., Charbonneau, D., Bryson, S. T., Christiansen, J., Dressing,

C. D., Jenkins, J. M., Walkowicz, L. M., and Batalha, N. M. (2013). The False Positive Rate of Kepler and the Occurrence of Planets. ApJ, 766(2):81.

Fridlund, M., Baglin, A., Lochard, J., and Conroy, L. (2006). *The CoRoT Mission Pre-Launch Status-Stellar Seismology and Planet Finding*, volume 1306.

Fulton, B. J. and Petigura, E. A. (2018). The California-Kepler Survey. VII. Precise Planet Radii Leveraging Gaia DR2 Reveal the Stellar Mass Dependence of the Planet Radius Gap. AJ, 156(6):264.

Fulton, B. J., Petigura, E. A., Howard, A. W., Isaacson, H., Marcy, G. W., Cargile, P. A., Hebb, L., Weiss, L. M., Johnson, J. A., and Morton, T. D. (2017). The California-Kepler Survey. III. A Gap in the Radius Distribution of Small Planets. AJ, 154(3):109.

Gail, H. P., Keller, R., and Sedlmayr, E. (1984). Dust formation in stellar winds. I - A rapid computational method and application to graphite condensation. A&A, 133(2):320–332.

Gail, H. P. and Sedlmayr, E. (1988). Dust formation in stellar winds. IV. Heteromolecular carbon grain formation and growth. A&A, 206:153–168.

Gail, H.-P. and Sedlmayr, E. (2013). *Physics and Chemistry of Circumstellar Dust Shells*. Cambridge Astrophysics. Cambridge University Press.

Gail, H. P., Wetzel, S., Pucci, A., and Tamanai, A. (2013). Seed particle formation for silicate dust condensation by SiO nucleation. A&A, 555:A119.

Gan, T., Wang, S. X., Wang, S., Mao, S., Huang, C. X., Collins, K. A., Stassun, K. G., Shporer, A., Zhu, W., Ricker, G. R., Vanderspek, R., Latham, D. W., Seager, S., Winn, J. N., Jenkins, J. M., Barkaoui, K., Belinski, A. A., Ciardi, D. R., Evans, P., Girardin, E., Maslennikova, N. A., Mazeh, T., Panahi, A., Pozuelos, F. J., Radford, D. J., Schwarz, R. P., Twicken, J. D., Wünsche, A., and Zucker, S. (2023). Occurrence Rate of Hot Jupiters Around Early-type M Dwarfs Based on Transiting Exoplanet Survey Satellite Data. AJ, 165(1):17.

Gänsicke, B. T., Koester, D., Farihi, J., Girven, J., Parsons, S. G., and Breedt, E. (2012). The chemical diversity of exo-terrestrial planetary debris around white dwarfs. MNRAS, 424(1):333–347.

Gao, P. and Benneke, B. (2018). Microphysics of KCl and ZnS Clouds on GJ 1214 b. ApJ, 863(2):165.

Gao, P., Marley, M. S., and Ackerman, A. S. (2018). Sedimentation Efficiency of Condensation Clouds in Substellar Atmospheres. ApJ, 855(2):86.

Gao, P., Wakeford, H. R., Moran, S. E., and Parmentier, V. (2021). Aerosols in Exoplanet Atmospheres. *Journal of Geophysical Research (Planets)*, 126(4):e06655.

Gent, M. R., Bergemann, M., Serenelli, A., Casagrande, L., Gerber, J. M., Heiter, U., Kovalev, M., Morel, T., Nardetto, N., Adibekyan, V., Silva Aguirre, V.,

Asplund, M., Belkacem, K., del Burgo, C., Bigot, L., Chiavassa, A., Rodríguez Díaz, L. F., Goupil, M.-J., González Hernández, J. I., Mourard, D., Merle, T., Mészáros, S., Marshall, D. J., Ouazzani, R.-M., Plez, B., Reese, D., Trampedach, R., and Tsantaki, M. (2022). The SAPP pipeline for the determination of stellar abundances and atmospheric parameters of stars in the core program of the PLATO mission. A&A, 658:A147.

GharibNezhad, E., Shayesteh, A., and Bernath, P. F. (2013). Einstein A coefficients for rovibronic lines of the A $^2\,\Pi \rightarrow$ X $^2\Sigma^+$ and B' $^2\Sigma^+ \rightarrow$ X $^2\,\Sigma^+$ transitions of MgH. MNRAS, 432(3):2043–2047.

Gobrecht, D., Plane, J. M. C., Bromley, S. T., Decin, L., Cristallo, S., and Sekaran, S. (2022). Bottom-up dust nucleation theory in oxygen-rich evolved stars. I. Aluminium oxide clusters. A&A, 658:A167.

Gorman, M. N., Yurchenko, S. N., and Tennyson, J. (2019). ExoMol molecular line lists XXXVI: X $^2\Pi$ - X $^2\Pi$ and A $^2\Sigma^+$ - X $^2\Pi$ transitions of SH. MNRAS, 490(2):1652–1665.

Grant, D., Lewis, N. K., Wakeford, H. R., Batalha, N. E., Glidden, A., Goyal, J., Mullens, E., MacDonald, R. J., May, E. M., Seager, S., Stevenson, K. B., Valenti, J. A., Visscher, C., Alderson, L., Allen, N. H., Cañas, C. I., Colón, K., Clampin, M., Espinoza, N., Gressier, A., Huang, J., Lin, Z., Long, D., Louie, D. R., Peña-Guerrero, M., Ranjan, S., Sotzen, K. S., Valentine, D., Anderson, J., Balmer, W. O., Bellini, A., Hoch, K. K. W., Kammerer, J., Libralato, M., Mountain, C. M., Perrin, M. D., Pueyo, L., Rickman, E., Rebollido, I., Sohn, S. T., van der Marel, R. P., and Watkins, L. L. (2023). JWST-TST DREAMS: Quartz Clouds in the Atmosphere of WASP-17b. ApJ, 956(2):L32.

Gray, D. F. (2021). *The Observation and Analysis of Stellar Photospheres*. Cambridge University Press, 4 edition.

Guillot, T., Fletcher, L. N., Helled, R., Ikoma, M., Line, M. R., and Parmentier, V. (2022). Giant Planets from the Inside-Out. *arXiv e-prints*, page arXiv:2205.04100.

Gupta, A. and Schlichting, H. E. (2019). Sculpting the valley in the radius distribution of small exoplanets as a by-product of planet formation: the core-powered mass-loss mechanism. MNRAS, 487(1):24–33.

Gustafsson, B., Bell, R. A., Eriksson, K., and Nordlund, A. (1975). A grid of model atmospheres for metal-deficient giant stars. I. A&A, 42:407–432.

Gustafsson, B., Edvardsson, B., Eriksson, K., Jørgensen, U. G., Nordlund, Å., and Plez, B. (2008). A grid of MARCS model atmospheres for late-type stars. I. Methods and general properties. A&A, 486(3):951–970.

Gustafsson, B. and Nissen, P. E. (1972). The metal-to-hydrogen ratio in F1 - F5 stars, as determined by a model-atmosphere analysis of photoelectric observations of a group of weak metal lines. A&A, 19:261.

Hammond, I., Christiaens, V., Price, D. J., Toci, C., Pinte, C., Juillard, S., and Garg, H. (2023). Confirmation and Keplerian motion of the gap-carving protoplanet HD 169142 b. MNRAS, 522(1):L51–L55.

Hansen, B. M. S. and Murray, N. (2012). Migration Then Assembly: Formation of Neptune-mass Planets inside 1 AU. ApJ, 751(2):158.

Hargreaves, R. J., Gordon, I. E., Rothman, L. S., Tashkun, S. A., Perevalov, V. I., Lukashevskaya, A. A., Yurchenko, S. N., Tennyson, J., and Müller, H. S. P. (2019). Spectroscopic line parameters of NO, NO_2, and N_2O for the HITEMP database. J. Quant. Spec. Radiat. Transf., 232:35–53.

Harrison, J. H. D., Bonsor, A., and Madhusudhan, N. (2018). Polluted white dwarfs: constraints on the origin and geology of exoplanetary material. MNRAS, 479(3):3814–3841.

Hartman, J. D., Bayliss, D., Brahm, R., Bakos, G. Á., Mancini, L., Jordán, A., Penev, K., Rabus, M., Zhou, G., Butler, R. P., Espinoza, N., de Val-Borro, M., Bhatti, W., Csubry, Z., Ciceri, S., Henning, T., Schmidt, B., Arriagada, P., Shectman, S., Crane, J., Thompson, I., Suc, V., Csák, B., Tan, T. G., Noyes, R. W., Lázár, J., Papp, I., and Sári, P. (2015). HATS-6b: A Warm Saturn Transiting an Early M Dwarf Star, and a Set of Empirical Relations for Characterizing K and M Dwarf Planet Hosts. AJ, 149(5):166.

Hauschildt, P. H. and Baron, E. (1999). Numerical solution of the expanding stellar atmosphere problem. *Journal of Computational and Applied Mathematics*, 109(1):41–63.

Helled, R., Bodenheimer, P., Podolak, M., Boley, A., Meru, F., Nayakshin, S., Fortney, J. J., Mayer, L., Alibert, Y., and Boss, A. P. (2014). Giant Planet Formation, Evolution, and Internal Structure. In Beuther, H., Klessen, R. S., Dullemond, C. P., and Henning, T., editors, *Protostars and Planets VI*, pages 643–665.

Helling, C. (2019). Exoplanet Clouds. *Annual Review of Earth and Planetary Sciences*, 47:583–606.

Helling, C., Ackerman, A., Allard, F., Dehn, M., Hauschildt, P., Homeier, D., Lodders, K., Marley, M., Rietmeijer, F., Tsuji, T., and Woitke, P. (2008a). A comparison of chemistry and dust cloud formation in ultracool dwarf model atmospheres. MNRAS, 391(4):1854–1873.

Helling, C., Dehn, M., Woitke, P., and Hauschildt, P. H. (2008b). Consistent Simulations of Substellar Atmospheres and Nonequilibrium Dust Cloud Formation. ApJ, 675(2):L105.

Helling, C. and Fomins, A. (2013). Modelling the formation of atmospheric dust in brown dwarfs and planetary atmospheres. *Philosophical Transactions of the Royal Society of London Series A*, 371(1994):20110581–20110581.

Helling, C., Gourbin, P., Woitke, P., and Parmentier, V. (2019a). Sparkling nights

and very hot days on WASP-18b: the formation of clouds and the emergence of an ionosphere. A&A, 626:A133.

Helling, C., Iro, N., Corrales, L., Samra, D., Ohno, K., Alam, M. K., Steinrueck, M., Lew, B., Molaverdikhani, K., MacDonald, R. J., Herbort, O., Woitke, P., and Parmentier, V. (2019b). Understanding the atmospheric properties and chemical composition of the ultra-hot Jupiter HAT-P-7b. I. Cloud and chemistry mapping. A&A, 631:A79.

Helling, C. and Woitke, P. (2006). Dust in brown dwarfs. V. Growth and evaporation of dirty dust grains. A&A, 455(1):325–338.

Helling, C., Woitke, P., Rimmer, P. B., Kamp, I., Thi, W.-F., and Meijerink, R. (2014). Disk Evolution, Element Abundances and Cloud Properties of Young Gas Giant Planets. *Life*, 4(2):142–173.

Helling, C., Woitke, P., and Thi, W. F. (2008c). Dust in brown dwarfs and extrasolar planets. I. Chemical composition and spectral appearance of quasi-static cloud layers. A&A, 485(2):547–560.

Helling, Ch., Kawashima, Y., Graham, V., Samra, D., Chubb, K. L., Min, M., Waters, L. B. F. M., and Parmentier, V. (2020). Mineral cloud and hydrocarbon haze particles in the atmosphere of the hot Jupiter JWST target WASP-43b. A&A, 641:A178.

Helling, Ch., Lewis, D., Samra, D., Carone, L., Graham, V., Herbort, O., Chubb, K. L., Min, M., Waters, R., Parmentier, V., and Mayne, N. (2021). Cloud property trends in hot and ultra-hot giant gas planets (WASP-43b, WASP-103b, WASP-121b, HAT-P-7b, and WASP-18b). A&A, 649:A44.

Helling, Ch., Samra, D., Lewis, D., Calder, R., Hirst, G., Woitke, P., Baeyens, R., Carone, L., Herbort, O., and Chubb, K. L. (2023). Exoplanet weather and climate regimes with clouds and thermal ionospheres. A model grid study in support of large-scale observational campaigns. A&A, 671:A122.

Henning, T., Begemann, B., Mutschke, H., and Dorschner, J. (1995). Optical properties of oxide dust grains. A&AS, 112:143.

Henning, T. and Mutschke, H. (1997). Low-temperature infrared properties of cosmic dust analogues. A&A, 327:743–754.

Henry, G. W., Marcy, G. W., Butler, R. P., and Vogt, S. S. (2000). A Transiting "51 Peg-like" Planet. ApJ, 529(1):L41–L44.

Henyey, L., Vardya, M. S., and Bodenheimer, P. (1965). Studies in Stellar Evolution. III. The Calculation of Model Envelopes. ApJ, 142:841.

Henyey, L. G. and Greenstein, J. L. (1941). Diffuse radiation in the Galaxy. ApJ, 93:70–83.

Ho, C. S. K., Rogers, J. G., Van Eylen, V., Owen, J. E., and Schlichting, H. E.

(2024). Shallower radius valley around low-mass hosts: evidence for icy planets, collisions, or high-energy radiation scatter. MNRAS, 531(3):3698–3714.

Howard, A. W., Marcy, G. W., Bryson, S. T., Jenkins, J. M., Rowe, J. F., Batalha, N. M., Borucki, W. J., Koch, D. G., Dunham, E. W., Gautier, Thomas N., I., Van Cleve, J., Cochran, W. D., Latham, D. W., Lissauer, J. J., Torres, G., Brown, T. M., Gilliland, R. L., Buchhave, L. A., Caldwell, D. A., Christensen-Dalsgaard, J., Ciardi, D., Fressin, F., Haas, M. R., Howell, S. B., Kjeldsen, H., Seager, S., Rogers, L., Sasselov, D. D., Steffen, J. H., Basri, G. S., Charbonneau, D., Christiansen, J., Clarke, B., Dupree, A., Fabrycky, D. C., Fischer, D. A., Ford, E. B., Fortney, J. J., Tarter, J., Girouard, F. R., Holman, M. J., Johnson, J. A., Klaus, T. C., Machalek, P., Moorhead, A. V., Morehead, R. C., Ragozzine, D., Tenenbaum, P., Twicken, J. D., Quinn, S. N., Isaacson, H., Shporer, A., Lucas, P. W., Walkowicz, L. M., Welsh, W. F., Boss, A., Devore, E., Gould, A., Smith, J. C., Morris, R. L., Prsa, A., Morton, T. D., Still, M., Thompson, S. E., Mullally, F., Endl, M., and MacQueen, P. J. (2012). Planet Occurrence within 0.25 AU of Solar-type Stars from Kepler. ApJS, 201(2):15.

Howard, A. W., Marcy, G. W., Johnson, J. A., Fischer, D. A., Wright, J. T., Isaacson, H., Valenti, J. A., Anderson, J., Lin, D. N. C., and Ida, S. (2010). The Occurrence and Mass Distribution of Close-in Super-Earths, Neptunes, and Jupiters. *Science*, 330(6004):653.

Hu, R., Damiano, M., Scheucher, M., Kite, E., Seager, S., and Rauer, H. (2021). Unveiling Shrouded Oceans on Temperate sub-Neptunes via Transit Signatures of Solubility Equilibria versus Gas Thermochemistry. ApJ, 921(1):L8.

Huber, D., Silva Aguirre, V., Matthews, J. M., Pinsonneault, M. H., Gaidos, E., García, R. A., Hekker, S., Mathur, S., Mosser, B., Torres, G., Bastien, F. A., Basu, S., Bedding, T. R., Chaplin, W. J., Demory, B.-O., Fleming, S. W., Guo, Z., Mann, A. W., Rowe, J. F., Serenelli, A. M., Smith, M. A., and Stello, D. (2014). Revised Stellar Properties of Kepler Targets for the Quarter 1-16 Transit Detection Run. ApJS, 211(1):2.

Ida, S. and Lin, D. N. C. (2008). Toward a Deterministic Model of Planetary Formation. V. Accumulation Near the Ice Line and Super-Earths. ApJ, 685(1):584–595.

Ito, Y., Ikoma, M., Kawahara, H., Nagahara, H., Kawashima, Y., and Nakamoto, T. (2015). Theoretical Emission Spectra of Atmospheres of Hot Rocky Super-Earths. ApJ, 801(2):144.

Jaeger, C., Molster, F. J., Dorschner, J., Henning, T., Mutschke, H., and Waters, L. B. F. M. (1998). Steps toward interstellar silicate mineralogy. IV. The crystalline revolution. A&A, 339:904–916.

Jaeger, C., Mutschke, H., Begemann, B., Dorschner, J., and Henning, T. (1994). Steps toward interstellar silicate mineralogy. I. Laboratory results of a silicate glass of mean cosmic composition. A&A, 292:641–655.

Jäger, C., Dorschner, J., Mutschke, H., Posch, T., and Henning, T. (2003). Steps toward interstellar silicate mineralogy. VII. Spectral properties and crystallization behaviour of magnesium silicates produced by the sol-gel method. A&A, 408:193–204.

Jeong, K. S., Chang, C., Sedlmayr, E., and Sülzle, D. (2000). Electronic structure investigation of neutral titanium oxide molecules Ti_xO_y. *Journal of Physics B Atomic Molecular Physics*, 33(17):3417–3430.

Johansen, A. and Lambrechts, M. (2017). Forming Planets via Pebble Accretion. *Annual Review of Earth and Planetary Sciences*, 45(1):359–387.

John, T. L. (1967). The Free-Free Transitions of Heˆ at Threshold. ApJ, 149:449.

Jørgensen, U. G. (1992). Sampling Methods. Rev. Mexicana Astron. Astrofis., 23:195.

Jørgensen, U. G., Amadio, F., Campos Estrada, B., Holten Møller, K., Schneider, A. D., Balduin, T., D'Alessandro, A., Symeonidou, E., Helling, C., Nordlund, Å., and Woitke, P. (2024). A grid of self-consistent MSG (MARCS-StaticWeather-GGchem) cool stellar, sub-stellar, and exoplanetary model atmospheres. *arXiv e-prints*, page arXiv:2407.09397.

Jørgensen, U. G., Hammer, D., Borysow, A., and Falkesgaard, J. (2000). The atmospheres of cool, helium-rich white dwarfs. A&A, 361:283–292.

Jørgensen, U. G., Johnson, H. R., and Nordlund, A. (1992). Effects of sphericity in carbon star atmospheres. A&A, 261:263–273.

Juncher, D., Jørgensen, U. G., and Helling, C. (2017). Self-consistent atmosphere modeling with cloud formation for low-mass stars and exoplanets. A&A, 608:A70.

Jura, M. and Young, E. D. (2014). Extrasolar Cosmochemistry. *Annual Review of Earth and Planetary Sciences*, 42(1):45–67.

Jurgenson, C., Fischer, D., McCracken, T., Sawyer, D., Szymkowiak, A., Davis, A., Muller, G., and Santoro, F. (2016). EXPRES: a next generation RV spectrograph in the search for earth-like worlds. In Evans, C. J., Simard, L., and Takami, H., editors, *Ground-based and Airborne Instrumentation for Astronomy VI*, volume 9908 of *Society of Photo-Optical Instrumentation Engineers (SPIE) Conference Series*, page 99086T.

Kang, W., Ding, F., Wordsworth, R., and Seager, S. (2021). Escaping Outflows from Disintegrating Exoplanets: Day-side versus Night-side Escape. ApJ, 906(2):67.

Kargel, J. S. and Lewis, J. S. (1993). The Composition and Early Evolution of Earth. Icarus, 105(1):1–25.

Karzas, W. J. and Latter, R. (1961). Electron Radiative Transitions in a Coulomb Field. ApJS, 6:167.

Kawahara, H., Hirano, T., Kurosaki, K., Ito, Y., and Ikoma, M. (2013). Starspots-Transit Depth Relation of the Evaporating Planet Candidate KIC 12557548b. ApJ, 776(1):L6.

Kawashima, Y. and Ikoma, M. (2018). Theoretical Transmission Spectra of Exoplanet Atmospheres with Hydrocarbon Haze: Effect of Creation, Growth, and Settling of Haze Particles. I. Model Description and First Results. ApJ, 853(1):7.

Kimura, H., Mann, I., Biesecker, D. A., and Jessberger, E. K. (2002). Dust Grains in the Comae and Tails of Sungrazing Comets: Modeling of Their Mineralogical and Morphological Properties. Icarus, 159(2):529–541.

Kippenhahn, R., Weigert, A., and Weiss, A. (2013). *Stellar Structure and Evolution*.

Kirchhoff, G. (1860). Ueber das Verhältniss zwischen dem Emissionsvermögen und dem Absorptionsvermögen der Körper für Wärme und Licht. *Annalen der Physik*, 185(2):275–301.

Kirkpatrick, J. D. (2005). New Spectral Types L and T. ARA&A, 43(1):195–245.

Kite, E. S., Fegley, Bruce, J., Schaefer, L., and Gaidos, E. (2016). Atmosphere-interior Exchange on Hot, Rocky Exoplanets. ApJ, 828(2):80.

Kite, E. S. and Schaefer, L. (2021). Water on Hot Rocky Exoplanets. ApJ, 909(2):L22.

Kitzmann, D. and Heng, K. (2018). Optical properties of potential condensates in exoplanetary atmospheres. MNRAS, 475(1):94–107.

Koike, C., Kaito, C., Yamamoto, T., Shibai, H., Kimura, S., and Suto, H. (1995a). Extinction spectra of corundum in the wavelengths from UV to FIR. Icarus, 114(1):203–214.

Koike, C., Kaito, C., Yamamoto, T., Shibai, H., Kimura, S., and Suto, H. (1995b). Extinction spectra of corundum in the wavelengths from UV to FIR. Icarus, 114(1):203–214.

Konacki, M., Torres, G., Jha, S., and Sasselov, D. D. (2003). An extrasolar planet that transits the disk of its parent star. Nature, 421(6922):507–509.

Kreidberg, L. (2018). *Exoplanet Atmosphere Measurements from Transmission Spectroscopy and Other Planet Star Combined Light Observations*, pages 2083–2105. Springer International Publishing, Cham.

Kreidberg, L., Bean, J. L., Désert, J.-M., Line, M. R., Fortney, J. J., Madhusudhan, N., Stevenson, K. B., Showman, A. P., Charbonneau, D., McCullough, P. R., Seager, S., Burrows, A., Henry, G. W., Williamson, M., Kataria, T., and Homeier, D. (2014). A Precise Water Abundance Measurement for the Hot Jupiter WASP-43b. ApJ, 793(2):L27.

Kreidberg, L., Koll, D. D. B., Morley, C., Hu, R., Schaefer, L., Deming, D.,

Stevenson, K. B., Dittmann, J., Vanderburg, A., Berardo, D., Guo, X., Stassun, K., Crossfield, I., Charbonneau, D., Latham, D. W., Loeb, A., Ricker, G., Seager, S., and Vanderspek, R. (2019). Absence of a thick atmosphere on the terrestrial exoplanet LHS 3844b. Nature, 573(7772):87–90.

Lam, J., Amans, D., Dujardin, C., Ledoux, G., and Allouche, A.-R. (2015). Atomistic Mechanisms for the Nucleation of Aluminum Oxide Nanoparticles. *Journal of Physical Chemistry A*, 119(33):8944–8949.

Lambert, D. L., Gustafsson, B., Eriksson, K., and Hinkle, K. H. (1986). The Chemical Composition of Carbon Stars. I. Carbon, Nitrogen, and Oxygen in 30 Cool Carbon Stars in the Galactic Disk. ApJS, 62:373.

Lambrechts, M., Johansen, A., and Morbidelli, A. (2014). Separating gas-giant and ice-giant planets by halting pebble accretion. A&A, 572:A35.

Langmuir, I. (1913). The Vapor Pressure of Metallic Tungsten. *Physical Review*, 2(5):329–342.

Lecavelier des Etangs, A. and Lissauer, J. J. (2022). The iau working definition of an exoplanet. *New Astronomy Reviews*, 94:101641.

Lecoq-Molinos, H., Gobrecht, D., Sindel, J. P., Helling, C., and Decin, L. (2024). Vanadium oxide clusters in substellar atmospheres: A quantum chemical study. *arXiv e-prints*, page arXiv:2401.02784.

Lee, E., Dobbs-Dixon, I., Helling, C., Bognar, K., and Woitke, P. (2016). Dynamic mineral clouds on HD 189733b. I. 3D RHD with kinetic, non-equilibrium cloud formation. A&A, 594:A48.

Lee, E., Helling, C., Dobbs-Dixon, I., and Juncher, D. (2015). Modelling the local and global cloud formation on HD 189733b. A&A, 580:A12.

Lee, E. J., Karalis, A., and Thorngren, D. P. (2022). Creating the Radius Gap without Mass Loss. ApJ, 941(2):186.

Lee, E. K. H., Blecic, J., and Helling, C. (2018). Dust in brown dwarfs and extra-solar planets. VI. Assessing seed formation across the brown dwarf and exoplanet regimes. A&A, 614:A126.

Lesur, G., Ercolano, B., Flock, M., Lin, M. K., Yang, C. C., Barranco, J. A., Benitez-Llambay, P., Goodman, J., Johansen, A., Klahr, H., Laibe, G., Lyra, W., Marcus, P., Nelson, R. P., Squire, J., Simon, J. B., Turner, N., Umurhan, O. M., and Youdin, A. N. (2022). Hydro-, Magnetohydro-, and Dust-Gas Dynamics of Protoplanetary Disks. *arXiv e-prints*, page arXiv:2203.09821.

Li, G., Gordon, I. E., Rothman, L. S., Tan, Y., Hu, S.-M., Kassi, S., Campargue, A., and Medvedev, E. S. (2015). Rovibrational Line Lists for Nine Isotopologues of the CO Molecule in the X $^1\Sigma^+$ Ground Electronic State. ApJS, 216(1):15.

Lichtenberg, T. (2021). Redox Hysteresis of Super-Earth Exoplanets from Magma Ocean Circulation. ApJ, 914(1):L4.

Lieshout, R. v. and Rappaport, S. A. (2018). *Disintegrating Rocky Exoplanets*, pages 1527–1544. Springer International Publishing, Cham.

Lihrmann, J.-M. (2008). Thermodynamics of the al2o3–al4c3 system: I. thermochemical functions of al oxide, carbide and oxycarbides between 298 and 2100k. *Journal of the European Ceramic Society*, 28(3):633 – 642.

Line, M. R., Stevenson, K. B., Bean, J., Desert, J.-M., Fortney, J. J., Kreidberg, L., Madhusudhan, N., Showman, A. P., and Diamond-Lowe, H. (2016). No Thermal Inversion and a Solar Water Abundance for the Hot Jupiter HD 209458b from HST/WFC3 Spectroscopy. AJ, 152(6):203.

Liu, M. C., Dupuy, T. J., and Allers, K. N. (2016). The Hawaii Infrared Parallax Program. II. Young Ultracool Field Dwarfs. ApJ, 833(1):96.

Liu, P., Biller, B. A., Vos, J. M., Whiteford, N., Zhang, Z., Liu, M. C., Fontanive, C., Manjavacas, E., Henning, T., Kenworthy, M. A., Bonavita, M., Bonnefoy, M., Bubb, E., Petrus, S., and Schlieder, J. (2024). A near-infrared variability survey of young planetary-mass objects. MNRAS, 527(3):6624–6674.

Looyenga, H. (1965). Dielectric constants of heterogeneous mixtures. *Physica*, 31(3):401–406.

Lopez, E. D. and Fortney, J. J. (2013). The Role of Core Mass in Controlling Evaporation: The Kepler Radius Distribution and the Kepler-36 Density Dichotomy. ApJ, 776(1):2.

Lothringer, J. D., Rustamkulov, Z., Sing, D. K., Gibson, N. P., Wilson, J., and Schlaufman, K. C. (2021). A New Window into Planet Formation and Migration: Refractory-to-Volatile Elemental Ratios in Ultra-hot Jupiters. ApJ, 914(1):12.

Ludwig, H. G., Allard, F., and Hauschildt, P. H. (2002). Numerical simulations of surface convection in a late M-dwarf. A&A, 395:99–115.

Luna, J. L. and Morley, C. V. (2021). Empirically Determining Substellar Cloud Compositions in the Era of the James Webb Space Telescope. ApJ, 920(2):146.

Lunine, J. I., Hubbard, W. B., and Marley, M. S. (1986). Evolution and Infrared Spectra of Brown Dwarfs. ApJ, 310:238.

Luque, R. and Pallé, E. (2022). Density, not radius, separates rocky and water-rich small planets orbiting M dwarf stars. *Science*, 377(6611):1211–1214.

Macintosh, B., Graham, J. R., Barman, T., De Rosa, R. J., Konopacky, Q., Marley, M. S., Marois, C., Nielsen, E. L., Pueyo, L., Rajan, A., Rameau, J., Saumon, D., Wang, J. J., Patience, J., Ammons, M., Arriaga, P., Artigau, E., Beckwith, S., Brewster, J., Bruzzone, S., Bulger, J., Burningham, B., Burrows, A. S., Chen, C., Chiang, E., Chilcote, J. K., Dawson, R. I., Dong, R., Doyon, R., Draper, Z. H., Duchêne, G., Esposito, T. M., Fabrycky, D., Fitzgerald, M. P., Follette, K. B., Fortney, J. J., Gerard, B., Goodsell, S., Greenbaum, A. Z., Hibon, P., Hinkley, S., Cotten, T. H., Hung, L. W., Ingraham, P., Johnson-

Groh, M., Kalas, P., Lafreniere, D., Larkin, J. E., Lee, J., Line, M., Long, D., Maire, J., Marchis, F., Matthews, B. C., Max, C. E., Metchev, S., Millar-Blanchaer, M. A., Mittal, T., Morley, C. V., Morzinski, K. M., Murray-Clay, R., Oppenheimer, R., Palmer, D. W., Patel, R., Perrin, M. D., Poyneer, L. A., Rafikov, R. R., Rantakyrö, F. T., Rice, E. L., Rojo, P., Rudy, A. R., Ruffio, J. B., Ruiz, M. T., Sadakuni, N., Saddlemyer, L., Salama, M., Savransky, D., Schneider, A. C., Sivaramakrishnan, A., Song, I., Soummer, R., Thomas, S., Vasisht, G., Wallace, J. K., Ward-Duong, K., Wiktorowicz, S. J., Wolff, S. G., and Zuckerman, B. (2015). Discovery and spectroscopy of the young jovian planet 51 Eri b with the Gemini Planet Imager. *Science*, 350(6256):64–67.

Madhusudhan, N., Piette, A. A. A., and Constantinou, S. (2021). Habitability and Biosignatures of Hycean Worlds. ApJ, 918(1):1.

Madhusudhan, N., Sarkar, S., Constantinou, S., Holmberg, M., Piette, A. A. A., and Moses, J. I. (2023). Carbon-bearing Molecules in a Possible Hycean Atmosphere. ApJ, 956(1):L13.

Mahapatra, G., Helling, C., and Miguel, Y. (2017). Cloud formation in metal-rich atmospheres of hot super-Earths like 55 Cnc e and CoRoT7b. MNRAS, 472(1):447–464.

Mandel, K. and Agol, E. (2002). Analytic Light Curves for Planetary Transit Searches. ApJ, 580(2):L171–L175.

Manjavacas, E., Tremblin, P., Birkmann, S., Valenti, J., Alves de Oliveira, C., Beck, T. L., Giardino, G., Lützgendorf, N., Rauscher, B. J., and Sirianni, M. (2024). Medium-resolution 0.97–5.3 μm Spectra of Very Young Benchmark Brown Dwarfs with NIRSpec on Board the James Webb Space Telescope. AJ, 167(4):168.

Marley, M. S., Seager, S., Saumon, D., Lodders, K., Ackerman, A. S., Freedman, R. S., and Fan, X. (2002). Clouds and Chemistry: Ultracool Dwarf Atmospheric Properties from Optical and Infrared Colors. ApJ, 568(1):335–342.

Marois, C., Macintosh, B., Barman, T., Zuckerman, B., Song, I., Patience, J., Lafrenière, D., and Doyon, R. (2008). Direct Imaging of Multiple Planets Orbiting the Star HR 8799. *Science*, 322(5906):1348.

Martin, E. C., Mace, G. N., McLean, I. S., Logsdon, S. E., Rice, E. L., Kirkpatrick, J. D., Burgasser, A. J., McGovern, M. R., and Prato, L. (2017). Surface Gravities for 228 M, L, and T Dwarfs in the NIRSPEC Brown Dwarf Spectroscopic Survey. ApJ, 838(1):73.

Masseron, T., Plez, B., Van Eck, S., Colin, R., Daoutidis, I., Godefroid, M., Coheur, P. F., Bernath, P., Jorissen, A., and Christlieb, N. (2014). CH in stellar atmospheres: an extensive linelist. A&A, 571:A47.

Matthews, E. C., Carter, A. L., Pathak, P., Morley, C. V., Phillips, M. W., P. M, S. K., Feng, F., Bonse, M. J., Boogaard, L. A., Burt, J. A., Crossfield, I. J. M.,

Douglas, E. S., Henning, T., Hom, J., Ko, C. L., Kasper, M., Lagrange, A. M., Petit dit de la Roche, D., and Philipot, F. (2024). A temperate super-jupiter imaged with jwst in the mid-infrared. *Nature*.

Mayor, M., Marmier, M., Lovis, C., Udry, S., Ségransan, D., Pepe, F., Benz, W., Bertaux, J. L., Bouchy, F., Dumusque, X., Lo Curto, G., Mordasini, C., Queloz, D., and Santos, N. C. (2011). The HARPS search for southern extra-solar planets XXXIV. Occurrence, mass distribution and orbital properties of super-Earths and Neptune-mass planets. *arXiv e-prints*, page arXiv:1109.2497.

Mayor, M., Pepe, F., Queloz, D., Bouchy, F., Rupprecht, G., Lo Curto, G., Avila, G., Benz, W., Bertaux, J. L., Bonfils, X., Dall, T., Dekker, H., Delabre, B., Eckert, W., Fleury, M., Gilliotte, A., Gojak, D., Guzman, J. C., Kohler, D., Lizon, J. L., Longinotti, A., Lovis, C., Megevand, D., Pasquini, L., Reyes, J., Sivan, J. P., Sosnowska, D., Soto, R., Udry, S., van Kesteren, A., Weber, L., and Weilenmann, U. (2003). Setting New Standards with HARPS. *The Messenger*, 114:20–24.

Mayor, M. and Queloz, D. (1995). A Jupiter-mass companion to a solar-type star. Nature, 378(6555):355–359.

Mazeh, T., Naef, D., Torres, G., Latham, D. W., Mayor, M., Beuzit, J.-L., Brown, T. M., Buchhave, L., Burnet, M., Carney, B. W., Charbonneau, D., Drukier, G. A., Laird, J. B., Pepe, F., Perrier, C., Queloz, D., Santos, N. C., Sivan, J.-P., Udry, S., and Zucker, S. (2000). The Spectroscopic Orbit of the Planetary Companion Transiting HD 209458. ApJ, 532(1):L55–L58.

McGovern, M. R., Kirkpatrick, J. D., McLean, I. S., Burgasser, A. J., Prato, L., and Lowrance, P. J. (2004). Identifying Young Brown Dwarfs Using Gravity-Sensitive Spectral Features. ApJ, 600(2):1020–1024.

McKemmish, L. K., Masseron, T., Hoeijmakers, H. J., Pérez-Mesa, V., Grimm, S. L., Yurchenko, S. N., and Tennyson, J. (2019). ExoMol molecular line lists - XXXIII. The spectrum of Titanium Oxide. MNRAS, 488(2):2836–2854.

McKemmish, L. K., Yurchenko, S. N., and Tennyson, J. (2016). ExoMol line lists - XVIII. The high-temperature spectrum of VO. MNRAS, 463(1):771–793.

Metchev, S. A., Heinze, A., Apai, D., Flateau, D., Radigan, J., Burgasser, A., Marley, M. S., Artigau, É., Plavchan, P., and Goldman, B. (2015). Weather on Other Worlds. II. Survey Results: Spots are Ubiquitous on L and T Dwarfs. ApJ, 799(2):154.

Mie, G. (1908). Beiträge zur Optik trüber Medien, speziell kolloidaler Metallösungen. *Annalen der Physik*, 330(3):377–445.

Miguel, Y., Kaltenegger, L., Fegley, B., and Schaefer, L. (2011). Compositions of Hot Super-earth Atmospheres: Exploring Kepler Candidates. ApJ, 742(2):L19.

Mihalas, D. (1965). Model Atmospheres and Line Profiles for Early-Type Stars. ApJS, 11:184.

Mihalas, D. (1978). *Stellar atmospheres*.

Miles, B. E., Biller, B. A., Patapis, P., Worthen, K., Rickman, E., Hoch, K. K. W., Skemer, A., Perrin, M. D., Whiteford, N., Chen, C. H., Sargent, B., Mukherjee, S., Morley, C. V., Moran, S. E., Bonnefoy, M., Petrus, S., Carter, A. L., Choquet, E., Hinkley, S., Ward-Duong, K., Leisenring, J. M., Millar-Blanchaer, M. A., Pueyo, L., Ray, S., Sallum, S., Stapelfeldt, K. R., Stone, J. M., Wang, J. J., Absil, O., Balmer, W. O., Boccaletti, A., Bonavita, M., Booth, M., Bowler, B. P., Chauvin, G., Christiaens, V., Currie, T., Danielski, C., Fortney, J. J., Girard, J. H., Grady, C. A., Greenbaum, A. Z., Henning, T., Hines, D. C., Janson, M., Kalas, P., Kammerer, J., Kennedy, G. M., Kenworthy, M. A., Kervella, P., Lagage, P.-O., Lew, B. W. P., Liu, M. C., Macintosh, B., Marino, S., Marley, M. S., Marois, C., Matthews, E. C., Matthews, B. C., Mawet, D., McElwain, M. W., Metchev, S., Meyer, M. R., Molliere, P., Pantin, E., Quirrenbach, A., Rebollido, I., Ren, B. B., Schneider, G., Vasist, M., Wyatt, M. C., Zhou, Y., Briesemeister, Z. W., Bryan, M. L., Calissendorff, P., Cantalloube, F., Cugno, G., De Furio, M., Dupuy, T. J., Factor, S. M., Faherty, J. K., Fitzgerald, M. P., Franson, K., Gonzales, E. C., Hood, C. E., Howe, A. R., Kraus, A. L., Kuzuhara, M., Lagrange, A.-M., Lawson, K., Lazzoni, C., Liu, P., Llop-Sayson, J., Lloyd, J. P., Martinez, R. A., Mazoyer, J., Quanz, S. P., Redai, J. A., Samland, M., Schlieder, J. E., Tamura, M., Tan, X., Uyama, T., Vigan, A., Vos, J. M., Wagner, K., Wolff, S. G., Ygouf, M., Zhang, X., Zhang, K., and Zhang, Z. (2023). The JWST Early-release Science Program for Direct Observations of Exoplanetary Systems II: A 1 to 20 μm Spectrum of the Planetary-mass Companion VHS 1256-1257 b. ApJ, 946(1):L6.

Min, M., Dominik, C., and Waters, L. B. F. M. (2004). Spectroscopic diagnostic for the mineralogy of large dust grains. A&A, 413:L35–L38.

Min, M., Ormel, C. W., Chubb, K., Helling, C., and Kawashima, Y. (2020). The ARCiS framework for exoplanet atmospheres. Modelling philosophy and retrieval. A&A, 642:A28.

Misener, W., Schlichting, H. E., and Young, E. D. (2023). Atmospheres as windows into sub-Neptune interiors: coupled chemistry and structure of hydrogen-silane-water envelopes. MNRAS, 524(1):981–992.

Mollière, P., Molyarova, T., Bitsch, B., Henning, T., Schneider, A., Kreidberg, L., Eistrup, C., Burn, R., Nasedkin, E., Semenov, D., Mordasini, C., Schlecker, M., Schwarz, K. R., Lacour, S., Nowak, M., and Schulik, M. (2022). Interpreting the Atmospheric Composition of Exoplanets: Sensitivity to Planet Formation Assumptions. ApJ, 934(1):74.

Mollière, P. and Mordasini, C. (2012). Deuterium burning in objects forming via the core accretion scenario. Brown dwarfs or planets? A&A, 547:A105.

Mollière, P., van Boekel, R., Bouwman, J., Henning, T., Lagage, P. O., and Min, M. (2017). Observing transiting planets with JWST. Prime targets and their synthetic spectral observations. A&A, 600:A10.

Morbidelli, A., Lambrechts, M., Jacobson, S., and Bitsch, B. (2015). The great dichotomy of the Solar System: Small terrestrial embryos and massive giant planet cores. Icarus, 258:418–429.

Morello, G., Gerber, J., Plez, B., Bergemann, M., Cabrera, J., Ludwig, H.-G., and Morel, T. (2022). First Release of PLATO Consortium Stellar Limb-darkening Coefficients. *Research Notes of the American Astronomical Society*, 6(11):248.

Morley, C. V., Mukherjee, S., Marley, M. S., Fortney, J. J., Visscher, C., Lupu, R., Gharib-Nezhad, E., Thorngren, D., Freedman, R., and Batalha 7, N. (2024). The Sonora Substellar Atmosphere Models. III. Diamondback: Atmospheric Properties, Spectra, and Evolution for Warm Cloudy Substellar Objects. *arXiv e-prints*, page arXiv:2402.00758.

Mukherjee, S., Batalha, N. E., Fortney, J. J., and Marley, M. S. (2023). PICASO 3.0: A One-dimensional Climate Model for Giant Planets and Brown Dwarfs. ApJ, 942(2):71.

Mulders, G. D., Pascucci, I., Apai, D., and Ciesla, F. J. (2018). The Exoplanet Population Observation Simulator. I. The Inner Edges of Planetary Systems. AJ, 156(1):24.

Mysen, B. O. and Kushiro, I. (1988). Condensation, evaporation, melting, and crystallization in the primitive solar nebula: experimental data in the system MgO-SiO-H_2 to 1.0×10^{-9}bar and 1870°C with variable oxygen fugacity. *American Mineralogist*, 73(1):1–19.

Nagahara, H., Kushiro, I., and Mysen, B. O. (1994). Evaporation of olivine: Low pressure phase relations of the olivine system and its implication for the origin of chondritic components in the solar nebula. Geochim. Cosmochim. Acta, 58(8):1951–1963.

Neil, A. R., Liston, J., and Rogers, L. A. (2022). Evaluating the Evidence for Water World Populations Using Mixture Models. ApJ, 933(1):63.

Neil, A. R. and Rogers, L. A. (2020). A Joint Mass-Radius-Period Distribution of Exoplanets. ApJ, 891(1):12.

Nikolov, N., Sing, D. K., Fortney, J. J., Goyal, J. M., Drummond, B., Evans, T. M., Gibson, N. P., De Mooij, E. J. W., Rustamkulov, Z., Wakeford, H. R., Smalley, B., Burgasser, A. J., Hellier, C., Helling, C., Mayne, N. J., Madhusudhan, N., Kataria, T., Baines, J., Carter, A. L., Ballester, G. E., Barstow, J. K., McCleery, J., and Spake, J. J. (2018). An absolute sodium abundance for a cloud-free 'hot Saturn' exoplanet. Nature, 557(7706):526–529.

Noll, K. S., Geballe, T. R., Leggett, S. K., and Marley, M. S. (2000). The Onset of Methane in L Dwarfs. ApJ, 541(2):L75–L78.

Nordlund, A. (1974). On Convection in Stellar Atmospheres. A&A, 32:407.

Nuth, Joseph A., I. and Ferguson, F. T. (2006). Silicates Do Nucleate in

Oxygen-rich Circumstellar Outflows: New Vapor Pressure Data for SiO. ApJ, 649(2):1178–1183.

Öberg, K. I., Murray-Clay, R., and Bergin, E. A. (2011). The Effects of Snowlines on C/O in Planetary Atmospheres. ApJ, 743(1):L16.

Ohno, K. and Okuzumi, S. (2017). A Condensation-coalescence Cloud Model for Exoplanetary Atmospheres: Formulation and Test Applications to Terrestrial and Jovian Clouds. ApJ, 835(2):261.

Okuya, A., Okuzumi, S., Ohno, K., and Hirano, T. (2020). Constraining the Bulk Composition of Disintegrating Exoplanets Using Combined Transmission Spectra from JWST and SPICA. ApJ, 901(2):171.

O'Neill, H. S. C. and Palme, H. (1998). *Composition of the Silicate Earth: Implications for Accretion and Core Formation*, pages 3 – 126. Cambridge University Press.

Ormel, C. W. and Min, M. (2019). ARCiS framework for exoplanet atmospheres. The cloud transport model. A&A, 622:A121.

Owen, J. E. and Adams, F. C. (2014). Magnetically controlled mass-loss from extrasolar planets in close orbits. MNRAS, 444(4):3761–3779.

Owen, J. E. and Wu, Y. (2013). Kepler Planets: A Tale of Evaporation. ApJ, 775(2):105.

Owen, J. E. and Wu, Y. (2017). The Evaporation Valley in the Kepler Planets. ApJ, 847(1):29.

Owens, A., Dooley, S., McLaughlin, L., Tan, B., Zhang, G., Yurchenko, S. N., and Tennyson, J. (2022). ExoMol line lists - XLV. Rovibronic molecular line lists of calcium monohydride (CaH) and magnesium monohydride (MgH). MNRAS, 511(4):5448–5461.

Palik, E. D. (1985). *Handbook of optical constants of solids.*

Palik, E. D. (1991). *Handbook of optical constants of solids II.*

Patrascu, A. T., Yurchenko, S. N., and Tennyson, J. (2015). ExoMol molecular line lists - IX. The spectrum of AlO. MNRAS, 449(4):3613–3619.

Paulose, G., Barton, E. J., Yurchenko, S. N., and Tennyson, J. (2015). ExoMol molecular line lists - XII. Line lists for eight isotopologues of CS. MNRAS, 454(2):1931–1939.

Peach, G. (1970). Continuous absorption coefficients for non-hydrogenic atoms. MmRAS, 73:1.

Pearson, S. G. and McCaughrean, M. J. (2023). Jupiter Mass Binary Objects in the Trapezium Cluster. *arXiv e-prints*, page arXiv:2310.01231.

Pepe, F., Cristiani, S., Rebolo, R., Santos, N. C., Dekker, H., Cabral, A., Di Marcantonio, P., Figueira, P., Lo Curto, G., Lovis, C., Mayor, M., Mégevand, D., Molaro, P., Riva, M., Zapatero Osorio, M. R., Amate, M., Manescau, A., Pasquini, L., Zerbi, F. M., Adibekyan, V., Abreu, M., Affolter, M., Alibert, Y., Aliverti, M., Allart, R., Allende Prieto, C., Álvarez, D., Alves, D., Avila, G., Baldini, V., Bandy, T., Barros, S. C. C., Benz, W., Bianco, A., Borsa, F., Bourrier, V., Bouchy, F., Broeg, C., Calderone, G., Cirami, R., Coelho, J., Conconi, P., Coretti, I., Cumani, C., Cupani, G., D'Odorico, V., Damasso, M., Deiries, S., Delabre, B., Demangeon, O. D. S., Dumusque, X., Ehrenreich, D., Faria, J. P., Fragoso, A., Genolet, L., Genoni, M., Génova Santos, R., González Hernández, J. I., Hughes, I., Iwert, O., Kerber, F., Knudstrup, J., Landoni, M., Lavie, B., Lillo-Box, J., Lizon, J. L., Maire, C., Martins, C. J. A. P., Mehner, A., Micela, G., Modigliani, A., Monteiro, M. A., Monteiro, M. J. P. F. G., Moschetti, M., Murphy, M. T., Nunes, N., Oggioni, L., Oliveira, A., Oshagh, M., Pallé, E., Pariani, G., Poretti, E., Rasilla, J. L., Rebordão, J., Redaelli, E. M., Santana Tschudi, S., Santin, P., Santos, P., Ségransan, D., Schmidt, T. M., Segovia, A., Sosnowska, D., Sozzetti, A., Sousa, S. G., Spanò, P., Suárez Mascareño, A., Tabernero, H., Tenegi, F., Udry, S., and Zanutta, A. (2021). ESPRESSO at VLT. On-sky performance and first results. A&A, 645:A96.

Perez-Becker, D. and Chiang, E. (2013). Catastrophic evaporation of rocky planets. MNRAS, 433(3):2294–2309.

Petigura, E. A., Marcy, G. W., Winn, J. N., Weiss, L. M., Fulton, B. J., Howard, A. W., Sinukoff, E., Isaacson, H., Morton, T. D., and Johnson, J. A. (2018). The California-Kepler Survey. IV. Metal-rich Stars Host a Greater Diversity of Planets. AJ, 155(2):89.

Petigura, E. A., Rogers, J. G., Isaacson, H., Owen, J. E., Kraus, A. L., Winn, J. N., MacDougall, M. G., Howard, A. W., Fulton, B., Kosiarek, M. R., Weiss, L. M., Behmard, A., and Blunt, S. (2022). The California-Kepler Survey. X. The Radius Gap as a Function of Stellar Mass, Metallicity, and Age. AJ, 163(4):179.

Petrus, S., Whiteford, N., Patapis, P., Biller, B. A., Skemer, A., Hinkley, S., Suárez, G., Palma-Bifani, P., Morley, C. V., Tremblin, P., Charnay, B., Vos, J. M., Wang, J. J., Stone, J. M., Bonnefoy, M., Chauvin, G., Miles, B. E., Carter, A. L., Lueber, A., Helling, C., Sutlieff, B. J., Janson, M., Gonzales, E. C., Hoch, K. K. W., Absil, O., Balmer, W. O., Boccaletti, A., Bonavita, M., Booth, M., Bowler, B. P., Briesemeister, Z. W., Bryan, M. L., Calissendorff, P., Cantalloube, F., Chen, C. H., Choquet, E., Christiaens, V., Cugno, G., Currie, T., Danielski, C., De Furio, M., Dupuy, T. J., Factor, S. M., Faherty, J. K., Fitzgerald, M. P., Fortney, J. J., Franson, K., Girard, J. H., Grady, C. A., Henning, T., Hines, D. C., Hood, C. E., Howe, A. R., Kalas, P., Kammerer, J., Kennedy, G. M., Kenworthy, M. A., Kervella, P., Kim, M., Kitzmann, D., Kraus, A. L., Kuzuhara, M., Lagage, P.-O., Lagrange, A.-M., Lawson, K., Lazzoni, C., Leisenring, J. M., Lew, B. W. P., Liu, M. C., Liu, P., Llop-Sayson, J., Lloyd, J. P., Macintosh, B., Mâlin, M., Manjavacas, E., Marino, S., Mar-

ley, M. S., Marois, C., Martinez, R. A., Matthews, E. C., Matthews, B. C., Mawet, D., Mazoyer, J., McElwain, M. W., Metchev, S., Meyer, M. R., Millar-Blanchaer, M. A., Mollière, P., Moran, S. E., Mukherjee, S., Pantin, E., Perrin, M. D., Pueyo, L., Quanz, S. P., Quirrenbach, A., Ray, S., Rebollido, I., Adams Redai, J., Ren, B. B., Rickman, E., Sallum, S., Samland, M., Sargent, B., Schlieder, J. E., Stapelfeldt, K. R., Tamura, M., Tan, X., Theissen, C. A., Uyama, T., Vasist, M., Vigan, A., Wagner, K., Ward-Duong, K., Wolff, S. G., Worthen, K., Wyatt, M. C., Ygouf, M., Zurlo, A., Zhang, X., Zhang, K., Zhang, Z., and Zhou, Y. (2024). The JWST Early Release Science Program for Direct Observations of Exoplanetary Systems. V. Do Self-consistent Atmospheric Models Represent JWST Spectra? A Showcase with VHS 1256–1257 b. ApJ, 966(1):L11.

Planck, M. (1906). *Vorlesungen über die Theorie der Wärmestrahlung*. Leipzig.

Pollacco, D. L., Skillen, I., Collier Cameron, A., Christian, D. J., Hellier, C., Irwin, J., Lister, T. A., Street, R. A., West, R. G., Anderson, D. R., Clarkson, W. I., Deeg, H., Enoch, B., Evans, A., Fitzsimmons, A., Haswell, C. A., Hodgkin, S., Horne, K., Kane, S. R., Keenan, F. P., Maxted, P. F. L., Norton, A. J., Osborne, J., Parley, N. R., Ryans, R. S. I., Smalley, B., Wheatley, P. J., and Wilson, D. M. (2006). The WASP Project and the SuperWASP Cameras. PASP, 118(848):1407–1418.

Pollack, J. B., Hollenbach, D., Beckwith, S., Simonelli, D. P., Roush, T., and Fong, W. (1994). Composition and Radiative Properties of Grains in Molecular Clouds and Accretion Disks. ApJ, 421:615.

Polyansky, O. L., Kyuberis, A. A., Zobov, N. F., Tennyson, J., Yurchenko, S. N., and Lodi, L. (2018). ExoMol molecular line lists XXX: a complete high-accuracy line list for water. MNRAS, 480(2):2597–2608.

Pontoppidan, K. M., Barrientes, J., Blome, C., Braun, H., Brown, M., Carruthers, M., Coe, D., DePasquale, J., Espinoza, N., Marin, M. G., Gordon, K. D., Henry, A., Hustak, L., James, A., Jenkins, A., Koekemoer, A. M., LaMassa, S., Law, D., Lockwood, A., Moro-Martin, A., Mullally, S. E., Pagan, A., Player, D., Proffitt, C., Pulliam, C., Ramsay, L., Ravindranath, S., Reid, N., Robberto, M., Sabbi, E., Ubeda, L., Balogh, M., Flanagan, K., Gardner, J., Hasan, H., Meinke, B., and Nota, A. (2022). The JWST Early Release Observations. ApJ, 936(1):L14.

Posch, T., Kerschbaum, F., Fabian, D., Mutschke, H., Dorschner, J., Tamanai, A., and Henning, T. (2003). Infrared Properties of Solid Titanium Oxides: Exploring Potential Primary Dust Condensates. ApJS, 149(2):437–445.

Powell, D., Louden, T., Kreidberg, L., Zhang, X., Gao, P., and Parmentier, V. (2019). Transit Signatures of Inhomogeneous Clouds on Hot Jupiters: Insights from Microphysical Cloud Modeling. ApJ, 887(2):170.

Powell, D., Zhang, X., Gao, P., and Parmentier, V. (2018). Formation of Silicate and Titanium Clouds on Hot Jupiters. ApJ, 860(1):18.

Prandtl, L. (1925). 7. Bericht über Untersuchungen zur ausgebildeten Turbulenz. *Zeitschrift Angewandte Mathematik und Mechanik*, 5(2):136–139.

Press, W. H., Teukolsky, S. A., Vetterling, W. T., and Flannery, B. P. (2002). *Numerical recipes in C++ : the art of scientific computing.* Cambridge University Press.

Radica, M., Welbanks, L., Espinoza, N., Taylor, J., Coulombe, L.-P., Feinstein, A. D., Goyal, J., Scarsdale, N., Albert, L., Baghel, P., Bean, J. L., Blecic, J., Lafrenière, D., MacDonald, R. J., Zamyatina, M., Allart1, R., Artigau, É., Batalha, N. E., Cook, N. J., Cowan, N. B., Dang, L., Doyon, R., Fournier-Tondreau, M., Johnstone, D., Line, M. R., Moran, S. E., Mukherjee, S., Pelletier, S., Roy, P.-A., Talens, G. J., Filippazzo, J., Pontoppidan, K., and Volk, K. (2023). Awesome SOSS: transmission spectroscopy of WASP-96b with NIRISS/SOSS. MNRAS, 524(1):835–856.

Rappaport, S., Barclay, T., DeVore, J., Rowe, J., Sanchis-Ojeda, R., and Still, M. (2014). KOI-2700b—A Planet Candidate with Dusty Effluents on a 22 hr Orbit. ApJ, 784(1):40.

Rappaport, S., Levine, A., Chiang, E., El Mellah, I., Jenkins, J., Kalomeni, B., Kite, E. S., Kotson, M., Nelson, L., Rousseau-Nepton, L., and Tran, K. (2012). Possible Disintegrating Short-period Super-Mercury Orbiting KIC 12557548. ApJ, 752(1):1.

Ribas, I., Reiners, A., Zechmeister, M., Caballero, J. A., Morales, J. C., Sabotta, S., Baroch, D., Amado, P. J., Quirrenbach, A., Abril, M., Aceituno, J., Anglada-Escudé, G., Azzaro, M., Barrado, D., Béjar, V. J. S., Benítez de Haro, D., Bergond, G., Bluhm, P., Calvo Ortega, R., Cardona Guillén, C., Chaturvedi, P., Cifuentes, C., Colomé, J., Cont, D., Cortés-Contreras, M., Czesla, S., Díez-Alonso, E., Dreizler, S., Duque-Arribas, C., Espinoza, N., Fernández, M., Fuhrmeister, B., Galadí-Enríquez, D., García-López, A., González-Álvarez, E., González Hernández, J. I., Guenther, E. W., de Guindos, E., Hatzes, A. P., Henning, T., Herrero, E., Hintz, D., Huelmo, Á. L., Jeffers, S. V., Johnson, E. N., de Juan, E., Kaminski, A., Kemmer, J., Khaimova, J., Khalafinejad, S., Kossakowski, D., Kürster, M., Labarga, F., Lafarga, M., Lalitha, S., Lampón, M., Lillo-Box, J., Lodieu, N., López González, M. J., López-Puertas, M., Luque, R., Magán, H., Mancini, L., Marfil, E., Martín, E. L., Martín-Ruiz, S., Molaverdikhani, K., Montes, D., Nagel, E., Nortmann, L., Nowak, G., Pallé, E., Passegger, V. M., Pavlov, A., Pedraz, S., Perdelwitz, V., Perger, M., Ramón-Ballesta, A., Reffert, S., Revilla, D., Rodríguez, E., Rodríguez-López, C., Sadegi, S., Sánchez Carrasco, M. Á., Sánchez-López, A., Sanz-Forcada, J., Schäfer, S., Schlecker, M., Schmitt, J. H. M. M., Schöfer, P., Schweitzer, A., Seifert, W., Shan, Y., Skrzypinski, S. L., Solano, E., Stahl, O., Stangret, M., Stock, S., Stürmer, J., Tabernero, H. M., Tal-Or, L., Trifonov, T., Vanaver-

beke, S., Yan, F., and Zapatero Osorio, M. R. (2023). The CARMENES search for exoplanets around M dwarfs. Guaranteed time observations Data Release 1 (2016-2020). A&A, 670:A139.

Ricker, G. R., Winn, J. N., Vanderspek, R., Latham, D. W., Bakos, G. Á., Bean, J. L., Berta-Thompson, Z. K., Brown, T. M., Buchhave, L., Butler, N. R., Butler, R. P., Chaplin, W. J., Charbonneau, D. B., Christensen-Dalsgaard, J., Clampin, M., Deming, D., Doty, J. P., Lee, N. D., Dressing, C., Dunham, E. W., Endl, M., Fressin, F., Ge, J., Henning, T., Holman, M. J., Howard, A. W., Ida, S., Jenkins, J. M., Jernigan, G., Johnson, J. A., Kaltenegger, L., Kawai, N., Kjeldsen, H., Laughlin, G., Levine, A. M., Lin, D., Lissauer, J. J., MacQueen, P., Marcy, G., McCullough, P. R., Morton, T. D., Narita, N., Paegert, M., Palle, E., Pepe, F., Pepper, J., Quirrenbach, A., Rinehart, S. A., Sasselov, D., Sato, B., Seager, S., Sozzetti, A., Stassun, K. G., Sullivan, P., Szentgyorgyi, A., Torres, G., Udry, S., and Villasenor, J. (2014). Transiting Exoplanet Survey Satellite. *Journal of Astronomical Telescopes, Instruments, and Systems*, 1(1):014003.

Rivlin, T., Lodi, L., Yurchenko, S. N., Tennyson, J., and Le Roy, R. J. (2015). ExoMol molecular line lists - X. The spectrum of sodium hydride. MNRAS, 451(1):634–638.

Roberge, A. and Seager, S. (2018). *The "Spectral Zoo" of Exoplanet Atmospheres*, pages 2063–2082. Springer International Publishing, Cham.

Robertson, H. P. (1937). Dynamical effects of radiation in the solar system. MNRAS, 97:423.

Rogers, J. G., Janó Muñoz, C., Owen, J. E., and Makinen, T. L. (2023a). Exoplanet atmosphere evolution: emulation with neural networks. MNRAS, 519(4):6028–6043.

Rogers, J. G. and Owen, J. E. (2021). Unveiling the planet population at birth. MNRAS, 503(1):1526–1542.

Rogers, J. G., Schlichting, H. E., and Owen, J. E. (2023b). Conclusive evidence for a population of water worlds around m dwarfs remains elusive. *The Astrophysical Journal Letters*, 947(1):L19.

Rogers, L. A. (2015). Most 1.6 Earth-radius Planets are Not Rocky. ApJ, 801(1):41.

Rogers, L. A. and Seager, S. (2010). A Framework for Quantifying the Degeneracies of Exoplanet Interior Compositions. ApJ, 712(2):974–991.

Rossow, W. B. (1978). Cloud Microphysics: Analysis of the Clouds of Earth, Venus, Mars, and Jupiter. Icarus, 36(1):1–50.

Rustamkulov, Z., Sing, D. K., Mukherjee, S., May, E. M., Kirk, J., Schlawin, E., Line, M. R., Piaulet, C., Carter, A. L., Batalha, N. E., Goyal, J. M., López-Morales, M., Lothringer, J. D., MacDonald, R. J., Moran, S. E., Stevenson, K. B., Wakeford, H. R., Espinoza, N., Bean, J. L., Batalha, N. M., Benneke,

B., Berta-Thompson, Z. K., Crossfield, I. J. M., Gao, P., Kreidberg, L., Powell, D. K., Cubillos, P. E., Gibson, N. P., Leconte, J., Molaverdikhani, K., Nikolov, N. K., Parmentier, V., Roy, P., Taylor, J., Turner, J. D., Wheatley, P. J., Aggarwal, K., Ahrer, E., Alam, M. K., Alderson, L., Allen, N. H., Banerjee, A., Barat, S., Barrado, D., Barstow, J. K., Bell, T. J., Blecic, J., Brande, J., Casewell, S., Changeat, Q., Chubb, K. L., Crouzet, N., Daylan, T., Decin, L., Désert, J., Mikal-Evans, T., Feinstein, A. D., Flagg, L., Fortney, J. J., Harrington, J., Heng, K., Hong, Y., Hu, R., Iro, N., Kataria, T., Kempton, E. M. R., Krick, J., Lendl, M., Lillo-Box, J., Louca, A., Lustig-Yaeger, J., Mancini, L., Mansfield, M., Mayne, N. J., Miguel, Y., Morello, G., Ohno, K., Palle, E., Petit dit de la Roche, D. J. M., Rackham, B. V., Radica, M., Ramos-Rosado, L., Redfield, S., Rogers, L. K., Shkolnik, E. L., Southworth, J., Teske, J., Tremblin, P., Tucker, G. S., Venot, O., Waalkes, W. C., Welbanks, L., Zhang, X., and Zieba, S. (2023). Early Release Science of the exoplanet WASP-39b with JWST NIRSpec PRISM. Nature, 614(7949):659–663.

Rybicki, G. B. (1971). A modified Feautrier method. J. Quant. Spec. Radiat. Transf., 11:589–595.

Rybicki, G. B. and Lightman, A. P. (1986). *Radiative Processes in Astrophysics*.

Ryde, N., Lambert, D. L., Richter, M. J., and Lacy, J. H. (2002). Detection of Water Vapor in the Photosphere of Arcturus. ApJ, 580(1):447–458.

Samra, D., Helling, Ch., Chubb, K. L., Min, M., Carone, L., and Schneider, A. D. (2023). Clouds form on the hot Saturn JWST ERO target WASP-96b. A&A, 669:A142.

Sanchis-Ojeda, R., Rappaport, S., Pallè, E., Delrez, L., DeVore, J., Gandolfi, D., Fukui, A., Ribas, I., Stassun, K. G., Albrecht, S., Dai, F., Gaidos, E., Gillon, M., Hirano, T., Holman, M., Howard, A. W., Isaacson, H., Jehin, E., Kuzuhara, M., Mann, A. W., Marcy, G. W., Miles-Páez, P. A., Montañés-Rodríguez, P., Murgas, F., Narita, N., Nowak, G., Onitsuka, M., Paegert, M., Van Eylen, V., Winn, J. N., and Yu, L. (2015). The K2-ESPRINT Project I: Discovery of the Disintegrating Rocky Planet K2-22b with a Cometary Head and Leading Tail. ApJ, 812(2):112.

Schaaf, S. A. (1963). Mechanics of Rarefied Gases. *Handbuch der Physik*, 3:591–624.

Schaefer, L. and Fegley, B. (2004). A thermodynamic model of high temperature lava vaporization on Io. Icarus, 169(1):216–241.

Schaefer, L. and Fegley, B. (2009). Chemistry of Silicate Atmospheres of Evaporating Super-Earths. ApJ, 703(2):L113–L117.

Schlawin, E., Herter, T., Zhao, M., Teske, J. K., and Chen, H. (2016). Reduced Activity and Large Particles from the Disintegrating Planet Candidate KIC 12557548b. ApJ, 826(2):156.

Schlawin, E., Hirano, T., Kawahara, H., Teske, J., Green, E. M., Rackham, B. V., Fraine, J., and Bushra, R. (2018). Back to "Normal" for the Disintegrating Planet Candidate KIC 12557548 b. AJ, 156(6):281.

Schlawin, E., Su, K. Y. L., Herter, T., Ridden-Harper, A., and Apai, D. (2021). LBT Reveals Large Dust Particles and a High Mass-loss Rate for K2-22 b. AJ, 162(2):57.

Schlichting, H. E. (2018). Formation of Super-Earths. In Deeg, H. J. and Belmonte, J. A., editors, *Handbook of Exoplanets*, page 141.

Schlichting, H. E. and Young, E. D. (2022). Chemical Equilibrium between Cores, Mantles, and Atmospheres of Super-Earths and Sub-Neptunes and Implications for Their Compositions, Interiors, and Evolution. *The Planetary Science Journal*, 3(5):127.

Schneider, A. D. and Bitsch, B. (2021a). How drifting and evaporating pebbles shape giant planets. I. Heavy element content and atmospheric C/O. A&A, 654:A71.

Schneider, A. D. and Bitsch, B. (2021b). How drifting and evaporating pebbles shape giant planets. II. Volatiles and refractories in atmospheres. A&A, 654:A72.

Schneider, J. (2018). Definition of Exoplanets and Brown Dwarfs. In Deeg, H. J. and Belmonte, J. A., editors, *Handbook of Exoplanets*, page 119.

Schwab, C., Rakich, A., Gong, Q., Mahadevan, S., Halverson, S. P., Roy, A., Terrien, R. C., Robertson, P. M., Hearty, F. R., Levi, E. I., Monson, A. J., Wright, J. T., McElwain, M. W., Bender, C. F., Blake, C. H., Stürmer, J., Gurevich, Y. V., Chakraborty, A., and Ramsey, L. W. (2016). Design of NEID, an extreme precision Doppler spectrograph for WIYN. In Evans, C. J., Simard, L., and Takami, H., editors, *Ground-based and Airborne Instrumentation for Astronomy VI*, volume 9908 of *Society of Photo-Optical Instrumentation Engineers (SPIE) Conference Series*, page 99087H.

Schwarzschild, K. (1906). Ueber das gleichgewicht der sonnenatmosphäre. *Nachrichten von der Gesellschaft der Wissenschaften zu Göttingen, Mathematisch-Physikalische Klasse*, 1906:41–53.

Seager, S. (2010). *Exoplanet Atmospheres: Physical Processes*.

Seager, S., Kuchner, M., Hier-Majumder, C. A., and Militzer, B. (2007). Mass-Radius Relationships for Solid Exoplanets. ApJ, 669(2):1279–1297.

Seager, S. and Mallén-Ornelas, G. (2003). A Unique Solution of Planet and Star Parameters from an Extrasolar Planet Transit Light Curve. ApJ, 585(2):1038–1055.

Seager, S. and Sasselov, D. D. (2000). Theoretical Transmission Spectra during Extrasolar Giant Planet Transits. ApJ, 537(2):916–921.

Sharp, C. M. and Huebner, W. F. (1990). Molecular Equilibrium with Condensation. ApJS, 72:417.

Sherwood Lollar, B., Warr, O., and Higgins, P. M. (2024). The hidden hydrogeosphere: The contribution of deep groundwater to the planetary water cycle. *Annual Review of Earth and Planetary Sciences*, 52(Volume 52, 2024):443–466.

Sindel, J. P., Gobrecht, D., Helling, C., and Decin, L. (2022). Revisiting fundamental properties of TiO_2 nanoclusters as condensation seeds in astrophysical environments. A&A, 668:A35.

Sindel, J. P., Helling, C., Gobrecht, D., Chubb, K. L., and Decin, L. (2023). Infrared spectra of TiO_2 clusters for hot Jupiter atmospheres. A&A, 680:A65.

Sing, D. K., Fortney, J. J., Nikolov, N., Wakeford, H. R., Kataria, T., Evans, T. M., Aigrain, S., Ballester, G. E., Burrows, A. S., Deming, D., Désert, J.-M., Gibson, N. P., Henry, G. W., Huitson, C. M., Knutson, H. A., Lecavelier Des Etangs, A., Pont, F., Showman, A. P., Vidal-Madjar, A., Williamson, M. H., and Wilson, P. A. (2016). A continuum from clear to cloudy hot-Jupiter exoplanets without primordial water depletion. Nature, 529(7584):59–62.

Sing, D. K., Rustamkulov, Z., Thorngren, D. P., Barstow, J. K., Tremblin, P., Alves de Oliveira, C., Beck, T. L., Birkmann, S. M., Challener, R. C., Crouzet, N., Espinoza, N., Ferruit, P., Giardino, G., Gressier, A., Lee, E. K. H., Lewis, N. K., Maiolino, R., Manjavacas, E., Rauscher, B. J., Sirianni, M., and Valenti, J. A. (2024). A warm Neptune's methane reveals core mass and vigorous atmospheric mixing. Nature, 630(8018):831–835.

Siqueira-Mello, C., Chiappini, C., Barbuy, B., Freeman, K., Ness, M., Depagne, E., Cantelli, E., Pignatari, M., Hirschi, R., Frischknecht, U., Meynet, G., and Maeder, A. (2016). Looking for imprints of the first stellar generations in metal-poor bulge field stars. A&A, 593:A79.

Somerville, W. B. (1964). The Continuous Absoprtion Coefficient of the Negative Hydrogen Molecular Ion. ApJ, 139:192.

Somerville, W. B. (1965). The Continuous Absorption Coefficient of HE$\hat{}$. ApJ, 141:811.

Spiewak, R., Bailes, M., Barr, E. D., Bhat, N. D. R., Burgay, M., Cameron, A. D., Champion, D. J., Flynn, C. M. L., Jameson, A., Johnston, S., Keith, M. J., Kramer, M., Kulkarni, S. R., Levin, L., Lyne, A. G., Morello, V., Ng, C., Possenti, A., Ravi, V., Stappers, B. W., van Straten, W., and Tiburzi, C. (2018). PSR J2322-2650 - a low-luminosity millisecond pulsar with a planetary-mass companion. MNRAS, 475(1):469–477.

Stephens, D. C., Leggett, S. K., Cushing, M. C., Marley, M. S., Saumon, D., Geballe, T. R., Golimowski, D. A., Fan, X., and Noll, K. S. (2009). The 0.8-14.5 μm Spectra of Mid-L to Mid-T Dwarfs: Diagnostics of Effective Temperature,

Grain Sedimentation, Gas Transport, and Surface Gravity. ApJ, 702(1):154–170.

Stone, J. M. and Norman, M. L. (1992). ZEUS-2D: A Radiation Magnetohydrodynamics Code for Astrophysical Flows in Two Space Dimensions. I. The Hydrodynamic Algorithms and Tests. ApJS, 80:753.

Stone, J. M. and Proga, D. (2009). Anisotropic Winds from Close-In Extrasolar Planets. ApJ, 694(1):205–213.

Strubbe, L. E. and Chiang, E. I. (2006). Dust Dynamics, Surface Brightness Profiles, and Thermal Spectra of Debris Disks: The Case of AU Microscopii. ApJ, 648(1):652–665.

Struve, O. (1952). Proposal for a project of high-precision stellar radial velocity work. *The Observatory*, 72:199–200.

Suárez, G. and Metchev, S. (2022). Ultracool dwarfs observed with the Spitzer infrared spectrograph - II. Emergence and sedimentation of silicate clouds in L dwarfs, and analysis of the full M5-T9 field dwarf spectroscopic sample. MNRAS, 513(4):5701–5726.

Tan, X. and Showman, A. P. (2019). Atmospheric Variability Driven by Radiative Cloud Feedback in Brown Dwarfs and Directly Imaged Extrasolar Giant Planets. ApJ, 874(2):111.

Taylor, J., Radica, M., Welbanks, L., MacDonald, R. J., Blecic, J., Zamyatina, M., Roth, A., Bean, J. L., Parmentier, V., Coulombe, L.-P., Feinstein, A. D., Espinoza, N., Benneke, B., Lafrenière, D., Doyon, R., and Ahrer, E.-M. (2023). Awesome SOSS: atmospheric characterization of WASP-96 b using the JWST early release observations. MNRAS, 524(1):817–834.

Thompson, S. E., Coughlin, J. L., Hoffman, K., Mullally, F., Christiansen, J. L., Burke, C. J., Bryson, S., Batalha, N., Haas, M. R., Catanzarite, J., Rowe, J. F., Barentsen, G., Caldwell, D. A., Clarke, B. D., Jenkins, J. M., Li, J., Latham, D. W., Lissauer, J. J., Mathur, S., Morris, R. L., Seader, S. E., Smith, J. C., Klaus, T. C., Twicken, J. D., Van Cleve, J. E., Wohler, B., Akeson, R., Ciardi, D. R., Cochran, W. D., Henze, C. E., Howell, S. B., Huber, D., Prša, A., Ramírez, S. V., Morton, T. D., Barclay, T., Campbell, J. R., Chaplin, W. J., Charbonneau, D., Christensen-Dalsgaard, J., Dotson, J. L., Doyle, L., Dunham, E. W., Dupree, A. K., Ford, E. B., Geary, J. C., Girouard, F. R., Isaacson, H., Kjeldsen, H., Quintana, E. V., Ragozzine, D., Shabram, M., Shporer, A., Silva Aguirre, V., Steffen, J. H., Still, M., Tenenbaum, P., Welsh, W. F., Wolfgang, A., Zamudio, K. A., Koch, D. G., and Borucki, W. J. (2018). Planetary Candidates Observed by Kepler. VIII. A Fully Automated Catalog with Measured Completeness and Reliability Based on Data Release 25. ApJS, 235(2):38.

Toon, O. B., Turco, R. P., Hamill, P., Kiang, C. S., and Whitten, R. C. (1979). A One-Dimensional Model Describing Aerosol Formation and Evolution in the

Stratosphere: II. Sensitivity Studies and Comparison with Observations. *Journal of the Atmospheric Sciences*, 36(4):718–736.

Tremblin, P., Amundsen, D. S., Chabrier, G., Baraffe, I., Drummond, B., Hinkley, S., Mourier, P., and Venot, O. (2016). Cloudless Atmospheres for L/T Dwarfs and Extrasolar Giant Planets. ApJ, 817(2):L19.

Tremblin, P., Amundsen, D. S., Mourier, P., Baraffe, I., Chabrier, G., Drummond, B., Homeier, D., and Venot, O. (2015). Fingering Convection and Cloudless Models for Cool Brown Dwarf Atmospheres. ApJ, 804(1):L17.

Tremblin, P., Padioleau, T., Phillips, M. W., Chabrier, G., Baraffe, I., Fromang, S., Audit, E., Bloch, H., Burgasser, A. J., Drummond, B., González, M., Kestener, P., Kokh, S., Lagage, P. O., and Stauffert, M. (2019). Thermo-compositional Diabatic Convection in the Atmospheres of Brown Dwarfs and in Earth's Atmosphere and Oceans. ApJ, 876(2):144.

Tremblin, P., Phillips, M. W., Emery, A., Baraffe, I., Lew, B. W. P., Apai, D., Biller, B. A., and Bonnefoy, M. (2020). Rotational spectral modulation of cloudless atmospheres for L/T brown dwarfs and extrasolar giant planets. A&A, 643:A23.

Tripathi, A., Kratter, K. M., Murray-Clay, R. A., and Krumholz, M. R. (2015). Simulated Photoevaporative Mass Loss from Hot Jupiters in 3D. ApJ, 808(2):173.

Tsuji, T. (2002). Dust in the Photospheric Environment: Unified Cloudy Models of M, L, and T Dwarfs. ApJ, 575(1):264–290.

Udalski, A. (2007). Transit Campaigns of the OGLE-III Survey. In Afonso, C., Weldrake, D., and Henning, T., editors, *Transiting Extrapolar Planets Workshop*, volume 366 of *Astronomical Society of the Pacific Conference Series*, page 51.

Ueda, K., Yanagi, H., Noshiro, R., Hosono, H., and Kawazoe, H. (1998). Vacuum ultraviolet reflectance and electron energy loss spectra of ? *Journal of Physics Condensed Matter*, 10(16):3669–3677.

Underwood, D. S., Tennyson, J., Yurchenko, S. N., Huang, X., Schwenke, D. W., Lee, T. J., Clausen, S., and Fateev, A. (2016). ExoMol molecular line lists - XIV. The rotation-vibration spectrum of hot SO_2. MNRAS, 459(4):3890–3899.

Unterborn, C. T., Dismukes, E. E., and Panero, W. R. (2016). Scaling the Earth: A Sensitivity Analysis of Terrestrial Exoplanetary Interior Models. ApJ, 819(1):32.

Upadhyay, A., Conway, E. K., Tennyson, J., and Yurchenko, S. N. (2018). ExoMol line lists XXV: a hot line list for silicon sulphide, SiS. MNRAS, 477(2):1520–1527.

Valencia, D., Ikoma, M., Guillot, T., and Nettelmann, N. (2010). Composition and fate of short-period super-Earths. The case of CoRoT-7b. A&A, 516:A20.

Valencia, D., Sasselov, D. D., and O'Connell, R. J. (2007). Detailed Models of Super-Earths: How Well Can We Infer Bulk Properties? ApJ, 665(2):1413–1420.

Van Eylen, V., Agentoft, C., Lundkvist, M. S., Kjeldsen, H., Owen, J. E., Fulton, B. J., Petigura, E., and Snellen, I. (2018). An asteroseismic view of the radius valley: stripped cores, not born rocky. MNRAS, 479(4):4786–4795.

Van Eylen, V., Astudillo-Defru, N., Bonfils, X., Livingston, J., Hirano, T., Luque, R., Lam, K. W. F., Justesen, A. B., Winn, J. N., Gandolfi, D., Nowak, G., Palle, E., Albrecht, S., Dai, F., Campos Estrada, B., Owen, J. E., Foreman-Mackey, D., Fridlund, M., Korth, J., Mathur, S., Forveille, T., Mikal-Evans, T., Osborne, H. L. M., Ho, C. S. K., Almenara, J. M., Artigau, E., Barragán, O., Barros, S. C. C., Bouchy, F., Cabrera, J., Caldwell, D. A., Charbonneau, D., Chaturvedi, P., Cochran, W. D., Csizmadia, S., Damasso, M., Delfosse, X., De Medeiros, J. R., Díaz, R. F., Doyon, R., Esposito, M., Fűrész, G., Figueira, P., Georgieva, I., Goffo, E., Grziwa, S., Guenther, E., Hatzes, A. P., Jenkins, J. M., Kabath, P., Knudstrup, E., Latham, D. W., Lavie, B., Lovis, C., Mennickent, R. E., Mullally, S. E., Murgas, F., Narita, N., Pepe, F. A., Persson, C. M., Redfield, S., Ricker, G. R., Santos, N. C., Seager, S., Serrano, L. M., Smith, A. M. S., Suárez Mascareño, A., Subjak, J., Twicken, J. D., Udry, S., Vanderspek, R., and Zapatero Osorio, M. R. (2021). Masses and compositions of three small planets orbiting the nearby M dwarf L231-32 (TOI-270) and the M dwarf radius valley. MNRAS, 507(2):2154–2173.

van Lieshout, R., Min, M., and Dominik, C. (2014). Dusty tails of evaporating exoplanets. I. Constraints on the dust composition. A&A, 572:A76.

van Lieshout, R., Min, M., Dominik, C., Brogi, M., de Graaff, T., Hekker, S., Kama, M., Keller, C. U., Ridden-Harper, A., and van Werkhoven, T. I. M. (2016). Dusty tails of evaporating exoplanets. II. Physical modelling of the KIC 12557548b light curve. A&A, 596:A32.

van Werkhoven, T. I. M., Brogi, M., Snellen, I. A. G., and Keller, C. U. (2014). Analysis and interpretation of 15 quarters of Kepler data of the disintegrating planet KIC 12557548 b. A&A, 561:A3.

Vanderburg, A., Rappaport, S. A., Xu, S., Crossfield, I. J. M., Becker, J. C., Gary, B., Murgas, F., Blouin, S., Kaye, T. G., Palle, E., Melis, C., Morris, B. M., Kreidberg, L., Gorjian, V., Morley, C. V., Mann, A. W., Parviainen, H., Pearce, L. A., Newton, E. R., Carrillo, A., Zuckerman, B., Nelson, L., Zeimann, G., Brown, W. R., Tronsgaard, R., Klein, B., Ricker, G. R., Vanderspek, R. K., Latham, D. W., Seager, S., Winn, J. N., Jenkins, J. M., Adams, F. C., Benneke, B., Berardo, D., Buchhave, L. A., Caldwell, D. A., Christiansen, J. L., Collins, K. A., Colón, K. D., Daylan, T., Doty, J., Doyle, A. E., Dragomir, D., Dressing, C., Dufour, P., Fukui, A., Glidden, A., Guerrero, N. M., Guo, X., Heng, K., Henriksen, A. I., Huang, C. X., Kaltenegger, L., Kane, S. R., Lewis, J. A., Lissauer, J. J., Morales, F., Narita, N., Pepper, J., Rose, M. E., Smith, J. C.,

Stassun, K. G., and Yu, L. (2020). A giant planet candidate transiting a white dwarf. Nature, 585(7825):363–367.

Venturini, J., Guilera, O. M., Haldemann, J., Ronco, M. P., and Mordasini, C. (2020). The nature of the radius valley. Hints from formation and evolution models. A&A, 643:L1.

Vos, J. M., Biller, B. A., Bonavita, M., Eriksson, S., Liu, M. C., Best, W. M. J., Metchev, S., Radigan, J., Allers, K. N., Janson, M., Buenzli, E., Dupuy, T. J., Bonnefoy, M., Manjavacas, E., Brandner, W., Crossfield, I., Deacon, N., Henning, T., Homeier, D., Kopytova, T., and Schlieder, J. (2019). A search for variability in exoplanet analogues and low-gravity brown dwarfs. MNRAS, 483(1):480–502.

Vos, J. M., Faherty, J. K., Gagné, J., Marley, M., Metchev, S., Gizis, J., Rice, E. L., and Cruz, K. (2022). Let the Great World Spin: Revealing the Stormy, Turbulent Nature of Young Giant Exoplanet Analogs with the Spitzer Space Telescope. ApJ, 924(2):68.

Waage, P. and Guldberg, C. (1864). Studier over affiniteten forhandlinger. *VIdenskabs-Selskabet i ChrIstIana*, 35:111–120.

Wagner, K., Follette, K. B., Close, L. M., Apai, D., Gibbs, A., Keppler, M., Müller, A., Henning, T., Kasper, M., Wu, Y.-L., Long, J., Males, J., Morzinski, K., and McClure, M. (2018). Magellan Adaptive Optics Imaging of PDS 70: Measuring the Mass Accretion Rate of a Young Giant Planet within a Gapped Disk. ApJ, 863(1):L8.

Wakeford, H. R., Wilson, T. J., Stevenson, K. B., and Lewis, N. K. (2019). Exoplanet Atmosphere Forecast: Observers Should Expect Spectroscopic Transmission Features to be Muted to 33%. *Research Notes of the American Astronomical Society*, 3(1):7.

Weiss, L. M., Marcy, G. W., Petigura, E. A., Fulton, B. J., Howard, A. W., Winn, J. N., Isaacson, H. T., Morton, T. D., Hirsch, L. A., Sinukoff, E. J., Cumming, A., Hebb, L., and Cargile, P. A. (2018). The California-Kepler Survey. V. Peas in a Pod: Planets in a Kepler Multi-planet System Are Similar in Size and Regularly Spaced. AJ, 155(1):48.

Welbanks, L., Bell, T. J., Beatty, T. G., Line, M. R., Ohno, K., Fortney, J. J., Schlawin, E., Greene, T. P., Rauscher, E., McGill, P., Murphy, M., Parmentier, V., Tang, Y., Edelman, I., Mukherjee, S., Wiser, L. S., Lagage, P.-O., Dyrek, A., and Arnold, K. E. (2024). A high internal heat flux and large core in a warm Neptune exoplanet. Nature, 630(8018):836–840.

Wende, S., Reiners, A., Seifahrt, A., and Bernath, P. F. (2010). CRIRES spectroscopy and empirical line-by-line identification of FeH molecular absorption in an M dwarf. A&A, 523:A58.

Whitworth, A. (2018). Brown Dwarf Formation: Theory. *arXiv e-prints*, page arXiv:1811.06833.

Winn, J. N. (2010). *Exoplanet Transits and Occultations*, pages 55–77.

Winn, J. N. and Petigura, E. (2024). Planet Occurrence from Doppler and transit surveys, 2nd ed. *arXiv e-prints*, page arXiv:2401.16451.

Witte, S. (2011). *Simulation of atmospheric dust clouds*. PhD thesis, Staats-und Universitätsbibliothek Hamburg Carl von Ossietzky.

Witte, S., Helling, C., Barman, T., Heidrich, N., and Hauschildt, P. H. (2011). Dust in brown dwarfs and extra-solar planets. III. Testing synthetic spectra on observations. A&A, 529:A44.

Witte, S., Helling, C., and Hauschildt, P. H. (2009). Dust in brown dwarfs and extra-solar planets. II. Cloud formation for cosmologically evolving abundances. A&A, 506(3):1367–1380.

Woitke, P. and Helling, C. (2003). Dust in brown dwarfs. II. The coupled problem of dust formation and sedimentation. A&A, 399:297–313.

Woitke, P. and Helling, C. (2004). Dust in brown dwarfs. III. Formation and structure of quasi-static cloud layers. A&A, 414:335–350.

Woitke, P., Helling, C., and Gunn, O. (2020). Dust in brown dwarfs and extra-solar planets. VII. Cloud formation in diffusive atmospheres. A&A, 634:A23.

Woitke, P., Helling, C., Hunter, G. H., Millard, J. D., Turner, G. E., Worters, M., Blecic, J., and Stock, J. W. (2018). Equilibrium chemistry down to 100 K. Impact of silicates and phyllosilicates on the carbon to oxygen ratio. A&A, 614:A1.

Wolf, S. and Voshchinnikov, N. V. (2004). Mie scattering by ensembles of particles with very large size parameters. *Computer Physics Communications*, 162(2):113–123.

Wolszczan, A. and Frail, D. A. (1992). A planetary system around the millisecond pulsar PSR1257 + 12. Nature, 355(6356):145–147.

Wright, J. T. (2018). Radial Velocities as an Exoplanet Discovery Method. In Deeg, H. J. and Belmonte, J. A., editors, *Handbook of Exoplanets*, page 4.

Wright, J. T., Tusay, N., Beatty, T. G., Colon, K., Desch, S., Foley, B., Herbst, A., Mittal, T., and Stevens, D. J. (2023). Measuring the Interior Composition of a Terrestrial Planet. JWST Proposal. Cycle 2, ID. #3315.

Yousefi, M. and Bernath, P. F. (2018). Line Lists for AlF and AlCl in the $X^1\Sigma^+$ Ground State. ApJS, 237(1):8.

Yousefi, M., Bernath, P. F., Hodges, J., and Masseron, T. (2018). A new line list for the $A^2\Sigma^+$ -X^2 Π electronic transition of OH. J. Quant. Spec. Radiat. Transf., 217:416–424.

Yurchenko, S. N., Amundsen, D. S., Tennyson, J., and Waldmann, I. P. (2017). A hybrid line list for CH_4 and hot methane continuum. A&A, 605:A95.

Yurchenko, S. N., Bond, W., Gorman, M. N., Lodi, L., McKemmish, L. K., Nunn, W., Shah, R., and Tennyson, J. (2018a). ExoMol molecular line lists - XXVI: spectra of SH and NS. MNRAS, 478(1):270–282.

Yurchenko, S. N., Mellor, T. M., Freedman, R. S., and Tennyson, J. (2020). ExoMol line lists - XXXIX. Ro-vibrational molecular line list for CO_2. MNRAS, 496(4):5282–5291.

Yurchenko, S. N., Sinden, F., Lodi, L., Hill, C., Gorman, M. N., and Tennyson, J. (2018b). ExoMol line lists XXIV: a new hot line list for silicon monohydride, SiH. MNRAS, 473(4):5324–5333.

Yurchenko, S. N., Szabó, I., Pyatenko, E., and Tennyson, J. (2018c). ExoMol line lists XXXI: spectroscopy of lowest eights electronic states of C_2. MNRAS, 480(3):3397–3411.

Yurchenko, S. N., Tennyson, J., Syme, A.-M., Adam, A. Y., Clark, V. H. J., Cooper, B., Dobney, C. P., Donnelly, S. T. E., Gorman, M. N., Lynas-Gray, A. E., Meltzer, T., Owens, A., Qu, Q., Semenov, M., Somogyi, W., Upadhyay, A., Wright, S., and Zapata Trujillo, J. C. (2022). ExoMol line lists - XLIV. Infrared and ultraviolet line list for silicon monoxide ($^{28}Si^{16}O$). MNRAS, 510(1):903–919.

Yurchenko, S. N., Williams, H., Leyland, P. C., Lodi, L., and Tennyson, J. (2018d). ExoMol linelists XXVIII: the rovibronic spectrum of AlH. MNRAS, 479(1):1401–1411.

Zeidler, S., Posch, T., Mutschke, H., Richter, H., and Wehrhan, O. (2011a). Near-infrared absorption properties of oxygen-rich stardust analogs. The influence of coloring metal ions. A&A, 526:A68.

Zeidler, S., Posch, T., Mutschke, H., Richter, H., and Wehrhan, O. (2011b). Near-infrared absorption properties of oxygen-rich stardust analogs. The influence of coloring metal ions. A&A, 526:A68.

Zhu, W., Petrovich, C., Wu, Y., Dong, S., and Xie, J. (2018). About 30% of Sun-like Stars Have Kepler-like Planetary Systems: A Study of Their Intrinsic Architecture. ApJ, 860(2):101.

Zieba, S., Kreidberg, L., Ducrot, E., Gillon, M., Morley, C., Schaefer, L., Tamburo, P., Koll, D. D. B., Lyu, X., Acuña, L., Agol, E., Iyer, A. R., Hu, R., Lincowski, A. P., Meadows, V. S., Selsis, F., Bolmont, E., Mandell, A. M., and Suissa, G. (2023). No thick carbon dioxide atmosphere on the rocky exoplanet TRAPPIST-1 c. Nature, 620(7975):746–749.

Zieba, S., Zilinskas, M., Kreidberg, L., Nguyen, T. G., Miguel, Y., Cowan, N. B., Pierrehumbert, R., Carone, L., Dang, L., Hammond, M., Louden, T., Lupu, R., Malavolta, L., and Stevenson, K. B. (2022). K2 and Spitzer phase curves

of the rocky ultra-short-period planet K2-141 b hint at a tenuous rock vapor atmosphere. A&A, 664:A79.

Zilinskas, M., van Buchem, C. P. A., Miguel, Y., Louca, A., Lupu, R., Zieba, S., and van Westrenen, W. (2022). Observability of evaporating lava worlds. A&A, 661:A126.

Zink, J. K., Hardegree-Ullman, K. K., Christiansen, J. L., Petigura, E. A., Dressing, C. D., Schlieder, J. E., Ciardi, D. R., and Crossfield, I. J. M. (2020). Scaling K2. III. Comparable Planet Occurrence in the FGK Samples of Campaign 5 and Kepler. AJ, 160(2):94.